DCU

Dublin City University
Ollscoil Chathair Bhaile Átha Cliath

Fundamental studies towards the fabrication of electroactive monolithic stationary phases in microfluidic channels

by
Jérémy Galineau

Thesis submitted for the Degree of Doctor of Philosophy

Supervisor:
Prof. Malcolm R. Smyth
Dr. Blánaid White
&
Dr. Aoife Morrin

Dublin City University **January 2011**

DECLARATION

I hereby certify that this material, which I now submit for assessment on the programme of study leading to the award of PhD, is entirely my own work, that I have exercised reasonable care to ensure that the work is original, and does not to the best of my knowledge breach any law of copyright, and has not been taken from the work of others save and to the extent that such work has been cited and acknowledged within the text of my work.

Signed: ____________

(Candidate) ID No.: ____57112819_______

Date: __19/01/2011_____

ACKNOWLEDGEMENTS

First of all, I would like to thank Prof. Malcolm Smyth for giving me the opportunity to work in the sensors and separations group in Dublin City University.

I also would like to thank Dr. Blanaid White, Dr. Aoife Morrin and Prof. Tony Killard for all their support during the last 3 years.

Thanks to Prof. Gordon Wallace, Dr. Micheal Higgins and Dr. Paul Molino for their warm welcome during my research visit to IPRI.

I want to thank Laura, Kyriaki, Ewa, Karl, Subbu and Hannah for their support and kindness throughout my PhD.

Thanks to all my friends, Cuny, Phillipe, Chouket, Chips, Beberto, Sandra, Petra, Anne, Eugénie for all the laughing over the many years we have spent together.

I want to thank my mother who has always been supportive and encouraged me during the worst moments, my stepfather who will always be there and my grandparents.

Finally, thanks Cyrielle for being so supportive and understanding, especially during the writing of this thesis.

DEDICATION

I would like to dedicate this thesis to my father (1956-2008) and my grand father (1931-2008) who tragically lost their lives during the course of this thesis.

TABLE OF CONTENTS

ABBREVIATIONS

A-term	A-term of Van Deemter equation, multiple paths term
AAO	Anodized Aluminium Oxide
AFM	Atomic Force Microscopy
AIBN	Azobisisobutyronitrile
AMPS	2-Acrylamido-2-methylpropane Sulfonic acid
B-term	B-term of Van Deemter equation, diffusion term
BET	Method Brunauer, Emmett and Teller
BSA	Bovine Serum Albumin
C	Concentration
C-18	Octadecyl carbon chain bonded silica stationary phase
C-8	Octyl carbon chain bonded silica stationary phase
C-term	C-term of Van Deemter Equation, resistance to mass transfer term
C^4D	Capacitively Coupled Contactless Conductivity Detector
CD1	Chip design 1
CD2	Chip Design 2
CE	Capillary/Chip Electrophoresis
CEC	Capillary/Chip Electrochromatography
CFD	Computational Fluid Dynamics
CMC	Critical Micellar Concentration
COC	Cyclic Olefin Co-polymer
CV	Cyclic Voltammogram
D	Diffusion Coefficient
DNA	Desoxyribo Nucleic Acid
d_p	Particle diameter
E	Electric field amplitude

EC-AFM	Electrochemical Atomic Force Microscopy
EDL	Electrical Double Layer
EMLC	Electro-Modulated Liquid Chromatography
EMμ	Electroactive Monolithic microchip
EOF	Electroosmotic Flow
E_p	Peak potential
ETMOS	Ethyltrimethoxysilane
FCC	Face Centered Cubic
FITC	Fluorescein isothiocyanate
GDMA	Glycerin 1,3-dimethacrylate
HC	Hexagonal Compact
HETP	Height Equivalent to a Theoretical Plate
HIPE	High Internal Phase Emulsion
HPLC	High Performance Liquid Chromatography
i	Curent intensity
ID	Internal Diameter
i_p	Peak current intensity
i_{pa}	Anodic peak current intensity
i_{pc}	Cathodic peak current intensity
K	Darcy’s flow
k	Reciprocal of EDL thickness
L	Length (precision given in text)
LC	Liquid Chromatography
LLC	Lyotropic Liquid Crystals
LOC	Lab-On-a-Chip
MEMS	Micro-Electromechanical System
m-PD	1,3-PhenyleneDiamine
MTMOS	Methyltrimethoxysilane
N	Plate number

n	Number of electrons involved in an electrochemical reaction
NaDBS	Sodium Dodecylbenzene Sulfonate
NHE	Normal Hydrogen Electrode
ODS	Octadecyl silica (= C-18)
P	Pressure
PAHs	Polycyclic aromatic hydrcarbons
PANI	Polyaniline
PCB	Printed Circuit Board
pDADMAC	PolyDiAllylDiMethylAmmonium Chloride
PDF	Pressure Driven Flow
PDMS	PolyDiMethylSiloxane
Pe	Peclet number
PEG	PolyEthylene Glycol
PET	Polyethylene Terephthalate
PMMA	PolyMethyl Methacrylate
PPy	Polypyrrole
PS	Polystyrene
PSA	Pressure Sensitive Adhesive
PSS	Polystyrene Sulfonate
PTMOS	Phenethyltrimethoxysilane
PVDF	Polyvinylidene fluoride
PVS	Polyvinyl sulfonate
q	Darcy's flow
R	Capillary radius
R^2	Coefficient of determination
Re	Reynolds number
R_s	Solution/electrolyte resistance
RSD	Relative Standard Deviation
SCE	Saturated Calomel Electrode

SDS	Sodium Dodecyl Sulfate
SEM	Scanning Electron Microscopy
STM	Scanning Tunneling Microscopy
TEM	Transmission Electron Microscopy
TMOS	Tetramethoxysilane
t_r	Retention time
u	fluid/mobile phase velocity
UHPLC	Ultra High Performance Liquid Chromatography
u_p	Average fluid velocity
UV	Ultra Violet
V	Fluid velocity/Potential drop
V_1	Potential drop across the induced bulk charge in EDL diffuse layer
V_2	Potential drop across a particle
V_3	Potential drop across the EDL situated downstream
$w_{1/2}$	Peak width at half-height
f	External forces
Q	Volumetric flow rate
α	Particle shape and the packing structure coefficient
β	Dimensionless parameter (Equation 3.14)
ε_0	Vaccum permittivity
ε_r	Media permittivity
η	overpotential
λ_d	EDL thickness
μ	Fluid viscosity
µTAS	Micro-Total Analysis Systems
ν	Scan rate
ρ_0	Fluid density
ρ_e	Net electrical charge density
σ^*	Packed column filled with electrolyte conductivity

σ_b	Empty column filled with electrolyte conductivity
ψ	Electric potential due to the wall charges
ζ	zeta-potential
ζ_p	Particle zeta-potential
ζ_p^*	Apparent zeta-potential
ζ_w	Wall zeta-potential

ABSTRACT

The long term goal of this project is to develop a monolithic stationary phase which utilises an electroactive polymer combining the advantages of EMLC, monolithic technology and microfluidic separation, thus creating an electroactive monolithic microchip (EMμ).

In this thesis, fundamental studies towards the fabrication of EMμ are presented, *i.e.* integration of an electrochemical cell into a microfluidic chip, colloidal crystallization in microfluidic channels and PANI growth through a colloidal crystal template.

Polyaniline was selected as the electroactive material for the fabrication of the monolithic stationary phase as its use for EMLC had already been demonstrated. Colloidal crystals have been used to microstructure materials and the inverse opal structure comprises pore sizes of the order of what was needed for EMμ; therefore electropolymerization of aniline through a polystyrene colloidal crystal template strategy was chosen.

Two alternative chip designs, CD1 and CD2, were investigated for this thesis. Their applicability for EMμ was assessed in terms of their flow velocity profile using computational fluid dynamic, colloidal crystallization feasibility and electrochemical behavior using ferricyanide electrochemistry.

The integration of a fully operational three-electrode electrochemical cell within a microfluidic channel and its use for polyaniline electropolymerization was demonstrated, and self-assembly of the sacrificial polystyrene template in these channels was shown. Polyaniline microstructure morphology exhibited a dependence on the surfactant concentration present in the polystyrene suspension.

Finally, electrochemical switching of conducting polymer within microfluidic channels was assessed by studying polypyrrole switching by atomic force microscopy (AFM). Pore swelling and contraction was observed on application of a potential, demonstrating that the monolith properties could be dynamically controlled. It was found that volume increase in the polymer could be responsible for a deformation of flow through pores due to physical confinement of the polymer.

CHAPTER 1 LITERATURE SURVEY

The extensive application of monolithic columns for HPLC is severely hindered by a lack of column-to-column reproducibility. The EMµ (electroactive monolithic microchip) concept developed throughout this thesis aims to solve these significant reproducibility problems, as well as allowing miniaturization and improving overall efficiency through dynamic separations. The long-term goal of this project is to use an electroactive microstructured monolith to perform dynamic separations as the monolithic stationary phase surface properties can be finely tuned before and during separations by applying an electrical potential to it. Unlike alternative monoliths, which are usually UV or thermally polymerized, EMµ monolith is comprised of an electroactive polymer such as polyaniline (PANI) and can be electropolymerized, enabling a controllable and reproducible fabrication process. In addition, this monolith is microstructured and sacrificial polystyrene colloidal crystal template approach was investigated this goal. This thesis presents fundamental studies required to fabricate an electroactive monolith in microfluidic format, *i.e.* integration of an electrochemical cell into a microfluidic chip, colloidal crystallization in microfluidic channels and PANI growth through a colloidal crystal template.

1.1 INTRODUCTION TO CHROMATOGRAPHY

1.1.1 DEFINITION OF CHROMATOGRAPHY

Liquid chromatography is a separation technique used to isolate a targeted compound (preparative chromatography) or to quantitatively analyze individual compounds in a solution (analytical chromatography). A mobile phase loaded with a plug of solution containing analytes is passed through a porous bed or stationary phase packed in a column. The targeted analytes are separated as they migrate through the column and are detected as they elute from the column. Analyte molecules repeatedly equilibrate between the mobile and stationary phases. The difference in migration observed for each analyte (*i.e.* the separation of analytes) results from the equilibrium distribution of the different analytes between the stationary phase and the mobile phase[1]. For instance, when an analyte has a greater affinity for the mobile phase it is retained to a lesser extent by the stationary phase. Thus, it will elute from the column first. This situation is reversed for the compound eluting from the column last: it has more affinity for the stationary phase and, thus is more retained by it. Efficient mass transfer between the two phases is key to achieving high separation efficiencies.

Rapid mass transfer is optimized by having a small diffusion distance through the porous bed and a large surface area for analyte adsorption. Decreasing stationary phase particle sizes allows for more rapid mass transfer, therefore, higher efficiency. In the early days of liquid chromatography large particles were employed (50 μm)[2]. It was only in the 1950s that particle size was decreased dramatically, and by pressurizing the mobile phase, High Performance Liquid Chromatography (HPLC) emerged[3, 4]. The hydraulic resistance of the stationary phase should be low enough to permit the use of a low pressure pumping system or a long length of stationary phase. These two requirements: rapid mass transfer between mobile phase and stationary phase and low hydraulic resistance of stationary phase are not necessarily compatible and finding the optimum compromise has driven research in this area for the last 40 years[5].

1.1.2 FACTORS INFLUENCING BAND BROADENING

Two factors contribute to how well compounds are separated by chromatography: difference in elution times between peaks, and broadness of peaks – the wider the peaks, the poorer the separation. Separation efficiency of a chromatographic system can be considered in terms of theoretical plates with each plate representing the equilibrium of analyte molecules between the mobile phase and the stationary phase. The number of these theoretical plates in a separation column is directly related to its separation efficiency. The number of plates is calculated by examining the elution peak of the analyte as shown by Equation 1.1.

$$N = 5.55\left(\frac{t_r}{w_{1/2}}\right)^2 \qquad \text{(Equation 1.1)}$$

where:

- N is the number of theoretical plates;
- t_r is the analyte retention time (min);
- $w_{1/2}$ is the analyte peak width at half-height (min).

The number of plates is therefore different for each analyte. Knowing the length of the chromatographic column (L in m), the height equivalent of a theoretical plate (HETP in plates/m) can be calculated (Equation 1.2).

$$HETP = \frac{L}{N} \qquad \text{(Equation 1.2)}$$

The smaller HETP, the narrower the chromatographic band, the better the separation.

Broadening of analyte chromatographic bands (band broadening) can be observed during chromatographic separations. A number of factors including multiple paths (formerly called Eddy diffusion) and mass transfer affect band broadening. Multiple paths term refers to the microscopic flow streams observed in the mobile phase. Movement of analytes in these flow paths of different length, leads to an increase in the final bandwidth. Mass transfer is complex and arises from three different phenomena, the mobile phase mass transfer (analyte molecules are moving faster in the center of a flow path than at the edge of the stationary phase), the stagnant mobile phase mass transfer (stationary phases are often porous and mobile phase is non-moving in these pores, analytes can diffuse into these pores, but all analytes do not travel the same distance into the pores, thus they do not spend the same time inside the pores) and stationary phase mass transfer (when analytes penetrate the stationary phase they do not all spend the same time traveling through the stationary phase)[1]. Tailoring of stationary phases to reduce band broadening, and thus improve separation efficiency, is one of the most exciting areas in chromatography research.

The Van Deemter equation[6] given below (Equation 1.3) allows the mobile phase velocity (u) at which the plate height is lowest, i.e. the column efficiency highest, to be determined.

$$HETP = A + \frac{B}{u} + C.u \qquad \text{(Equation 1.3)}$$

where:

- A represents multiple flow paths;
- B longitudinal diffusion of analytes in mobile phase;
- C the resistance of the analytes molecules to mass transfer between stationary phase and mobile phase.

1.1.3 LIMITATIONS OF HPLC

The search for high throughput separations of complex samples has driven conventional HPLC to its limits. Reducing stationary phase particle sizes in a packed bed columns is known to increase column efficiency as mass transfer is reduced. However, the hydraulic resistance of the packed bed increases dramatically when particle size is reduced[1, 5, 7] (pressure drop through a column is inversely proportional to the square of the particle diameter), necessitating high pressure pumping systems. For decades, pumping systems limited the particle size to 3-5 μm in diameter, operating at pressures of the order of 400-500 bar. More recently however, commercial systems can use sub-2 μm particles by using pressures up to 1200 bar, leading to the emergence of a new field, Ultra High Performance Liquid Chromatography (UHPLC). However, the use of sub-2 μm particles in combination with a high pressure pumping system is costly, both in terms of the instrumentation required as well as maintenance. Fused core technology is another emerging solution to reduce resistance to mass transfer. Fused core particles are particles with a solid silica core and a porous silica shell. The analytes can only diffuse in the porous outer shell, reducing diffusion lengths of the analytes, thus enabling the use of high flow rates without band broadening due to slow mass transfer[8, 9].

Although these new techniques described above are promising, they all rely on the ability of packing small particles into a column. The packing of these small particles is not trivial. An alternative technology to UHPLC and fused core particles is monolithic stationary phases, discussed in Section 1.2.

1.2 INTRODUCTION TO MONOLITHIC STATIONARY PHASES

The pursuit of a superior method to fabricate a stationary phase without compromising on column efficiency and analysis time has lead researchers to develop silica and organic polymer monolithic columns for separations in the late 1980’s[10-12]. Given its success, the use of monolithic columns in chromatography has since been widely studied over the past two decades[5, 13]. These stationary phases are fabricated from a single piece of porous solid with a bimodal pore size distribution (meso-and macro-pores). Macro-pores, with a size range of 2-5 μm and interconnected flow paths (Figure 1.1) provide high permeability required for low hydraulic resistance while mesopores with a size range of 15-50 nm provide the large surface area required for high column efficiency[5].

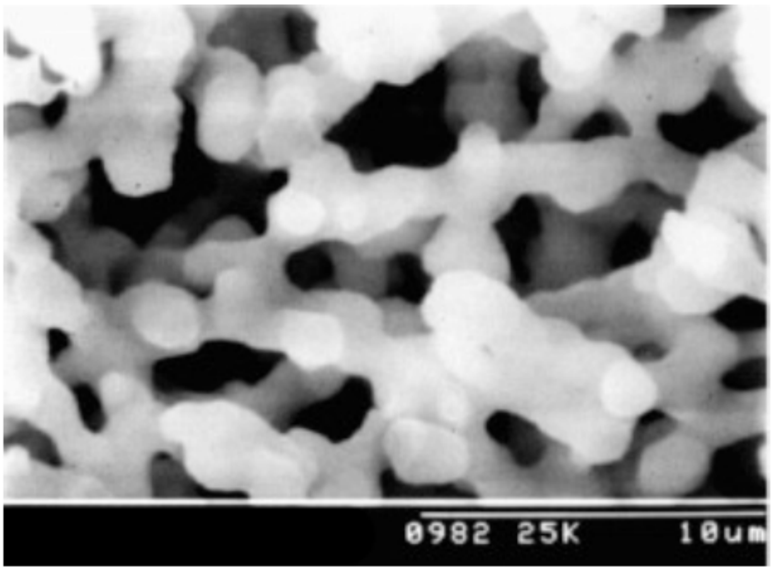

Figure 1.1: Scanning electron micrograph (SEM) of a silica monolith fabricated by Tanaka *et al.*[14]

1.2.1 TYPES OF MONOLITHIC STATIONARY PHASES

There are two different materials from which monoliths are generally fabricated: silica and organic polymer. Silica monoliths were pioneered by Nakanishi and Tanaka[15-18] while organic polymer monoliths were initially developed by Hjertèn *et al.*[12] in the form of hydrophilic gels and followed by Svec and Fréchet[19] in the form of hydrophobic gels.

The main difference between the silica and organic polymer materials used for fabrication of monoliths resides in the pore structure of the porous beds. Silica monoliths exhibit a bimodal pore distribution: macropores with a size > 1 µm (decreasing hydraulic resistance) and mesopores with a size comprised of 15-50 nm (increasing surface area, required for retention and selectivity). They are fabricated by a sol-gel process. During this process a porogen, which is usually a water-soluble polymer such as poly(acrylic acid), first creates the macropores by phase separation between the inorganic polymer and the water soluble polymer while urea (present in the mixture from the start) decomposes, liberating ammonia which creates mesopores during aging and hydrothermal processes. Silica monoliths have large surface areas and are suitable for high efficiency separations of small and large molecules. However, the narrow range of pore and domain size distributions attainable with silica monoliths has largely contributed to the drive to develop organic polymer monoliths[5]. The domain size is the sum of the average size of the flow-through pores and the mesopores (often estimated using SEM images of the stationary phases). The pH in which the silica monolith can be used is limited, as pH above 9 would result in the destruction of the silica backbone. However, silica monoliths have a higher pressure stability than organic polymer monoliths as the latter can be compressed when high pressures are used. The pressure an organic polymer can withstand is directly related to the throughpore size.

Organic polymer (*e.g.* polystyrene (PS), polyacrylate) monoliths display only macropores. The fabrication process of organic polymer monoliths for separation generally involves three steps. First, the column is treated so that the polymer will adhere to the column surface. Thus there is no bypassing of the flow (channeling) between the column wall and the stationary phase. The second step is the polymerization or polycondensation of the monomers in the presence of a porogen. The mixture containing the monomers, porogen or mixture of porogen and initiator is loaded into the column. When initiated, the polymeric chain formed precipitates as a phase separation occurs between the porogen and polymer. The third step is the modification of the polymer surface chemistry. The polymer is not mesoporous itself and so only a unimodal pore size is observed. Organic polymer monoliths have, as a consequence, a smaller surface area than silica monoliths. They are usually used for separation of large molecules, for which mesopores are not required, as the large molecules cannot diffuse through them. These monoliths show high throughput separations of large biomolecules, *e.g.* nucleotides and proteins and as such are usually used in genomics and proteomics. In addition, biologists are reluctant to use silica for separation of labile samples even after the publications of Horváth, 25 years agoas reported in the literature[5, 20] where Horváth demonstrated that there was no evidence to fear biomolecule separations on silica.

Silica monoliths should be used for high efficiency separations of small molecules whereas organic polymer monoliths can be used for high throughput separations of large (biological) molecules. They are, therefore, complimentary. However, to date only BIA separations® and Dionex® commercially offer polymer monoliths. Silica monoliths on the other hand are widely available commercially. As opposed to silica, a large variety of polymeric columns can be made but selecting the right material has been an issue for industry[5] with no material emerging as a viable alternative to silica to date.

1.2.2 ADVANTAGES OF MONOLITHIC STATIONARY PHASES

By employing a monolithic column instead of a conventional packed column, the multiple flow path term (A-term) is significantly reduced as induced laminar flow and large flow-through pores result in fewer available paths through the column. As it is a single piece of material, the absence of interparticular voids further decreases the A-term[21]. The column efficiency is therefore improved.

Mass transfer, the C-term of Van Deemter equation, is greatly improved in monolithic columns due to the enhanced convective mass transfer[22, 23]. Monolithic columns can be thought of as if the column was packed with a single gigantic flow-through particle (the size of the column). Thus, monolith permeability is high as compared to a packed column and less intraparticle mass transfer resistance is observed. Therefore, the C-term of the Van Deemter equation also decreases. The reduction of intraparticle mass transfer resistance is due to the shorter length of the diffusion path through the monolith skeleton compared to porous silica particles used in conventional packed beds columns.

The decrease in both the A-term and C-term for monolithic columns reduces HETP resulting in more efficient separations than packed column technologies[23]. However, Van Deemter plots do not assess separation throughput and so knowing the A-term and C-term are not enough to compare inter-column performance. Analysis time must also be taken into account and by compiling Van Deemter plots with analysis time, kinetics plots are developed giving a better measure for column comparisons.

In monoliths, higher flow rates can be used as the pressure drop is lowered. It was demonstrated by Leinweber *et al.*[24] that the mass transfer properties of typical monolithic columns corresponded with an equivalent dispersion particle diameter of 3 µm in a packed column. The hydraulic permeability, however, of monolithic columns corresponded with an equivalent permeability particle diameter of 15 µm. Therefore, monolithic columns combine mass transfer properties of particulate columns packed with small particles, with the low back pressure that is observed with particulate columns packed with large particles. Thus, kinetic plots illustrate a significant improvement of column performance for a monolithic column compared with a conventional 5 µm C18-silica bead column.

The unique properties of monolithic columns and their distinct advantages over packed column technology make them an ideal candidate for the next generation of column technology. The low backpressure observed for monolithic columns enable their use on existing HPLC instruments, as opposed to sub-2 µm particle technologies that require high pressures and hence expensive instrumentation. Despite the higher separation throughput, monoliths have yet to experience widespread commercialization. It is believed, however, that when the patents protecting monolithic columns expire this decade, monolithic materials could quickly dominate the market of chromatographic columns[5].

In addition, the search for lower solvent consumption and analysis of low sample quantities while maintaining high throughput separations has resulted in a decrease in column size. The miniaturization of separation techniques has first lead to narrow bore columns, followed by separations being carried out on-chip as part of lab-on-chip (LOC) or micro Total Analysis Systems (μTAS). Packed bed technologies are not suitable for such miniaturized systems as the packing of the stationary phase in such small channels is extremely difficult. Monoliths, however, can be readily formed in any desired shape and dimension. This versatility of monolithic stationary phases make them ideal candidates candidate for μTAS.

1.2.3 LIMITATIONS OF MONOLITHIC COLUMNS

An observed lack of column-to-column reproducibility[22] as well as low efficiencies (compared to theoretical expectations) have limited widespread implementation of monolithic columns. The lack of reproducibility arises from the monolith fabrication process. Silica monoliths are usually fabricated according to the technique described by Tanaka *et al.*[15, 25, 26] For a silica-based monolith, a slight fluctuation in temperature within the material (caused by localized exothermic reactions during polymerization) can drastically alter the resulting monolith morphology, thus leading to a lack of column-to-column reproducibility[27]. Tanaka *et al.* concluded that the “individual preparation and subsequent chemical bonding can lead to problems in reproducibility”[28] after reporting a column-to-column reproducibility of 15% for HETP and pressure drop. Chemical bonding is necessary to graft C-18 or C-8 (the most commonly used phases) hydrophobic moieties onto the silica backbone for reversed-phase chromatography and this adds to irreproducibility as the grafting yield varies for different monolithic structures.

For both organic and silica monoliths formation, UV-and thermal-initiations of polymerization reactions are usually used. Exothermic reactions such as polycondensation, polymerization and crosslinking can occur during the reaction causing unpredictability in fabrication as well as variability in the final separation efficiency. These exothermic reactions create a radial thermal gradient from the centre of the monolith to the edges, which leads to radial heterogeneities. Radial heterogeneities are responsible for many of the observed reduced efficiencies in monolithic columns. In particular, flow-through pore size heterogeneities have been reported[28, 29]. Mobile phase velocity is determined by local permeability (Darcy's Law). Therefore if permeability varies across the column or channel, so too will the linear velocity of the mobile phase. This leads to band broadening (therefore to reduced separation efficiency) as described by the Van Deemter equation (Section 1.2). Galarneau *et al.*[29] reported that poor column performance (HETP of 40 μm) using narrow bore silica monolithic columns, which could be explained by a high number of radial heterogeneities, which resulted in random fluctuations of throughpore size.

Theoretically, monolithic stationary phases should decrease HETP, hence increase column efficiency due to a reduction of the multiple paths and resistance to mass transfer terms in Van Deemter equation (Equation 1.3). However, in practice, radial heterogeneities, created during monolith fabrication, decrease expected performances and monolithic stationary phases performances merely match conventional packed column efficiencies. In addition, monolithic stationary phases are not batch-to-batch reproducible and therefore, they cannot dominate the column market.

1.3 RECENT ADVANCES IN CHIP CHROMATOGRAPHY STATIONARY PHASES

1.3.1 CONVENTIONAL PARTICULATE PACKED SEPARATION CHANNELS

In the early years of chip chromatography, microfluidic channels were packed as for conventional liquid chromatography using silica particles. Packing techniques were derived from those used for packing fused silica capillaries with only a few research publications reporting the use of such particulate packing materials in microfluidic channels, as described below.

1.3.1.1 Use of frits

To pack a fused silica capillary, frits are usually used to prevent bleeding of the stationary phase beads. Retention frits are fabricated by heating the silica beads to sinter them. Thus, they act as a filter and retain the silica beads within the capillary.

Yin *et al.*[30] recently used silica bead sintering on microfluidic chips for Agilent technologies®. Frits were fabricated and the enrichment (40 nL) and separation (75 µm wide x 50 µm deep x 45 mm long) channels were loaded with ZORBAX 300SB-C18 5-µm particles and ZORBAX 300SB-C18 3.5-µm particles respectively. Using a gradient separation, the chip was used to separate 20 fmol of bovine serum albumine (BSA) digest at 100 nL/min (Figure 1.2). A standard deviation of less than 1 % for retention time and 5% for peak area on four selected ions was found for triplicate analysis.

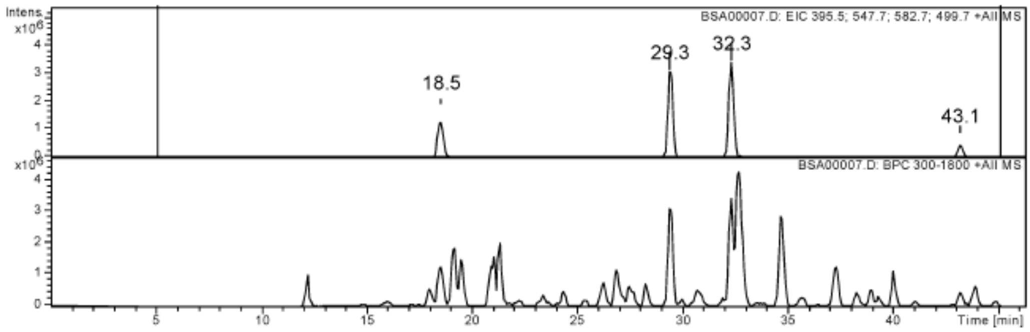

Figure 1.2: (top) Extracted ion current (EIC) chromatogram of four ions (395.5, 547.7, 582.7, 499.7) and (bottom) base peak chromatogram of 20-fmol BSA digest at 100 nL/min. From Yin *et al.*[30]

Xie *et al.*[31] used microfabricated posts, fabricated during the photolithographic fabrication of the chip, as a frit to pack a 1.2 cm long column (100 µm wide x 20 µm deep) with Polaris 3-µm C18-A silica-beads. The chip was used for separation of trypsin digest of BSA. However, the incorporation of on chip electro-pumps lead to non-reproducible separations.

The use of frits is a widely used technique in LC. However, it cannot be used in chip electrochromatography (CEC) as problems can occur[32, 33]. Heating the chip where the frits are formed increases the fragility of the chip, the frit induces non-uniformity of the electroosmostic flow (EOF), and air bubbles are formed at the junction between the packed and the open tube. The EOF inhomogeneities in the frit region cause band broadening during sample injection at the inlet frit and band broadening when analytes migrate from packed areas to an open area before detection at the outlet frit. Frits could also decrease the sensitivity as the analytes can be adsorbed on the frit surface[34]. In addition, the formation of bubbles, while not fully understood, has a dramatic effect on CEC efficiency[35].

1.3.1.2 Frit-less packing

In order to overcome the issues raised by frits in employing CEC, frit-less alternatives have been proposed. The frit-less alternatives all require a specific chip design.

1.3.1.2.1 Use of weirs

Weirs have been explored as an alternative to frits in microfluidic devices. Weirs are a sudden reduction of the channel depth so that particles become trapped but liquid flow can be achieved.

Oleschuk *et al.*[36] used a simple glass chip for solid phase extraction and CEC in which octadecylsilica beads (1.5 µm in diameter) were entrapped between 2 weirs. A slurry of silica beads in acetonitrile was electroosmotically pumped into a 10 µm deep and 200 µm long chamber. The beads were retained between two 9 µm weirs (Figure 1.3).

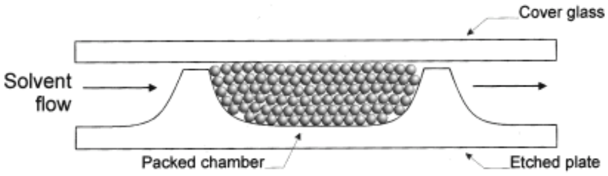

Figure 1.3: Schematic of cross section of packed chamber, showing weir heights in relation to channel depth and particle size. Electroosmotic flow is driven by the walls and by free silanol groups on particles. From Oleschuk *et al.*[36]

The efficiency of this short channel was only 50,000 – 100,000 plates/m (HETP: 10-20 µm) for the separation of two fluorescent dyes in a 30% acetonitrile/70% 50 mM sodium acetate mobile phase. This low efficiency was due to the instability of the packing inside the channel. Indeed, the particles were only stabilized by hydrophobic interactions so after repeated runs voids in the bed were created. By using a mobile phase with a higher concentration of acetonitrile, it was demonstrated that the bed was further destabilized [37].

The stability of this was improved by entrapping the particles in a monolithic poly(ethylene di-methacrylate) plug immediately after packing. Improved efficiencies of 420 000 plates/m and 115 000 plates/m were achieved for acridine orange and boron-dipyrromethene (BODIPY) respectively.

Further improvements using pressure driven packing in addition to electroosmotic packing to prevent voids were developed by this research group [38]. 1 and 2 mm long separation channels showed great enhancements of separation efficiencies with up to 330,000 plates/m for the 1 mm long channel and up to 590,000 plates/m for the 2 mm long channel for the separation of BODIPY fluorescent dye. However, the 5 mm long channel showed decreased efficiencies as some voids were formed in the bed during packing.

However, the use of weirs requires design, which could be not amenable to mass production, In addition, the formed weirs could disrupt the flow velocity profiles and therefore, increase band broadening (see Chapter 3, Section 3.4.1).

1.3.1.2.2 Use of tapers

Tapers have also been investigated as an alternative to frits. Tapers and restrictors were used by Lord *et al.*[39] to eliminate frits in capillaries. They suggested that by making one end of the capillary narrower (Figure 1.4) than the inner diameter of the capillary, a key stone effect could occur in this taper, thus no frits were required. Capillaries were packed with 3 μm silica particles and separation of 6 steroids was demonstrated.

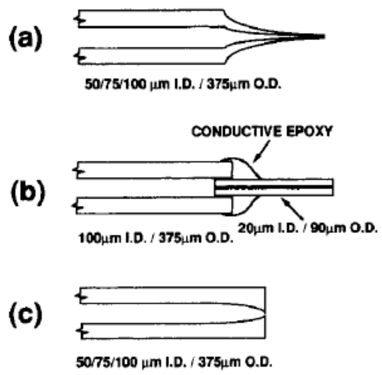

Figure 1.4: Cross sections of capillary inlet/outlet profiles. (a) Single external taper for column outlet/inlet, (b) restrictor capillary for column outlet/inlet, (c) single internal taper for column outlet. From Lord *et al.*[39]

This taper technique was also applied in microchips. Ceriotti *et al.*[40] described a new channel design in polydimethylsiloxane (PDMS) with a taper layout (Figure 1.5).

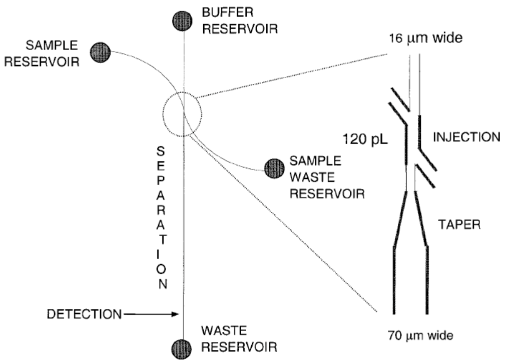

Figure 1.5: Chip layout for fritless CEC in PDMS. The channel structure consists of two side channels entering into the main channel to form slanted T intersections. This so-called “double-T” injection allows pinched injection of small, well-defined volumes of sample into the straight column. As shown in the close-up, the separation column includes a gradual tapering just below the intersection, which is used to stop stationary-phase particles, leaving the injector particle-free. From Ceriotti *et al.*[40]

The chromatographic properties of this packing were assessed using methanol as an unretained compound and benzaldehyde. The baseline separation of these two compounds was achieved in less than 15 s in a 1.7 cm long column at 500 V/cm demonstrating the high throughput separation capabilities of the microfluidic chip. A mixture of four amino acids was also separated successfully (Figure 1.6) in less than 60 s. A run-to-run retention time reproducibility of less than 0.3 s was observed but column-to-column reproducibility was poor due to differences in the packing length and the instability of PDMS.

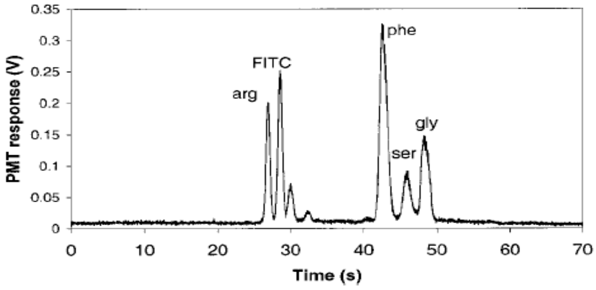

Figure 1.6: Electropherogram of a mixture of 10 μM FITC-labeled amino acids, achieved in an oxidized PDMS/glass device. Total column length: 6 cm; effective column length: 2.5 cm; E: 580 V/cm; buffer, 100 mM Tris-20mM boric acid (pH 9); detection system, Ar^+ laser (488 nm) and band-pass filter at 520 nm; and control system, PC with Labview®. From Ceriotti *et al.*[40]

Gaspar *et al.*[41] created a temporary taper by pressing onto the chip using a metal rod and a magnetic valve where the end of the packing was desired (Figure 1.7) before releasing the pressure to bring the channel back to its original dimensions. The stationary phase bed was stabilized by sintering the stationary phase reverse-phase C-18 beads and by strong interactions between the C-18 particles and the hydrophobic PDMS surface. Gaspar *et al.*[42] later demonstrated the use of this packed chromatographic bed in CEC mode by separating three cephalosporin antibiotics. As the applied pressure application zone was manually adjusted, it was expected that column-to-column reproducibility would be variable.

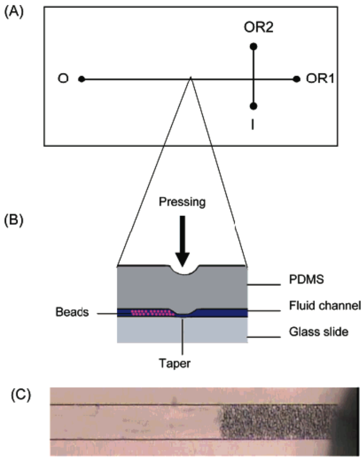

Figure 1.7: (A, B) Schematic illustration of the packing of a microchannel in a PDMS chip through pressing the top of the flexible PDMS chip to trap the chromatographic beads (not to scale; I, sample inlet; O, separation outlet; OR1 and OR2 are outlet reservoirs; the suspension of particles is pumped from O, (C) optical micrographs of the fluid channel in front of the tapering after the pumping of the suspension of C18 particles. From Gaspar *et al.*[41].

1.3.1.2.3 Self-assembly

Another well-known technique to avoid the formation of frits is to pack the chip channel by self-assembly. This technique is the most amenable to mass production. The property of colloidal particles to form colloidal crystals has been widely studied[43, 44].

Kamp *et al.*[45] demonstrated the colloidal crystallization of polystyrene (PS) microspheres (225 nm) in capillary by pressure assisted microsphere assembly. The formed colloidal crystal was infused with silica precursors and silica inverse opals were created. The use of the colloidal crystal and inverse opals as a chromatographic stationary phase was however not demonstrated.

However, self-assembly of microspheres has not been widely applied to fabrication of stationary phases in microchips. Park *et al.*[46] have used a self-assembly technique to pack a simple cross chip (Figure 1.8) with colloidal silica (diameter: 800

nm). The technique employed to pack this column was based on the capillary forces generated inside the channel (Figure 1.8). Separation of FITC-derivatized amino acids was achieved in a 2.5 mm long channel in less than 50 s. Large band broadening was observed, possibly due to the injection and the quality of the packing at the channel walls.

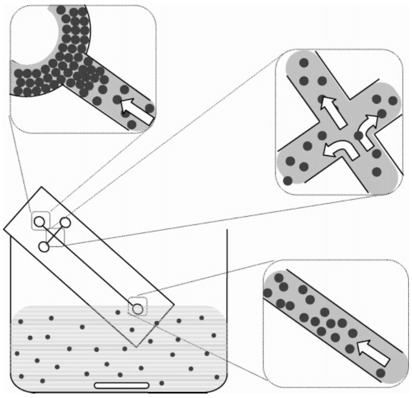

Figure 1.8: Illustration of self-assembly silica packing of microchannels. From Park *et al.*[46]

The reproducibility of the migration time and peak height was assessed using FITC-derivated arginine injected 10 times and detected after 2 mm from injection. An RSD of 1.3% was found for retention time, and an RSD of 3.4% was achieved for peak height. This technique will be discussed in more detail in Chapter 6.

1.3.2 MONOLITHIC STATIONARY PHASES FOR ON-CHIP CHROMATOGRAPHY

Over the past few years, particulate packed beds have not been commonly used for chip chromatography. The difficulty in obtaining reproducible packed chromatographic beds in microfluidic platforms and the need of singular designs (*e.g.* microfabricated frits, tapers or weirs) have pushed research towards developing new materials for chip chromatography.

Monolithic stationary phases, constituted from a single piece of porous material, are at the heart of research in chip chromatography. These materials are generally chemically polymerized on-chip. A monomer mixture mixed with a porogen is loaded into the microfluidic channel and polymerized using heat or UV irradiation. By using a mask when UV light is used, the polymerization can be localized in selected parts of the chips. The ease of fabrication and the numerous monomer combinations possible have attracted a lot of research in the past decade. Typically, inorganic (*e.g.* silica) monoliths are fabricated by sol-gel polymerization and polymer-based monoliths are made by radical polymerization.

Although silica monoliths have been largely studied in fused silica capillaries[47-55] for CEC, organic polymer monoliths are the most widely studied stationary phase for chip chromatography.

1.3.2.1 Silica based monoliths for on-chip chromatography

Silica monoliths are fabricated on-chip using the method developed by Tanaka *et al.*[15, 25, 26] The formation of the silica skeleton is a sol-gel process[25, 26]: first, the silica precursor, tetramethoxysilane (TMOS) is hydrolysed in an acidic media. The second step, called gelation, involves the condensation of silica in the presence of polyethylene glycol (PEG), a porogen. A phase separation between the silica/PEG system and the water generated occurs forming a bicontinuous network of micropores and micrometer sized silica skeleton. In a third step, mesopores are formed by a dissolution-reprecipitation in a basic media at 120ºC (hydrothermal restructuration). The final step is a drying and calcination step: the silica skeleton is treated at 330ºC or higher in order to dry it and calcinate the organic moieties. As a consequence, silica monoliths with bimodal pore sizes can only be made on materials stable at such temperatures (*e.g.* glass, quartz).

Silica monolith advantages include requirement for column pre-treatment for adhesion of the monolith to the channel walls on glass or quartz substrates, as silanol groups present on glass surfaces are integrated in the sol-gel process. In addition, no swelling of silica stationary phases is observed upon use of organic solvent[56].

However, silica monoliths' fabrication process is a sol-gel process, therefore the silica sols need to be introduced into the microfluidic device in discrete zones (where separations are to take place). This need to confine the silica sol plug before gelation is a major drawback for microfluidic device usage[56].

Techniques to localize polymerization in discrete microfluidic zones have been investigated to try to circumvent issues raised by the sol-gel polymerization process. The most successful of these techniques are discussed below.

Ishida *et al.*[57] developed a Pyrex® microfluidic platform with off-chip amperometric detection through a capillary connected to the end of the microfluidic channel. The placement of the plug of monomers and porogen in the microfluidic channel (tetramethoxysilane (TMOS), poly(ethylene glycol) (PEG), urea and acetic acid) was adjusted by controlling the air pressure around it using syringes. After sol-gel polymerization, the silica monolith was converted to a C-18 reverse phase monolith by pumping a 10% (w/w) octadecyltrichlorosilane solution at 100ºC for 12 h through the formed monolith. The microchannel/detection capillary interface was also filled with octadecyl silica (ODS) monolith in order to reduce band broadening at the connection. Three catechins were separated in LC mode at 300 nL/min using this monolith with efficiencies of 15,000 – 18,000 plates/m in a 42 cm long separation channel.

However, this technique is not scalable for mass production, as air pressure in syringes must be adjusted for each device.

In 2008, Giordano *et al.*[58] developed a new microfluidic platform for explosives separations. The microfluidic platform comprised of an electroosmotic pump channel (3 cm x 230 µm x 100 µm) packed with silica particles, a separation channel (2.6 cm (effective length) x 230 µm x 100 µm) filled with a silica monolith and a UV detector (*via* optical fibers) (Figure 1.9).

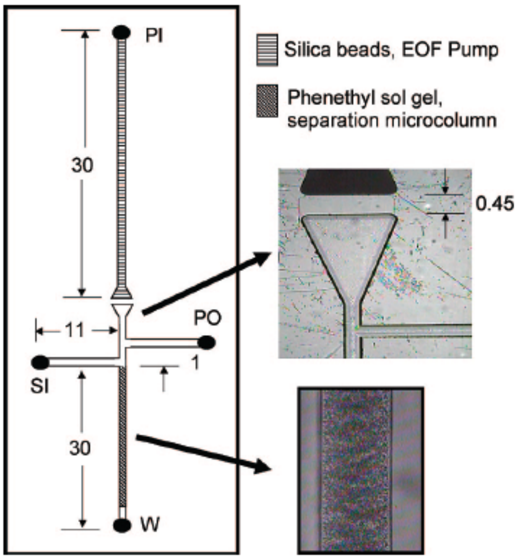

Figure 1.9: Diagram of LC microfluidic device including close-ups of the weir structure and the sol-gel stationary phase. Units are in mm. PI: pump inlet, PO: pump outlet, SI: sample inlet, and W: waste. From Giordano *et al.*[58]

A quartz microchip was developed by Giordano *et al.*[59] with the silica monolith fabricated from a monomer mixture of methyl trimethoxysilane (MTMOS), ethyltrimethoxysilane (ETMOS), ethanol, PEG and acetic acid. The sol-gel silica monolith completely filled the microfluidic channels and was dissolved in the injection and elution channels (Y-junction) using 3 M NaOH. It was found that increasing the hydrophobicity of the silica monolith by increasing the ratio of ETMOS increased the separation resolution of seven explosives.

However, this technique is not scalable for mass production. In addition, reproducibility of the silica monolith removal length could be an issue. For reasons outlined, none of these techniques have been widely adopted.

Photo-initiated sol-gel processes have been extensively studied for the preparation of hybrid polymer/silica monoliths used as stationary phases for CEC[60-66].

Morishima *et al.*[67] demonstrated the use of photo-initiated sol-gel hybrid monoliths in microfluidic format. They developed a hybrid polymer/silica monolith on microfluidic chip using a mixture containing a silica precursor, 3-methacryloxypropyltrimethoxysilane, a porogen and a photo-initiator. Thus, UV-irradiation through a mask enabled photo-initiated sol-gel polymerization to occur only in desired area. Separation capabilities were demonstrating by separating coumarin dyes. Efficiencies of up to 18,500 plates were observed with RSD < 3%.

Of the four techniques presented in this section, this is the technique of choice to fabricate silica monoliths and has been widely used in capillaries. However, the monolith formed is not purely a silica monolith, as organic moieties exist within the formed polymer.

1.3.2.2 Polymer-based monoliths

1.3.2.2.1 Polymer-based monoliths and their advantages

In 1992, Svec *et al.*[19] reported the fabrication of continuous rods of macroporous polymer for HPLC application. Using a 40:60 volume ratio of monomers (glycidylmethacrylate and ethylene dimethacrylate, 60:40 volume ratio) and porogen (cyclohexanol and dodecanol, 80:20 volume ratio) in the presence of azobisisobutyronitrile (AIBN) (1 wt% with respect to monomers), they obtained the first macroporous polymer monolith after thermal polymerization at 70ºC, suitable for chromatographic separation. Polymerization in the presence of the porogen was such that a single piece of macroporous material with a globular structure was obtained. The surface chemistry of these monoliths could be adjusted by grafting new functionalities on the surface (*e.g.* diol, amino groups) or by changing the monomer mixture[19, 68-71].

As early as 2000, Svec *et al.*[72] reported the possible use of such materials on microfluidic platforms for chromatography. They used capillaries to demonstrate the feasibility and ease of fabrication of organic polymer monolithic stationary phases in microfluidic devices, employing a mixture of ethylene dimethacrylate, butyl methacrylate, and 2-acrylamido-2-methyl-1-propanesulfonic acid in the presence of a porogenic solvent consisting of 1-propanol, 1,4-butanediol, and water. The polymerization was initiated by UV-irradiation (thermally initiated polymerization is not well suited for chip application where the stationary phase is required only in specific locations). As compared to silica monolithic stationary phases, photoinitiation is widely used for polymerization and is nowadays, the most used technique to initiate polymerization for the fabrication of monolithic material on chip. Over the past few years photo-initiated acrylate-[73-77] and polystyrene-based[76, 78, 79] monoliths on microfluidic devices have attracted most attention.

In addition, a wide range of polymer materials can be fabricated using photo-initiated polymerization. Porosities and surface properties can be well controlled using this method making polymer-based monolith the most commonly used stationary phase for electrochromatographic separations[80].

In microfluidic separations, research has been focused on making low cost, "all plastic" chips. As described earlier, silica monolithic stationary phases can only be made on expensive glass or quartz microchips, therefore, silica monoliths are not well suited for microfluidic applications. PDMS[56, 75, 81] and cyclic olefin copolymer (COC)[56, 74] chips seem to be the most used due to their chemical stability. However, surface treatment of the channel walls is required to achieve bonding of the stationary phase onto it so that channeling is not observed.

1.3.2.2.2 Channel wall treatment in PDMS and COC microfluidic chips and its influence on monolith morphology

Faure *et al.* [75] used a hexyl acrylate monolith, previously reported by this research group[73], for the separation of two catecholamines, noradrenaline and dopamine on a PDMS/glass chip (PDMS chip bonded onto a glass substrate). The hexyl acrylate monolith was prepared according to Ngola *et al.*[82] from a mixture of 1,3-butanediol diacrylate and hexyl acrylate (24:76 molar %) also containing 0.5 vol% of 2-acrylamido-2-methylpropane sulfonic acid AMPS, 0.2 molar % of trimethoxysilylpropyl acrylate acting as EOF promoter and silica/monolith bonding agent, respectively. The porogen used was a mixture of ethanol, 5 mM phosphate buffer (pH=6.8) and acetonitrile (20:20:60). A 2:1 volume ratio of porogen to monomer was used. The polymerization was photoinitiated by UV irradiation of azobisisobutyronitrile (AIBN) (0.5% w/w relative to monomers). The trimethoxysilylpropyl acrylate used in the monomer mixture served to ensure covalent bonding of the monolith to the glass substrate. To covalently bond the monolith to the PDMS channel walls, the channel was UV-grafted according to Hu *et al.* [83] . A solution containing 8% AMPS, 2% PEG diacrylate, and 0.5% benzyl alcohol in aqueous solution of 5 mM sodium periodate was introduced in the bonded channel and irradiated with UV. After washing the unreacted solution, an acrylate layer was covalently attached to the PDMS walls. The subsequent photopolymerization of hexyl acrylate lead to a monolith covalently attached to the four sides of the channel (Figure 1.10).

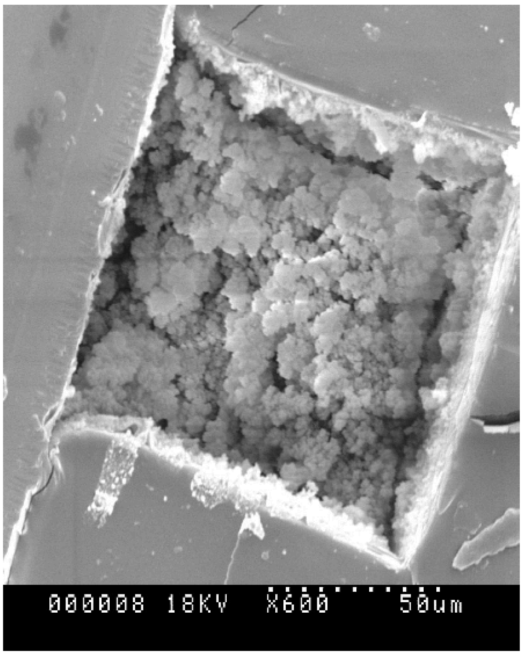

Figure 1.10: SEM micrograph of hexyl acrylate monolith in PDMS/glass microfluidic device. From Faure *et al.* [75]

On a COC microfluidic device, the method demonstrated by Stachowiak *et al.*[84] to covalently bond acrylate monolith to the COC substrate is the most commonly used. In this technique, ethylene dimethacrylate was covalently grafted on the COC wall and acted as a crosslinker when the monolith was polymerized.

Faure *et al.*[74] also demonstrated the electro-separation of five polycyclic aromatic hydrcarbons (PAHs) using a lauryl acrylate monolith. The monolith was fabricated in a COC microchip with hot embossed channels using a method described by Bedair *et al.*[85] The polymerization mixture consisted of porogenic solvents and monomers with a ratio of 5/3 v/v. The porogenic solvent was a mixture of 5% methanol and 95% 2-propanoland and the monomers were a mixture of lauryl acrylate and ethylene dimethacrylate with a ratio of 2/1v/v. Acrylamidomethyl propylsulfonate (0.12% w/w monomers) was added as charged monomer to generate EOF and 10 mg benzoin methyl ether as photo-initiator. The lauryl acrylate monolith was bonded to the COC channel walls using the Stachowiak *et al.*[84] technique.

Liu *et al.*[77] also used the method of Stachowiak *et al.*[84] method to covalently bond a polyacrylate monolith (15 cm) in a COC microchip for the separation of peptides and BSA trypsin digest in LC mode. The reverse phase monolithic stationary phase was photopolymerized from a solution containing 24.5 wt% butyl methacrylate, 14.5 wt% trimethylolpropane trimethacrylate, 30.0 wt% 1-propanol, 30.0 wt% 1,4-butanediol, and 1.0 wt% 2,2′-dimethoxy-2-phenylacetophenone.

All examples cited above resulted in organic monolith stationary phases covalently bonded to the channel walls. Therefore, no channeling was observed.

1.3.2.2.3 Dependence of chip separation efficiency on structural properties of polymer-based monolithic stationary phases

Chip separation efficiency is closely related to the structural properties of the monolithic stationary phase. As demonstrated earlier (Section 1.2.3), radial heterogeneities in the flow-through pore size can have a dramatic effect on monolithic stationary phase efficiency. In macro-scale monoliths, Guiochon *et al.*[5] observed radial heterogeneities due to a temperature gradient within the confined space of the monolith mold. However, in capillaries and microfluidic formats, such thermal disparities do not exist and radial heterogeneities are induced near the capillary or channel walls due to wall/polymer (monomer) interactions as well as flow-through pore sizes/capillary diameter ratio[86].

He *et al.*[87] studied the influence of the confinement of the porosity of polymeric monoliths of various hydrophobicity and pore sizes (pore sizes were modified by varying the monomer/porogen ratio). It was found that the wettabilitty of the capillary walls by the monomer and changes in pore sizes influenced the resulting polymer structure. When the capillary diameter/pore size ratio was between 5 and 10, the morphology of the polymer did not possess pore size uniformity (Figure 1.11). When this ratio was < 5, it was possible to obtain an even coating on the capillary walls (Figure 1.11). However, in this study, the capillary walls were not modified, and therefore were hydrophilic. As a consequence, the influence of the wettabilitty of the capillary walls by the monomer solution could not be assessed.

Gibson *et al.*[88] studied the influence of capillary wall modifier on the thermally initiated polymerization of acrylate precursors in a porogenic solvent, with AIBN as an initiator. Different silanizing agents were used to modify the wettabillity of the inner walls of fused-silica capillaries by the monomer solution. It was demonstrated that heterogeneities of the pore sizes of the polymer differed near the walls from the bulk polymer and was attributed to monomer/walls interaction, therefore to the capillary pretreatment. This phenomenon was also reported by Courtois *et al.*[89] and Nischang *et al.*[90] more recently, who observed the formation of a non-porous layer near the capillary walls (Figure 1.11) contributing to heterogeneities near the capillary walls, therefore decreasing capillary efficiency.

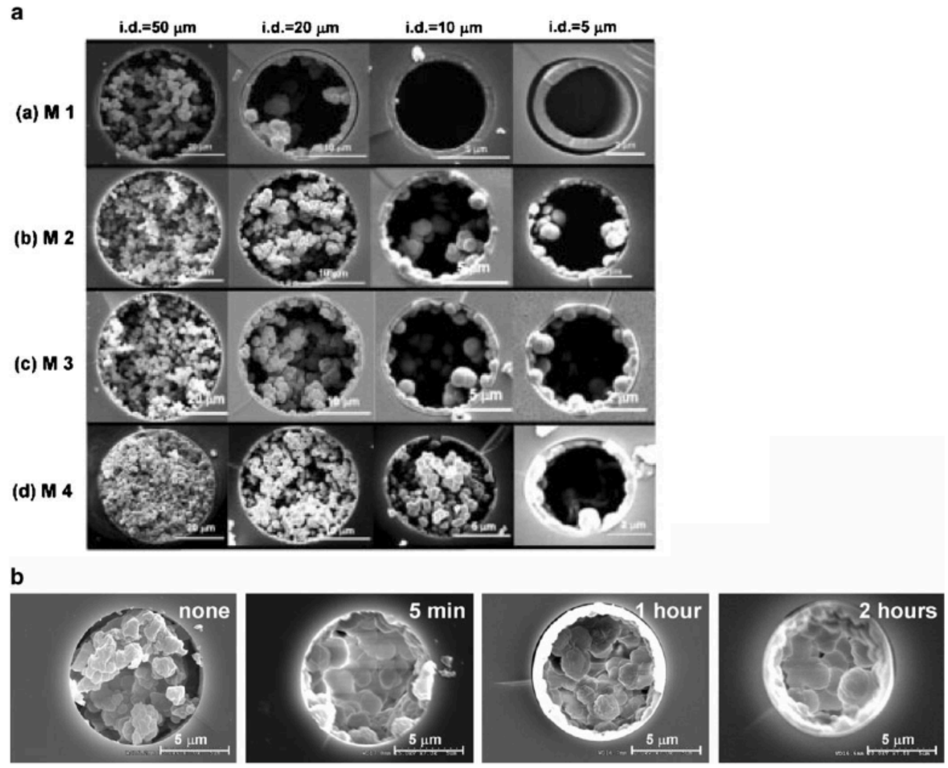

Figure 1.11: Impact of confinement and wall surface properties on the porous structure of a monolith. (a) Dependence on the capillary diameter of the morphology

of photopolymerized monoliths derived from a variety of polymerization mixtures resulting in different macropore sizes (decreasing macropore size M1 to M4). No surface treatment was used on the fused-silica capillaries. (b) SEM images of the cross section of porous poly(butyl methacrylate-co-ethylene dimethacrylate) monoliths in 10-µm-ID fused-silica capillaries, modified with 3-(trimethoxysilyl)propyl methacrylate for different periods of time. (a) From He *et al.*[87]

1.3.2.2.4 Chromatographic separations of small molecules using polymer monoliths

Polymer-based monolithic stationary phases usually exhibit high performances in the separation of large biological molecules due to their excellent biocompatibilities and lack of mesopores (mono-modal pore size distribution). Stagnant zones in mesopores induce high band broadening in large molecule separation due to slow mass transfer of those large molecules. However, for the separation of small molecules, mesopores are required to increase the stationary phase surface area needed for retention and selectivity. In the past two years, efforts have been made to fabricate bimodal pore size distributions with large flow-through pores and mesopores to enable efficient separation of small analytes using polymer-based monoliths.

Aoki *et al.*[91] used a finely tuned standard PS porogenic solution to introduce bimodal pore structure during viscoeleastic phase separation at the early stage of the polymerization. This method was applied to a glycerin 1,3-dimethacrylate (GDMA) and epoxy monolith. Brunauer, Emett and Teller (BET) measurements were used to demonstrate the bimodal pore size distribution of the monoliths as well as the influence of the PS porogenic solution concentration on the resulting pore size. The separation of small analytes was demonstrated by the elution of acetophenone with efficiency increasing from 886 plates for a monomodal monolith to 2,908 plates for a bimodal poly-GDMA monolith.

Trojer *et al.*[92] terminated polymerization in the early stages of polymerization (after 45 min) in order to fabricate bimodal structures. The surface area increased from 20 m^2/g after full conversion of the monomer to 75 m^2/g when polymerization was stopped after only 45 min. Good separation efficiencies (60,000-70,000 plates/m) were recorded for the separation of oligonucleotides and phenols.

1.4 THE INTELLIGENT STATIONARY PHASE CONCEPT

Improvements in separation efficiency have primarily focused on the manipulation and optimization of the mobile phase for individual analyses. Stationary phase optimization is based on strategic choice of material and structure, which minimize band broadening as determined by Van Deemter. The ability to manipulate and optimize stationary phases for individual separations would increase versatility for separations. This could be achieved by use of an electroactive polymer stationary phase, which was controllable after fabrication. For example, if the pore size stationary phase could be controlled (thus affecting the mobile phase velocity and hence the separation efficiency of the column), both before and during the separation, such a column could result in a wide variety of applications. For instance, when several columns are required to separate analytes in a complex sample, a column with a switchable polymer as the stationary phase could fill the need for just a single column rather than several consecutive columns with different properties. For example, typically, in order to adjust the hydrophobicity of silica, C8 and C18 groups are irreversibly grafted onto the stationary phase. The hydrophobicity of a switchable polymer, however, can be easily tuned by varying the pH or by applying a potential to it[93]. Pore size can also be altered if the polymer has the ability to swell or retract when its oxidation state changes due to conformation changes[94].

A range of electroactive polymers could be employed for tunable separations. This was first demonstrated by Wallace *et al.*[95], who used polypyrrole (PPy)-modified glassy carbon particles as a stationary phase to perform separations. Other conductive polymers such as polyaniline (PANI) or poly(3,4-ethylenedioxythiophene) are also known to have controllable properties based on their oxidation states. Each oxidation state represents different properties in terms of volume, hydrophobicity, ionic capacity, color (see Chapter 4 Section 4.1.3). Switching the oxidation state of a conducting polymer by, for example, applying a potential, results in a change in their properties[96, 97] making them suitable candidates for an "intelligent stationary phase". The functionality of these polymers as stationary phases has previously been demonstrated, albeit as coatings on stationary phase particles, as discussed below.

Porter *et al.*[98-100] developed the concept of Electrochemically Modulated Liquid Chromatography (EMLC) using conductive, glassy carbon stationary phases (Figure 1.12).

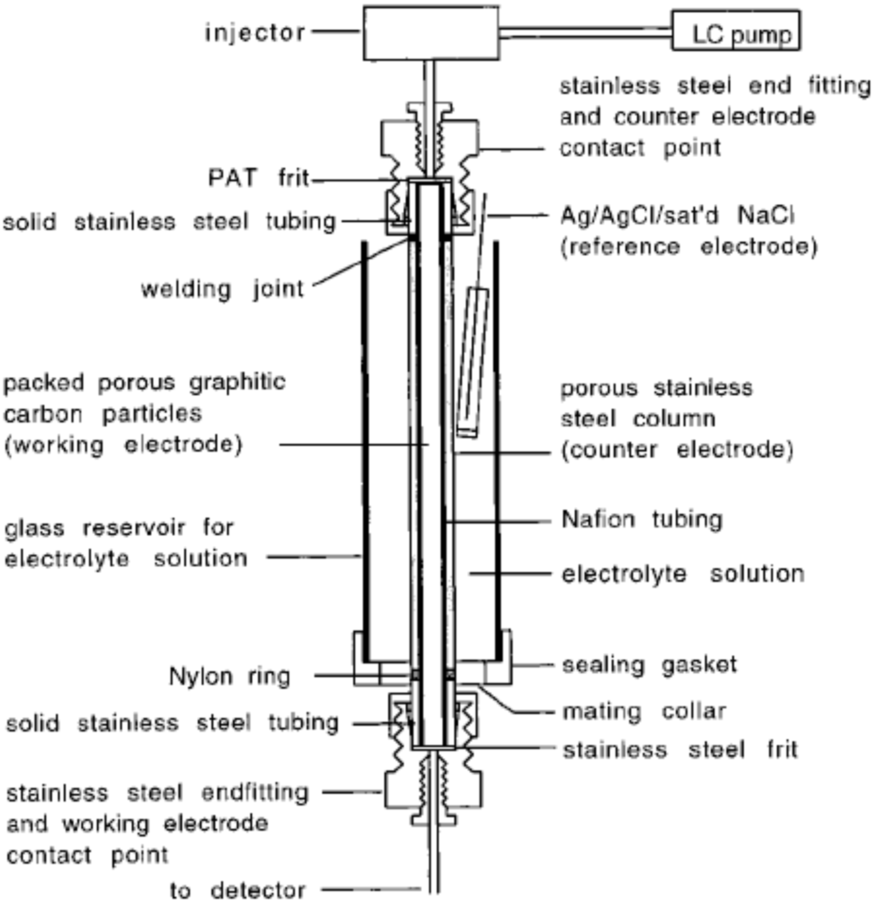

Figure 1.12: EMLC chromatographic column scheme. From Porter *et al.*[100].

Porter *et al.*[100] illustrated the enhancement over conventional chromatographic separations of EMLC with the separation of aromatic sulfonate derivatives using EMLC. The column used was made in-house (Figure 1.12). The stationary phase was fabricated with 7 μ m glassy carbon beads packed into a Nafion® tube. The Nafion® tube was encased in a porous stainless steel column, which was used as the auxiliary electrode. The porous stainless steel also provided casing for the stationary phase to avoid deformation while the pressure driven mobile phase flowed through the column. Nafion® was used to avoid physical contact between the working electrode (the glassy carbon beads) and the auxiliary electrode (the porous stainless steel) while providing good ionic conductivity. A reference electrode was placed in an electrolyte bath to complete the three-electrode electrochemical cell setup. The applied potential on the stationary phase changed the retention factor (ratio of time analyte spends in stationary phase to time it spends in mobile phase) of the analyte based on electrostatic interactions. It was observed for aromatic sulfonate derivatives that the retention time increased by applying a positive potential of +500 mV to the beads and that the retention time decreased when a negative potential of -600 mV was applied as compared to when a 0 mV potential was applied. It was theorized that the orientation of the analyte molecules at the surface of the beads varied according to the applied potential, and thus affected the separation.

Wallace *et al.*[95] employed crushed glassy carbon particles coated with PPy packed in a chromatographic column as shown in Figure 1.13 to perform EMLC. These materials permitted fine-tuning of the stationary phase properties before and during separations. The stationary phase in this instance was the PPy-modified glassy carbon particulate working electrode of a three-electrode electrochemical cell, which permitted control of the potential. The PPy coating improved EMLC over bare glassy carbon as it increased surface area and ionic capacity of the stationary phase. Successful separation of polar, non-polar, acidic and basic compounds was performed, as well as the separation of phthalates and toluic acid isomers without any applied potential. However, low separation efficiencies were observed because of the large size distribution of the particles. On application of a negative potential, an increase in the retention factor for basic compounds was observed. For acidic compounds a decrease of the retention factor was observed when a negative or a positive potential was applied. The mechanism of stationary phase/analytes interactions while a potential is applied is complex as the ion exchange, exclusion and hydrophobic interactions can all be altered by varying the applied potential.

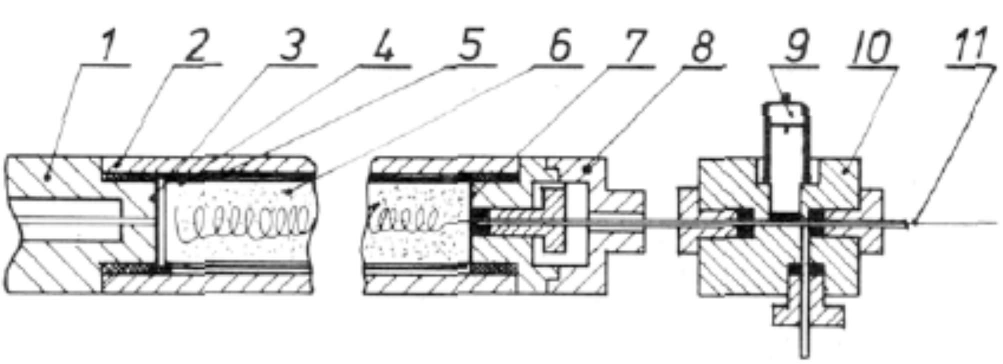

Figure 1.13: Scheme of the column used by Wallace et al., (1) stainless steel wing, (2) Teflon column tube, (3) filter, (4) membrane, (5) auxiliary electrode (carbon fiber), (6) Glassy carbon coated with PPy, (7) filter, (8) fitting, (9) reference electrode, (10) Teflon fitting: (11) Tantalum coil. From Wallace *et al.*[95].

In order to improve separation efficiencies using EMLC, it was necessary to replace crushed glassy carbon with monodispersed particulate material. Wallace *et al.*[101] chemically polymerized PPy on monodispersed silica beads to perform EMLC separations. The beads were then packed in a standard chromatographic column, thus the need for a singular column design was circumvented. PPy was chemically oxidized or reduced by flushing the chromatographic column using $FeCl_3$ and Na_2SO_3 respectively. It was demonstrated that chemically induced redox states of the PPy stationary phase influenced greatly separation. Theophylline and caffeine were not separated using this stationary phase in its neutral state. However, these two coumpounds were separated when PPy stationary phase was reduced or oxidized and the elution order was dependent on the oxidation state of the PPy (Figure 1.14).

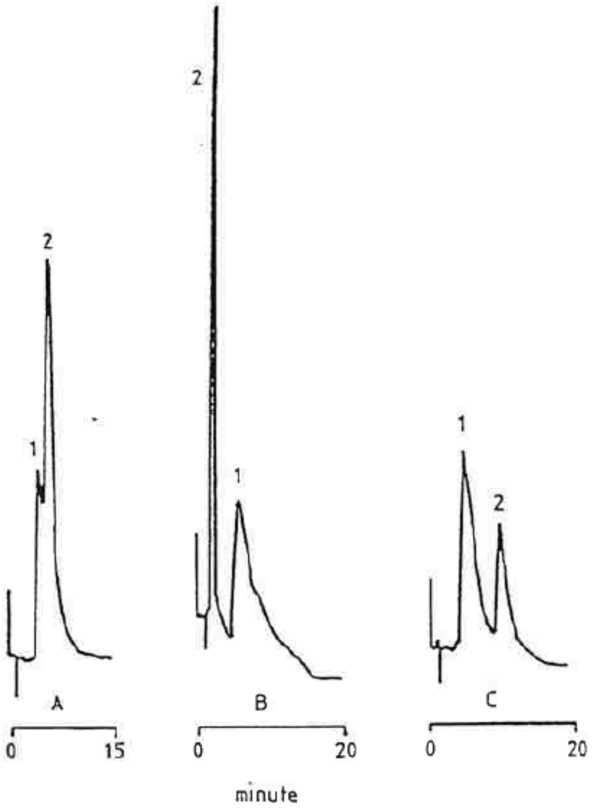

Figure 1.14: Effects of injected redox reagents on PPy (doped with Cl$^-$) stationary phase for the chromatographic separation of (1) theophylline and (2) caffeine. (A) Before injection of any redox reagents, (B) after injection of 1 ml of 0.1 M Na_2SO_3, (C) after injection of 0.8 ml of 0.1 M $FeCl_3$. From Wallace *et al.*[101]

Nagaoka *et al.*[102-104] performed ion chromatography on a glassy carbon powder (average particle diameter 75 μm), coated with PANI stationary phase. Inorganic anions (Cl$^-$, I$^-$, and SCN$^-$) were separated and the retention time was found to depend on the potential applied to the stationary phase[102] (Figure 1.15). It was also observed that the retention time of inorganic anions not only depended on the applied potential but also on the pH of the mobile phase. Indeed, PANI properties changed when applying a potential but also with pH[103] (see Chapter 4, Section 4.1.3.2.2.). Finally Nagaoka *et al.*[104] observed that by pertubating the stationary phase with potential pulses, the retention times could be greatly influenced. What they defined as the duty ratio (ratio between the pulse length and the pulse period) could increase the retention time of analytes by a factor of more than 20 even for a very short column (3 cm effective length).

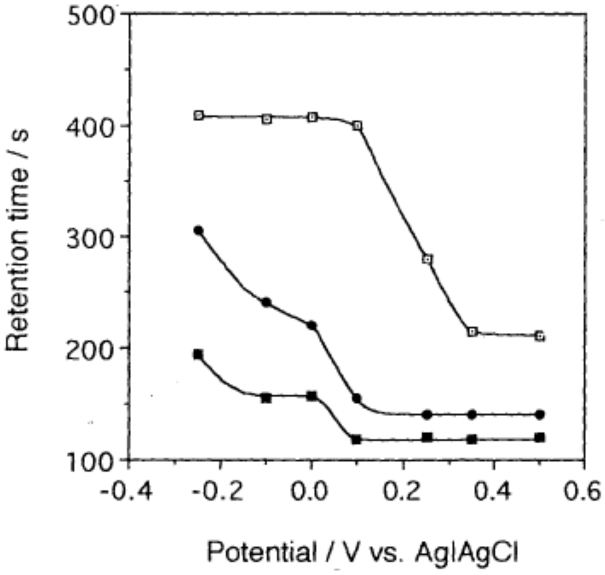

Figure 1.15: Potential dependence of retention times for 20 µl injections of alkali metal ions, (□) K^+, (●) Na^+, (■) Li^+. From Nagaoka *et al.*[102]

Intelligent stationary phases are therefore stationary phases with adjustable properties. In the examples given above, electroactive stationary phases enable electrochemical adjustments of the stationary phase retention factor. However, only particulate columns have been reported and, to my knowledge, no monolithic electroactive stationary phases have been reported. This is certainly due to the poor mechanical stability of electroactive polymer such as PANI and PPy.

1.5 CONCLUDING REMARKS: IN SEARCH OF THE "ULTIMATE" MONOLITH

Monolithic columns should give high throughput separation, i.e. fast and efficient separations. However, due to structural inhomogeneities, the performance of monolithic columns has not equaled the performance of UHPLC (high pressure and sub-2µm particles) and fused core technologies. Two types of monolithic columns are described in the literature; silica stationary phases, which have a bimodal pore size distribution, resulting in high surface area, along with complimentary organic polymer monoliths, which have low surface area as only unimodal pore size is observed. Thus, silica stationary phases are more suitable for small molecule separation and organic polymer stationary phases are more suitable for large molecules such as peptides and DNA.

In microfluidic devices, both particulate and monolithic staionary phases have been used. However, monolithic stationary phases were demonstrated to be the most practical stationary phase for miniaturized separation devices due to their ease of preparation in nano/micro dimensions. Silica monolith fabrication requires relatively high temperatures for the hydrothermal treatment of the monolith (*i.e.* for the tailoring of mesopores) and as such, silica monoliths are fabricated on expensive glass or quartz devices. For mass production, low-cost microfluidic devices are preferred and research has focused on all polymer chips, which cannot house a silica monolith with mesopores, which has driven research into organic polymer monolithic stationary phases (acrylate- or styrene-based).

For monolithic columns, tailored structures with optimum possible performance and selectivity for different applications can be designed. In search for a perfect monolith, Liapis *et al.*[105] described it a decade ago, as follows:

> *If "... in monoliths the size of through-pores could be controlled independently from the size of the skeletons, then if one could construct monolith structures having (a) relatively large through-pores with high through-pore connectivity that can provide high flow rates at low pressure drops and (b) small-sized skeletons with mesopores having an appropriate pore size distribution [...] and high pore connectivity, nT, the following positive results which are necessary for obtaining efficient separations, could be realized: (i) the value of the pore diffusion coefficient, D , of the analyte would be large, (ii) the diffusion path length in the skeletons would be short, (iii) the diffusion velocity, v , would be high, and (iv) the diffusional response time, t , would be small."*

Micro-structured monoliths, with a periodic structure, have the potential to behave as an ideal monolith as described by Liapis *et al.*[105] Micro-structured columns could provide large flow-through pores with high inter-connectivity. They would also result in a higher column-to column reproducibility of the columns as the pore size and distribution of the pores would be accurately controlled. In addition, the multiple flow paths (A-term) would be decreased when using micro-structured monoliths as demonstrated by Vervoort *et al.*[21] (Figure 1.16). Figure 1.16 depicts an example of an ideal periodic monolithic structure showing the paths taken by the analytes when traveling through it, illustrating that in such periodic structures the number of paths available for one analyte molecule is restricted. Therefore microstructuring monoliths should result in a decrease of band broadening and a higher separation efficiency.

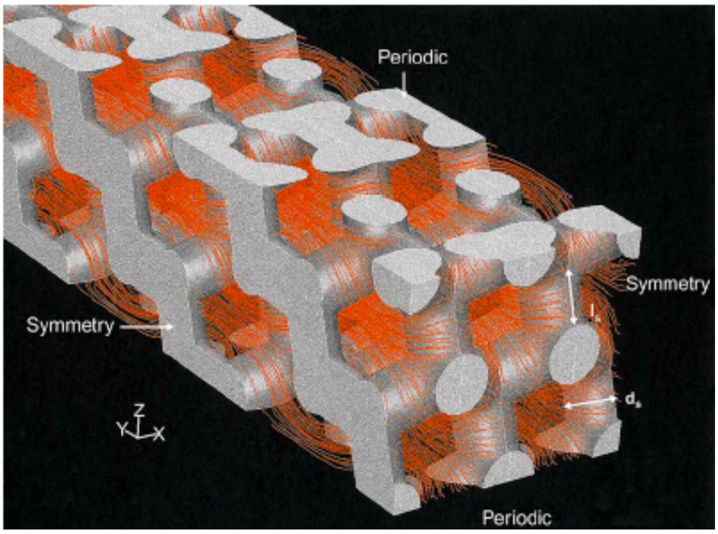

Figure 1.16: 3D simulation of analyte flow field on a tetrahedral skeleton column calculated using the particle tracking method of the Fluent® solver. From Vervoort *et al.*[21]

It has also been demonstrated that electroactive polymer could be used as a stationary phase for chromatography. By applying a potential to them or by adjusting the pH of the mobile phase, it has been demonstrated that the retention time of analyte could be altered. The versatility of such stationary phase was not developed further because large and polydispersed glassy carbon particles were used, thus no efficient separations were achieved.

Prof. Malcolm Smyth's group has already reported micro-structured films of PANI for sensor applications by colloidal crystal templating[106-108]. By using this knowledge, a micro-structured monolith can be envisaged fabricated from PANI, which would have large flow-through pores structure (*i.e.* further decrease of the A-term) and the versatility given by electroactive PANI in terms of tunability, thus, leading to the fabrication of what could potentially be the "ultimate" monolith.

1.6 THESIS OUTLINE

This research thesis aims to investigate the fundamental steps required to fabricate EMµ. The chip design is of primary importance and should enable efficient separations and efficient colloidal crystallization while housing a valid 3-electrode electrochemical cell for the electropolymerization of aniline. A colloidal crystals template strategy was adopted to microstructure PANI and the influence of the template on the PANI structures was investigated. Finally, the growth of a PANI monolith in microfluidic channels was demonstrated and the influence of polymer actuation on pores morphology was addressed using atomic force microscopy (AFM).

In Chapter 2, the material, instrumentation and methods used throughout this thesis are outlined.

In Chapter 3, the chip design and its applicability for chromatographic separation and colloidal crystallization are addressed. The design of the separation channel to house both an electrode system for polymerization and control of the electroactive polymer, and to facilitate the growth of colloidal crystal templates for the microstructuring of the monolith was investigated. Pressure driven flow through two designs, Chip Design 1 and 2 (CD1 and CD2), was simulated by computing fluid dynamics (CFD) to minimize stagnant zones existing within the microfluidic device.

In Chapter 4, the electrochemical cell configuration for the growth and control of an elecroactive polymer, PANI is discussed. The validity of designs is demonstrated using standard ferri/ferrocyanide electrochemistry, and the growth of PANI and its control within a microfluidic channel are demonstrated.

In Chapter 5, the parameters influencing the colloidal crystal growth in CD1 fluidic channel is first addressed. Then the parameters influencing PANI growth through the PS colloidal crystal template and hence, its structure, are discussed.

In Chapter 6, the growth of microstructured PANI and PPy monoliths within microfluidic channels is demonstrated. PPy inverse opal structures are investigated using electrochemical atomic force microscopy (EC-AFM) to help elucidate the actuation behavior of PPy inverse opals in microfluidic devices.

Finally, in Chapter 7 and 8, concluding remarks and future developments for this research are presented. Specifically, CD2 needs to be further optimized in order to improve on-chip electrochemistry. Proposed advances to achieve this are outlined here. In addition, improved solutions to obtain defect free microstructured monoliths in microfluidic channel are discussed.

1.7 REFERENCES

1. Snyder, L. R.; Kirkland, J. J., *Introduction to modern liquid chromatography 2nd edition*. John Wiley & Sons: 1979.
2. Meyer, V., *Chromatographia* **1992,** *34* (5), 342-346.
3. Horvath, C. G.; Preiss, B. A.; Lipsky, S. R., *Analytical Chemistry* **1967,** *39* (12), 1422-1428.
4. Knox, J. H., *Analytical Chemistry* **1966,** *38* (2), 253-261.
5. Guiochon, G., *Journal of Chromatography A* **2007,** *1168* (1-2), 101-168.
6. Van Deemter, J. J.; Zuiderweg, F. J.; Klinkenberg, A., *Chemical Engineering Science* **1995,** *50* (24), 3869-3882.
7. Cabooter, D.; Billen, J.; Terryn, H.; Lynen, F.; Sandra, P.; Desmet, G., *Journal of Chromatography A* **2008,** *1178* (1-2), 108-117.
8. Dittmann, M. M. In *Theoretical and Experimental Comparison of Porous and Superficially-Porous Particles for High Speed and High Resolution Applications in HPLC.*, HPLC, Baltimore, Baltimore, 2008.
9. Kirkland, J. J. In *New Fused-Core™ Particles for Very Fast HPLC Separations*, PITTCON, Chicago, Chicago, 2007.
10. Nakanishi, K.; Soga, N. Inorganic Porous Column. 1993 Patent number 05-200392.
11. Nakanishi, K.; Soga, N. Production of Inorganic Porous Body. 1993 Patent number 05-208642.
12. Hjertén, S.; Liao, J.-L.; Zhang, R., *Journal of Chromatography A* **1989,** *473*, 273-275.
13. Rieux, L.; Niederländer, H.; Verpoorte, E.; Bischoff, R., *Journal of Separation Science* **2005,** *28* (14), 1628-1641.
14. Núñez, O.; Nakanishi, K.; Tanaka, N., *Journal of Chromatography A* **2008,** *1191* (1-2), 231-252.
15. Ishizuka, N.; Minakuchi, H.; Nakanishi, K.; Soga, N.; Hosoya, K.; Tanaka, N., *Journal of High Resolution Chromatography* **1998,** *21* (8), 477-479.
16. Kobayashi, H.; Tokuda, D.; Ichimaru, J.; Ikegami, T.; Miyabe, K.; Tanaka, N., *Journal of Chromatography A* **2006,** *1109* (1), 2-9.

17. Nakanishi, K.; Minakuchi, H.; Soga, N.; Tanaka, N., *Journal of Sol-Gel Science and Technology* **1998,** *13* (1), 163-169.

18. Nakanishi, K.; Minakuchi, H.; Soga, N.; Tanaka, N., *Journal of Sol-Gel Science and Technology* **1997,** *8* (1), 547-552.

19. Svec, F.; Frechet, J. M. J., *Analytical Chemistry* **1992,** *64* (7), 820-822.

20. Ettre, L., *Chromatographia* **1995,** *40* (1), 6-7.

21. Vervoort, N.; Gzil, P.; Baron, G. V.; Desmet, G., *Journal of Chromatography A* **2004,** *1030* (1-2), 177-186.

22. Unger, K. K.; Skudas, R.; Schulte, M. M., *Journal of Chromatography A* **2008,** *1184* (1-2), 393-415.

23. Siouffi, A. M., *Journal of Chromatography A* **2006,** *1126* (1-2), 86-94.

24. Leinweber, F. C.; Lubda, D.; Cabrera, K.; Tallarek, U., *Analytical Chemistry* **2002,** *74* (11), 2470-2477.

25. Ishizuka, N.; Minakuchi, H.; Nakanishi, K.; Soga, N.; Nagayama, H.; Hosoya, K.; Tanaka, N., *Analytical Chemistry* **2000,** *72* (6), 1275-1280.

26. Tanaka, N.; Nagayama, H.; Kobayashi, H.; Ikegami, T.; Hosoya, K.; Ishizuka, N.; Minakuchi, H.; Nakanishi, K.; Cabrera, K.; Lubda, D., *Journal of High Resolution Chromatography* **2000,** *23* (1), 111-116.

27. Roux, R.; Jaoude, M. A.; Demesmay, C.; Rocca, J. L., *Journal of Chromatography A* **2008,** *1209* (1-2), 120-127.

28. Tanaka, N.; Kobayashi, H.; Ishizuka, N.; Minakuchi, H.; Nakanishi, K.; Hosoya, K.; Ikegami, T., *Journal of Chromatography A* **2002,** *965* (1-2), 35-49.

29. Galarneau, A.; Iapichella, J.; Brunel, D.; Fajula, F.; Bayram-Hahn, Z.; Unger, K.; Puy, G.; Demesmay, C.; Rocca, J. L., *Journal of Separation Science* **2006,** *29* (6), 844-855.

30. Yin, H.; Killeen, K.; Brennen, R.; Sobek, D.; Werlich, M.; van de Goor, T., *Analytical Chemistry* **2004,** *77* (2), 527-533.

31. Xie, J.; Miao, Y.; Shih, J.; Tai, Y.-C.; Lee, T. D., *Analytical Chemistry* **2005,** *77* (21), 6947-6953.

32. Seifar, R. M.; Kraak, J. C.; Kok, W. T.; Poppe, H., *Journal of Chromatography A* **1998,** *808* (1-2), 71-77.

33. van den Bosch, S. E.; Heemstra, S.; Kraak, J. C.; Poppe, H., *Journal of Chromatography A* **1996,** *755* (2), 165-177.

34. Pyell, U., *Journal of Chromatography A* **2000,** *892* (1-2), 257-278.

35. Carney, R. A.; Robson, M. M.; Bartle, K. D.; Myers, P., *Journal of High Resolution Chromatography* **1999,** *22* (1), 29-32.

36. Oleschuk, R. D.; Shultz-Lockyear, L. L.; Ning, Y.; Harrison, D. J., *Analytical Chemistry* **2000,** *72* (3), 585-590.

37. Jemere, A. B.; Oleschuk, R. D.; Ouchen, F.; Fajuyigbe, F.; Harrison, D. J., *Electrophoresis* **2002,** *23* (20), 3537-3544.

38. Jemere, A. B.; Oleschuk, R. D.; Harrison, D. J., *Electrophoresis* **2003,** *24*, 3018-3025.

39. Lord, G. A.; Gordon, D. B.; Myers, P.; King, B. W., *Journal of Chromatography A* **1997,** *768* (1), 9-16.

40. Ceriotti, L.; de Rooij, N. F.; Verpoorte, E., *Analytical Chemistry* **2002,** *74* (3), 639-647.

41. Gaspar, A.; Piyasena, M. E.; Gomez, F. A., *Analytical Chemistry* **2007,** *79* (20), 7906-7909.

42. Gaspar, A.; Hernandez, L.; Stevens, S.; Gomez, F. A., *Electrophoresis* **2008,** *29* (8), 1638-1642.

43. Stein, A.; Li, F.; Denny, N. R., *Chemistry of Materials* **2008,** *20* (3), 649-666.

44. Sun, Z.; Yang, B., *Nanoscale Research Letters* **2006,** *1* (1), 46-56.

45. Kamp, U.; Kitaev, V.; von Freymann, G.; Ozin, G. A.; Mabury, S. A., *Advanced Materials* **2005,** *17* (4), 438-443.

46. Park, J.; Lee, D.; Kim, W.; Horiike, S.; Nishimoto, T.; Lee, S. H.; Ahn, C. H., *Analytical Chemistry* **2007,** *79* (8), 3214-3219.

47. Huang, G.; Zeng, W.; Lian, Q.; Xie, Z., *Journal of Separation Science* **2008,** *31* (12), 2244-2251.

48. Jaafar, J.; Watanabe, Y.; Ikegami, T.; Miyamoto, K.; Tanaka, N., *Analytical and Bioanalytical Chemistry* **2008,** *391*, 2551-2556.

49. Xu, L.; Lee, H. K., *Journal of Chromatography A* **2008,** *1195* (1-2), 78-84.

50. Ou, J.; Li, X.; Feng, S.; Dong, J.; Dong, X.; Kong, L.; Ye, M.; Zou, H., *Analytical Chemistry* **2007,** *79* (2), 639-646.

51. Tian, Y.; Feng, R.; Liao, L.; Liu, H.; Chen, H.; Zeng, Z., *Electrophoresis* **2008,** *29* (15), 3153-3159.

52. Preinerstorfer, B.; Hoffmann, C.; Lubda, D.; Lammerhofer, M.; Lindner, W., *Electrophoresis* **2008,** *29* (8), 1626-1637.

53. Dong, J.; Ou, J.; Dong, X.; Wu, R.; Ye, M.; Zou, H., *Journal of Separation Science* **2007,** *30* (17), 2986-2992.
54. Zhang, T.; Khadra, I.; Euerby, M. R.; Skellern, G. G.; Watson, D. G.; Tettey, J. N. A., *Electrophoresis* **2008,** *29* (4), 944-951.
55. Hu, J.; Xie, C.; Tian, R.; He, Z.; Zou, H., *Journal of Separation Science* **2007,** *30* (6), 891-899.
56. Faure, K., *Electrophoresis* **2010,** *31* (15), 2499-2511.
57. Ishida, A.; Yoshikawa, T.; Natsume, M.; Kamidate, T., *Journal of Chromatography A* **2006,** *1132* (1-2), 90-98.
58. Borowsky, J. F.; Giordano, B. C.; Lu, Q.; Terray, A.; Collins, G. E., *Analytical Chemistry* **2008,** *80* (21), 8287-8292.
59. Giordano, B. C.; Terray, A.; Collins, G. E., *Electrophoresis* **2006,** *27* (21), 4295-4302.
60. Dulay, M. T.; Choi, H. N.; Zare, R. N., *Journal of Separation Science* **2007,** *30* (17), 2979-2985.
61. Dulay, M. T.; Quirino, J. P.; Bennett, B. D.; Kato, M.; Zare, R. N., *Analytical Chemistry* **2001,** *73* (16), 3921-3926.
62. Dulay, M. T.; Quirino, J. P.; Bennett, B. D.; Zare, R. N., *Journal of Separation Science* **2002,** *25* (1-2), 3-9.
63. Kato, M.; Dulay, M. T.; Bennett, B. D.; Quirino, J. P.; Zare, R. N., *Journal of Chromatography A* **2001,** *924* (1-2), 187-195.
64. Kato, M.; Sakai-Kato, K.; Jin, H. M.; Kubota, K.; Miyano, H.; Toyo'oka, T.; Dulay, M. T.; Zare, R. N., *Analytical Chemistry* **2004,** *76* (7), 1896-1902.
65. Kato, M.; Sakai-Kato, K.; Toyo'oka, T.; Dulay, M. T.; Quirino, J. P.; Bennett, B. D.; Zare, R. N., *Journal of Chromatography A* **2002,** *961* (1), 45-51.
66. Zheng, J.; Rizvi, S. A. A.; Shamsi, S. A.; Hou, J. G., *Journal of Liquid Chromatography & Related Technologies* **2007,** *30* (1), 43-57.
67. Faure, K., *Electrophoresis 31* (15), 2499-2511.
68. Frantisek, S., *Journal of Separation Science* **2005,** *28* (8), 729-745.
69. Peters, E. C.; Svec, F.; Fréchet, J. M. J., *Advanced Materials* **1999,** *11* (14), 1169-1181.
70. Eeltink, S.; Hilder, E. F.; Geiser, L.; Svec, F.; Frèchet, J. M. J.; Rozing, G. P.; Schoenmakers, P. J.; Kok, W. T., *Journal of Separation Science* **2007,** *30* (3), 407-413.

71. Eeltink, S.; Svec, F., *Electrophoresis* **2007,** *28* (1-2), 137-147.

72. Yu, C.; Svec, F.; Fréchet, J. M. J., *Electrophoresis* **2000,** *21* (1), 120-127.

73. Blas, M.; Delaunay, N.; Rocca, J.-L., *Journal of separation Science* **2007,** *30* (17), 3043-3049.

74. Faure, K.; Albert, M.; Dugas, V.; Cretier, G.; Ferrigno, R.; Morin, P.; Rocca, J.-L., *Electrophoresis* **2008,** *29* (24), 4948-4955.

75. Faure, K.; Blas, M.; Yassine, O.; Delaunay, N.; Cretier, G.; Albert, M.; Rocca, J.-L., *Electrophoresis* **2007,** *28* (11), 1668-1673.

76. Levkin, P. A.; Eeltink, S.; Stratton, T. R.; Brennen, R.; Robotti, K.; Yin, H.; Killeen, K.; Svec, F.; Frechet, J. M. J., *Journal of Chromatography A* **2008,** *1200* (1), 55-61.

77. Liu, J.; Chen, C.-F.; Tsao, C.-W.; Chang, C.-C.; Chu, C.-C.; De, V. D. L., *Analytical Chemistry* **2009,** *81* (7), 2545-2554.

78. Walsh, Z.; Abele, S.; Lawless, B.; Heger, D.; Klan, P.; Breadmore, M. C.; Paull, B.; Macka, M., *Chemical Communications* **2008,** (48), 6504-6506.

79. Walsh, Z. Exotic monoliths. Dublin City University, 2010.

80. Hilder, E. F.; Svec, F.; Fréchet, J. M. J., *Electrophoresis* **2002,** *23* (22-23), 3934-3953.

81. Xu, Y.; Zhang, W.; Zeng, P.; Cao, Q., *Sensors* **2009,** *9* (5), 3437-3446.

82. Ngola, S. M.; Fintschenko, Y.; Choi, W.-Y.; Shepodd, T. J., *Analytical Chemistry* **2001,** *73* (5), 849-856.

83. Hu, S.; Ren, X.; Bachman, M.; Sims, C. E.; Li, G. P.; Allbritton, N. L., *Analytical Chemistry* **2004,** *76* (7), 1865-1870.

84. Stachowiak, T. B.; Rohr, T.; Hilder, E. F.; Peterson, D. S.; Yi, M.; Svec, F.; Fréchet, J. M. J., *Electrophoresis* **2003,** *24* (21), 3689-3693.

85. Bedair, M. F.; Oleschuk, R. D., *Analytical Chemistry* **2006,** *78* (4), 1130-1138.

86. Nischang, I.; Brueggemann, O.; Svec, F., *Analytical and Bioanalytical Chemistry* **2010,** *397* (3), 953-960.

87. He, M.; Zeng, Y.; Sun, X.; Harrison, D. J., *Electrophoresis* **2008,** *29* (14), 2980-2986.

88. Gibson, G. T. T.; Mugo, S. M.; Oleschuk, R. D., *Polymer* **2008,** *49* (13-14), 3084-3090.

89. Courtois, J.; Szumski, M.; Byström, E.; Iwasiewicz, A.; Shchukarev, A.; Irgum, K., *Journal of Separation Science* **2006,** *29* (1), 14-24.

90. Nischang, I.; Svec, F.; Fréchet, J. M. J., *Analytical Chemistry* **2009,** *81* (17), 7390-7396.

91. Aoki, H.; Tanaka, N.; Kubo, T.; Hosoya, K., *Journal of Separation Science* **2009,** *32* (3), 341-358.

92. Trojer, L.; Bisjak, C. P.; Wieder, W.; Bonn, G. K., *Journal of Chromatography A* **2009,** *1216* (35), 6303-6309.

93. Hato, M., *Chemistry Letters* **1988**, 1959-1962.

94. Lizarraga, L.; Andrade, E. M.; Molina, F. V., *Electrochimica Acta* **2007,** *53* (2), 538-548.

95. Ge, H.; Wallace, G. G., *Analytical Chemistry* **1989,** *61* (21), 2391-2394.

96. Wallace, G.; Spinks, G. M.; Kane-Maguire, L. A. P.; Teasdale, P. R., Properties of Polypyrroles. In *Conductive Electroactive Polymers*, CRC Press: 2008, pp 103-136.

97. Wallace, G.; Spinks, G. M.; Kane-Maguire, L. A. P.; Teasdale, P. R., Properties of Polyanilines. In *Conductive Electroactive Polymers*, CRC Press: 2008, pp 179-196.

98. Deinhammer, R. S.; Ting, E.-Y.; Porter, M. D., *Analytical Chemistry* **1995,** *67* (2), 237-246.

99. Keller, D. W.; Ponton, L. M.; Porter, M. D., *Journal of Chromatography A* **2005,** *1089* (1-2), 72-81.

100. Ting, E.-Y.; Porter, M. D., *Analytical Chemistry* **1998,** *70* (1), 94-99.

101. Chriswanto, H.; Wallace, G. G., *Journal of Liquid Chromatography & Related Technologies* **1996,** *19*, 2457-2476.

102. Nagaoka, T.; Fujimoto, M.; Nakao, H.; Kakuno, K.; Yano, J.; Ogura, K., *Journal of Electroanalytical Chemistry* **1993,** *350* (1-2), 337-344.

103. Nagaoka, T.; Kakuno, K.; Fujimoto, M.; Nakao, H.; Yano, J.; Ogura, K., *Journal of Electroanalytical Chemistry* **1994,** *368* (1-2), 315.

104. Nagaoka, T.; Nakao, H.; Tabusa, K.; Yano, J.; Ogura, K., *Journal of Electroanalytical Chemistry* **1994,** *371* (1-2), 283-286.

105. Liapis, A. I.; Meyers, J. J.; Crosser, O. K., *Journal of Chromatography A* **1999,** *865* (1-2), 13-25.

106. Luo, X.; Killard, A. J.; Smyth, M. R., *Chemistry – A European Journal* **2007,** *13* (7), 2138-2143.

107. Luo, X.; Killard, A. J.; Morrin, A.; Smyth, M. R., *Chemical Communications* **2007,** (30), 3207-3209.

108. Luo, X.; Vidal, G.; Killard, A. J.; Morrin, A.; Smyth, M. R., *Electroanalysis* **2007,** *19* (7-8), 876-883.

CHAPTER 2 MATERIALS AND METHODS

2.1 REAGENTS

Aniline and pyrrole were purchased from Sigma-Aldrich and were used after purification by distillation under vacuum and stored at -18ºC. Sodium dodecyl sulfate (SDS), poly(styrene sulfonate) (PSS), dodecyl benzene sulfonic acid sodium salt (NaDBS) and ferricyanide were all reagent grade, bought from Sigma-Aldrich and used without further purification. All other reagents were of analytical grade. Water, deionized to a resistance of over 18 MΩ/cm using a Millipore Q water purification system was used throughout.

2.2 MATERIALS

Transparent polymethyl methacrylate (PMMA) sheets (500 × 400 × 4 mm) were purchased from Radionics Ltd. (Dublin 12, Ireland). Inert acrylic pressure sensitive adhesive (PSA) polyester film was obtained from 3M (UK). 1 µm 10% (w/v) and 200 nm 1% (w/v) PS bead suspensions (RSD < 5%) were purchased from Duke Scientific (Palo Alto, California, USA). Glass microfluidic chips with channels 110 µm wide and 50 µm deep were purchased from Micronit Microfluidics BV (Eschende, Netherlands). Clear polydimethylsiloxane (PDMS), Sylgard 184, was obtained from Dow Corning Corporation (USA). Silver epoxy glue was purchased from Chemtronics (USA). Screen-printing silver ink (Acheson) was provided by Henkel (Germany) and silver ink for ink-jet printing, Silverjet DGP-45LT-15C, was purchased from Advanced Nano Products Co., Ltd. (South Korea). Pt and Ag wires, 0.5 mm in diameter were purchased from Sigma-Aldrich.

2.3 INSTRUMENTATION

A computer controlled micro-milling machine (Datron 3D M6, Datron Technology Ltd., Milton Keynes, UK) was used for Chip Design 1 (CD1) micromilling.

The chip holder (Appendix 3) was fabricated in polycarbonate by Parsec Precision Tooling (Dublin 15, Ireland)

Scanning electron microscopy (SEM) was performed with a Hitachi S3400N scanning electron microscope, and an acceleration voltage of 5-20 kV was employed. Microchip channels for electrode fabrication and samples for SEM analysis were gold sputtered using a SC7640 Sputter Coater **(**Quorum Technologies, UK).

All electrochemical experiments were performed using a BAS 100W potentiostat using a BAS Ag/AgCl reference electrode unless otherwise stated (Bas Inc., USA).

A DEK 248 (DEK printing machines Ltd., UK) was used for screen-printing upper pieces of CD2 chips.

Ink-jet printing was performed using a Dimatix® ink-jet printer (Fujifilm Dimatix Inc., USA) (Model DMP-2831).

A syringe microinjection pump CMA/100 (CMA Microdialysis, Sweden) was used to maintain constant flow through the microfluidic chips. All flow rates stated were taken directly from the syringe pump readout.

Flow simulation were carried out using Comsol® v 4.0 software (Comsol Inc., USA).

AFM was performed using an Asylum MFP-3D™ Stand Alone atomic force microscope (Asylum Research, USA).

2.4 METHODS

2.4.1 CHIP DESIGN 1

2.4.1.1 Fabrication

Microfluidic chips (43mm x 23 mm) were designed using CAD 3D Excalibur software (Progressive software corporation, USA) according to Appendix 1.2 and 1.3 for the base and upper pieces respectively and were fabricated through direct micromilling in PMMA. The upper piece was cut to allow an electrical connection to the gold sputtered electrode after bonding.

2.4.1.2 3-electrode electrochemical cell assembly

A mask was fabricated around the separation channel (20 mm x 2 mm x 0.020 mm) using sticky tape according to Appendix 1.2. The chip was gold sputtered for 20 min at 2kV, 20-25 mA. Thus, a 200 nm (according to charts provided by Quorum technologies) gold coating was deposited on the main channel surface. This served as the working electrode of the electrochemical cell.

A silver wire (0.5 mm in diameter) was cycled ten times in saturated KCl between – 500 mV and 1000 mV *vs.* Ag/AgCl to coat it with AgCl. The wire was then inserted into the first sub-channel of the upper piece of CD1 (Appendix 1.3) and served as the reference electrode.

A platinum wire (0.5 mm in diameter) was inserted in the second sub-channel situated on the upper piece of CD1 (Appendix 1.3) and served as the auxiliary electrode. Both reference and auxiliary electrodes protruded through 0.5 mm holes and were glued in place using epoxy glue.

2.4.1.3 Chip bonding

PSA was manually cut as seen in Appendix 1.1 using a chip as the template. The PSA was then aligned with the base piece of CD1 and applied onto it. A 20 x 2 mm piece of PVDF membrane was incorporated in the upper piece of CD1 (Appendix 1.1 and 1.5) prior to CD1 bonding. Pressure was applied manually until no air bubbles could be seen between the substrate and the PSA. 1 mm (outer diameter) peek tubing was aligned in inlet and outlet holes and glued in place using epoxy.

A leakage test was performed on the chip by applying a 50 µl/min flow through the four inlets and outlets alternatively.

2.4.2 CHIP DESIGN 2

2.4.2.1 Working electrode fabrication

A mask was fabricated on the base piece of Chip Design 2 (CD2) according to Appendix 2.2. The chip was then gold-sputtered for 10 min at 2kV, 20-25 mA so that a 100 nm gold coating was obtained. This gold electrode served as the working electrode.

2.4.2.2 CD2 upper piece fabrication

2.4.2.2.1 Printed circuit board (PCB) fabrication of CD2 upper piece

For the upper piece, the design illustrated in Chapter 4, Figure 4.19 was laser printed onto acetate. The design was heat-transferred onto the copper side of a PCB. The PCB was then placed in ammonium persulfate (10-20%) at 75ºC and agitated manually until full etching of the copper was achieved. The PCB was then thoroughly rinsed with water and the ink transferred from the acetate was cleaned using acetone. The etched PCB was covered with epoxy and left overnight to cure. The glue was then polished with successively finer grades of sand paper until the copper became visible.

The PCB was pierced for the bolts (used with chip holder) and a hole was made to access the working electrode on the base piece of the chip.

A 20 mm x 0.5 mm cut was made in PSA and aligned over the copper auxiliary electrode. The Base piece was aligned and the chip bonded. It was then placed in the chip holder with a PDMS gasket (Appendix 2.1) and securely fastened using fourteen bolts and nuts. Care was taken at this step not to exert a pressure too great to break the chip.

2.4.2.2.2 Ink-jet printing of CD2 upper piece

Silver ink was loaded into a Dimatix picoliter cartridge. The angle at which the cartridge is tilted was set so that each print was 10 μm wide. Five layers of the pattern described in Chapter 4, Figure 4.20 were printed onto PSA. After curing (20 min at 110ºC), the conductivity of the printed tracks was assessed using a multimeter.

2.4.2.2.3 Screen-printing of CD2 upper piece

Polyethylene terephthalate (PET) sheets were pre-shrunk at 110ºC to ensure no shrinkage during ink curing. Silver ink was used to screen-print electrodes according the Appendix 2.3. The silver ink was cured for 15 min at 110ºC. A cut was made to access the working electrode situated on the base piece of CD2. The reference electrode was then chlorinated by cycling it in saturated KCl (10 cycles) between -500 mV and +1100 mV *vs.* Ag/AgCl at 100 mV/s.

Two incisions of 1 x 0.5 mm and 0.5 x 0.5 mm (see Appendix 2.1) were made in PSA. This PSA was applied on CD2 upper piece after aligning the screen-printed reference and auxiliary electrodes with the incisions. The base and upper pieces of CD2 were then aligned with the gold-sputtered working electrode between the auxiliary electrode branches as discussed in Chapter 4 Section 4.3.2.2.1. The chip was placed in the chip holder with a PDMS gasket (Appendix 2.1), which was fastened with 14 bolts and nuts to maintain an even pressure on the chip as previously stated.

2.4.3 PDMS GASKET CASTING

The mould used for PDMS gasket casting was fabricated from 2 PMMA substrates (10 x 10 cm), separated by microscope slides (1 mm thick). PDMS was mixed as indicated by Dow Corning (10:1 base to catalyst ratio) and degassed under vacuum until no bubbles remained. This solution was poured into the mold using a syringe and cured at 90ºC for 2 h.

2.4.4 FLOW SIMULATION

Flow simulation were carried out using Comsol® V 4.0 software (Comsol Inc., USA). For all simulations, a flow rate of 100 µl/min and a no-slip boundary condition was used. A tetrahedral mesh was constructed as finely as possible for simulation calculation times to remain under 90 min.

2.4.5 EVAPORATION INDUCED CONVECTIVE SELF-ASSEMBLY OF PS BEADS

2.4.5.1 Chip Design 1

2.4.5.1.1 Evaporation driven self assembly

A 200 nm or 1 µm 1% (w/v) PS bead suspension was drop-cast using a syringe into the open channel (*i.e.* before bonding of the chip). 1 μm, 1% (w/v) suspensions were obtained by diluting 10% (w/v) stock suspension. The PS bead suspension was allowed to fill the channel and solvent suspension was evaporated at 75ºC, with self-assembly occurring as evaporation progressed. This process was repeated successively (approx. 30-40 times) to build up a thickness equivalent to the separation channel depth.

2.4.5.1.2 Surface energy directed evaporation-driven convective self-assembly

A mask of equivalent dimensions to the separation channel of CD1 was cut into PSA, visually aligned with the base chip channel, and then adhered to the base, to create a temporary scaffold increasing the height of the channel. 1% (w/v) PS spheres were drop-coated into the channel as described in Section 2.4.5.1.1. Given the added depth of the channel and the hydrophobic nature of the PSA, which repelled the aqueous suspension, a larger volume of the PS suspension was confined to the channel. The process was repeated 20 times for complete packing of the separation channel. As in Section 2.4.5.1.1, solvent was evaporated at 75ºC, with self-assembly occurring as evaporation progressed. The hydrophobicity of the PSA ensured that the PS bead suspension was confined to the channel.

2.4.5.2 Chip design 2: capillary forces directed evaporation-driven convective self-assembly

1 μm PS bead suspensions 10% (w/v) were diluted to 1% (w/v) using deionized water. Approximately 1 ml of the diluted suspension was poured into a sample tube. The microfluidic chip was placed in the sample tube so that the outlet was submerged. The gold surface was pre-wetted with deionized water in order to aid filling of the channel with PS bead suspension by capillary forces. The chip was kept at 45ºC overnight (approximately 12 h). Colloidal crystals were then sintered at 100ºC for 30 min to stabilize them onto the electrode surface.

2.4.6 ELECTROCHEMICAL CELL CHARACTERIZATION

Electrochemical cell characterization was performed using potassium ferrocyanide redox chemistry to ensure the 3-electrode electrochemical cell inside the separation channel was valid. Ferrocyanide (2 mM) in KCl (0.1 M) electrolyte was pumped through the chip at 20 µl/min. When all trapped air bubbles were expelled from the channel, the flow rate was adjusted and cyclic voltammetry performed. For batch experiments, a 10 µl/min flow was applied for 5 min between each run to ensure renewal of ferrocyanide solution.

2.4.7 POLYANILINE ELECTROPOLYMERIZATION

2.4.7.1 Electropolymerization through PS bead templates

PANI electropolymerization through the PS bead colloidal crystal was only carried out in open channel, *i.e.* before bonding of the chip. The base piece of CD1 or CD2 was immersed in 0.2 M aniline in 1 M HCl. A commercial reference Ag/AgCl electrode and a platinum mesh auxiliary electrode were used. A +900 mV potential was applied for the desired amount of time. After polymerization, the polymer was thoroughly rinsed with deionized water and dried in air at room temperature. The base piece of the chip was then immersed in toluene overnight (about 12h) to ensure complete dissolution of the PS template. The base piece of the chip was rinsed with fresh toluene initially to remove any unwanted PS from the PANI surface and then with ethanol. Finally PANI was rinsed with water and dried in air at room temperature.

2.4.7.2 Electropolymerization of aniline in closed channel (without template)

After chip bonding, 0.2 M aniline solution in 1 M HCl was pumped through the channel at 20 µl/min. When necessary, 2 mg/ml of dopant was added to the monomer solution. When all trapped bubbles were expelled from the channel, a +900 mV potential was applied to the working electrode for the desired amount of time. For CD1, a sweep potential from -500 mV to +1100 mV was used for electropolymerization of aniline in the fluidic channels. After polymerization, 1 M HCl was pumped through the channel at 10 µl/min for 30 min to remove any residual monomer.

2.4.8 ELECTROCHEMICAL CHARACTERIZATION OF POLYANILINE

For open and closed chips, electrochemical characterization of PANI was performed in 1 M HCl using a potential sweep between -500 mV and +1,100 mV. In open chip the base piece was immersed in 1 M HCl, whereas for closed chips electrochemical characterization was performed with a flow rate of 10 µl/min.

2.4.9 PHYSICAL CHARACTERIZATION OF POLYANILINE INVERSE OPALS

2.4.9.1 Chip Design 1

To characterize the PANI structure obtained upon electropolymerization, the polymer monolith (grown through the PS template) was removed from the channel using sticky tape. The strip was immersed in toluene overnight to dissolve the PS. The intact pieces of monolith were then dried onto a glass slide for SEM analysis.

They were gold sputtered for 5 min at 2 kV, 20-25 mA prior to SEM analysis.

Note: The removal of the monolith from the channel was necessary for CD1, as the PS could not be removed on chip, as no solvent was found to dissolve PS without dissolving the PMMA chip itself.

2.4.9.2 Chip Design 2

To characterize the PANI structure grown in CD2 open channels, the chips were analyzed directly by SEM without gold sputtering. The use of low acceleration voltage coupled with the conductivity of the polymer enabled its direct analysis.

2.4.10 CHIP CLEANING OF BASE PIECE OF THE CHIPS

The base piece of CD1 and CD2 needed to be thoroughly cleaned after each use. The electrodes of the upper piece of CD1 were protected with a membrane so ethanol cleaning was sufficient. For CD2, the screen-printed upper piece was discarded after use.

2.4.10.1 Chip Design 1

CD1 base piece was mechanically cleaned with ethanol to remove the PANI monoliths and gold layers. The cleaning was not completely satisfactory but the use of solvents other than ethanol was prohibited due to dissolution of PMMA.

2.4.10.2 Chip Design 2

As for CD1, the base pieces were first mechanically cleaned to remove as much gold and PANI as possible. They were then immersed in *Aqua Regia* overnight. After dissolution of the gold, the chips were thoroughly rinsed with deionized water and dried in air at room temperature. The clean chips were stored in a dust free environment.

Note: *Aqua Regia* is very corrosive and oxidative, and as such, great care needs to be taken when manipulating it.

CHAPTER 3 FLOW VELOCITY PROFILE ASSESSMENT AND TEMPLATE ASSEMBLY IN CHIP DESIGN 1 AND CHIP DESIGN 2

3.1 INTRODUCTION

Lab-on-chip[1] (LOC) also known as a micro total analysis system[2] (μTAS) is a device with typical dimensions ranging from millimeters to centimeters in its longest dimension that integrates one or several bench processes[2-6]. LOC devices used in chromatographic sciences typically have separation channel diameters from 10 to 500 μm and length of 1-100 cm. To fabricate such devices, several techniques exist. The choice of technique depends on the material used, which is defined by the application. Increasingly "plastic" chips are being used, as they are more cost efficient to fabricate and thus enable mass production[7]. For chromatographic separations, PDMS[8-11] and COC[12, 13] microfluidic devices are increasingly encountered in literature.

In on-chip separation, band broadening effects are among the most significant problems encountered. Therefore, it is essential to predict band broadening in order to minimize it when designing the microfluidic device. Understanding the fluid transport in micro-channels is of critical importance. Pressure driven flow (PDF) and electroosmotic flow (EOF) are among most common fluid transport encountered for separation on LOC.

Pressure driven flow (PDF) occurs where fluid is transported via a pressure difference between the two ends of the channel. Transport is obtained by the use of external, mechanical pumping of the fluid.

Electroosmotic flow (EOF) occurs where fluid is transported via a difference of potential between electrodes placed at both end of the channel. This phenomenon is encountered in capillary electrophoresis, for instance.

In this chapter, flow profiles in microfluidic channels are described and analysed in depth for both PDF and EOF in capillaries. The flow profiles generated in the original prototype microfluidic chip (CD1) integrating a fully functional electrochemical cell, which had previously been designed for flow-through biosensing, was analysed. Fundamentals flaws, which rendered the design unsuitable for EMμ were demonstrated. Based on optimum desired flow profiles, a second-generation chip was designed (CD2). The improvements in flow profiles within this chip were illustrated. For each device, methods for optimal colloidal crystallization within separation channels and chip bonding approaches are discussed.

3.2 MICROFLUIDIC DEVICES DESIGN

3.2.1 INTRODUCTION TO MICROFLUIDICS

For effective device design, fluid mechanics must be first understood. The method used for driving liquid through a device is critical and can result in significant deterioration of output if not controlled. In a fluidic device, the shape and design of the channels as well as the materials used are of primary importance for flow characteristics. Flow is usually characterized by the velocity of the fluid at any point, also called the velocity field.

The equations describing the velocity field, u, are those of momentum conservation, known as the Navier-Stokes equation (Equation 3.1):

$$\rho_0\left(\frac{\partial u}{\partial t} + u \bullet \nabla u\right) = -\nabla P + \mu\nabla^2 u + f \qquad \text{(Equation 3.1)}$$

and continuity (for incompressible fluids) (Equation 3.2):

$$\nabla \bullet u = 0 \qquad \text{(Equation 3.2)}$$

where:

- ρ_0 is the density of the fluid (kg/m^3);
- μ is viscosity of the fluid (Pa.s);
- P is the fluid pressure (Pa);
- f represents external forces applied on the fluid such as gravity or applied electrical field (N).

Momentum is defined as the mass of an object multiplied by the velocity of the object. The conservation of momentum (Navier-Stokes) states that, within a discrete domain, the amount of momentum remains constant; momentum is neither created nor destroyed, but only changed through the action of forces as described by Newton's laws of motion. The continuity equation refers to the conservation of mass. The combination of both equations is used to calculate flow profiles for fluids in microfluidic devices.

As will be discussed below, certain assumptions must be made when applying these equations to separation devices employing pressure driven flows and electroosmotic flows of incompressible fluids. In addition, only the Reynolds number, Re, which provides information on the laminar or turbulent nature of the flow, and the Peclet number, Pe, which provides information on the diffusion and advection mass transport will considered, as they also contribute to band broadening.

Laminar flow occurs when a fluid flows with parallel flow layers without disruption between layers. Turbulent flow occurs when a fluid flows in a chaotic manner, *i.e.* with rapid changes of pressures and velocity in time and space. In a turbulent flow, band broadening is increased as the rapid change in flow velocities contributes to the dispersion of analytes. The Reynolds number (Re) is usually used to determine if the flow is laminar or turbulent. Re, a dimensionless number, measures the ratio between inertial forces and viscous forces. As such within a cylindrical geometry, when Re is lower than 1000 to 2000, viscous forces play a greater role than the inertial forces. The flow is qualified as laminar. When Re <<1 the inertial forces play no significant role and the flow is purely laminar and is, in that case, referred to as Stokes flow. For Stokes flow, the inertial forces can be neglected and the Navier-Stokes equation can be simplified by eliminating the contribution of inertial forces (Equation 3.3):

$$\nabla P = \mu \nabla^2 u + f \qquad \text{(Equation 3.3)}$$

Re is given by Equation 3.4:

$$\mathrm{Re} = \frac{\rho_0 L Q}{\mu A} \qquad \text{(Equation 3.4)}$$

where:

- Q is the volumetric flow rate (m^3/s);

- L is a characteristic linear dimension (i.e. diameter of the separation channel) (m);
- A is the cross sectional area (m^2);

In a 100 µm diameter capillary (equivalent to what is typically found in microfluidic devices) with a flow rate of water of 10 µL/min at 20ºC, the Re number is calculated at 0.005. Re is therefore <1, thus a Stokes flow is usually achieved in such devices. Therefore, the inertial forces can be neglected and the Naviers-Stokes equation simplified in order to calculate flow profiles.

For mass transport, two different processes can be encountered: advection and diffusion. Advection is transport with flow, while diffusion is driven by the concentration gradient of the target compound. The Peclet number for mass transport gives a ratio of advection to diffusion.

Peclet number is defined as in Equation 3.5:

$$Pe = \frac{Lu}{D} \qquad \text{(Equation 3.5)}$$

where:

- L is the characteristic length (*i.e.* length of the separation channel) (m);
- u is the flow velocity (m/s);
- D is the diffusion coefficient or diffusivity (m^2/s);

The higher the Peclet number, the more the advection transport is predominant. In separation science, mass transport by primarily advection needs to be achieved as diffusion will result in band broadening (B-term of Van Deemter equation). In pressure driven and electroosmotic flow, a high enough flow rate needs to be achieved so that the analytes are transported to the detector before diffusion of analytes contributes to a significant band broadening, *i.e.* high Peclet numbers are required.

3.2.2 PRESSURE DRIVEN FLOW (PDF) OF INCOMPRESSIBLE FLUIDS

3.2.2.1 Flow in a cylindrical capillary

To characterize the flow profile of incompressible fluids in a microfluidic device channel, flow profile through a cylindrical capillary is calculated. In a capillary, as for microfluidic devices, Reynolds number is <1, as discussed above. The inertial forces are neglected and the term on the left of the Navier-Stokes equation (Equation 3.1) is equal to 0 (Equation 3.3). All equations are projected in a cylindrical coordinates system (x,r,φ).

In addition, the following assumptions are made:

- in capillaries, at r = R (R being the radius of the capillary) the fluid velocity is null due to frictions at the wall. This is called the no slip boundary condition;
- the fluid flows in only one direction (x) as the flow is laminar (low Re). Thus the pressure gradient (responsible for the fluid motion) is only applied in the x-direction ($\frac{\partial P}{\partial y} = 0$ and $\frac{\partial P}{\partial z} = 0$);
- gravity does not influence the flow velocity;
- in cylindrical capillaries, no acceleration is observed along the length of the capillary (x-axis) and the fluid velocity only depends on r as a consequence of the two previous assumptions;
- the capillary surface is considered smooth and homogeneous and, as such, no discharge will be taken into account.

These assumptions allow simplification of Navier-Stokes equation (Equation 3.3) resulting in Equation 3.6 (after projection in cylindrical coordinate):

$$\frac{1}{r}\frac{\partial}{\partial r}\left(r\frac{\partial u}{\partial r}\right) = \frac{1}{\mu}\frac{\partial P}{\partial x} \qquad \text{(Equation 3.6)}$$

As u(r=R) = 0 (no-slip boundary condition) and $\frac{\partial u}{\partial r} = 0$ at r = 0 (maximum velocity at the centre of capillary) Equation 3.6 can be solved, resulting in Equation 3.7:

$$u(r) = \frac{\Delta P}{4\mu L}(R^2 - r^2) \qquad \text{(Equation 3.7)}$$

Equation 3.7 confirms the parabolic velocity profile of a flow of an incompressible fluid through a cylindrical capillary and agrees with published literature. Parabolic velocity contributes to band broadening. The analytes near the centre of the capillary or microfluidic channel travel faster through the separation channel than analytes present near the capillary walls. As a consequence, the analytes are spatially dispersed, resulting in band broadening.

However, in the calculations presented above, the capillary was assumed to be smooth. In real capillaries, the surface roughness can contribute to a pressure drop along the capillary due to friction forces at the capillary walls, which means that greater pressures need to be applied to achieve a known flow rate. In small capillaries and microfluidic channels, the surface friction forces can contribute to a larger extent to the pressure drop as the ratio between volume of fluid and walls surface of contact diminishes. As a consequence, a higher pressure needs to be exerted at one end of the capillary to achieve similar flow velocities. Pressure driven flow is therefore not the optimal solution for fluid motion in small capillaries and microfluidic channels.

3.2.2.2 Flow through porous beds

In porous media, flow is affected by the resistance of the porous media to the flow. This resistance induces a pressure drop through the porous media. Darcy's law (Equation 3.8) describes the pressure drop as a function of the flow rate exerted on a permeable material:

$$Q = \frac{-KA}{\mu}\frac{\Delta P}{L} \qquad \text{(Equation 3.8)}$$

where:

- Q is the flow rate (m^3/s);
- K is the permeability (m/s);
- μ is the viscosity of the fluid (Pa.s);
- ΔP is the pressure drop (Pa)
- A is the cross sectional area to flow (m^2)
- L is the length the pressure drop is taking place over (m).

Thus, the more permeable the material, the lower pressure drop observed at constant flow rate and viscosity. Therefore, for separation, an increase in permeability of the stationary phase enables the use of higher flow rates or lower backpressures, thus increase separation throughput.

The porous media used in separation science as stationary phases also destabilizes the flow velocity profile. It has been shown by Hlushkou *et al.*[14] that disparities appeared in velocity profiles when flowing an aqueous liquid through a randomly packed capillary. In his model, a cylinder was randomly packed with hard spheres and a pressure driven flow was applied. At a discrete position on the packed cylinder, flow velocities were calculated (Figure 3.1). For a pressure driven flow, a disparity in the flow velocities between interparticulate flow-through pore was observed. Flow profiles exhibited high velocities in large pores as seen in yellow in Figure 3.1a (right) while low velocities were observed in smaller pores as seen in dark red in Figure 3.1a (right). Therefore, the packing induced more flow disparities as compared to a parabolic flow velocity in an empty cylinder. The spatial dispersion of an analyte would, as a consequence, increase as compared to a non-packed cylinder. The packing increased the band broadening observed. The electroosmotic flow (EOF), seen on the left side of Figure 3.1-a and b, exhibited more uniform fluid velocities as no yellow or white colour high flow velocity areas were observed. EOF is considered to be a better method of transporting liquids in microfluidic format because its flow profile is plug-like as demonstrated in the next section.

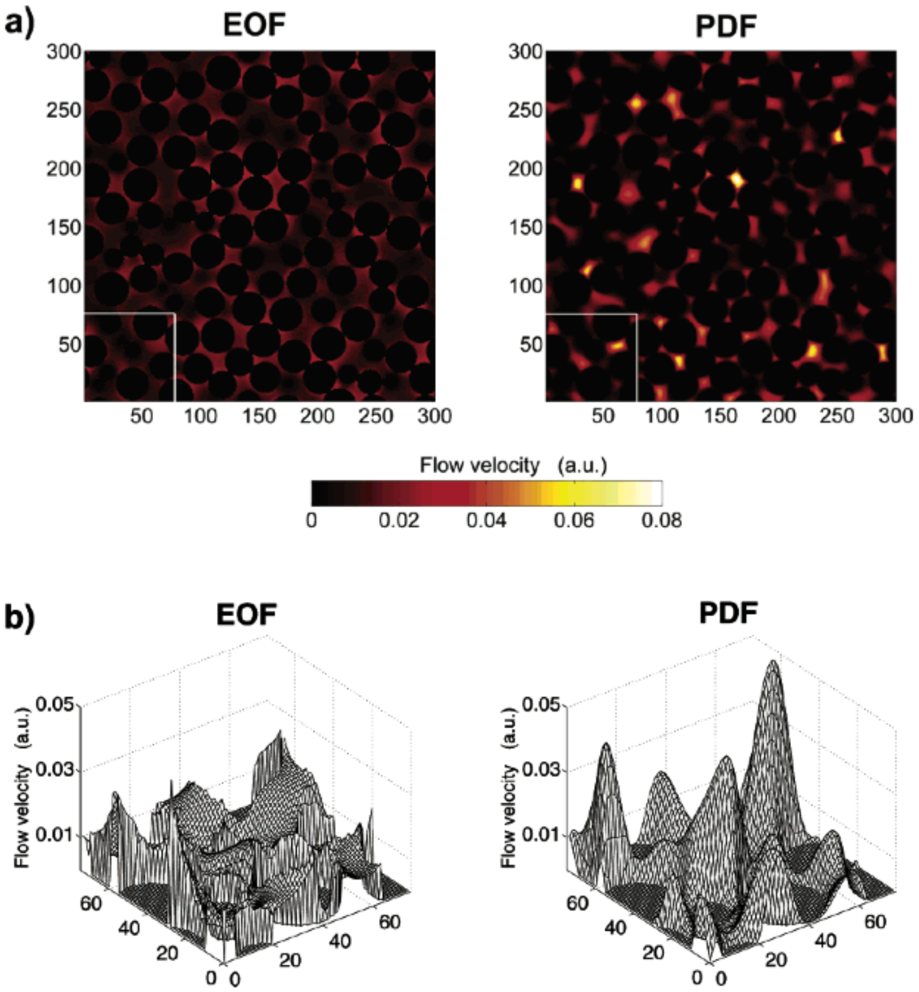

Figure 3.1: PDF and EOF velocity profile of flow through a random hard sphere packing (A) 3-dimensional representation of flow velocity profiles through the randomly packed bed. (B) 3-dimensional representation of flow profiles through the packed bed restricted to the area delimited by the white square in A. From Hlushkou *et al.*[14]

3.2.3 ELECTROOSMOTIC FLOW (EOF)

In CE and CEC, bulk transport of the mobile phase and analytes occurs by electroosmosis[15-19]. Electroosmosis is of primary importance, as in its absence, only the species with the right charge will reach the detector. In this Section, generation of electroosmotic flow at a charged liquid solid interface will be discussed. Using fluid Navier-Stokes and continuity equations, EOF profiles through capillaries and porous beds will be deduced and its influence on band broadening for electrochromatographic separations will be assessed.

3.2.3.1 Electrical double layer properties: electroosmotic flow generation

A silica capillary wall is negatively charged after conditioning with a basic solution. Silanol groups are ionized to silanate at pH values greater than 3.

$$\mathrm{SiOH} + \mathrm{OH^-} \longrightarrow \mathrm{SiO^-} + \mathrm{H_2O}$$

In the presence of an ionic liquid, the surface charge is balanced by oppositely charged ions (counterions) located in a thin layer near the capillary interface. This layer is charged as there are more counterions due to electro-attraction induced by the charged capillary wall. This charged thin layer is known as the electrical double layer (EDL). A schematic of the EDL is given in Figure 3.2.

At the capillary wall liquid interface, a layer (1-8 Å thick) composed of immobilized counterions is formed, known as the Stern layer.

From this charged layer to the neutral bulk solution, the net charge density gradient reduces to zero. The layer of mobile ions (after the Stern layer) is called the diffused layer of the EDL. Therefore, both the Stern layer and the diffused layer comprise the EDL. Between the Stern layer (which is static) and the diffused layer of the EDL (which is mobile), a shear plane exists. The potential of this shear plane is known as the zeta potential (ζ) and is calculated *versus* the capillary wall potential.

The thickness of the EDL, also known as the Debye length (λ_d), is the distance from the shear plane over which the EDL reduces to 1/e (≈ 37%) of ζ. The Debye length depends on the physico-chemical properties of the liquid and not on the surface properties.

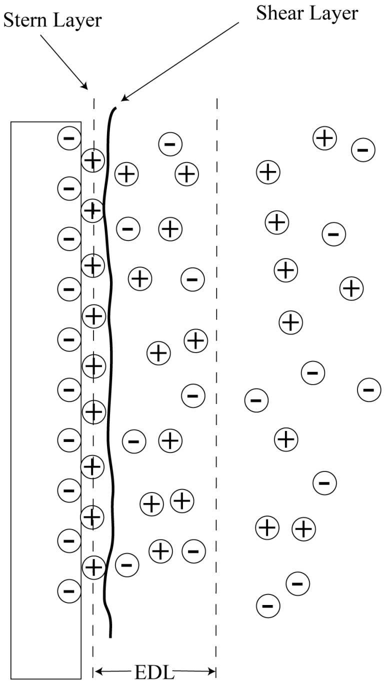

Figure 3.2: Schematic of the EDL formed at a negative wall /ionic liquid interface. Reproduced from Chakraborty[20].

When a steady electrical field is applied across the capillary, the solvated and clustered ions forming the double layer move and drag the bulk solution with them leading to the formation of EOF[16].

3.2.3.2 Linear DC electroosmosis in capillaries

The uniform velocity flow profile of the EOF is given by the Helmholtz-Smoluchowski equation[21] (Equation 3.9):

$$u = \frac{\varepsilon_0 \varepsilon_r \zeta E}{\mu} \qquad \text{(Equation 3.9)}$$

where:

- ε_0 is the permittivity of free space (F/m);
- ε_r is the dielectric constant or relative permitivitty of the media;
- ζ is the zeta potential (V);
- E is the electrical field strength (V);
- μ is the fluid viscosity (Pa.s).

This equation was developed for the movement induced near a flat, uniformly charged surface with an electrical field applied parallel to the surface.

However, this equation only describes the flat profile of the EOF with the thin layer approximation, namely when the effect of the EDL is negligible compared to the capillary diameter.

To study EOF at the capillary walls, to understand the impact of the EDL, a more general equation needs to be derived.

From the Navier-Stokes equation for EOF velocity, u, flow can be formulated as in Equation 3.10:

$$\rho_0\left(\frac{\partial u}{\partial t} + u \bullet \nabla u\right) = -\nabla P + \mu \nabla^2 u - \rho_e E \qquad \text{(Equation 3.10)}$$

where:

- $\rho_0$is the fluid density (kg/m^3);
- μ is the fluid viscosity (Pa.s);
- P is the applied pressure (Pa);

- E is the applied electric field (V)
- ρ_e is the net electrical charge density (C) (related to the electric potential due to the wall charges (ψ) by the Poisson-Boltzmann equation).

By assuming that the inertial forces can be neglected (Re <1) and using no-slip and $\psi_{wall} = \zeta$ boundary conditions, the Navier-Stokes equation can be solved resulting in Equation 3.11:

$$u = -\frac{\varepsilon_0 \varepsilon_r E_z \zeta}{\mu}\left(1 - \frac{\psi}{\zeta}\right) \qquad \text{Equation (3.11)}$$

ψ can be found using the Poisson-Boltzmann equation, which describes electrostatic interactions between molecules in ionic solutions. Rice and Whitehead[21], in 1965, found that, in the case of infinitely long and uniformly charged capillaries, the Poisson-Boltzmann equation results in a unique solution for ψ (Equation 3.12):

$$\psi = \zeta \frac{I_0(kr)}{I_0(kR)} \qquad \text{(Equation 3.12)}$$

Therefore, the EOF profile in cylindrical capillaries can be described by Equation 3.13

$$u(r) = \frac{\varepsilon_0 \varepsilon_r \zeta E}{\mu}\left[1 - \frac{I_0(kr)}{I_0(kR)}\right] \qquad \text{(Equation 3.13)}$$

where:

- k is the reciprocal of the double layer thickness;
- r is the distance from the centre of the channel;
- R is the radius of the capillary;
- I_0 is the 0 order modified Bessel function of the first kind.

Rice and Whitehead[21] studied EOF in narrow cylindrical capillaries and found that the plug-like profile of the EOF was lost when the radius of the capillary and the electrical double layer thickness were of similar dimension (kR=1). This was also shown more recently by Hlushkou[22] (Figure 3.3). When the ratio between capillary radius and electrical double layer thickness ($r_c/\lambda_D = kR$) was > 50 the plug-like velocity flow profiles remained. However, for r_c/λ_D= 20 and r_c/λ_D=10 the EOF lost its plug-like profile near the walls and the plug-like velocity profiles remained only in 80% and 50% of the capillary diameter respectively. For $r_c/\lambda_D < 5$, the plug-like flow velocity profile was completely lost, due to EDL overlap, and the flow profile was parabolic.

The main advantage of EOF is that the EOF velocity profile is plug-like in the thin EDL approximation whereas the pressure driven flow, the velocity profile is parabolic. During separations, when using an EOF plug-like velocity profile, analytes injected would not be subject to a large spatial dispersion as the fluid velocity near the capillary walls is equal to the fluid velocity at the centre of it. As a consequence plug-like EOF flow does not contribute to band broadening as much as pressure driven flow[15]. However, to keep all the advantages of the flat profile of the EOF, the radius of the capillary has to be kept 50-100 times larger than the electrical double layer (thin EDL approximation). If conditions are not controlled to keep the thin EDL approximation, the flow velocity profile resembles a pressure driven flow, thus leading to band broadening (Figure 3.3) as described in Section 3.2.2.1.

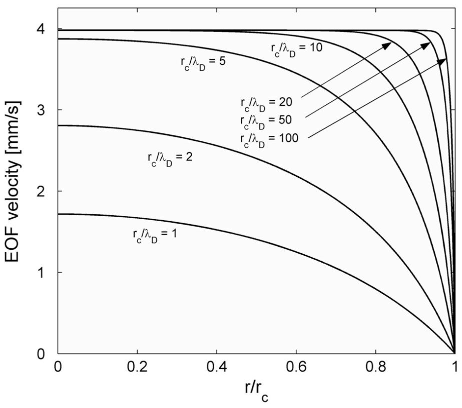

Figure 3.3: Cross sectional velocity profiles for EOF through a straight cylindrical capillary (with capillary radius r_c) at different values of r_c/λ_D (λ_D: the electrical double layer thickness). Applied electrical field strength E = 50 kV/m, $\zeta = -100$ mV, $\varepsilon_r = 80$; the density and viscosity of the liquid are 1,000 kg/m^3 and 0.00089 Pa.s, respectively. From Rice and Whitehead[21].

3.2.3.3 EOF in porous media

EMμ project intends to employ EOF through a uniformly microstructured PANI monolith in order to carry out separations, therefore, the parameters which affect EOF in capillaries filled with such media must be considered. As a consequence, EOF through porous media and through conductive packings is developed in this section. Rathore and Horváth[19] made a comprehensive review of the two main theories developed for EOF in porous media: the Overbeek's Model[23, 24] in the case of charged walls and a non-conducting packing material and Dukhin's Model[25-27] in the case of charged walls and a packing material more conductive than the electrolyte.

In Overbeek's model,[23, 24] particles are used to pack the column and are assumed to be non-conductive, with a uniform ζ. A thin double layer thickness is also assumed and Equation 3.14 is found for describing the EOF profile:

$$u = u_p\left[1+\left(\frac{d_p}{R}\right)\left(\frac{2}{\beta}\right)\left(\frac{\zeta_w}{\zeta_p}-1\right)\right]$$ (Equation 3.14)

where:

- u is the average velocity (m/s);
- u_p is the average velocity generated at the packing surface (m/s);
- d_p is the particles diameter (m);
- R is the capillary radius (m);
- ζ_w is the zeta potential at the capillary walls (V);
- ζ_p is the zeta potential at the packing surface (V);
- β is a dimensionless parameter depending on the total column porosity (ε_c) and the particle shape and the packing structure (α).

Figure 3.4 shows the effect of particle diameter on the EOF velocity for different particle zeta potentials. From Figure 3.4, it can be seen that when ζ_p differs from ζ_w, the EOF can be faster or slower at the wall depending on ζ_p. The plug-like velocity profile is disturbed; therefore during separations spatial dispersion of analytes will be increased when using packing materials with ζ_p different from ζ_w. In addition, EOF is created from the surface of the packing material, therefore, interparticle flow-through pores sizes need to be greater than approximately 50-100 times the EDL thickness in order to retain the plug-like profile within the flow-through pores.

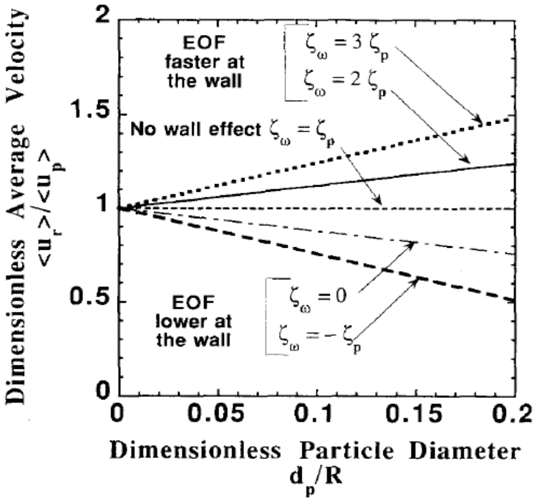

Figure 3.4: Illustration of the effect of the packing particle diameter on the average flow velocity for the case of charged walls and packing for different zeta potentials and particle diameter. Conditions : R= 50 μm and ε_c=0.4. From Rathore *et al.*[19]

In addition, Figure 3.1 shows that the EOF through randomly packed beds gives flow profiles for EOF with flow velocity disparities, but which are lower than PDF where the flow velocities increase with increasing interparticle pore size. Therefore, band broadening induced by EOF through a packed bed is lower than band broadening induced by PDF.

In Dukhin's model[25-27], also called electroosmosis of the second kind, the column is packed with particles more conductive than the electrophoretic medium. An enhancement of the EOF can be seen when using conductive materials for packing. As an electroactive PANI monolith will be used in EMμ project, electroosmosis of the second kind could potentially be induced, in conditions when PANI is in its conductive form and the electrolyte conductivity is low.

Recently, Liapis[16] studied electroosmotic flows in conductive porous media, specifically examining intraparticulate pores, refining the mathematical model of EOF in conductive porous media to correlate mathematical models and experimental data. They demonstrated that, when using conductive porous particles and electrolyte conditions so that ka =1 in the mesopores of the conductive porous particles (EDL thickness = mesopores radius), intraparticulate EOF velocity was not null (Figure 3.3). EOF generated in the particles existed and contributed to the overall fluid transport. As the mobile phase was not stagnant in the pores, resistance to mass transfer was greatly reduced, thus reducing associated band broadening and increasing column efficiency.

Therefore, using a conductive stationary phase, as proposed for EMμ, for chromatography could potentially push the limits of chromatography towards high efficiency and high throughput separations by reducing resistance to mass transfer, through induction of EOF of the second kind.

In this chapter, flow velocity profiles through two chip designs, Chip Design 1 (CD1) and Chip Design 2 (CD2), will be assessed using computational fluid dynamics (CFD). The influence of flow velocity profiles on the band broadening, which would be observed during separation is discussed in depth. In addition, each design is assessed for its ability to form homogeneous PS colloidal crystal within the fluidic channel for microstructuring PANI for the EMμ project. Chip bonding using PSA is also discussed and evaluated.

3.3 EMμ CHIP DESIGN CONSIDERATIONS

The base piece of the chip houses the microfluidic channels for injection, separation and detection. The separation channel comprises a working electrode where electropolymerization of aniline will take place (see Chapter 4). The reference and auxiliary electrodes will be housed in the upper piece of the chip.

For separations, band broadening caused by the flow of mobile phase passing through the device should be minimized. To minimize band broadening, electroosmosis of the second kind, which reduces resistance to mass transfer in stationary phase pores, should be optimized. Additionally, stagnant zones (where mobile phase velocity is null) external to stationary phase pores must also be minimized, not only in the separation channel, but also in the channels leading into and out of the stationary phase-modified separation channel.

Stagnant zones are a significant problem in chromatography[28-30,31]. Analytes diffuse from mobile eluent to the stagnant zones. The analytes are therefore retained for a certain amount of time before diffusing back into the mobile eluent. This diffusion process between mobile and stagnant fluid portions increase the spatial dispersion of analytes, therefore, increasing band broadening.

Finally, for EMμ, the base chip of the microfluidic device must allow rapid colloidal crystallization of PS beads suspensions, which will serve as a template for microstructured PANI electropolymerization. The template is to be sacrificed after electropolymerization of aniline, therefore, the material used to fabricate the microfluidic device (base and upper chip) needs to be resistant to organic solvent, which are commonly used to dissolve PS. Additionally, the separation channel dimensions must allow for the incorporation of a three-electrode electrochemical cell.

3.4 EVALUATION OF CHIP DESIGN 1 FOR THE EMμ PROJECT

CD1 with rectangular channel cross section was fabricated by direct micromilling of PMMA substrates. In order to allow quick PANI growth into the fluidic channel, it was kept shallow (20 μm). However, injection and detection channel were 500 μm deep. In this section, flow velocity profiles through the chip are evaluated and their consequences on separation band broadening are discussed.

3.4.1 BAND BROADENING IN CHIP DESIGN 1

A microfluidic chip was designed previously by Prof. Malcolm Smyth group for flow through biosensing. The chip comprised a wide (2 mm) and shallow (20 μm) 20 mm long sensing channel (Appendix 1.2 and Figure 3.5). PANI was electropolymerized in this channel using an embedded electrochemical cell (Chapter 4, Section 4.2.3). EMμ further develops this concept, by attempting to fabricate a microstructured PANI monolith in the microchannel for separation applications. Therefore, the chip developed for biosensing was investigated for growing the PANI monolith for EMμ. However, before using CD1, it was necessary to assess it in terms of flow velocity profiles to ensure no band broadening would be caused by the flow going through the chip at any point from injection to detection. Computational fluid dynamics (CFD) has been employed for the PDF of water at 20ºC to assess the performance of the design.

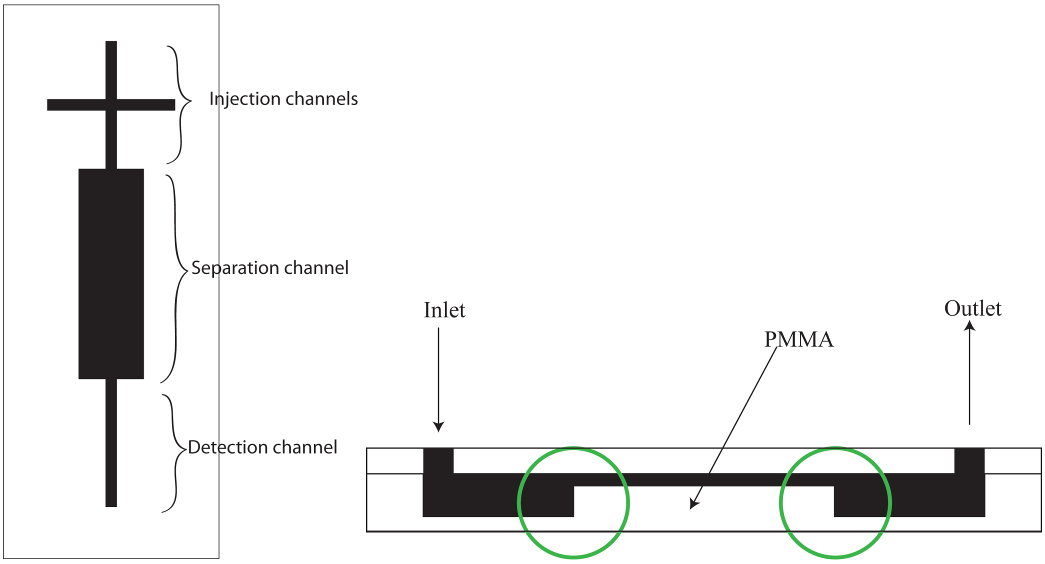

Figure 3.5: Schematic of CD1 (left) top view, (right) longitudinal cross section. Circled in green are areas where flow velocity profiles were calculated.

The simulation of PDF carried out using Comsol® software using a flow rate of 100 μl/min and a no slip boundary condition at the walls for a flow of water at 20ºC for the steady state are shown in Figure 3.6. All assumptions listed in Section 3.2.2.1 are maintained and the flow velocity profiles are generated using the Navier-Stokes equation. In CFD, a mesh needs to be created and the fluid velocity vectors are calculated at each point of the mesh. The quality of the meshing directly relates to the quality of the simulation as the mesh needs to be fine enough to create simulations close to reality but calculation times can become long. A compromise between accuracy of the simulation and calculation time needs to be made during the meshing of the studied geometry. In Comsol® the mesh for the complete system was too big (number of cells > 10^6) because of the difference between the depth of the injection channels and the separation channel and calculation times exceeded 12 h with no guarantee of convergence. Therefore, the junction between the injection channel and the separation channel and the junction between the separation channel and the detection channel were studied separately in order to simplify the simulations (see Figure 3.5 (green circles) and Appendix 1.4, for details of the junctions).

CD1 is intended to be used for LC (PDF) as well as CEC (EOF) mode. The PDF flow profile (when the thin EDL approximation can be used for EOF) will always be the flow profile where most disparities appear. Therefore, only PDF has been studied here by CFD. Additionally, EOF generation, both from the charged channel walls and from the conductive stationary phase is primarily dependent on the mobile phase used for the separation. Therefore, beyond ensuring that the base chip material is appropriate for sustaining a stable EOF, EOF will not be studied further in this chapter.

Figures 3.6 and 3.7 show the velocity field between injection channel and separation channel and the streamlines, respectively. In Figure 3.6, deep blue regions represent stagnant zones, where the fluid velocity is null, and red shows the regions where the fluid velocity is at its maximum. The scale in Figure 3.6A and B was adapted to show flow profile disparities in injection and separation channel respectively. Red lines in Figure 3.7 represent streamlines. The channel structure is represented in black. The blue dots appearing in the separation channel in Figure 3.6-B are simulation artifacts due to the mesh created in Comsol®. When only one tetrahedron from the mesh created for the simulation was used across the whole thickness of the channel, a null velocity was calculated as all 4 points of the tetrahedron were situated on the channel surface where the no slip boundary condition was applied. There are three main stagnant zones (circled in green) in Figure 3.6A and B. As explained in Section 3.3, stagnant zones have a significant impact on band broadening and therefore on separation efficiency. Figure 3.7 shows the streamlines, which would carry analytes into the separation channel. It can be seen that no analytes would, by advection, enter the stagnant zones. In a stagnant zone, the Peclet number is close to 0 so mass transport is only diffusion controlled. Therefore, analytes diffusing in a stagnant zone would be “trapped” and would slowly diffuse back into the mobile phase thus increasing band broadening. This is equivalent to saying that the resistance of mass transfer in these zones is very high as resistance to mass transfer (C-term of Van Deemter equation) is typically attributed to stagnant zones present in porous particle mesopores in conventional packed chromatographic columns. In addition, the volume of the stagnant zones is not negligible (approximately 20 µL or 2.5% of the total volume of the separation channel, calculated for the 4 zones present in the separation channel) so that the time analytes could be retained in these stagnant zones can be large, thus leading to an increase in band broadening.

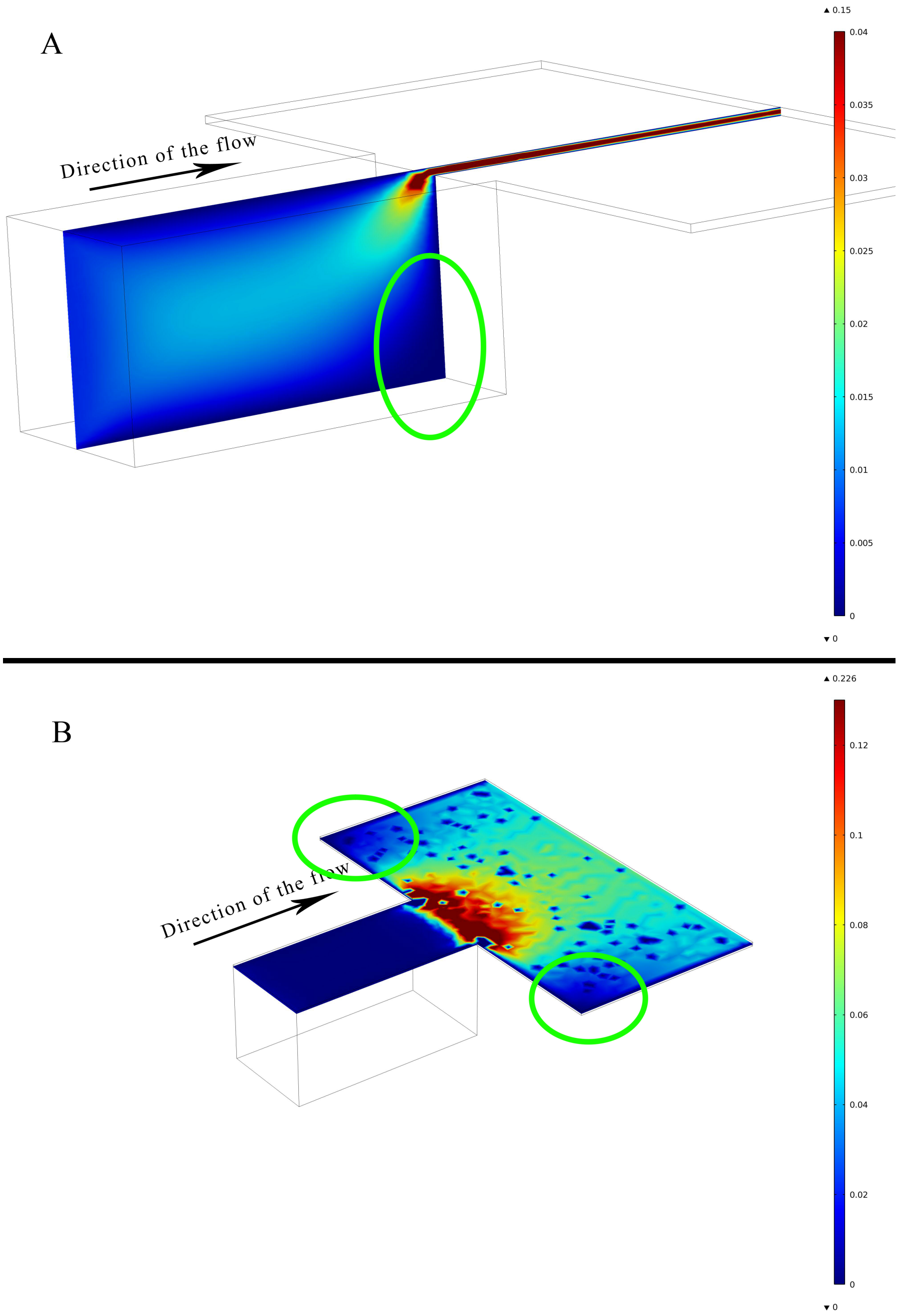

Figure 3.6: PDF velocity field of water at 20ºC through the CD1 injection/separation channel junction at a flow rate of 100 µl/min. (A) xz cross section, (B) xy cross section. Stagnant zones are circled in green. Generated using Comsol® V 4.0. Colored scale in m/s.

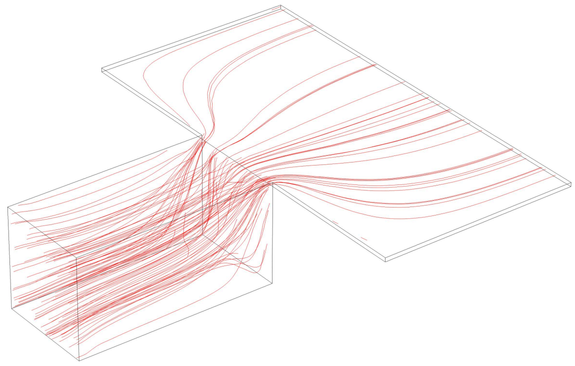

Figure 3.7: Streamlines representations through the injection/separation channels junction in CD1.Generated using Comsol® V 4.0.

Simulating the flow through the separation/detection channels junction, results in analogous flow profiles (data not shown). At this junction, 3 stagnant zones can also be seen. These stagnant zones will add to the band broadening already observed at the injection/separation channel junction. Therefore, the flow velocity profile in CD1 chip is such that separations could be compromised, *i.e.* effective separation could not be achieved because the peak widths would be expected to be so large that baseline resolution was not expected.

In chromatography, analytes' diffusion and resistance to mass transfer (B and C-term of Van Deemter equation) also contribute to band broadening. In CD1, the volume of stagnant zones is significant and increases this band broadening, significantly reducing the separation capacity of the device. Indeed, before entering the separation channel, analyte diffusion to the stagnant zones is expected to hinder analyte movement to the separation channel. Once inside the separation channel itself, analyte diffusion to the "corners" of the channel where stagnant zones exist will increase band broadening further. Finally, when entering the detection channels, *i.e.* after separation, the analytes might be re-mixed.

3.4.2 COLLOIDAL CRYSTALLIZATION OF PS TEMPLATE IN CHIP DESIGN 1

The chip design must also allow for rapid colloidal crystallization of PS bead suspensions in the separation channel. As shown in Chapter 5, colloidal crystallization in this broad channel must be carried out using surface energy directed evaporation driven self-assembly. This technique results in relatively fast crystal growth and the crystal quality is sufficient for PANI microstruturing.

However, the uniformity of the thickness of the colloidal crystal is difficult to control. This technique resulted in crystals of variable thicknesses. Although, the average thickness from crystal to crystal can be reproduced by carefully adding the same volume of suspension, the thickness variation within one crystal (*i.e.* on one chip) is highly heterogeneous as represented in Figure 3.8.

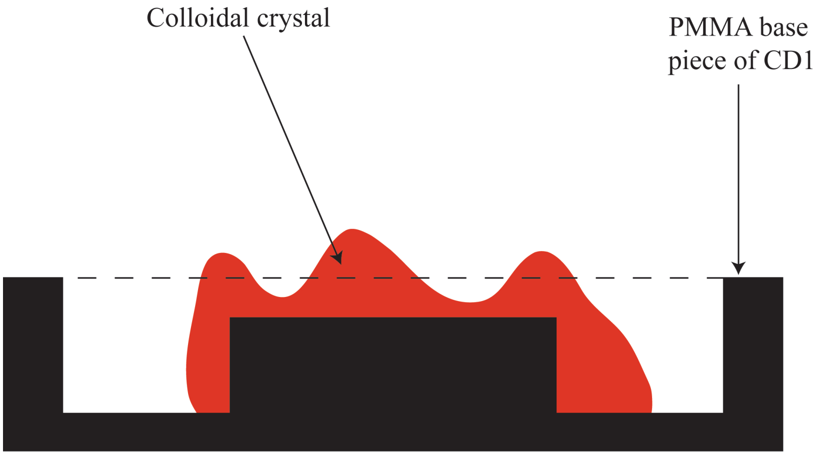

Figure 3.8: Schematic of colloidal crystal thickness grown using surface energy directive evaporation driven self-assembly in CD1.

To overcome this problem, an excess volume of the PS suspensions was added into the channel so that the colloidal crystal was overgrown through the entire length of the separation channel. However, when overfilled, crystal deposition also occurred on top of the PSA release liner outside the channel walls. On removal of the release liner, the brittle crystals, disintegrated. In addition, sealing of the chip could not occur due to the crystal thickness greater than the channel depth.

Therefore, CD1 was not suitable for the growth of an homogeneous PS template for microstructuring PANI monoliths.

3.4.3 EOF GENERATION ON PMMA

According to Section 3.2.3.2, EOF is generated at the electrolyte-PMMA interface and EOF velocity is directly dependent on the ζ-potential created at the electrolyte-PMMA interface. Therefore, stability of EOF is closely linked to stability and homogeneity of the ζ-potential along the length of channels from injection to detection[32-34].

PMMA is known to be able to adsorb analytes during separations, especially biomolecules[35-39]. Adsorption of analytes to the PMMA walls disturbs the homogeneity of the ζ-potential along the length of the separation channels. Therefore, EOF velocities vary depending on the ζ-potential and spatial distribution of analytes increases, hence increasing band broadening. To circumvent the adsorption of analytes to PMMA the channel walls are usually coated to reduce interaction between analytes and the walls[35-38]. However, in CD1, PMMA is coated with a gold layer in the separation channel to grow a PANI monolith. It is believed that the influence of the PANI monolith on the EOF velocity profile would make adsorption of analytes onto PMMA influence negligible. Therefore, no PMMA coating strategy was pursued.

This potential issue, in addition to the excessive band broadening expected and colloidal crystallization issues drove the development of a more suitable design, CD2. It should be noted, however, that given that electrochemical manipulation is such a fundamental component of EMμ, and that CD1 exhibits near ideal electrochemical behavior (see Chapter 4), CD1 was not abandoned at this point. Until any alternative device was proven viable, CD1 was the only device with proven potential.

3.5 CHIP DESIGN 2

To increase separation efficiency and the colloidal crystallization process, the base chip design was enhanced.

CD2 needed to overcome the drawbacks identified in the previous section for CD1, *i.e.* stagnant zones and heterogeneous colloidal crystal thicknesses. Design constraints, which needed to be accommodated, included:

- all channels should have the same width and depth to minimise stagnant zones;
- channels should be wide enough to accommodate electrodes (Chapter 4) and shallow enough for rapid PANI growth;
- channels should be narrow enough to induce capillary forces;
- substrate material should be resistant to template removal solvents;
- substrate material should be capable of generating a stable EOF.

For CD2, Micronit® glass chips were chosen as base chips. The channels were 110 μm wide and 50 μm deep. The chip dimensions are given in Appendix 2. The microfluidic channels were wet etched into glass. Wet etching is isotropic, thus, the channel corners are round. However, for chromatography, Svec *et al.*[40] demonstrated that the cross section shape of the channel has no influence over the chromatographic efficiency. Thus the wet etched profile of the channel should not deteriorate chromatographic performances. A schematic of Micronit® glass chips is given Figure 3.9.

3.5.1 FLUID MECHANICS AND FLOW PROFILES

As there are no depth or width differences between the injection, separation and detection channels, there are no disturbances of the flow, therefore the flow is parabolic for PDF as demonstrated in Section 3.2.2.1 and confirmed by CFD (Figure 3.10). There are no stagnant zones after the injection as it is a simple “tubular“ channel, as illustrated in Figure 3.10. The portion of channel being profiled in Figure 3.10 is circled in green in Figure 3.9. The injection cross is not taken into account and therefore, band broadening due to the injection channels width will not be discussed. In addition, in such a simple geometry, meshing was not an issue and a very fine mesh could be used without dramatically increasing simulation time. Therefore, flow velocity profiles shown in Figure 3.13 are as close to reality.

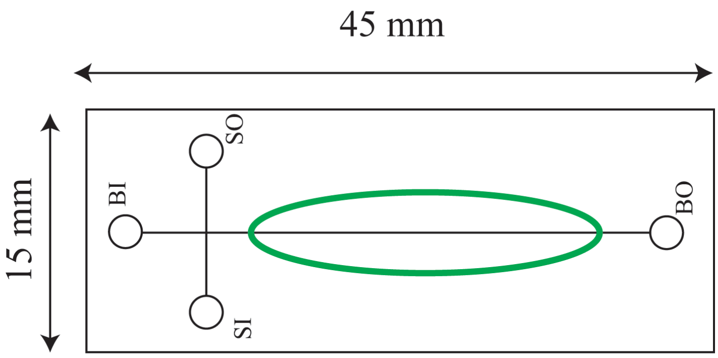

Figure 3.9: Schematic of CD2. Circled in green is the area where flow velocity profiles were calculated. BI: buffer inlet, BO: buffer outlet, SI: sample inlet, SO: sample outlet.

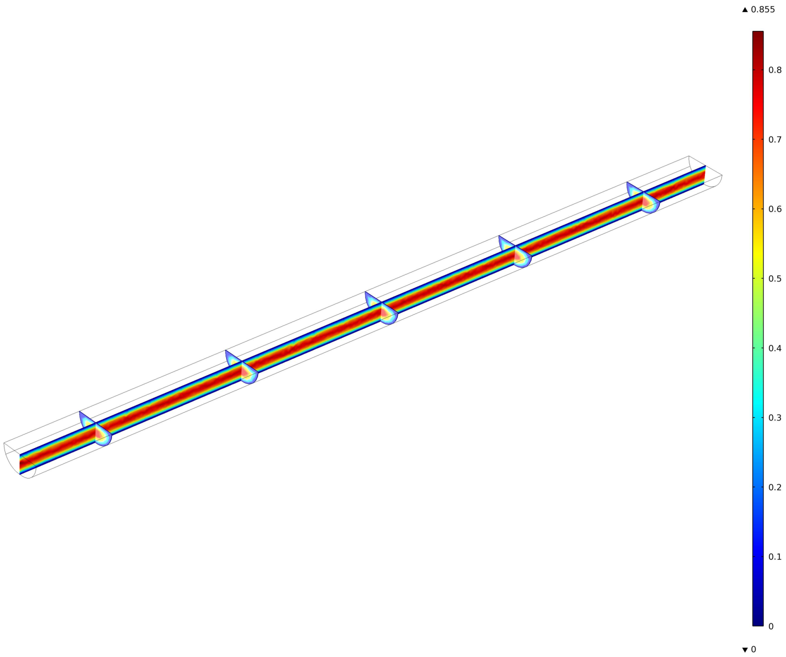

Figure 3.10: PDF velocity profile through CD2. Generated using Comsol® V 4.0. Colored scale in m/s.

3.5.2 COLLOIDAL CRYSTALLISATION OF SACRIFICIAL PS BEAD TEMPLATE

Colloidal crystallization in microfluidic channels has been extensively studied in recent years[18, 41-43]. Among techniques for colloidal crystallization in microchannels, the use of capillary forces have attracted much interest[18, 42, 43] due to the simplicity of the set-up and the high quality of the crystals obtained.

In this method, capillary forces drive the suspension into the microchannels, with one end of the channel being submerged in the suspension. Evaporation processes will begin at the meniscus inside the channel and evaporation induced convective self-assembly takes place. The receding meniscus will allow growth along the full length of the channel. The crystallization process is presented in Figure 3.11.

In contrast to CD1, capillary forces are enabled in CD2 because of the small dimension of the channel (110 µm x 50 µm) and the hydrophilicity of the material used, *i.e.* glass.

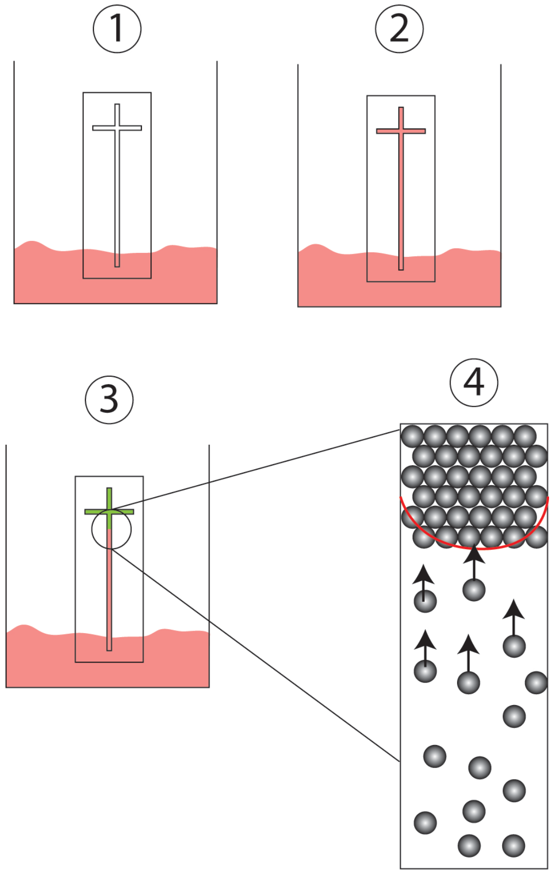

Figure 3.11: Colloidal crystallization in glass-based microchannels using capillary forces. 1: The chip bottom 5 mm of the base piece is submerged in PS bead suspension, 2: capillary forces drive suspension into microchannels, 3 & 4: evaporation induces PS bead self-assembly.

The main advantage of this technique is that its initial set-up is facile and evaporation rate, which can be slow, can be readily increased by increasing the temperature. However, it should be noted that by increasing the rate of evaporation, the crystal structures become more disordered (multicrystalline structure). In addition, this technique results in fully packed microfluidic channels in a single step. The crystal thickness is precisely controlled and equal to the channel depth, where packing occurs.

The results obtained in this research using this technique to make colloidal crystal are discussed in detail in Chapter 6.

3.5.3 EOF GENERATION ON GLASS

EOF generated on glass is well documented and understood[33]. Adsorption of analytes is a less significant issue for glass than for polymeric channels and thus a stable EOF can be generated. EOF velocities depend on pH and the electrolyte nature and concentration[33]. However, glass treatment can be found in the literature for chip electrophoresis to reduce analytes-glass interactions[33, 44], thus allowing more control over EOF velocities.

3.6 CHIP DESIGN 2 INTEGRATION INTO USABLE MICROFLUIDIC DEVICE

To utilise EMμ as a viable separation device, the separation channel must be closed. This is achieved by bonding the base and upper pieces. Chip bonding is a critical step as it ensures that the chip is not leaking. In this research, the upper piece of the chip was fabricated from different materials. PET and PCB were used, the choice of which depended on the type of electrochemical cell approach used (see Chapter 4).

Another requirement for EMμ is that the chip bases should be reusable, *i.e.* bonding should not be permanent. To study the monolithic material, the separation channel needs to be accessible. Thus, a non-permanent PSA was used for bonding.

3.6.1 CHIP-HOLDER DESIGN

To successfully bond a low surface energy material (*e.g.* PET or epoxy) to a high surface energy material (glass) and utilize it for separations is challenging, as an adhesive would adhere more strongly to one material than the other. As a consequence, maintaining pressure on the bonded chip to ensure no leakage may be difficult due to delamination of the material to which the adhesive does not adhere. Thus, a chip-holder was designed to maintain the desired pressure on the PSA for bonding.

The chip holder was composed of two parts. The lower plate was comprised of a polycarbonate plate. The top plate, also made in polycarbonate, contains connections allowing the chip to be interfaced as well as a pocket in which the chip is housed. Both the top and bottom parts are aligned and sealed using 14 bolts and nuts. By tightening the bolts, pressure is applied to the chip, ensuring a leak-free seal. A schematic of the top part of the chip holder is given in Figure 3.12 and all dimensions are given in Appendix 3.

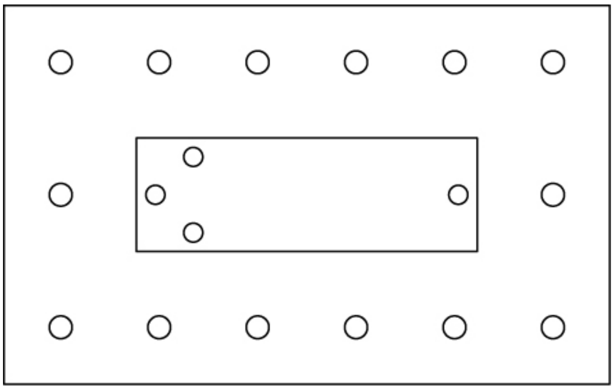

Figure 3.12: Schematic of the top plate of the chip-holder. The pocket is 1.5 mm deep and is used to house the microfluidic chip.

To ensure optimum connectivity, a leak-free connection between the chip and the chip holder was required. This was achieved by placing a compressible PDMS gasket in the pocket. The gasket was cast between two PMMA wafers separated by 1 mm thick glass slides (see Method 2.4.3) to ensure uniform gasket thickness.

A cross section of the bonded chip with chip holder is given in Figure 3.13.

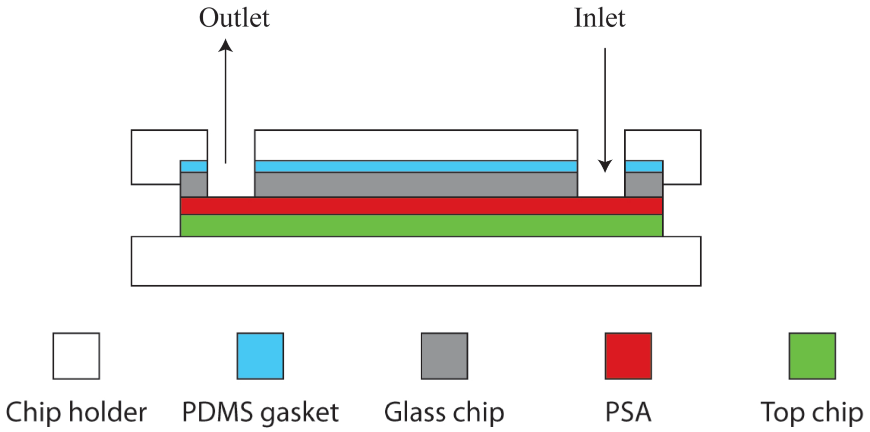

Figure 3.13: Schematic of bonded chip in the pocket of the chip holder. (Not to scale)

3.7 CONCLUSION

PDF and EOF in microfluidic devices were characterized and PDF is found to increase band broadening in separation as compared to EOF due to its parabolic flow profile. In addition, due to high surface to volume ratio, the pressure drop created by the microchannel walls increases the pressure required to achieve a specific flow rate. Therefore, for chromatographic separations, PDF is not the method of choice to manipulate fluid on microfluidic devices and EOF should be considered whenever possible.

In conducting porous media, when the conductivity of the porous material is 100 fold higher than the conductivity of electrolyte, EOF of the second kind can be observed when high potential is used to drive the EOF. In this research, microstructured PANI monoliths are fabricated in the microfluidic channel.

Therefore, under low electrolyte conductivity and the high applied potential, EOF of the second kind could be generated leading to an increase of separation speed.

The preliminary design (CD1), utilized initially for flow-through biosensing was designed to accommodate an electrochemical cell (Chapter 4). CFD was used to assess the flow velocity profile generated in CD1. It was shown that EOF flow profiles would not create band broadening as large as PDF but that, as the chip would be used in both LC and CEC modes, the assessment of flow profile for PDF defined the possibility employing CD1 for chromatographic separations. A total of 6 large stagnant zones were highlighted. The low Peclet number in these zones (mass transport was diffusion controlled) increased resistance to mass transfer and therefore increased band broadening. This increase in band broadening could potentially result in a loss of baseline resolution of elution peaks in chromatographic separations. In addition, the separation channel geometry restricted the techniques, which could be used to crystallize PS beads. Although evaporation induced self-assembly techniques create good quality crystals, the crystal thickness varies within one crystal due to the large area, which needs to be covered by colloidal crystal. Finally, PMMA dissolved when dissolving the PS template to reveal PANI microstructure. Therefore, CD1 was not suitable for chromatographic separations and an optimized chip needed to be designed.

Chip Design 2 (CD2) ensured that no stagnant zones existed so that no diffusion from mobile zones to stagnant zones occurred. Therefore, the flow profile in this 2nd generation chip did not add more band broadening to what is created by the flow itself (PDF or EOF) and the stationary phase. By reducing channel size, it is also possible to use capillary forces to help create the PS bead template. Combining capillary forces and evaporation induce convective self-assembly creates a well-ordered and uniform template where template thickness is equal to the channel depth. As a consequence, CD2 was suitable for chromatographic separation, hence for EMμ.

Finally, non-permanent bonding of glass to polymer was achieved with PSA. A chip-holder was designed, which applied pressure on the PSA ensuring leak-free bonding despite of the PSA adherence differences between glass and polymer due to different surface energies.

3.8 REFERENCES

1. Harrison, D. J.; Manz, A.; Fan, Z.; Luedi, H.; Widmer, H. M., *Analytical Chemistry* **1992,** *64* (17), 1926-1932.
2. Manz, A.; Graber, N.; Widmer, H. M., *Sensors and Actuators B: Chemical* **1990,** *1* (1-6), 244-248.
3. Mark, D.; Haeberle, S.; Roth, G.; von Stetten, F.; Zengerle, R., *Chemical Society Reviews 39* (3), 1153-1182.
4. Dittrich, P. S.; Tachikawa, K.; Manz, A., *Analytical Chemistry* **2006,** *78* (12), 3887-3908.
5. Reyes, D. R.; Iossifidis, D.; Auroux, P.-A.; Manz, A., *Analytical Chemistry* **2002,** *74* (12), 2623-2636.
6. West, J.; Becker, M.; Tombrink, S.; Manz, A., *Analytical Chemistry* **2008,** *80* (12), 4403-4419.
7. Becker, H.; Locascio, L. E., *Talanta* **2002,** *56* (2), 267-287.
8. Faure, K.; Blas, M.; Yassine, O.; Delaunay, N.; Cretier, G.; Albert, M.; Rocca, J.-L., *Electrophoresis* **2007,** *28* (11), 1668-1673.
9. Gaspar, A.; Hernandez, L.; Stevens, S.; Gomez, F. A., *Electrophoresis* **2008,** *29* (8), 1638-1642.
10. Gaspar, A.; Piyasena, M. E.; Gomez, F. A., *Analytical Chemistry* **2007,** *79* (20), 7906-7909.
11. Xu, Y.; Zhang, W.; Zeng, P.; Cao, Q., *Sensors* **2009,** *9* (5), 3437-3446.
12. Faure, K.; Albert, M.; Dugas, V.; Cretier, G.; Ferrigno, R.; Morin, P.; Rocca, J.-L., *Electrophoresis* **2008,** *29* (24), 4948-4955.
13. Park, J.; Lee, D.; Kim, W.; Horiike, S.; Nishimoto, T.; Lee, S. H.; Ahn, C. H., *Analytical Chemistry* **2007,** *79* (8), 3214-3219.
14. Hlushkou, D.; Khirevich, S.; Apanasovich, V.; Seidel-Morgenstern, A.; Tallarek, U., *Analytical Chemistry* **2006,** *79* (1), 113-121.
15. Gas, B.; Stedry, M.; Kenndler, E., *Journal of Chromatography A* **1995,** *709* (1), 63-68.
16. Liapis, A. I.; Grimes, B. A., *Journal of Chromatography A* **2000,** *877*, 181-215.
17. Martin, M.; Guiochon, G., *Analytical Chemistry* **1984,** *56* (4), 614-620.

18. Park, J.; Lee, D.; Kim, W.; Horiike, S.; Nishimoto, T.; Lee, S. H.; Ahn, C. H., *Analytical Chemistry* **2007,** *79* (8), 3214-3219.
19. Rathore, A. S.; Horvath, C., *Journal of Chromatography A* **1997,** *781* (1-2), 185-195.
20. Chakraborty, S.; Chakraborty, D., Microfluidic Transport and Micro-scale Flow Physics: An Overview. In *Microfluidics and Microfabrication*, Springer US: pp 1-85.
21. Rice, C. L.; Whitehead, R., *Journal of Physical Chemistry* **1965,** *69*, 4017-4024.
22. Hlushkou, D.; Kandhai, D.; Tallarek, U., *International Journal for Numerical Methods in Fluids* **2004,** *46* (5), 507-532.
23. Overbeek, J. T. G., *Colloid Science*. Elsevier: 1952.
24. Overbeek, J. T. G.; Wijga, P. W. O., *Recueil des Travaux Chimiques des Pays Bas* **1946,** *65*, 556.
25. Dukhin, S. S., *Advances in Colloid and Interface Science* **1991,** *35*, 173-196.
26. Dukhin, S. S.; Mishchuk, N. A., *Journal of Membrane Science* **1993,** *79* (2-3), 199-210.
27. Baran, A. A.; Babich, Y. A.; Tarovsky, A. A.; Mischuk, N. A., *Colloids and Surfaces* **1992,** *68* (3), 141-151.
28. Pasti, L.; Dondi, F.; van Hulst, M.; Schoenmakers, P.; Martin, M.; Felinger, A., *Chromatographia* **2003,** *57* (0), S171-S186.
29. Felinger, A.; Pasti, L.; Dondi, F.; van Hulst, M.; Schoenmakers, P. J.; Martin, M., *Analytical Chemistry* **2005,** *77* (10), 3138-3148.
30. Felinger, A., *Journal of Chromatography A* **2008,** *1184* (1-2), 20-41.
31. Svec, F., *Chemicke Listy* **2009,** *103* (4), 266-270.
32. Shadpour, H.; Musyimi, H.; Chen, J.; Soper, S. A., *Journal of Chromatography A* **2006,** *1111* (2), 238-251.
33. Kirby, B. J.; Hasselbrink, E. F., *Electrophoresis* **2004,** *25* (2), 187-202.
34. Kirby, B. J.; Hasselbrink, E. F., *Electrophoresis* **2004,** *25* (2), 203-213.
35. Bi, H.; Meng, S.; Li, Y.; Guo, K.; Chen, Y.; Kong, J.; Yang, P.; Zhong, W.; Liu, B., *Lab on a Chip* **2006,** *6* (6), 769-775.
36. Bi, H.; Zhong, W.; Meng, S.; Kong, J.; Yang, P.; Liu, B., *Analytical Chemistry* **2006,** *78* (10), 3399-3405.

37. Lin, Y.-W.; Chang, H.-T., *Journal of Chromatography A* **2005,** *1073* (1-2), 191-199.

38. Nagata, H.; Tabuchi, M.; Hirano, K.; Baba, Y., *Electrophoresis* **2005,** *26* (11), 2247-2253.

39. Ping, G.; Zhu, B.; Jabasini, M.; Xu, F.; Oka, H.; Sugihara, H.; Baba, Y., *Analytical Chemistry* **2005,** *77* (22), 7282-7287.

40. Nischang, I.; Svec, F.; Fréchet, J. M. J., *Journal of Chromatography A* **2009,** *1216* (12), 2355-2361.

41. Lee, S.-K.; Yi, G.-R.; Yang, S.-M., *Lab on a Chip* **2006,** *6* (9), 1171-1177.

42. Shiu, J.-Y.; Kuo, C.-W.; Chen, P., *Journal of the American Chemical Society* **2004,** *126* (26), 8096-8097.

43. Yang, S. M.; Ozin, G. A., *Chemical Communications* **2000,** (24), 2507-2508.

44. Belder, D.; Ludwig, M., *Electrophoresis* **2003,** *24* (21), 3595-3606.

CHAPTER 4 ELECTROCHEMICAL CELL INTEGRATION INTO MICROFLUIDIC CHIP DESIGNS

4.1 INTRODUCTION

Electrochemistry has been defined by Bard and Faulkner as being: "the branch of chemistry concerned with the interrelation of electrical and chemical effects"[1]. The field of electrochemistry is vast and encompasses the generation of electrical current from chemical reactions, *e.g.* in batteries, as well as the chemical changes caused by the passage of an electrical current, *e.g.* electroplating. It also includes important phenomena such as corrosion and electrophoresis[1]. Modern electrochemistry was developed in the late 18th century and the 19th century with the work of great scientists such as Galvani, Volta, Nicholson and Ritter, Nernst, Faraday, Daniell. Today, the field of analytical chemistry exploits electrochemistry as a mode of transduction for monitoring chemical and biochemical reactions and processes.

In this Section, electrochemical cells for analytical measurements and electrosynthesis will be discussed. In addition, issues raised by the integration of electrochemical system into microfluidic device are highlighted. In addition, a brief introduction to conducting polymers and their special electrochemical cell requirements are given.

4.1.1 TWO-ELECTRODE ELECTROCHEMICAL CELLS

The most basic electrochemical cell is comprised of two electrodes. The electrodes can be metallic (gold, platinum, copper), carbon (graphite, glassy carbon) or semi-conductor (indium-tin oxide, Silicium) in nature. The two electrodes are immersed in an electrolyte, an ionic conductor. When a potential difference is applied between the two electrodes, current (i) flows and chemical reactions can occur. The electrode potential is the driving force of the reaction. The process of losing electrons from a species is called oxidation while the gain of electrons is called reduction. The electrode at which the oxidation reaction occurs is called the anode and the electrode at which the reduction reaction occurs is called the cathode. The electrochemical reaction taking place in the electrochemical cell is the addition of two half-cell reactions (reduction and oxidation occur simultaneously at the cathode and anode, respectively)[1].

Usually, only one of the reactions (oxidation or reduction) is of interest. The electrode at which this reaction occurs is called the working electrode. In order to focus on the reaction taking place on the working electrode, the second electrode needs to be standardized. This electrode is called the reference electrode. A schematic of a 2-electrode cell with a working and a reference electrode is given in Figure 4.1. The reference electrode has a constant composition and, as a consequence, its potential is constant.

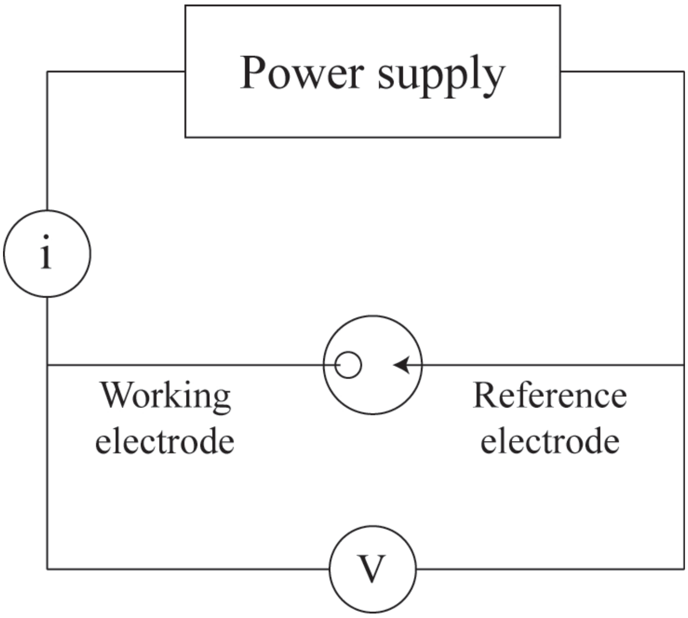

Figure 4.1: Schematic of a 2-electrode electrochemical cell. Reproduced from Bard and Faulkner[1].

The internationally accepted primary reference electrode is the normal hydrogen electrode (NHE) with all components at unit activity (Figure 4.2):

$$Pt/H_2(a = 1)/H^+(a = 1, \text{aqueous})$$

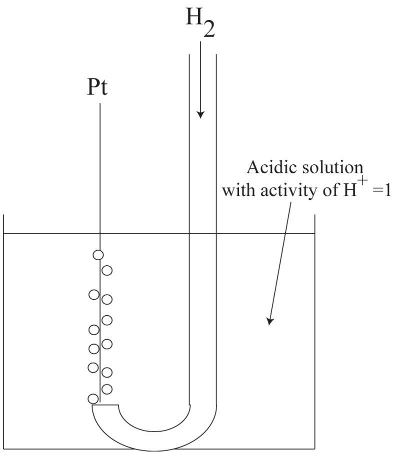

Figure 4.2: Schematic of NHE, where a is activity. Reproduced from Bard and Faulkner[1]

However, this electrode is not experimentally convenient and so other reference electrodes are typically used in practice. The most popular are the saturated calomel electrode (SCE) and the silver/silver chloride electrode (Ag/AgCl). The SCE has a potential of +242 mV *vs.* NHE and Ag/AgCl electrode has a potential of +197 mV *vs.* NHE. "*vs.* NHE" refers to the potential of the NHE, which is accepted to be 0 mV. When using an SCE or Ag/AgCl electrode, the potential will be noted "*vs.* SCE" or "*vs.* Ag/AgCl" as the potential measured or applied is relative to the reference electrode used. The potential of the working electrode is reported as being measured or applied with respect to the reference electrode.

4.1.2 THREE-ELECTRODE ELECTROCHEMICAL CELL

In a 3-electrode electrochemical cell, the potential is measured or applied with respect to the reference electrode, which should be positioned close to the working electrode. The device used to monitor the potential needs to have high input impedance so that only very small currents pass through the reference electrode. A schematic of a three-electrode electrochemical cell is given in Figure 4.3.

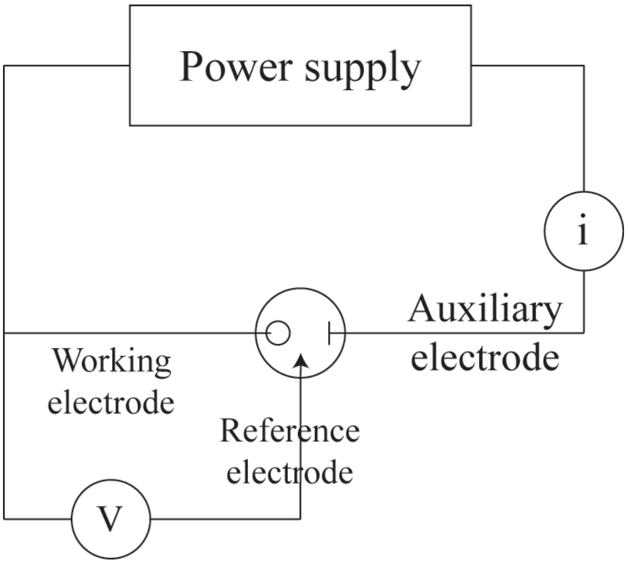

Figure 4.3: Schematic of a three-electrode electrochemical cell. Reproduced from Bard *et al.*[1].

In a three-electrode electrochemical cell, the majority of the iR drop is eliminated. However, a small fraction remains due to the potential profile between the working electrode and the auxiliary electrode and the position of the reference in between the two. The closer the reference is to the working electrode the lower the iR drop remaining. The potential profile between the working and auxiliary electrode depends greatly on the electrode material, geometry, shape and electrolyte conductivity. Great care needs to be taken when designing an electrochemical cell to minimize the iR drop, in order to obtain a potential reading as close as possible to the true value.

4.1.3 STATIONARY AND HYDRODYNAMIC ELECTROCHEMICAL CELLS

Two different electrochemical cells are used in practice, stationary and hydrodynamic. When the electrolyte and electrodes are not moving the system is called stationary cell whereas when the electrolyte or/and electrodes are in movement the system is called a hydrodynamic cell.

In a stationary cell, the mass transport of analytes to the electrode surface is usually diffusion controlled. The rate of reaction is controlled by the rate of diffusion of reactants to the working electrode surface and not by the kinetics of the reaction. Diffusion controlled electrochemistry is achieved when the kinetics of the electrochemical reaction happening on the working electrode surface is quicker than the diffusion time of analytes from the bulk solution to the working electrode, which is usually the case[1]. In cyclic voltammetry (CV), diffusion controlled reactions follow the Randles-Sevcik equation (Equation 4.1):

$$i_p = (2.69 \text{ x } 10^5)\, n^{3/2} A\, D^{1/2} C_i\, v^{1/2} \qquad \text{(Equation 4.1)}$$

where:

- i_p is the peak current (A);
- n is the number of electrons involved in the electrochemical process;
- A is the working electrode area (m^2);
- D is the diffusion coefficient of target analyte (m^2/s);
- C_i is the concentration of analyte (mol/l);
- v is the scan rate (V/s).

Therefore, the anodic and cathodic peak currents are proportional to the square root of the scan rate for any given system. Diffusion-controlled stationary electrochemical cells cannot assess the kinetics of a electrochemical reaction but the kinetics of diffusion of analytes to the working electrode[1].

In several electro-analytical cell configurations, such as flow cells and rotating disk electrodes, the electrolyte or working electrode is in motion. A steady state is quickly attained, in the case of hydrodynamic cells, because of the convective mass transport induced by agitation. Usually the rates of mass transfer by convection are greater than the rates of diffusion so that the contribution of mass transfer to electron transfer kinetics is small[1]. Therefore kinetics of electrochemical reactions can be assessed. In the case of hydrodynamic cell voltammetry, the peak current is usually a function of the flow created by the motion of the electrode (*e.g.* peak current is proportional to the square root of rotating speed for rotating disk electrodes) or by the flow rate in case of a flow cell.

4.1.4 ELECTROCHEMICAL CELL DESIGN IN MICROFLUIDIC DEVICES

Electrochemical cells have been designed in microfluidic dimensions in order to perform electrochemical detection after processing samples[2-7] or as flow-through sensors[8-16]. For microfluidic applications, electrodes need to be 2-dimensional (planar) so that they can be incorporated in the device without any risk of leakage. However, fabricating electrodes in microfluidic dimensions requires high precision micro-fabrication. Micro-electromechanical system (MEMS) techniques have been employed in microfluidics to fabricate electrodes with desired shape, material and dimensions[6, 13, 17-27].

4.1.4.1 Electrochemical detectors, sensors and biosensors

Three-electrode electrochemical cells integrated in microfluidic devices have been mostly used as electrochemical detectors[4-8, 23, 25, 28-34] and flow-through sensors and biosensors[2, 8, 10-16, 35]. Electrochemical detection and sensors on-chip are well-established techniques and, nowadays, research is driven by the need to increase the stability of the reference electrode[36-38] to perform reliable and reproducible measurements and to increase sensitivity and limits of detection[39].

Working and auxiliary electrodes are usually fabricated by lift-off techniques and comprise of the same material (typically gold or platinum) so that only one lift-off step is needed to pattern both electrodes[27, 38]. Working electrodes can also be modified to increase selectivity and limit of detection[39] when the electrochemical cell is used as a detector.

In terms of the reference electrode, there have been significant issues in stabilizing the potential of these "pseudo" reference electrodes on chip. The Ag/AgCl electrodes need a constant and highly chloride anionic environment to maintain a constant potential. In general on-chip sample processes before electrochemical detection are not carried out in these highly ionic conditions; instead, a buffer solution is usually used. To accommodate the buffer, Han *et al.*[36] developed a nanostructured platinum/platinum oxide (Pt/PtO) reference electrode by electrodepositing Pt using a liquid crystal template. 1,3-phenylenediamine (m-PD) was then electropolymerized on the Pt electrode. The Pt electrode was then oxidized. Poly(m-PD)-coated platinum electrode responded only to pH so its potential was stable in buffered solution. Ferricyanide in phosphate buffered saline (PBS) electrochemistry was used to demonstrate the stability of such a reference electrode in a conventional cell as well as integrated in a microfluidic device.

Karube's group has demonstrated work on isolating the Ag/AgCl reference electrode to increase its stability[9, 40-43]. Karube's group designed liquid junctions with channels filled with saturated KCl solution. A pinhole and a cellulose acetate plug were made to connect the isolated reference electrode with the channel where the measurement was made. However, Karube's group design required five lithographic processes and, as such, was not practical. To stabilize the Ag/AgCl reference electrode potential Kim *et al.*[37] developed a polyelectrolyte junction between the microfluidic channels where the detection occurred, and therefore where the working electrode was an Ag/AgCl reference electrode. The Ag/AgCl electrode was therefore isolated and stability over 30 h was observed (Figure 4.4). Polydiallyldimethylammonium chloride (pDADMAC) was used as the polyelectrolyte bridge.

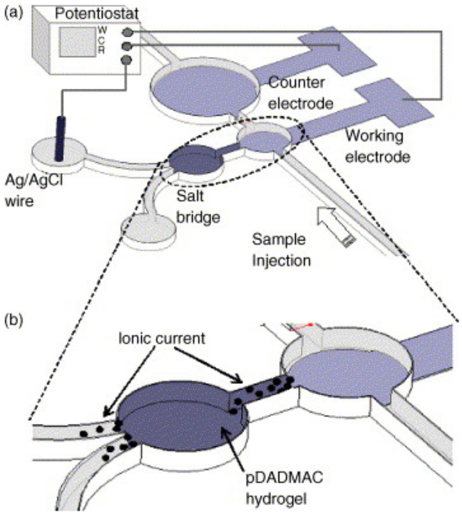

Figure 4.4: (a) Schematic diagram for the three-electrode system using a polyelectrolyte salt bridge. (b) Flux of Cl^-(•) in/out of polyelectrolyte. Current flows through the salt bridge in the form of Cl^- abundant in pDADMAC. The direction of current depends on the polarity of the potential difference between the working and reference electrodes. From Kim *et al.*[37].

Zhou *et al.*[38] developed further research building on Karube's work. They first microfabricated silver electrodes on glass slides by lift-off. The silver electrode was then chlorinated to serve as a reference electrode. A PDMS chip with two independent parallel channels was then aligned and sealed to the glass slide). One of the channels was filled with saturated KCl to stabilize the reference electrode potential. When sealing the chip, nanochannels were formed on the sides of the reference electrode, which acted as liquid junctions. Stability of the chip was tested using ferricyanide electrochemistry. A drift of ± 5 mV was found over an 8 h period. In addition, the chip was left for a week in normal laboratory conditions and when refilling the channel used to stabilize the reference electrode with saturated KCl, it was found that the potential of the reference electrode stabilized quickly. Therefore, this system possessed a high stability.

To date none of the techniques described above have been adopted as the solution for stabilizing Ag/AgCl reference electrode potential on-chip. In addition, these techniques are not easily amenable to mass production.

4.1.4.2 Electrochemical reactors in microfluidic devices

Electrochemical cells integrated into microfluidic devices have also been used or demonstrated for use as flow electrochemical reactors[27, 44]. To the best of my knowledge, only two peer reviewed papers describe the fabrication of electrochemical reactors on microfluidic devices.

Illa *et al.*[27] demonstrated the feasibility of an electrochemical reactor on a COC chip. Due to its high chemical stability, an array of fourteen gold electrodes was fabricated by lift-off microfabrication directly on a COC wafer (Figure 4.5). Of the fourteen electrodes only three were used as working, auxiliary and pseudo-reference electrodes. The auxiliary and pseudo-reference electrodes were placed downstream with respect to the working electrode so that products formed at the auxiliary electrode did not interfere with the reaction occurring at the working electrode. Electrochemistry of ferrocene in tetrabutylammonium perchlorate/acetonitrile and ferricyanide in KNO_3 was performed, demonstrating the feasibility of such a device for performing electrochemistry both in aqueous and organic media. This microfluidic device could, according to the authors, potentially be used for electrosynthesis in aqueous and in organic media. However, the total surface area will be small and therefore, its performance might be limited.

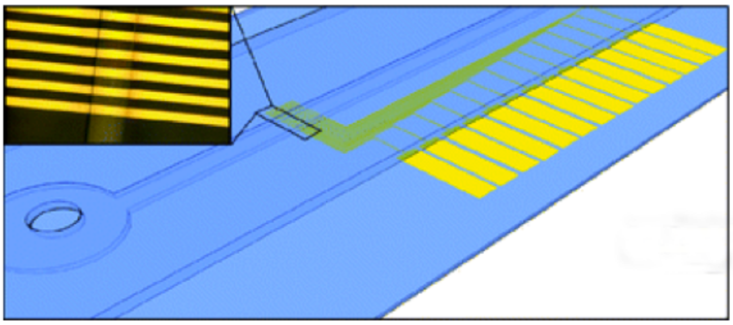

Figure 4.5: Schematic of the COC chip developed by Illa *et al.*[27] showing the fourteen gold microelectrodes. Insert: Optical image of the microfluidic channel crossing the set of gold microband electrodes. From Illa *et al.*[27]

Simms *et al.*[44] developed a two-electrode electrochemical cell comprising a steel electrode serving as the base of the channel and a glassy carbon electrode serving as the top of the channel (Figure 4.6). The width of the reactor was 1 mm, its length 52 mm. The channel depth was varied between 40 and 200 µm during chip fabrication. The glassy carbon plate was used as the working electrode and the steel plate as the auxiliary electrode. The electrochemical reactor performances were demonstrated by performing the anodic methoxylation of 2-pyrrolidinone to synthesize 5-methoxy-2-pyrrolidinone under galvanostatic conditions. The reaction was performed over several hours without any loss in yield of the reaction. It was observed, as expected that for a given flow rate, the reaction yield increased when increasing the current density on the working electrode and that when decreasing the flow rate for a given current density the yield increased due to a longer residence time of analytes in the reactor. It was also noted that the reaction could be carried out without supporting electrolyte in channel depths up to 130 µm.

However, the device described by Simms *et al.*[44] is a two-electrode electrochemical cell and as such the absolute potential of working electrode is not known. For reaction where galvanostatic operation is sufficient, this should not be an issue. However, for electrochemical reactions where the potential needs to be accurately controlled this two-electrode design could not be used.

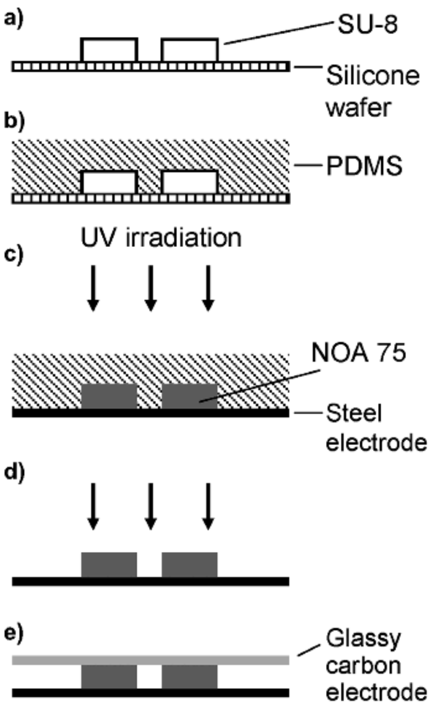

Figure 4.6: Schematic representation of the fabrication process of the microfluidic electrochemical cell capable of conducting electrosynthesis reactions. (SU-8 is a photoresist and NOA 75 an epoxy adhesive cured by UV). From Simms *et al.*[44]

4.1.5 ELECTROACTIVE SEMI-CONDUCTING POLYMERS

Semi-conducting organic polymers have been widely studied over the past 20 years[45-48]. They can be divided into three families: polypyrroles (PPy), polyanilines (PANI) and polythiophenes. These polymers are semiconductor in nature due to electronic delocalization. They already have extensive applications in chemical sensing, in batteries, as actuators and as corrosion inhibitors. The large range of applications comes from the remarkable properties of these conducting polymers. Films of these materials can be synthesized in various ways, including casting from nanoparticulate suspensions, vapor phase deposition and electropolymerization[45, 47]. Electropolymerization results in highly homogeneous reproducible films whose thickness can be accurately controlled. Here, we will focus on PPy and PANI and discuss their electrochemical synthesis and electrochemical properties.

4.1.5.1 Polypyrrole

PPy is synthesized by oxidation of pyrrole and its derivatives. The structure of PPy is shown in Figure 4.7. To induce polymerization of pyrrole, two main routes have been used: electrochemical oxidation and chemical oxidation. The electrochemical synthesis of PPy usually results in a film at the surface of the working electrode[45] while a chemical synthesis produces a PPy powder[45]. Here we will focus on the electrochemical synthesis of PPy and its electrochemical properties.

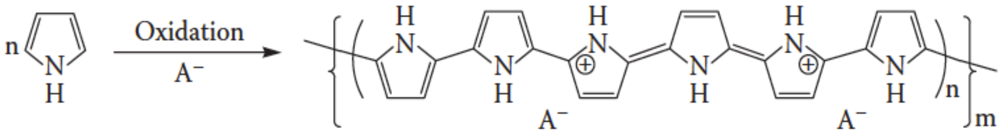

Figure 4.7: Synthesis of PPy by oxidation. From Wallace *et al.*[45]

4.1.5.1.1 Electrochemical synthesis of polypyrrole

The electropolymerization of pyrrole is believed to be a radical-to-radical coupling[49] where the natural repulsion of the radical is negated by the solvent. The accepted mechanism is given in Figure 4.8.

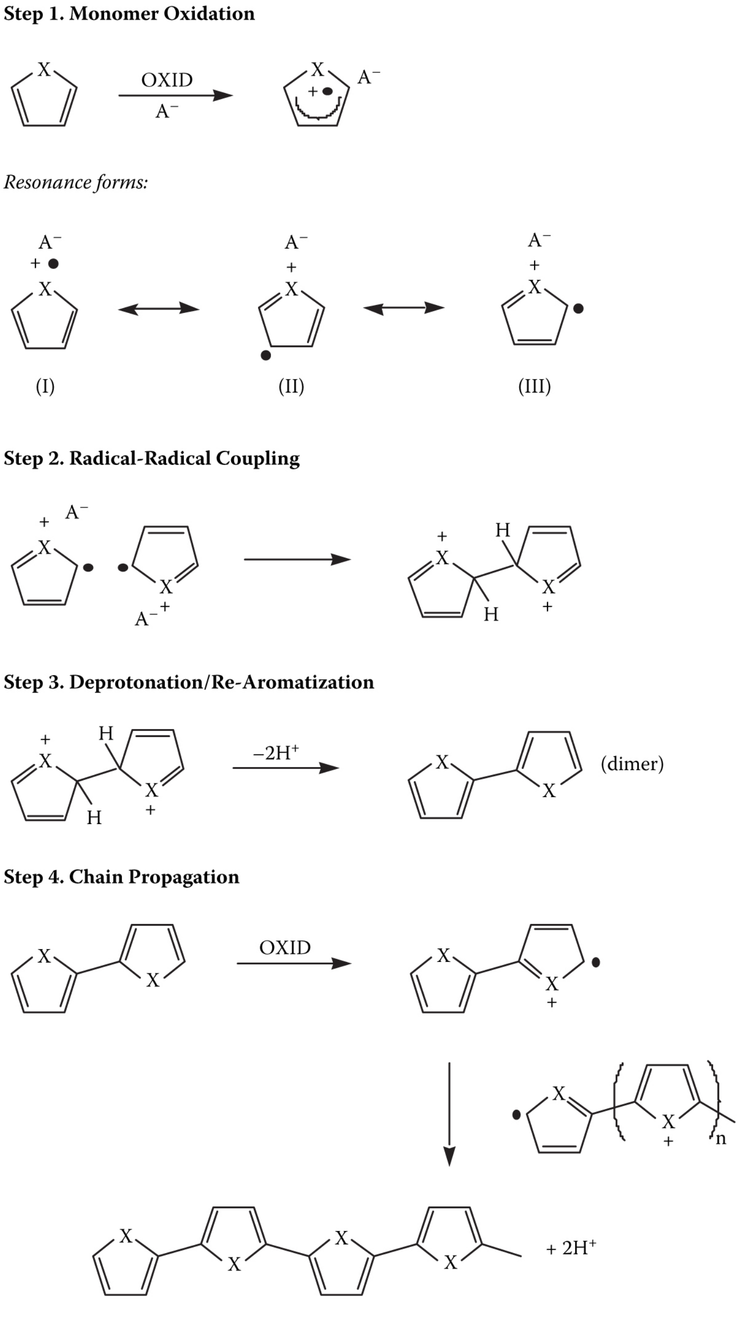

Figure 4.8: Mechanism of the electropolymerization of PPy (X=NH). From Wallace *et al.*[45]

The first step, the oxidation of the monomer, is the kinetic limiting step[50]. The radical-to-radical coupling, deprotonation and further oxidation are believed to be rapid. Chain growth continues until the incorporation of an anion (dopant), when the charge on the chain is defined. Eventually, when the chain length increases over a critical length, precipitation of the polymer onto the working electrode surface occurs[51-54]. The doped polymer is noted PPy/X, X being the dopant. Various dopants from small ions such as Cl^- and SO_4^{2-} to large polyelectrolyte such as PS sulphonate (PSS) have been used to dope PPy[45].

The solvent, the electrodes material, geometry, configuration, the nature of dopant, and the temperature all influence the final properties of the electropolymerized polymer[45]. The influence of these parameters will be discussed later in Section 4.1.6.

4.1.5.1.2 Electrochemical switching of polypyrrole

PPy is electroactive. A typical cyclic voltammogram (CV) (Figure 4.9) shows two redox peaks for PPy (one oxidation and one reduction peak).

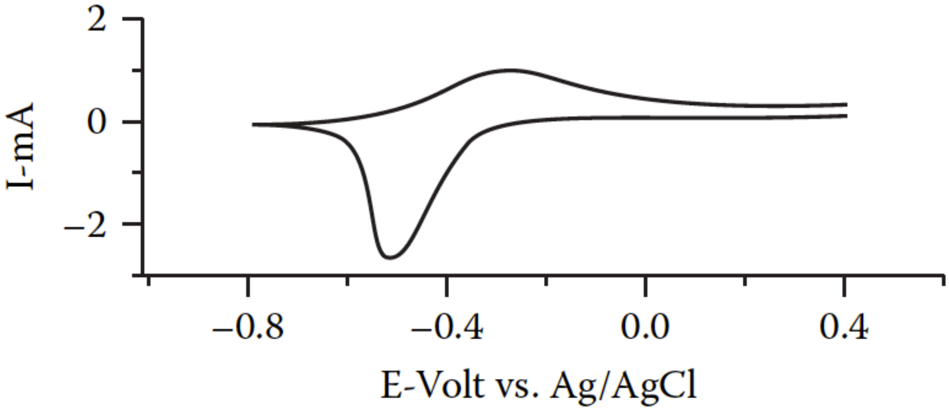

Figure 4.9: CV of PPy/DS (DS: dodecyl sulfate) in 1 M NaCl. From Talaie *et al.*[55]

The two redox states have different physical properties. One of the most remarkable properties in PPy is its electrochemical actuation[56-58]. When changing its oxidation state, the polymer can contract or expand. Further still, in a given oxidation state, the polymer can be contracted or expanded depending on the dopant incorporated during electropolymerization[59, 60].

If a small anion is incorporated during electropolymerization, on reduction of the polymer, it loses its charge. As a consequence the small anionic dopant is expelled with its solvatation layer from the polymer and so the polymer contracts. When re-oxidized, the anionic dopant moves back in the polymer and the polymer expands. A schematic of the effect on PPy of a small anionic dopant is shown Figure 4.10.

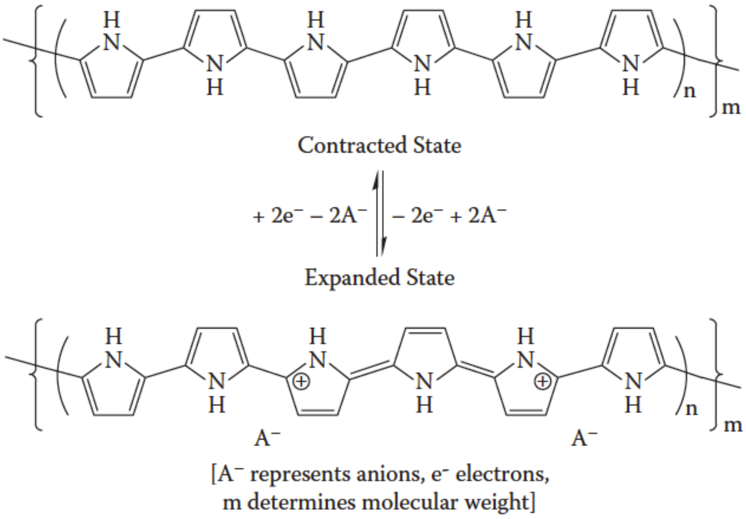

Figure 4.10: Effect of a small anionic dopant on the actuation of PPy. From Wallace *et al.*[59]

If a bulky anionic dopant, such as a polyelectrolyte, is incorporated during the electropolymerization process, the opposite phenomenon occurs. When reducing the polymer, the bulky dopant cannot be expelled. To counter balance the charges, an intake of cations is needed. As the cations have a solvatation layer, the intake of cations and solvent forces the polymer to expand. When oxidized, the cations and solvent are expelled and the polymer contracts. Figure 4.11 shows the effect of bulky anionic dopants on the PPy actuation.

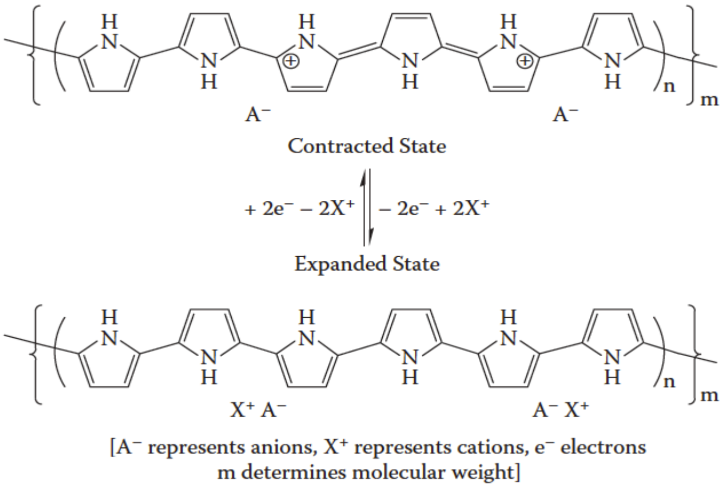

Figure 4.11: Effect of a bulky anionic dopant on the actuation of PPy. From Wallace *et al.*[59]

As demonstrated by Higgins *et al.*[58], several redox cycles between the oxidation and reduction states are necessary before the rate and magnitude of actuation becomes constant. The nature of the dopant and the electrolyte used for electrochemical actuation govern the amplitude of the actuation[60].

4.1.5.2 Polyanilines

PANI is synthesized by oxidation of aniline and its derivatives. The structure of PANI is shown in Figure 4.12 and 4.13. To induce polymerization of aniline, two main routes have been used: electrochemical oxidation and chemical oxidation. The electrochemical synthesis of PANI usually results in a film at the surface of the working electrode[47] while a chemical synthesis produces a PANI powder[47]. Here we will focus on the electrochemical synthesis of PANI and its electrochemical properties.

4.1.5.2.1 Electrochemical synthesis of polyaniline

PANI is synthesized by the oxidation of aniline and its derivatives. The accepted mechanism for PANI electropolymerization is, as for PPy, radical-to-radical coupling process as presented in Figure 4.12[47, 61]. The formation of the radical cation of aniline (Step 1) is considered to be the rate-determining step. It is follow by radical/radical coupling, mainly N- and *para*-forms, and the elimination of 2 protons. The formed dimer undergoes an oxidation on the electrode surface along with aniline. The coupling between the radical dimer and a radical aniline cation propagate the chain. Finally, the polymer is doped (Step 4).

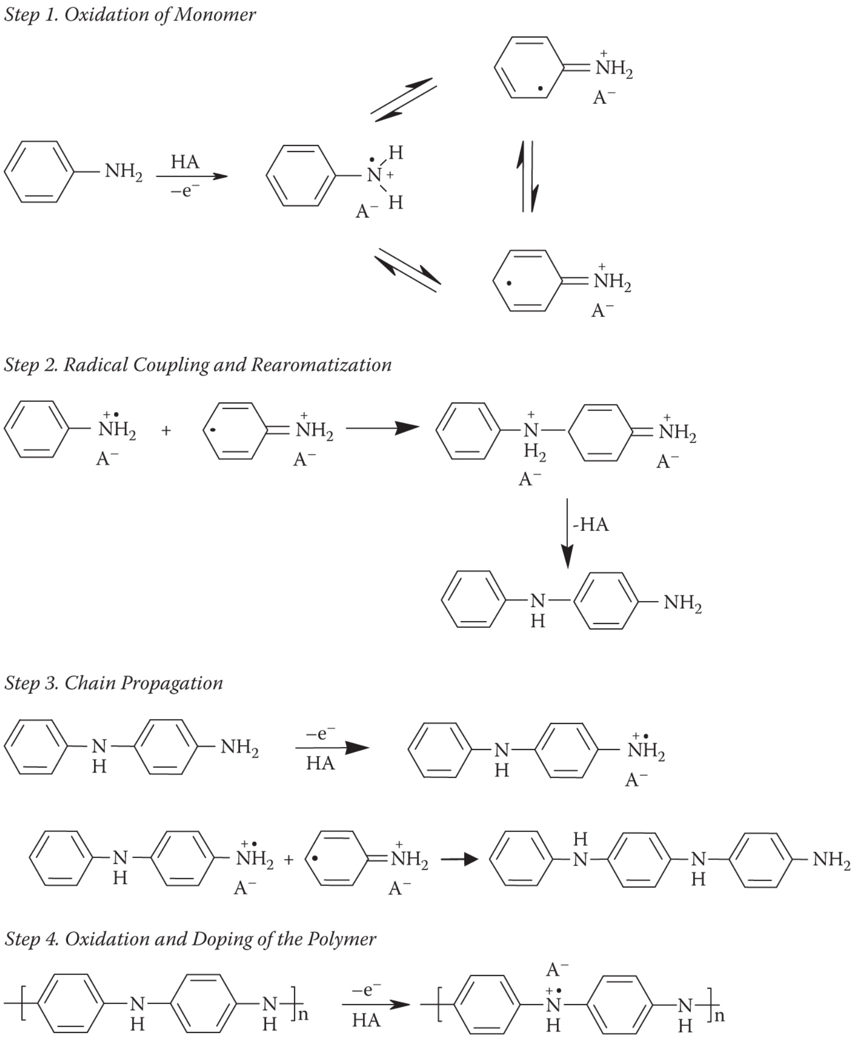

Figure 4.12: Mechanism of aniline electropolymerization. From Wallace *et al.*[47]

As for PPy, the electrochemical conditions, electrochemical cell design (geometry, electrode materials), nature of the dopant, will all affect PANI physico-chemical properties[45, 47].

4.1.5.2.2 Electrochemical switching of polyaniline

PANI and PPy have the ability to switch between several oxidation states. However, PANI has three oxidation states and for each oxidation state has two forms: a protonated form in acidic media and a deprotonated form in basic media[48]. The six forms of PANI are given Figure 4.13. The most conductive form is protonated emeraldine salt.

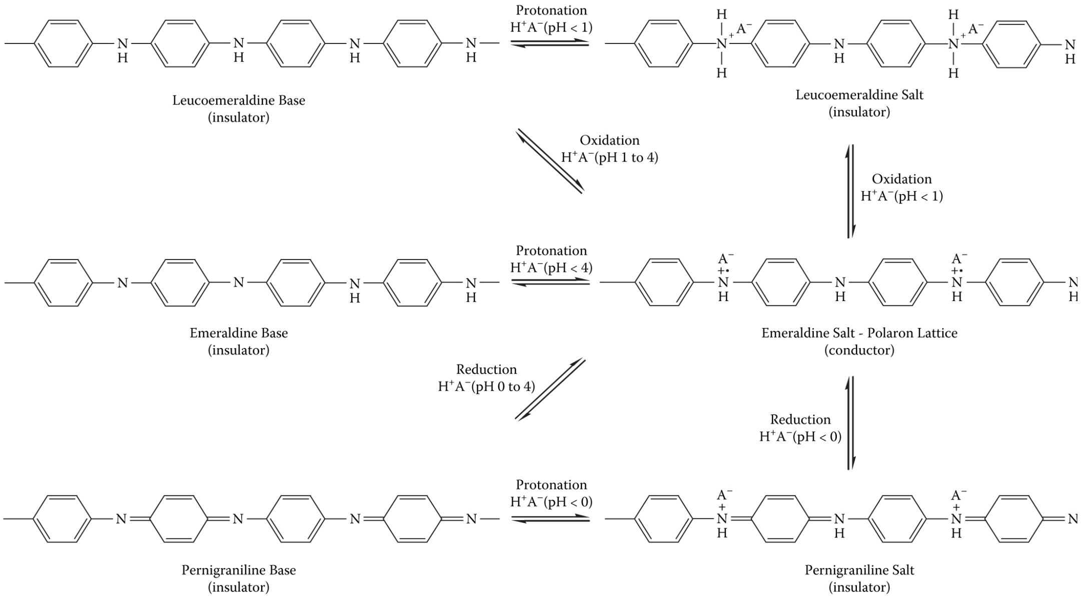

Figure 4.13: The six forms of PANI. From Wallace *et al.*[48]

Figure 4.14 presents a typical CV for PANI in acidic media. One of the most interesting properties of PANI is its chromic property. Each oxidation state and near oxidation state transition have different colors.

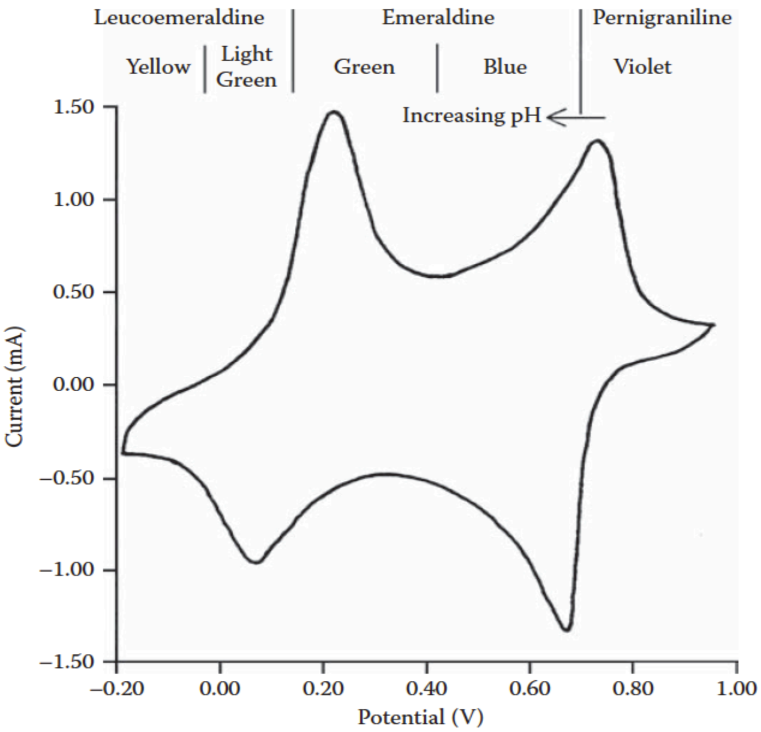

Figure 4.14: Typical cyclic voltammogram of PANI in acidic medium. From Wallace *et al.*[48].

As with PPy, actuation occurs with PANI when changing its oxidation state. Anodic or cathodic swelling can be observed depending on the size of the anionic dopant used[62-64].

PANI is also biocompatible and has often been used as a diffusionless mediator to develop biosensors[11, 65-67]. Enzymes are electrodeposited or adsorbed onto the PANI surface and their electrocatalytic response to target analytes can be quantitatively measured by monitoring the amount of charge passed at a given potential.

4.1.6 ELECTROCHEMICAL CELL DESIGN FOR CONDUCTIVE POLYMER ELECTROPOLYMERIZATION

It is possible to electro-deposit electroactive polymers such as PPy and PANI onto a working electrode. It has been demonstrated that the design of the cell for the deposition of electroactive conductive polymers has great impact on the physico-chemical properties of the polymers[45, 47]. Indeed, the electrode materials, temperature, solvent and dopant are all parameters influencing the structure and conductivity of the deposited polymer. Further still, when a flow of reactants is used, the position of the electrodes with respect to the direction of the flow also influences the polymer structure and conductivity[45, 47]. Due to their unique properties, conductive polymers have specific needs regarding the electrochemical cell design for their electropolymerization.

It has been shown that the cell design and electrode shape can have dramatic effects on the polymer formed[68]. The set-up usually used for electropolymerization of electroactive polymers is a three-electrode potentiostated system to ensure control over the potential of the working electrode, thus reproducible growth can be achieved. Two-electrode set-ups can also be used, however, it can result in irreproducible polymer films as the absolute growth potential is not controlled. When designing a suitable cell for the electropolymerization of conducting polymer, some major considerations must be taken into account, due to the intrinsic properties of the polymers. These considerations include iR drop and the cell hydrodynamics.

To deposit polymer to a working electrode surface, the polymerization rate needs to be rapid enough to produce oligomers with a molecular weight sufficiently large for the polymer to precipitate and, hence, deposit on the working electrode[45, 47]. For deposition, the oligomers formed must be rendered insoluble at the electrode surface. For example, if the working electrode material is too polar at the potential employed for polymerization, precipitation of the polymer onto the electrode become difficult. This was demonstrated by Huang *et al.*[69] for depositing PANI on patterned indium tin oxide (ITO). The ITO electrode surface was treated to obtain a pattern of hydrophilic and hydrophobic surfaces. The rate of electrodeposition of PANI was greater on the hydrophobic areas than on the hydrophilic ones.

Other working electrode materials employed include platinum, gold, glassy carbon. The working electrode needs to be stable at the potential selected for electrochemical growth of conductive polymer. As a positive potential is usually employed, the working electrode could potentially oxidize liberated metallic cations, *e.g.* Fe^{3+}, Cu^{2+}, which could interfere with the oxidation of monomer. In such scenarios, passivation agents such as oxalic acid[70, 71] and molybdate[72] have been added to the monomer mixture used to electropolymerize both PPy and PANI on aluminium. It has also been shown that the conductivity of the working electrode has dramatic effect on the conductivity of the deposited PANI, *i.e.* PANI conductivity increased when increasing electrode conductivity[73].

The auxiliary electrode material and its position relative to the working electrode are also of primary importance. As for the working electrode, the material must be inert as the liberation of interfering species could negate the polymerization. In addition, the reduction of monomer or solvent at the auxiliary electrode could also create interfering species[45].

When a working electrode is modified with a non-conducting or semi-conductive material (*e.g.*, electroactive polymer), the resistance of the electrode increases. As such, the magnitude of the iR drop between the working and the reference electrode increases. Thus, the applied potential on the working electrode surface decreases and the polymerization is therefore slowed down.

Temperature also determines rates of undesired side reactions. It is known that the radicals formed during the first polymerization step (oxidation of monomer) can react with dissolved oxygen to produce low conductivity products. The higher the temperature, the higher the rate of such a reaction. For PPy, for example, it has been shown that carrying out electropolymerization at -28ºC in propylene carbonate as solvent is necessary to achieve maximal conductivity[45]. Influence of temperature on PANI has been less studied but influences have been noted[47].

The hydrodynamics of the cell control the rate of transport of reactants (monomers, dopant, soluble oligomers) and products (polymer) to and from the electrode surface. Therefore the hydrodynamics of the cell will have a large impact on electrochemical growth of polymer. For instance, flow through cells have been used to produce colloidal suspensions of PPy[74,75]. Hydrodynamics during electropolymerization have been studied using a flow cell system[76, 77]. As the flow of monomer was increased, the electrochromic properties of PANI were improved. This was attributed to the side reaction products not being incorporated into the polymer as they were carried away by the flow of monomer. However, it has also been shown that cell hydrodynamics can transport undesired species onto the working electrode, resulting in less conductive polymers films[78]. Therefore, care must be taken, when designing a flow through electrochemical cell for electroactive polymer electropolymerization, so as not to decrease polymer conductivity due to undesired hydrodynamic effects. If flow is applied to the electrochemical cell, the auxiliary electrode needs, if possible, to be down stream from the working electrode so the interfering species created on the electrode surface are moved away from the working electrode[45].

4.1.7 SUMMARY

In summary, electrochemical cells fabricated on microfluidic devices are mostly used for electrochemical detection and sensing applications. However, two- and three-electrode electrochemical cells used as flow cells to perform electrochemical reactions can be found in the literature. It has also been demonstrated that integrating viable electrochemical cells into microfluidic devices requires sophisticated microfabrication. In addition in microfluidics, stabilization of the 2-dimensional reference electrode is an issue and research is underway in order to find facile and efficient ways of stabilizing it.

Electroactive polymers, as functional materials, are very attractive due to their remarkable switching properties. Each of the properties (*i.e.* actuation, electrochroism) can be finely tuned according to the experimental conditions used during electrochemical polymerization. All intrinsic properties however are linked to the polymeric chain arrangement and conformation and as such are not independent[45-48].

Electroactive polymers have specific electrochemical cell design requirements for their electropolymerization. The materials used for the working and auxiliary electrodes should be chosen so that the polymer becomes insoluble at the working electrode surface and is chemically stable at the applied potential selected for electropolymerization so as not to release interferents during the polymerization process. Hydrodynamics should also be taken into account and, if possible, the auxiliary electrode should be placed downstream from the working electrode in a flow cell configuration.

In this chapter, the integration of an electrochemical cell in a microfluidic device suitable for electroactive polymer electropolymerization is presented. The objective of this work is to fabricate an electroactive monolithic stationary phase for the EMμ project. First, an electrochemical cell integrated into a large fluidic channel (CD1) is presented. Then two- and three-electrode systems integrated into microfluidic channels (CD2) are presented. The electrochemical behavior of each cell is assessed using standard ferricyanide electrochemistry. Then, electropolymerization of aniline and its redox switching capabilities using the proposed electrochemical cells is extensively discussed.

4.2 CHIP DESIGN 1

CD1 was initially designed for incorporating a flow-through biosensor based on PANI in a microfluidic chip. Following electropolymerization of PANI in the fluidic channel, an enzyme could be electrostatically immobilized or adsorbed onto the PANI permitting real time, LOC-based biosensing. The PANI was successfully electropolymerized in the fluidic channel of CD1. In order to achieve this and to perform amperometric biosensing on the enzyme-modified PANI, the fluidic channel was required to house a 3-electrode electrochemical cell with properties approaching that of an ideal configuration. This section describes this design and assesses it for its viability as an electrochemical reactor for application in EMμ.

4.2.1 ELECTROCHEMICAL CELL DESIGN

The working electrode was fabricated by sputtering gold onto the base piece of the chip through a mask as described in Appendix 1. The pseudo-reference and auxiliary electrodes were fabricated from 0.5 mm Ag and Pt wire, respectively. These wires were housed in the upper piece of the chip as described in Appendix 1. The Pt and Ag wires ran the full length of the fluidic channel in order to minimize the iR drop between the pseudo-reference and working electrode and to maximise the surface area of the auxiliary electrode. A polyvinylidene fluoride (PVDF) membrane was applied between the upper and base pieces of the chip in order to prevent physical contact between the PANI monolith to be grown and the pseudo-reference and auxiliary electrodes during electropolymerization. The hydrophilicity and porosity of the PVDF membrane, however, permitted electrical contact between the auxiliary, pseudo-reference and working electrodes via the electrolyte. However, in practice, it was shown that PANI could physically permeate through the PVDF membrane pores so the effectiveness of the membrane was reduced. The membrane, however was used to indicate when the channel was filled with PANI as when the PANI began to permeate the membrane, the green color of the emeraldine salt form of PANI was observed visually. At this point, it was assumed that the fluidic channel was filled with monolithic PANI.

Although the membrane proved a useful component of CD1 for monolith fabrication, from a separations point of view, liquid trapped in the membrane constitutes a stagnant zone and adds to the band broadening discussed in Chapter 3. As demonstrated, stagnant zones in CD1 are an issue which could potentially prevent its use as a separation tool due to large band broadening.

4.2.2 ON-CHIP FERROCYANIDE ELECTROCHEMISTRY

In order to verify the validity of the embedded 3-electrode electrochemical cell within the chip, CVs of ferricyanide/ferrocyanide ($Fe(CN)_6^{3-}/Fe(CN)_6^{4-}$) were performed in the channel. Figure 4.15 shows typical voltammograms recorded at a scan rate of 100 mV/s. Oxidation of $Fe(CN)_6^{4-}$ occurred at a potential (E_p) of +270 mV vs. Ag/AgCl during the forward scan. Reduction of ferricyanide to ferrocyanide occurred at an Ep of +200 mV vs. Ag/AgCl. This resulted in a ΔE_p of 70 mV, which had been previously found to be close to ideal for ferrocyanide on bare gold electrodes (for a one electron process ΔE_p is ideally 59 mV) and thus proves the reversibility of the reaction[79]. By extracting the cathodic peak current (i_{pc}) and the anodic peak current (i_{pa}), it was also shown that the reaction was reversible at the gold electrode surface as $i_{pa}/i_{pc}=0.77$. A scan rate study was also undertaken which demonstrated the linear proportionality between peak current and (scan rate)$^{1/2}$ for both the i_{pc} and i_{pa} currents (Figure 4.15, insert). The scan rate study showed a diffusion limited reaction. Peaks shapes, the scan rate study and the observed reversibility of the ferri/ferrocyanide couple (ΔE_p= 0.70 V, i_{pc}/i_{pa}= 1.3) indicated that the electrochemical cell inside the separation channel was valid. Therefore electrochemical growth and control of a PANI monolith could potentially be realized within the cell.

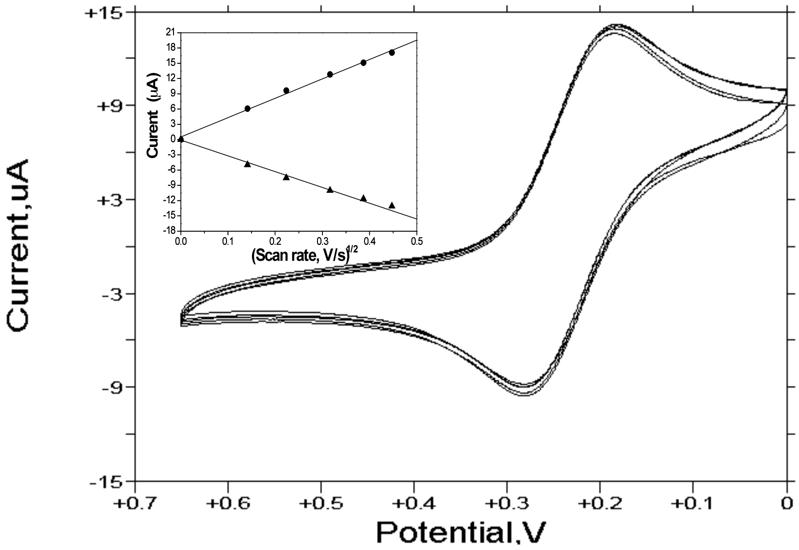

Figure 4.15: Typical voltammograms for $Fe(CN)_6^{3-}/Fe(CN)_6^{4-}$ (2 mM) in 0.1 M KCl at 100 mV/s. Insert: Scan rate study showing linearity between anodic (▲) and cathodic (●) peak currents versus (scan rate)$^{1/2}$. Courtesy of Dr. Fuqiang Nie.

4.2.3 ANILINE ELECTROPOLYMERIZATION IN THE FLUIDIC CHANNEL OF CHIP DESIGN 1 COMPRISING AN ELECTROCHEMICAL CELL

With the validity of the electrochemical cell embedded within the fluidic channel confirmed, it was therefore possible to electropolymerize aniline into the fluidic channel (where the base and the two side walls were gold-sputtered to serve as a working electrode) in closed chip configuration. In this work, carried out by Dr. Fuqiang Nie, the method used to polymerize aniline was cyclic voltammetry (scan rate: 100 mV/s. Polyvinyl sulfonate (PVS) was used as a dopant to increase PANI conductivity and stability). The typical cyclic voltammetric behaviour during the electropolymerization process is shown in Figure 4.16. The redox peaks observed were typical for PANI/PVS with two oxidation peaks (A) and (B) and two reduction peaks (C) and (D). Similar CVs in acidic media had been reported by other researchers[11]. The polymerization current increased with the number of potential cycles, which confirmed that the polymer was conducting and electroactive and indicated that the PANI was growing on the three gold-sputtered walls of the channel. It was also found that shifts in peak potentials began to occur after a number of potential cycles, which may have been the result of increased resistance of the electrode due to increasing thickness in the PANI/PVS film[65] or a shift in the pseudo-reference electrode potential.

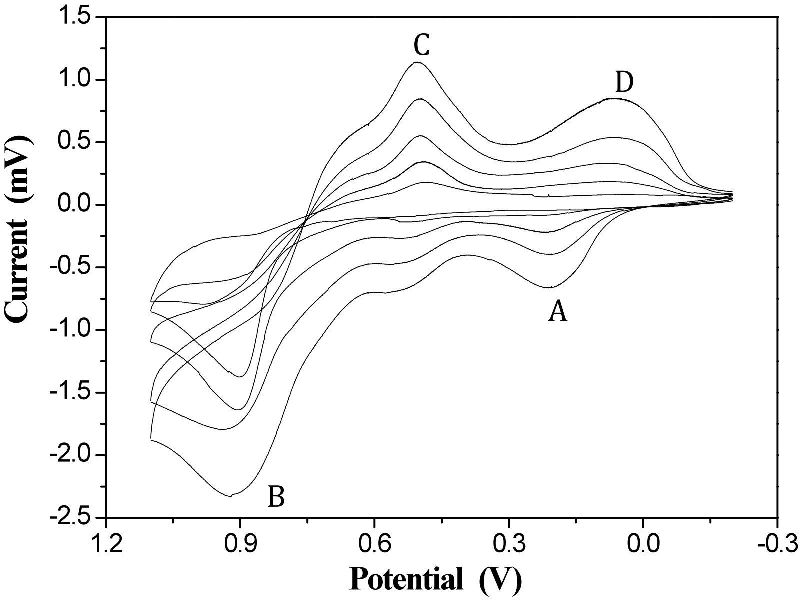

Figure 4.16: Electropolymerization of PANI/PVS on the gold-sputtered walls of the fluidic channel in CD1 (20 mm x 2 mm x 20 μm), scan rate = 100 mV/s, flow rate 10 μl/min. (Pt auxiliary electrode, Ag/AgCl pseudo-reference electrode). Courtesy of Dr. Fuquiang Nie.

4.3 CHIP DESIGN 2

CD2 comprised of a glass base piece purchased from Micronit®, with a main fluidic channel (dimensions: 40 mm x 110 μm x 50 μm) and an upper piece comprising flexible polyethylene terephthalate (PET) (thickness: 175 μm). All dimensions are given in Appendix 2. In CD2 the working electrode comprised a gold sputtered film as described in Chapter 2, Section 2.4.2.1. The use of wires as reference and auxiliary electrodes was prohibited by the smaller dimensions of this channel compared with CD1 and so a different approach for designing the pseudo-reference and auxiliary electrodes was required. When designing this electrochemical cell, two configurations were possible. The electrochemical cell can comprise of two or three electrodes (see Sections 4.1.1.1 and 4.1.1.2). Two-electrode systems are simpler to implement, particularly in microfluidic channels. However they give a lesser degree of control over the absolute potential of the working electrode than three-electrode cells. Both two-electrode and three-electrode cells have been designed to create electrochemical cells within the fluidic channel of the glass chips (CD2) and are discussed in this section.

4.3.1 THREE-ELECTRODE ELECTROCHEMICAL CELL DESIGN

A 3-electrode electrochemical cell allows control over the potential of the working electrode as it is defined from the reference electrode, which has a known and constant potential. The current is measured between the working and the auxiliary electrodes. The three-electrode configuration is the most commonly used cell for performing electrochemistry. In particular, it is standard practice for performing electropolymerization of electroactive polymers due to the level of control over the potential applied to the working electrode in order to achieve reliable high quality polymerization and reproducibility of the physico-chemical properties of the polymers. For the 3-electrode system for CD2, two designs using different printing approaches and polymer substrates were investigated for fabricating the pseudo-reference and auxiliary electrodes. The working electrode comprised of the gold-sputtered base and walls of the channel, as before.

4.3.1.1 Design

In the research group of Prof. Malcolm Smyth, screen-printed carbon paste and silver electrodes are fabricated routinely for bio- and chemical-sensing. Screen-printing as a method is low-cost and easily scalable. Given the extensive knowledge of screen-printing in the research group, this approach was selected to print the pseudo-reference and auxiliary electrodes for the microfluidic electrochemical cell. A screen was designed for the silver-paste based electrodes to be printed onto flexible PET substrate. A photograph of the screen-printed electrodes is shown in Figure 4.17.

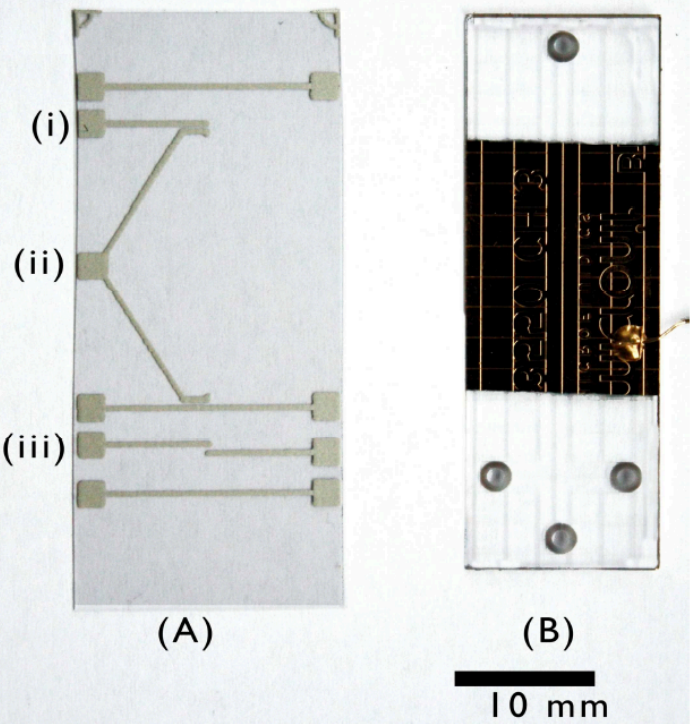

Figure 4.17: (A) Photograph of the screen-printed upper chip piece with the reference electrode (i), the branched auxiliary electrode (ii) and C^4D detector electrodes (iii). Isolating electrodes are used to isolate each electrical component (the electrochemical cell, the C^4D detector and electrodes used to generate the EOF when

performing electroseparations situated at the inlet and outlet of the base piece of CD2). (B) Photograph of microfluidic base piece of CD2 with gold-sputtered fluidic channel serving as the working electrode.

The design comprises a pseudo-reference electrode chlorinated according to Method 2.4.2.2.3 and a double branched auxiliary electrode. The reference electrode was designed so as to place it at the beginning of the fluidic channel, and the auxiliary electrode was designed to have interfaces exposed both at the beginning and end of the channel. The combined electrode area of the auxiliary electrode was 2.5×10^{-7} m^2. This branched configuration was used to minimize the iR drop as well as increase the surface area of the auxiliary electrode. PET was used as the substrate as it was not possible to screen-print directly onto PSA using screen-printing as screen-printing is operated in contact mode, which would damage the adhesive properties of the PSA. In this instance PSA cutting was still required but was kept to a minimum at both ends of the channel, *i.e.* outside the working electrode area. The cuts were 2 mm x 1 mm and 1mm x 1mm at the beginning and end of the channel respectively and were fabricated using a standard hole puncher. The void space created in this instance was a distance from the working electrode and therefore, will not contribute to inhomogeneities of the stationary phase structure. However, these voids need to be kept to a minimum and laser cutting of the PSA should be investigated in the future.

The design presented in Figure 4.17 also includes contactless conductivity detector electrodes as well as electrodes to isolate each electrical component from each other. All electrodes are comprised of silver-paste ink and thus, all electrodes were fabricated in a single print.

The thickness of the printed tracks of the screen-printed silver paste electrodes was < 3 µm, which was low enough for the PSA to adhere to PET-based screen-printed upper piece of CD2 to the base piece without issue. A schematic of the electrochemical cell after bonding is given in Figure 4.18.

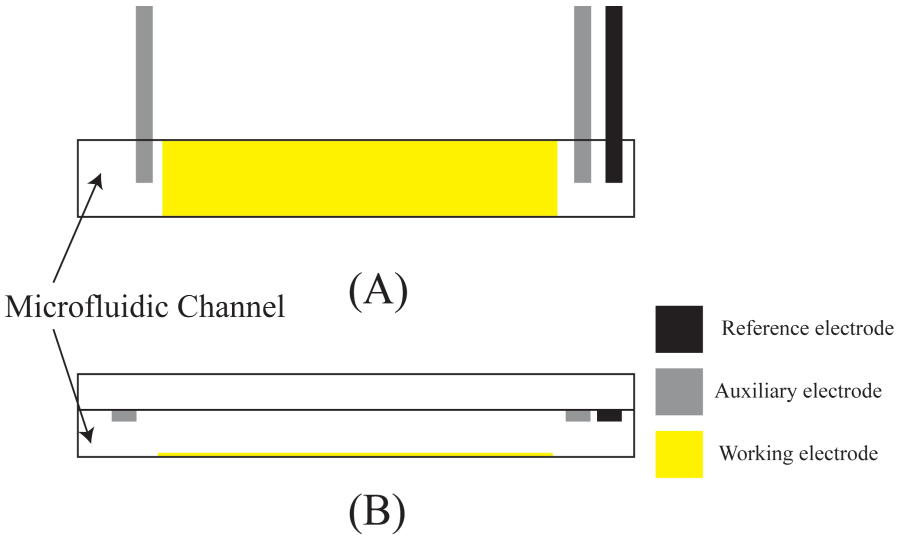

Figure 4.18: Schematic of the three-electrode electrochemical microfluidic cell with the gold-sputtered channel as the working, the screen-printed pseudo-reference and the auxiliary electrodes in the upper piece, (A) top view, (B) cross section (not to scale). See also Appendix 2.

4.3.1.2 Validity of the 3-electrode electrochemical cell in Chip Design 2

In order to verify the validity of the embedded 3-electrode electrochemical cell within the microfluidic channel of CD2, cyclic voltammetry of ferri/ferrocyanide ($Fe(CN)_6^{3-}/Fe(CN)_6^{4-}$) was performed in the channel. Ferricyanide in 0.1 M KCl was injected into the channel using a syringe pump. The validity of the electrochemical cell was assessed in batch mode, *i.e.*, without flow. However, due to the small volume of the channel (~100 nL) with respect to the high working electrode surface area (0.32 mm^2), the ferricyanide solution was replaced after each voltammetric scan. All CVs show typical behavior, after stabilization of the current, which typically occurs after 1 to 2 cycles.

As a control, ferricyanide redox activity on the gold-sputtered working electrode (*i.e.* base channel) was also measured by performing cyclic voltammetry using a commercially available external Ag/AgCl reference electrode and a platinum mesh auxiliary electrode. The voltammogram is given in Figure 4.19 (red). Oxidation occurred at +330 mV and reduction at +170 mV so the ΔE_p = 160 mV. However, in an ideal reversible electrochemical system the ΔE_p is 59 mV for this one-electron process. Therefore, as $\Delta Ep > 59$ mV, the system, in this case, is termed to be quasi-reversible. There are several possible reasons for this. It is possible that organic impurities/oxides were present at the gold surface that could potentially interfere with ferricyanide electrochemistry, or slow down the reaction kinetics thus increasing ΔE_p[1]. An attempt to clean the gold surface by voltammetric cycling the electrode in H_2SO_4 (1 M) was unsuccessful as the gold-sputtered layer delaminated from the glass base piece during this process. Indeed, the gold layer was just 100 nm thick and it seemed that during voltammetric cycling in H_2SO_4, the gold completely removed itself from the glass surface after just 2 cycles. During cycling, a gold oxidation/reduction takes place. Au^0 is oxidized to Au^{3+}, then reduced back to Au^0. During this process, impurities and oxides should be eliminated but in this case, it served to destabilize the gold-sputtered film itself.

The conducting paths of the electrodes can also influence the reversibility of an electrochemical reaction. The connection between the gold-sputtered working electrode and a copper wire was made using silver loaded epoxy glue. The resistance of this connection could potentially induce an increase of the ΔE_p and thus decrease the reversibility of the reaction on the working electrode surface. In CD1, electrochemistry close to ideal was obtained on the gold-sputtered working electrode (Figure 4.15). However, the potentiostat was directly connected to the working electrode layer *via* a crocodile clip. However, in CD2, the working electrode could not be directly connected as the microfluidic chip was embedded in a chip holder. Therefore, there was no access to connect the potentiostat directly to the chip and a connection *via* a silver-loaded epoxy glue was necessary. This is not an ideal approach and may well contribute to the quasi-reversibility of the system.

When the microfluidic chip was closed, CVs were carried out in 2 mM Ferricyanide in 0.1 M KCl as for the control (Figure 4.19, blue). In this instance, the on-board pseudo reference and auxiliary electrodes were used. The screen-printed reference electrode was chlorinated to form a Ag/AgCl pseudo-reference according to Chapter 2, Section 2.4.2.2.3. The resulting anodic peak had a potential of +200 mV and the cathodic peak of +40 mV resulting in a $\Delta Ep = 160$ mV. Therefore, the ΔE_p value did not change from the control experiments, *i.e.* using the open chip configuration using standard external reference and auxiliary electrodes. This shows that the screen-printed reference and auxiliary electrodes did not influence the reversibility of the reaction on the working electrode. Thus, the large ΔE_p was, as a consequence attributed to either impurities on the working electrode or the resistance of the conduction path. A shift of 130 mV in the cathodic direction was observed for the CVs generated using the on-board screen-printed pseudo reference and auxiliary electrodes. This was almost certainly due to the chlorinated silver paste screen-printed reference electrode having a standard potential that was significantly different from the commercial standard Ag/AgCl electrode. The commercial reference should have a potential of approximately +200 mV *vs.* NHE[1]. The on-board silver paste reference therefore has a potential of +70 mV *vs.* NHE. This shift in potential was not an issue, as the potential of the on-board reference electrode remained constant over time, as seen in Figures 4.20 and 4.22.

It can also be seen on Figure 4.19 that the currents generated when the chip was open and closed were significantly different. When open, the current recorded was in the 200 µA region while when closed the current generated was in the 3 µA region. This approximately 100-fold decrease in the current was expected as the effective surface area decreased from open to closed chip configuration. In open chip configuration, the working electrode was the complete gold-sputtered area (300 mm^2). However, when recording the voltammograms in closed chip configuration, the area of the electrode was defined as the base and two walls of the channel (3.2 mm^2), *i.e.* the surface area of the working electrode in contact with the electrolyte decreased dramatically on closing the microfluidic chip.

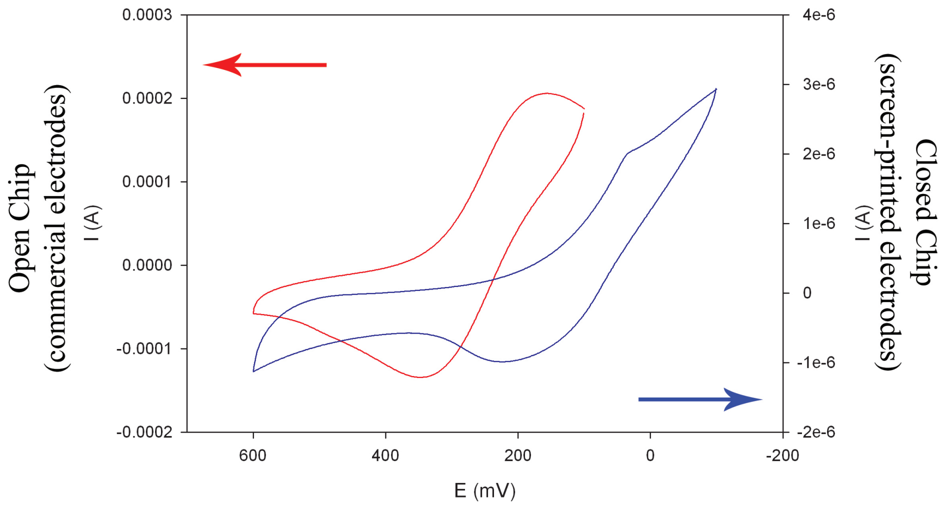

Figure 4.19: Typical CVs for ferri/ferrocyanide (2 mM in 0.1 M KCl) recorded at 100 mV/s for a gold-sputtered working electrode on chip with: (red, left y-axis) a commercial external Ag/AgCl reference electrode and platinum mesh as auxiliary electrode; open chip configuration (working electrode area: 300 mm^2) and (blue, right y-axis) using the on-board screen-printed pseudo-reference and auxiliary electrodes (Figure 4.19) electrodes; closed chip configuration (working electrode area: 3.2 mm^2) (n=3).

A scan rate study was carried out in the closed microfluidic chip, *i.e.* using the on-board screen-printed reference and auxiliary electrodes. Typical CVs obtained at each scan rate (batch mode) are shown in Figure 4.20. The ΔE_p increased with scan rate as expected for diffusion controlled reactions[1]. No true baseline can be seen for the cathodic scan. Therefore the absolute cathodic current was used to graph peak current *vs.* scan rate and therefore was offset from zero. However, the graph showed linear relationships between the cathodic and anodic current and square root of the scan rate (Figure 4.21). The linear fit of the cathodic current gives an R^2 of 0.967 and the anodic linear fit gives an R^2 of 0.983. Therefore, there was a linear relationship between the cathodic and anodic currents and the square root of the scan rate showing that the redox peaks were diffusion-controlled, as would be expected.

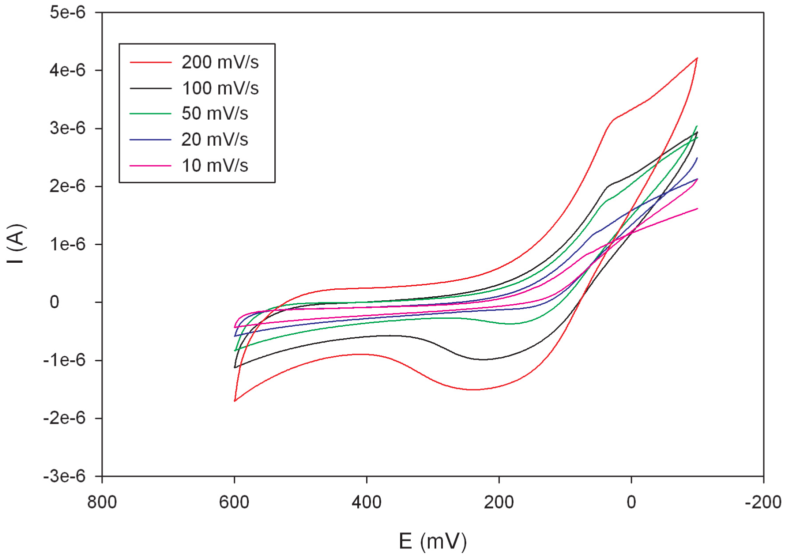

Figure 4.20: CVs of ferri/ferrocyanide recorded at different scan rates (10-200 mV/s) on the gold-sputtered working electrode (surface area: 0.32 mm^2) in closed chip configuration using the on-board screen-printed reference and auxiliary electrodes (n=3).

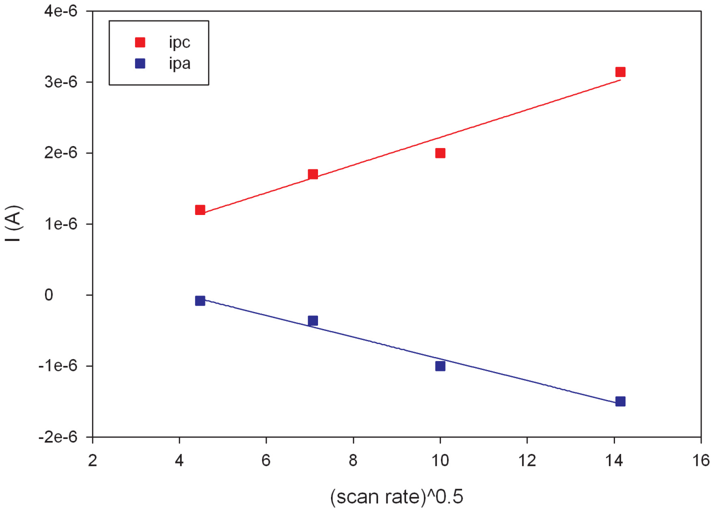

Figure 4.21: Anodic peak current (i_{pa}) and cathodic peak current (i_{pc}) as a function of the square root of the scan rate. (Data extrapolated from Figure 4.22)

For this study it can be concluded that the electrochemical cell design for the polymerization of aniline in the fluidic channel is not ideal as $\Delta Ep > 59$ mV for ferri/ferrocyanide system. However, given its quasi-reversible properties, it is realistic to expect that electropolymerization of aniline inside this electrochemical cell is possible, albeit not a perfect system. The pseudo-reference electrode potential appears to differ from a commercial reference electrode. However, it is stable and can be accounted for. Also, the nature of the auxiliary electrode is not the best. While the low surface area does not seem to be an issue for ferri/ferrocyanide electrochemistry, it did undergo reaction, *i.e.*, the auxiliary electrode underwent a color change from silver to black after a few CVs. A more inert material would be preferable, however, screen-printing platinum or gold is prohibitively expensive and therefore, it was decided to use silver, despite its drawbacks, for this initial proof of concept work.

4.3.1.2.1 Influence of flow on ferri/ferrocyanide electrochemical performance in Chip Design 2

The influence of flow over the electrochemical performance of the cell was investigated. Figure 4.22 shows CVs recorded at 100 mV/s for ferri/ferrocyanide at different flow rates varying from 0 to 20 µl/min.

When plotting the anodic and cathodic and anodic peak currents as a function of flow rate (Figure 4.23), (the cathodic current was taken without baseline correction as previously discussed), it can be seen that flow rate did not exert dramatic influence over the measured currents. In a flow-through electrochemical cell, the transport of analyte to the working electrode surface is expected to be no longer diffusion controlled but advection controlled. Therefore, an increase in current was expected when increasing the flow rate. In this instance, it was possible that over the flow rates investigated, ferri/ferrocyanide electrochemistry was still diffusion controlled because of the low flow rate and the small diffusion distances to the working electrode. However, Illa *et al.*[27] found that for smaller channel sizes (50 µm x 24 µm) and flow rates varying from 2-10 µl/min, the electrochemical behavior of ferri/ferrocyanide was controlled by flow rate and not by diffusion. However, the gold working electrode surface was just 7 x 10^{-4} mm^2 and therefore behaved as an ultramicroelectrode, *i.e.*, no diffusion controlled mass transfer is observed due to natural Brownian movement near the electrode. Thus, in experiments described by Illa *et al.*, it was possible that the ultramicroelectrodes were more sensitive to flow than the electrodes used in this study.

It was therefore expected, during electropolymerization of aniline in CD2, that the mass transfer of anilium ions to the electrode surface should be diffusion controlled, as illustrated in Figure 4.23.

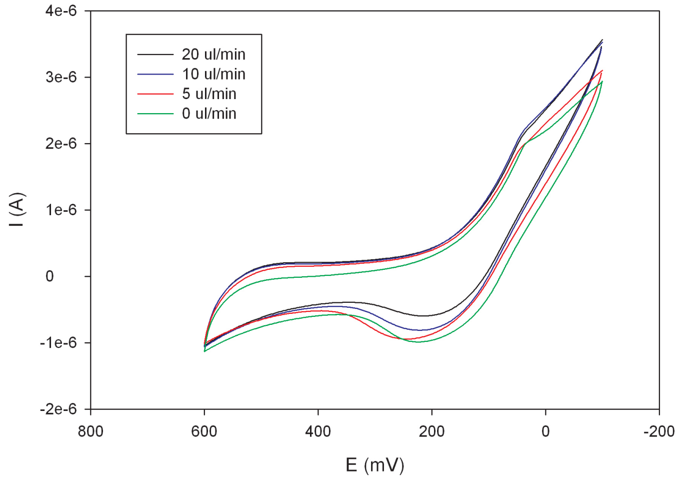

Figure 4.22: CVs of Fe^{3+}/Fe^{2+} (2 mM in 0.1 M KCl) recorded at 100 mV/s in CD2 in closed configuration for different flow rates. (n=3)

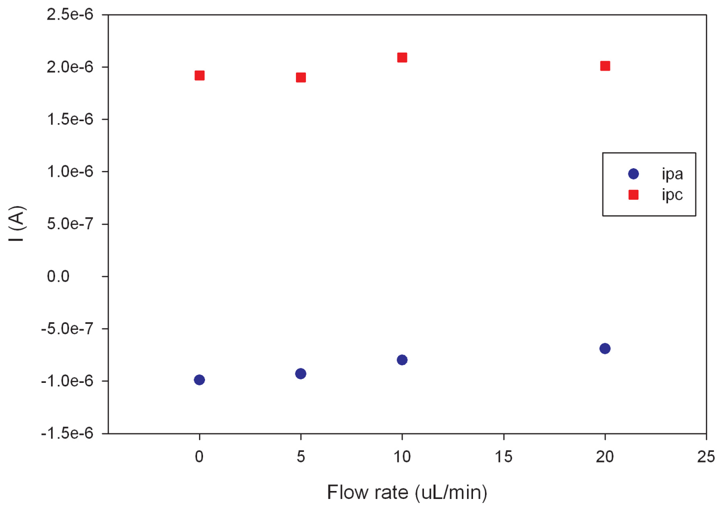

Figure 4.23: Dependency of anodic peak current (circles) and cathodic peak current (squares) on the flow rate. (Data extrapolated from Figure 4.24) (n=3)

4.3.1.2.2 PANI electropolymerization in Chip Design 2, closed configuration

A solution of 0.1 M aniline in 1 M HCl containing 2 mg/ml PSS was pumped through the channel at a flow rate of 10 µl/min. By applying a +900 mV potential between the working electrode and the on-board screen-printed pseudo-reference electrode, it was possible to grow PANI from the working electrode surface, *i.e.* on the surface of the base and sidewalls of the fluidic channel. Figure 4.29 shows a typical i-t curve resulting from the potentiostatic growth of PANI in the microfluidic channel.

Two regions can be observed in the i-t transient curve recorded for electropolymerization of aniline in CD2. First, an increase in current was observed (Figure 4.24 (I)) which was followed by a second region where a gradual decrease in current was observed before its stabilization (Figure 4.24 (II)). According to Mandic *et al.*[80], three regions exist when potentiostatically electropolymerizing aniline. The first region is characterized by an increase in current followed by an exponential decrease of the current and is attributed to the oxidation of aniline monomer at the working electrode surface, followed by its deposition onto the electrode. The second region observed by Mandic *et al.* is characterized by a second increase in current to a plateau and is attributed to the multiplication of polymerization sites in the polymer, *i.e.*, where aniline monomers can be added to the growing polymer chain. The third region is a plateau region and is attributed to a steady polymerization rate. Typical i-t transient curves observed by Mandic *et al.* are displayed in Figure 4.25. Mandic *et al.* also found that the transient i-t curves, hence the electropolymerization mechanism is affected by the counterions (dopant) and the polymerization potential applied. In this study, the two regions observed could potentially only be the first region described by Mandic *et al.* where an increase in current, due to aniline oxidation at the working electrode surface was followed by a decrease in current due to the polymer deposition on the electrode surface. The applied potential of +900 mV *vs.* on-board screen-printed pseudo-reference electrode could result in a lower absolute potential due to the shift in the potential of the screen-printed pseudo-reference electrode when compared to a standard Ag/AgCl electrode as discussed in Section 4.1.2.2.1. Therefore, electropolymerization processes may be slow and only the first region described by Mandic *et al.* was observed during the 6 min of the polymerization in the case presented here. However, polymerization was not pursued beyond 6 min to insure PANI did not block the channel.

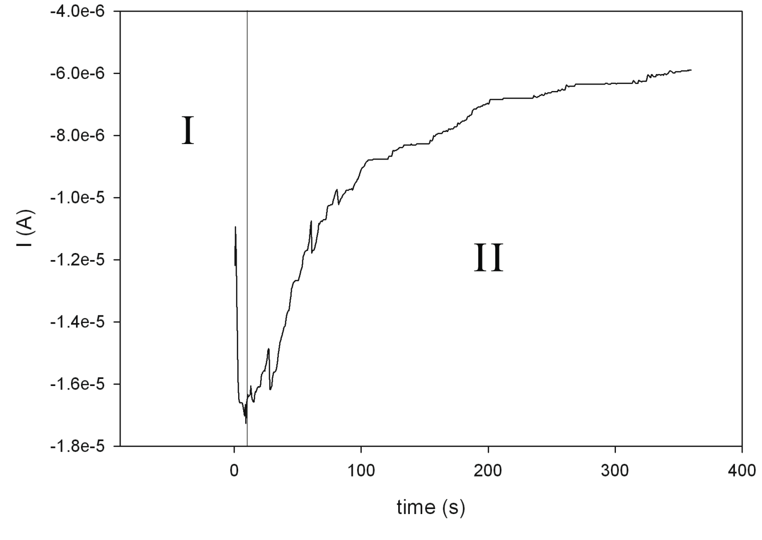

Figure 4.24: I-t curve of potentiostatic growth of PANI inside the microfluidic channel of CD2 in closed configuration.

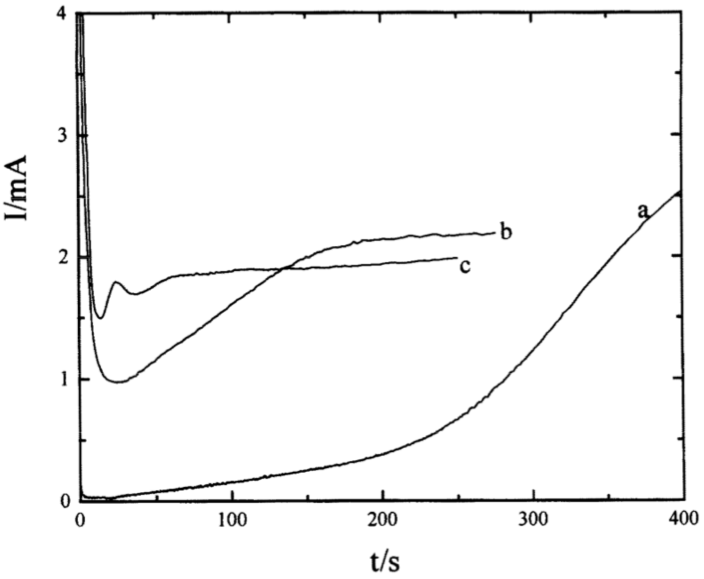

Figure 4.25: Current-time transients obtained for the electropolymerization of aniline at a Pt electrode (polymerization solution: 0.05 M aniline in 1 M H_2S0_4) at different potentials: (a) +800, (b) +1000, and (c) +1100 mV *vs.* saturated calomel electrode. From Mandic *et al.*[80]

During the initial stages of polymerization, preferential growth of PANI at the inlet and outlet of the microfluidic channel was observed, *i.e.* in areas closest to the auxiliary electrode branches (Figure 4.18). This is not attributed to an iR drop as iR drop is a previously stated negligible in this system. The symmetry of the phenomena in this instance, however, indicates that it was related to the position of the auxiliary electrode branches and so, must relate to the current. Current is a flow of charge carrier (*e.g.*, electrons in a metal or ions in an electrolyte) and always takes the least resistive path. In a three-electrode electrochemical cell the current flows between the working and the auxiliary electrode. In the microfluidic electrochemical cell developed here, the distance between each point on the working electrode and the auxiliary electrode varies, as the auxiliary electrode was branched and was positioned perpendicular to the working electrode at either end. As the distance between a point on the working electrode and the auxiliary electrode increased, so did the resistance at that point, due to the resistivity of the electrolyte. The current was therefore not evenly distributed over the length of the working electrode. As such the current density was greater closest to the auxiliary electrode branches. The oxidation of monomer was therefore more likely to occur where the current density was greatest and so electropolymerization began closest to the auxiliary electrode branches. This phenomena is called primary current distribution, *i.e.*, a current distribution solely controlled by the resistivity of the electrolyte solution between the working electrode and the auxiliary electrode[81].

After deposition of polymer at the inlet and outlet of the microfluidic channel, the resistance of the working electrode at these points increased. As the current always follows the path of least resistance, the electrode areas adjacent to the inlet and outlet became the points where the current flowed from the auxiliary electrode branches with the least resistance. Thus, polymerization occurs in these areas in the next stage. This process continued as the polymer in these areas reached a limiting resistance, and the areas where polymerization occurred next shifted further towards the centre of the electrode until the electrode became homogeneously coated with PANI.

After 6 min, polymerization was stopped to ensure the channel did not become entirely blocked with PANI and therefore a flow could be maintained. As seen in Figure 4.26, following polymerization the microfluidic channel comprised PANI in the fully oxidized pernigraniline state (blue color). Unfortunately, the thickness and morphology of the PANI grown could not be assessed in more detail using SEM as the re-opening of the chip destroyed the integrity of the polymer structure.

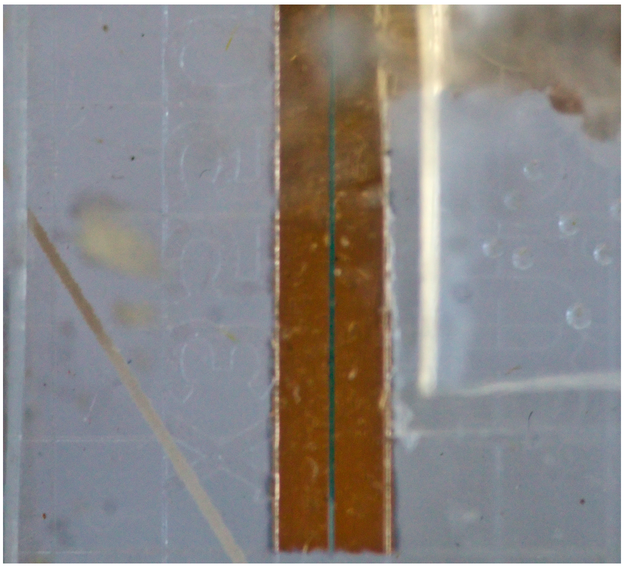

Figure 4.26: PANI electropolymerized in microfluidic channel for 6 min at +900 mV *vs.* Ag/AgCl. Flow rate 10 μl/min.

4.3.1.2.3 *In-situ* PANI electrochemical switching

After PANI was electropolymerized in the microfluidic channel for 6 min, HCl (1 M) was pumped through the PANI modified-microfluidic channel for 30 min at 10 μL/min to remove any residual aniline monomer remaining in the channel.

After this washing process, cyclic voltammetry was performed using HCl (1 M) as electrolyte. A typical CV recorded at 50 mV/s is shown Figure 4.27 a. The high background of the voltammogram shows that the polymer was highly capacitive. A single, broad oxidation peak between +400 and +800 mV (Figure 4.27 (i)) and two reduction peaks at approximately 0 mV (Figure 4.27 (iv)) and +500 mV (Figure 4.27 (ii) and (iii) were recorded. As each polymer chain length has its own oxidation and reduction potential, it is possible that the single large anodic peak is the superposition of the two or more oxidations peaks for varying polymer chain lengths: oxidation of emeraldine base to pernigraniline of long chain polymer occurring while the first oxidation, oxidation of leucoemeraldine to emeraldine base of smaller chain lengths occurred or *vice versa*. This phenomenon was also observed for the reduction process. This is observed on the first reduction peak at +500 mV where the two observed peaks at +500 mV (Figure 4.27 (ii)) and +700 mV (Figure

4.27 (iii)) are believed to be the first reduction (pernigraniline to emeraldine base) for polymer with different chain lengths. The inhomogeneous behavior of the polymer was also seen when studying the color changes of PANI in response to applied potential. When cycling the potential from -500 mV to +1000 mV, it was observed that the change in oxidation state occurred initially at the furthest point on the working electrode from the pseudo-reference electrode. This was followed by the oxidation of the PANI over the remaining electrode area. This behavior could not be attributed to an iR drop as the color change occurred first furthest from the pseudo-reference electrode.

The chain length may not have been the only reason for the observed gradual change in color. The film thickness may not have been homogeneous over the length of the working electrode and therefore electron transfer may have been quicker where the film was thinnest. Work is ongoing to fully elucidate the cause of this heterogeneous PANI behavior.

Figure 4.27b shows images of PANI film in the different oxidation states in the microfluidic channel of CD2 when the potential was held at +1000 mV (A), +500 mV (B) and 0 mV (C) *vs.* pseudo-reference electrode. The color changes from blue (Pernigraniline) to green (Emeraldine) to yellow/light green (Leucoemeraldine) demonstrated that physico-chemical properties of the polymer could be controlled by the applied potential in the microfluidic channel. In Figure 4.27b C the polymer was barely observed at 0 V. Leucoemeraldine is the contracted form of the polymer (self-doped PANI)[48] and is yellow, which makes is difficult to discern on the photograph.

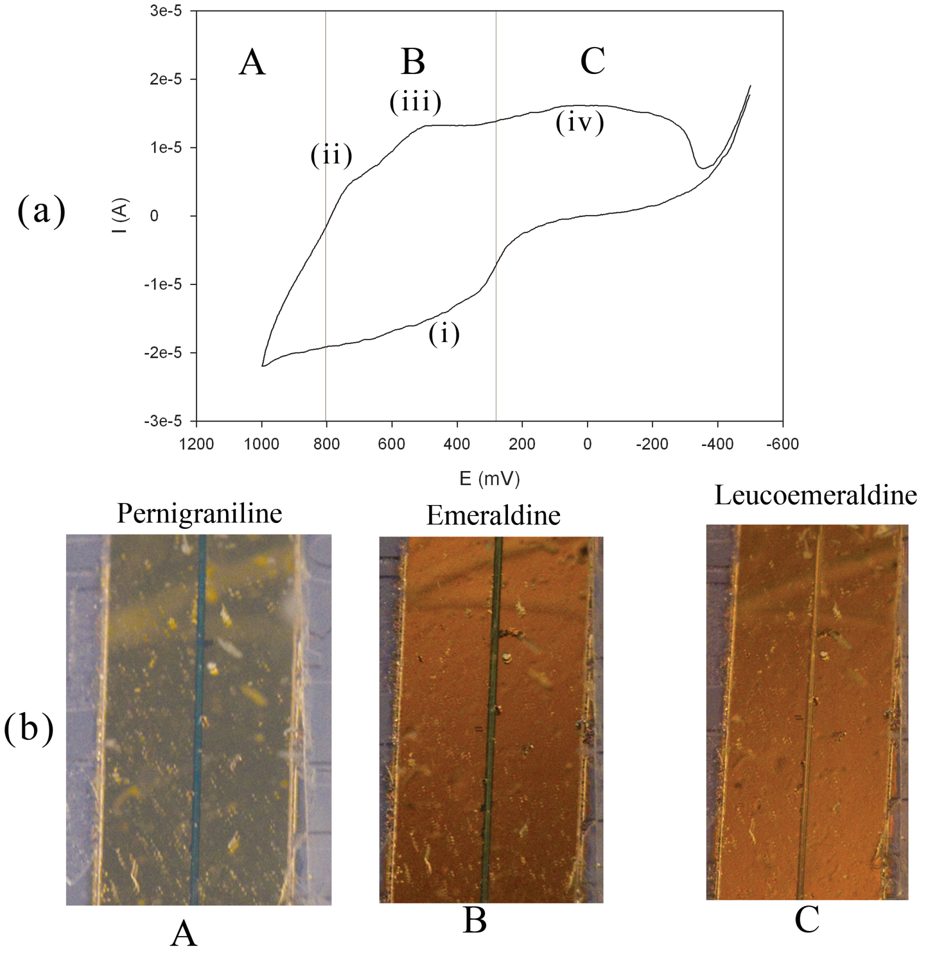

Figure 4.27: (a) CV of the PANI film grown in the microfluidic channel of CD2 (1 M HCl; 50 mV/s) (n=3). (b) Photographs of the PANI film in the fluidic channel of CD2 held at different potentials, (A) +1000 mV, (B) +500 mV and (C) 0 mV *vs.* on-board screen-printed Ag/AgCl electrode (n=3).

A scan rate study of the PANI film was performed (Figure 4.28), which showed that when cycling at scan rates greater than 50 mV/s, no redox activity was observed. The PANI response to applied potential was therefore slow. This was potentially due to the poor quality of the grown PANI attributed to the sub-optimal conditions of the electrochemical cell configuration. Indeed, when the scan rate was faster than the time for PANI to respond (at 100 mV/s or greater), color changes were not observed. At scan rates slower than 50 mV/s, bubbles formed at the inlet auxiliary electrode branch and passed through the channel preventing the generation of good quality data and so is not shown.

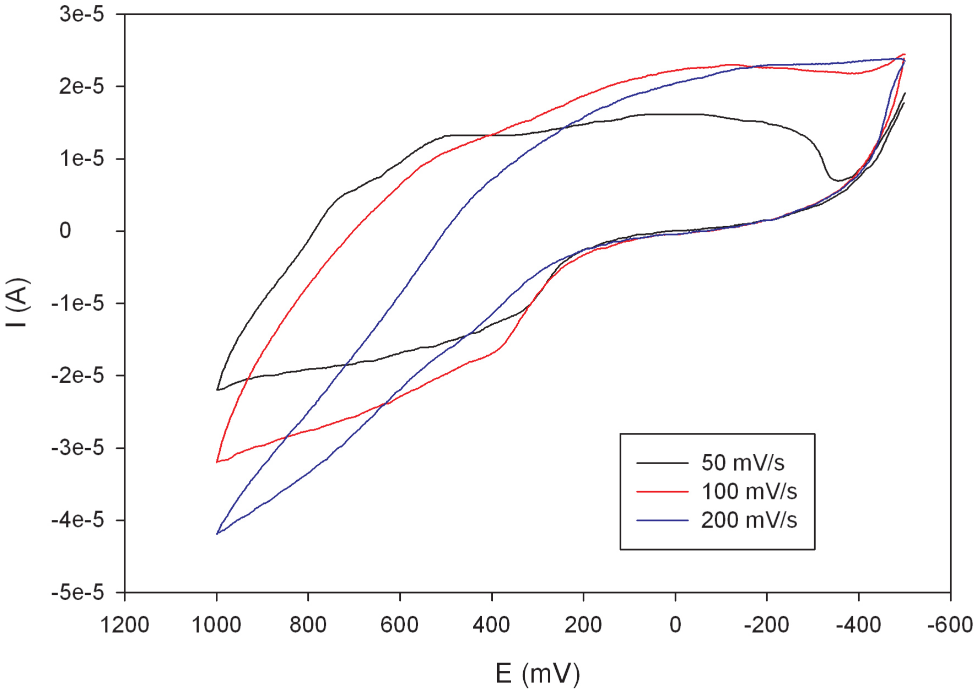

Figure 4.28: Scan rate study of a typical PANI film in the microfluidic channel of CD2 (Scan rate varied from 50 to 200 mV) in 1 M HCl.

The PANI film that was grown in the closed microfluidic channel of CD2 using on-board screen-printed electrodes was redox active albeit, not exhibiting ideal behavior. Although in this experiment, only the color changes were observed, it can be assumed that other physical changes were also taking place in the polymer film such as expansion/contraction and hydrophobicity transitions[48, 82, 83]. These are the desired properties, which will allow the PANI monolith to serve as a dynamic electrochemically controllable stationary phase for the EMμ project.

4.4 CONCLUSION

Electrochemical cell design is critical for all electrochemical processes. However, due to the intrinsic properties of electroactive polymers, the electrochemical cell for the electropolymerization of these polymers is of particular importance. The dimension restrictions imposed by microfluidics raise new challenges. In this study two types of on-chip electrochemical cells, two-electrode and three-electrode, have been investigated.

Although, CD1 was shown to be less than optimal for separations in Chapter 3, CD1 embedded a three-electrode electrochemical cell approaching ideal behavior within the fluidic channel. PANI electropolymerization in these channels was successful and PANI monoliths were fabricated and characterized. Two- and three-electrode electrochemical cells were investigated for CD2.

Three-electrode cells are complex to design, especially in microfluidic channels where cell dimensions are restricted. In the final CD2 upper piece design, the base channel was gold-sputtered to serve as the working electrode and the upper piece comprised of PET, where a silver-paste based pseudo-reference and auxiliary electrode configuration was screen-printed. Although it appeared that these electrodes exhibited good behaviour for ferri/ferrocyanide electrochemistry, impurities on the working electrode and/or poor electrical connections to the working electrode resulted in a large ΔE_p (160 mV) for the ferri/ferrocyanide system. Despite this, growth of PANI was successfully demonstrated onto the working electrode surface using this set-up. It was shown that the physico-chemical properties of PANI could be controlled electrochemically in CD2. This initial work demonstrated a critical proof of concept for the EMμ project: that it is possible to grow a conducting polymer monolith on-chip that can be manipulated electrochemically. However, PANI films have not to date been fully characterized. It is possible that there are inhomogeneities in the polymer, given that it has not been electropolymerized in an ideal configuration. Studies are ongoing to both characterize the polymer and to examine alternative electrochemical cell designs to obtain electrochemical behavior close to ideal.

4.5 REFERENCES

1. Bard, A. J.; Faulkner, L. R., Introduction and overview of electrode processes. In *Electrochemical methods*, John Wiley & sons: 2001; pp 1-43.
2. Chen, C.; Zhang, J.; Du, Y.; Yang, X.; Wang, E., *Analyst* **2010,** *135* (5), 1010-1014.
3. Chen, I. J.; Lindner, E., *Analytical Chemistry* **2009,** *81* (24), 9955-9960.
4. Chen, Q.-Z.; Fang, Y.-M.; Wei, H.; Huang, Z.-X.; Chen, G.-N.; Sun, J.-J., *Analyst* **2010,** *135* (5), 1124-1130.
5. Chen, S.-P.; Wu, J.; Yu, X.-D.; Xu, J.-J.; Chen, H.-Y., *Analytica Chimica Acta* **2010,** *665* (2), 152-159.
6. Crevillen, A. G.; Avila, M.; Pumera, M.; Gonzalez, M. C.; Escarpa, A., *Analytical Chemistry* **2007,** *79* (19), 7408-7415.
7. Fredrick, S. J.; Gross, E. M., *Bioanalysis* **2009,** *1* (1), 31-36.
8. Dounin, V.; Veloso, A. J.; Schulze, H.; Bachmann, T. T.; Kerman, K., *Analytica Chimica Acta* **2010,** *669* (1-2), 63-67.
9. Hiratsuka, A.; Kojima, K.-i.; Suzuki, H.; Muguruma, H.; Ikebukuro, K.; Karube, I., *Analyst* **2001,** *126* (5), 658-663.
10. Jang, A.; Zou, Z.; Lee, K. K.; Ahn, C. H.; Bishop, P. L., *Talanta* **2010,** *83* (1), 1-8.
11. Killard, A. J.; Zhang, S.; Zhao, H.; John, R.; Iwuoha, E. I.; Smyth, M. R., *Analytica Chimica Acta* **1999,** *400* (1-3), 109-119.
12. Kim, J. M.; Park, J.-J.; Lee, H.-J.; Kim, W.-S.; Muramatsu, H.; Chang, S.-M., *Bioprocess and Biosystems Engineering* **2010,** *33* (1), 47-53.
13. Merritt, J. R.; Wikswo, J. P.; Cliffel, D. In *A Multi-Analyte Platinum Screen-Printed Electrode for Real-Time Monitoring of Cellular Metabolism in a Microfluidic Device*, American Chemical Society: 2008; pp SERM-008.
14. Mir, M.; Homs, A.; Samitier, J., *Electrophoresis* **2009,** *30* (19), 3386-3397.
15. Yamanaka, K.; Saito, M.; Nagatani, N.; Tamiya, E., *Chemical Senses* **2010,** *26* (Suppl. A), 175-177.
16. Zou, Z.; Jang, A.; MacKnight, E.; Wu, P.-M.; Do, J.; Bishop, P. L.; Ahn, C. H., *Sensors and Actuators B* **2008,** *B134* (1), 18-24.

17. Gao, Y.; Chen, X.; Gupta, S.; Gillis, K.; Gangopadhyay, S., *Biomedical Microdevices* **2008,** *10* (5), 623-629.
18. Sreenivas, G.; Ang, S. S.; Fritsch, I.; Brown, W. D.; Gerhardt, G. A.; Woodward, D. J., *Analytical Chemistry* **1996,** *68* (11), 1858-1864.
19. Park, B. Y.; Zaouk, R.; Madou, M. J., Fabrication of Microelectrodes Using the Lift-Off Technique. 2005; Vol. 321, pp 23-26.
20. Schrott, W.; Svoboda, M.; Slouka, Z.; Snita, D., *Microelectronic Engineering* *86* (4-6), 1340-1342.
21. Ebina, W.; Rowat, A. C.; Weitz, D. A., *Biomicrofluidics* **2009,** *3* (3), 034104-1
22. Bai, H.-J.; Shao, M.-L.; Gou, H.-L.; Xu, J.-J.; Chen, H.-Y., *Langmuir* **2009,** *25* (17), 10402-10407.
23. Kong, Y.; Chen, H.; Wang, Y.; Soper, S. A., *Electrophoresis* **2006,** *27* (14), 2940-2950.
24. Hao, Z.; Chen, H.; Zhu, X.; Li, J.; Liu, C., *Journal of Chromatography A* **2008,** *1209* (1-2), 246-252.
25. Johirul, M.; Shiddiky, A.; Kim, R.-E.; Shim, Y.-B., *Electrophoresis* **2005,** *26* (15), 3043-3052.
26. Muck, A., Jr.; Wang, J.; Barek, J., *Chemicke Listy* **2003,** *97* (9), 957-960.
27. Illa, X.; Ordeig, O.; Snakenborg, D.; Romano-Rodriguez, A.; Compton, R. G.; Kutter, J. P., *Lab on a Chip* **2010,** *10* (10), 1254-1261.
28. Avila, M.; Zougagh, M.; Escarpa, A.; Rios, A., *Electrophoresis* **2009,** *30* (19), 3413-3418.
29. Bani-Yaseen, A. D.; Kawaguchi, T.; Price, A. K.; Culbertson, C. T.; Jankowiak, R., *Anal. BioAnalytical Chemistry* **2010**, No pp. yet given.
30. Dossi, N.; Susmel, S.; Toniolo, R.; Pizzariello, A.; Bontempelli, G., *Electrophoresis* **2009,** *30* (19), 3465-3471.
31. Dossi, N.; Toniolo, R.; Susmel, S.; Pizzariello, A.; Bontempelli, G., *Electrophoresis* **2010,** *31* (15), 2541-2547.
32. Dungchai, W.; Chailapakul, O.; Henry, C. S., *Analytical Chemistry* **2009,** *81* (14), 5821-5826.
33. Fernandez-la-Villa, A.; Pozo-Ayuso, D. F.; Castano-Alvarez, M., *Electrophoresis* **2010,** *31* (15), 2641-2649.

34. Ju, H.; Zhai, C. *Design and manufacture method of portable high-performance capillary electrophoresis chip using slit for sample injection*. 2009.

35. Kim, B.-K.; Yang, S.-Y.; Abdul, A. M.; Jo, K.; Sung, D.; Jon, S.; Woo, H. Y.; Yang, H., *Electroanalysis* **2010,** *22* (19), 2235-2244.

36. Han, J.-H.; Park, S.; Boo, H.; Kim, H. C.; Nho, J.; Chung, T. D., *Electroanalysis* **2007,** *19* (7-8), 786-792.

37. Kim, S. K.; Lim, H.; Chung, T. D.; Kim, H. C., *Sensors and Actuators B* **2006,** *B115* (1), 212-219.

38. Zhou, J.; Ren, K.; Zheng, Y.; Su, J.; Zhao, Y.; Ryan, D.; Wu, H., *Electrophoresis* **2010,** *31* (18), 3083-3089.

39. Pumera, M.; Escarpa, A., *Electrophoresis* **2009,** *30* (19), 3315-3323.

40. Suzuki, H.; Hirakawa, T.; Sasaki, S.; Karube, I., *Sensors and Actuators B: Chemical* **1998,** *46* (2), 146-154.

41. Suzuki, H.; Hirakawa, T.; Sasaki, S.; Karube, I., *Analytica Chimica Acta* **1999,** *387* (1), 103-112.

42. Suzuki, H.; Hiratsuka, A.; Sasaki, S.; Karube, I., *Sensors and Actuators B: Chemical* **1998,** *46* (2), 104-113.

43. Suzuki, H.; Shiroishi, H.; Sasaki, S.; Karube, I., *Analytical Chemistry* **1999,** *71* (22), 5069-5075.

44. Simms, R.; Dubinsky, S.; Yudin, A.; Kumacheva, E., *Lab on a Chip* **2009,** *9* (16), 2395-2397.

45. Wallace, G.; Spinks, G. M.; Kane-Maguire, L. A. P.; Teasdale, P. R., Assembly of Polypyrroles. In *Conductive Electroactive Polymers*, CRC Press: 2008; pp 59-101.

46. Wallace, G.; Spinks, G. M.; Kane-Maguire, L. A. P.; Teasdale, P. R., Properties of Polypyrroles. In *Conductive Electroactive Polymers*, CRC Press: 2008, pp 103-136.

47. Wallace, G.; Spinks, G. M.; Kane-Maguire, L. A. P.; Teasdale, P. R., Synthesis of Polyanilines. In *Conductive Electroactive Polymers*, CRC Press: 2008; pp 137-178.

48. Wallace, G.; Spinks, G. M.; Kane-Maguire, L. A. P.; Teasdale, P. R., Properties of Polyanilines. In *Conductive Electroactive Polymers*, CRC Press: 2008, pp 179-196.

49. Andrieux, C. P.; Audebert, P.; Hapiot, P.; Saveant, J. M., *The Journal of Physical Chemistry* **1991,** *95* (24), 10158-10164.

50. Scharifker, B. R.; GarcÌa-Pastoriza, E.; Marino, W., *Journal of Electroanalytical Chemistry* **1991,** *300* (1-2), 85-98.

51. Fermin, D. J.; Scharifker, B. R., *Journal of Electroanalytical Chemistry* **1993,** *357* (1-2), 273-287.

52. John, R.; Wallace, G. G., *Journal of Electroanalytical Chemistry* **1991,** *306* (1-2), 157-167.

53. Kranz, C.; Ludwig, M.; Gaub, H. E.; Schuhmann, W., *Advanced Materials* **1995,** *7* (1), 38-40.

54. Sutton, S. J.; Vaughan, A. S., *Polymer* **1996,** *37* (24), 5367-5374.

55. Talaie, A.; Wallace, G. G., *Materials Science forum* **1995,** *189-190*, 185-192.

56. Jager, E. W. H.; Smela, E.; Inganas, O., *Science* **2000,** *290* (5496), 1540-1545.

57. Jager, E. W. H.; Inganäs, O.; Lundström, I., *Advanced Materials* **2001,** *13* (1), 76-79.

58. Higgins, M. J.; McGovern, S. T.; Wallace, G. G., *Langmuir* **2009,** *25* (6), 3627-3633.

59. Yang, L.; Ge, X.; Wang, M.; Song, L.; He, X., *Materials Letters* **2008,** *62* (3), 429-431.

60. Lee, W.-K.; Song, Y.-M.; Ha, J.-M.; Park, H.; Lee, I. W.; Chun, H. H.; Jo, N.-J., *Materials research innovations* **2009,** *13*, 235-238.

61. Zotti, G.; Cattarin, S.; Comisso, N., *Journal of Electroanalytical Chemistry* **1988,** *239* (1-2), 387-396.

62. Kim, S. H.; Oh, K. W.; Choi, J. H., *Journal of Applied Polymer Science 116* (5), 2601-2609.

63. Binbin, X.; et al., *Smart Materials and Structures* **2007,** *16* (5), 1549.

64. Smela, E.; Lu, W.; Mattes, B. R., *Synthetic Metals* **2005,** *151* (1), 25-42.

65. Morrin, A.; Ngamna, O.; Killard, A. J.; Moulton, S.; Smyth, M. R.; Wallace, G. G., *Electroanalysis* **2005,** *17* (5-6), 423-430.

66. Ates, M.; Sarac, A. S., *Progress in Organic Coatings* **2009,** *66* (4), 337-358.

67. Karyakin, A. A. In *Biosensors based on conductive polymers and electroactive polycrystals*, American Scientific Publishers: 2006; pp 329-351.

68. Ding, J.; Liu, L.; Spinks, G. M.; Zhou, D.; Wallace, G. G.; Gillespie, J., *Synthetic Metals* **2003,** *138* (3), 391-398.

69. Huang, Z.; Wang, P.-C.; MacDiarmid, A. G.; Xia, Y.; Whitesides, G., *Langmuir* **1997,** *13* (24), 6480-6484.

70. Akundy, G. S.; Iroh, J. O., *Polymer* **2001,** *42* (24), 9665-9669.

71. Akundy, G. S.; Rajagopalan, R.; Iroh, J. O., *Journal of Applied Polymer Science* **2002,** *83* (9), 1970-1977.

72. Lehr, I. L.; Saidman, S. B., *Electrochimica Acta* **2006,** *51* (16), 3249-3255.

73. Patil, S. F.; Bedekar, A. G.; Agashe, C., *Materials Letters* **1992,** *14* (5-6), 307-312.

74. Barisci, J. N.; Hodgson, A. J.; Liu, L.; Wallace, G. G.; Harper, G., *Reactive and Functional Polymers* **1999,** *39* (3), 269-275.

75. Davey, J. M.; Innis, P. C.; Ralph, S. E.; Too, C. O.; Wallace, G. G.; Partridge, A. C., *Colloids and Surfaces A: Physicochemical and Engineering Aspects* **2000,** *175* (3), 291-301.

76. Lin, Y.; Wallace, G. G., *Electrochimica Acta* **1994,** *39* (10), 1409-1413.

77. Munoz, E.; Colina, A.; Heras, A.; Ruiz, V.; Palmero, S.; Lopez-Palacios, J., *Analytica Chimica Acta* **2006,** *573-574*, 20-25.

78. Munoz, E.; Heras, M. A.; Colina, A.; Ruiz, V.; Lopez-Palacios, J., *Electrochimica Acta* **2007,** *52* (14), 4778-4783.

79. Collyer, S. D.; Davis, F.; Lucke, A.; Stirling, C. J. M.; Higson, S. P. J., *Journal of Electroanalytical Chemistry* **2003,** *549*, 119-127.

80. Mandic, Z.; Duic, L.; Kovacicek, F., *Electrochimica Acta* **1997,** *42* (9), 1389-1402.

81. Hack, H. P.; Moran, P. J.; Scully, J. R., Influence of electrolyte resistance on electrochemical measurements and procedures to minimize or compensate for resistance errors. In *The measurement and correction of electrolyte resistance in electrochemical tests*, Scribner, L. L.; Taylor, S. R., Eds. American Society for Testing and Materials: 1990; pp 5-26.

82. Lizarraga, L.; Andrade, E. M.; Molina, F. V., *Electrochimica Acta* **2007,** *53* (2), 538-548.

83. Hato, M., *Chemistry letters* **1988**, 12, 1959-1962.

CHAPTER 5 CONTROL OF MICROSTRUCTURED POLYANILINEE GROWTH IN A FLUIDIC CHANNEL

5.1 INTRODUCTION

Both base piece and upper piece of CD2 have been investigated in the previous two chapters to form a viable microfluidic device for separation and conductive polymer growth.

EMμ consists in a microstructured PANI monolithic chromatographic stationary phase fabricated in a microchip. Therefore, PANI needs to be microstructured in the microfluidic separation channel. To microstructure PANI, a sacrificial template method has been chosen. In this method, a template is first fabricated within the separation channel, and then PANI is grown through the template before it is removed to reveal PANI microstructures. As discussed in Chapter 3, a colloidal crystal templating method was used as the templating method. Although significant band broadening effects were highlighted for CD1 in Chapter 3, its near ideal electrochemical behavior was illustrated in Chapter 4. As microstructuring the resultant PANI monolith might offset the band broadening effects expected from Chapter 3, successful sacrificial template assembly would increase the viability of CD1. Therefore, this chapter aims to successfully self-assemble polystyrene (PS) beads into colloidal crystal in the separation channel of CD1, to serve as a sacrificial template for the ultimate PANI monolith. (It was envisaged that PMMA/PS dissolution issues could be resolved by judicious choice of substrate subsequently). Colloidal crystallization gave, as described in chapter 3, uneven crystal thicknesses; therefore, this study was made in open channel, *i.e.* prior to chip bonding.

However, numerous templating methods have been used for templating materials. In this chapter, templating methods are reviewed and colloidal crystal was chosen as being the most suitable methods for EMμ. Then colloidal crystallization in CD1 separation channel is discussed. Among the techniques used to fabricate the PS beads template, surface energy directed evaporation induced self-assembly was found to create the best colloidal crystal structures and was the fastest of all techniques to fabricate colloidal crystal of the desired thickness.

Finally growth of PANI through the template is investigated. It was found that the structure (inverse opal or hollow spheres) was dependant on the surfactant concentration in the suspension used to form the colloidal crystal templates.

To obtain an ordered microstructured in a monolith, templating of the bulk polymer material is required. Templating has been widely used over the past decades to form highly organized nanoporous, mesoporous and macro-porous materials[1-4]. As described in Chapter 1 Section 1.3.2, silica and polymer monoliths are currently made using a porogen to induce porosity into the bulk material. However, utilizing a porogen is not strictly a templating method and as such can never produce ordered structures. Templating involves making a scaffold of a desired structure, around which the growth of the desired bulk material can take place. Once the desired material has grown, the template is sacrificed leaving behind the desired structure in the bulk material. The templating technique used depends on the resulting material structure desired. A porous membrane would, for instance, result in nano/micro wires or nano/micro tubes whereas surfactants or lyotropic liquid crystalline phases would result in porous structures. Templating techniques that are commonly used can be divided into two categories: “soft” and “hard” templating techniques. Here only the use of colloidal crystal as hard templates will be discussed.

Colloidal particles have the ability to self-assemble into well-organized crystals called colloidal crystals[30-32]. These colloidal crystal templates are the most widely studied of all templating techniques[4, 33, 34] resulting in structures, which are extremely well defined with long-range structural periodicity. Colloidal crystallization results in highly ordered 2-or 3-dimensional structures, which have direct applications in photonics[35-38], sensors[34] and lasers[36]. The biggest challenge of this technique is to form crack-free crystals[39, 40] especially for photonic applications[36-38] where crystals need to be as close to perfection as possible. Once the crystal has been grown, bulk material is then deposited or grown in the voids of the crystal structure before template sacrifice. Colloidal crystals have been widely used as templates for the formation of highly ordered micro/nanoporous materials. Colloidal crystal templates result in inverse opal structures of materials as seen in Figure 5.1. In our group[41-43], PANI films have been templated by colloidal crystals using nano-sized PS beads (50-100 nm). Electropolymerization of aniline was carried out with poly(vinyl sulfonate) (PVS) or poly(styrene sulfonate) (PSS) as dopant in HCl. Once polymer was grown, the template was removed by immersion in toluene. It was found that on positively charged beads, inverse opal structures resulted whereas on negatively charged PS beads, polymerization occurred from the bead surface leading to hollow sphere structures[41]. The reason for that difference is that the aniline monomer is positively charged in acidic solution; thus, electrostatic forces drive the polymerization from the bead surface when negatively charged PS beads are used. Colloidal crystal templating of PANI to form PANI inverse opal has also been reported by other groups[44-47].

The pore size of the bulk material can be finely tuned according to the size of the beads used. Beads such as PS or silica can be easily synthesized or are commercially available at nano-, micro-and macro-scale. Colloidal crystal templating was the method of choice for the EMμ monoliths as it gives highly ordered inverse opal structures. However, these colloidal crystal templates can be formed using different methods such as filtration, centrifuging or evaporation driven self-assembly techniques. Each technique has its own domain of application so a review of this technique is necessary to be able to determine which is most suitable for this research.

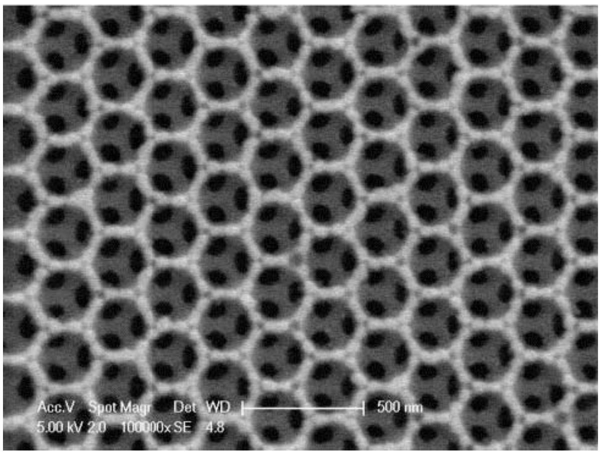

Figure 5.1: Inverse opal of Ceria (CeO_2) templating using poly(methyl methacrylate) (PMMA) microspheres of diameter ~325 nm arranged in face centered cubic (FCC) lattice. From Waterhouse *et al.*[37]

Filtration was used by Velev[48] using a 50 nm pore sized polycarbonate membrane to formed microstructured gold. In that work a 50 nm membrane was used to filter 300 nm PS beads into a closed packed structure for 2 hours at a pressure of 20 kPa. Gold nanoparticles (25 nm in diameter) were then packed into the cavities of the colloidal crystal by filtering the gold nanoparticles at a pressure of 95 kPa for 24-72 hours. This technique was promising as it was easy to set up and led to very well organized templates. However, this approach required high pressure and long time-scales. Although the resulting structure was close to perfection (some cracks where observed), the approach was limited to building thicknesses of only few microns (typically 35 µm). Gates *et al.*[35, 49] developed a technique deriving from filtration for building these crystal structures on-chip. In this set-up, a 200 nm gap etched into the upper piece of the chip was used as a filter (Figure 5.2). PS beads with a diameter of 480 nm were then packed into the chip using the 200 nm gap as a filter at the chip outlet. These packed beads were then used as the filter to pack smaller PS beads. The drawback of this technique was that it required the etching of 200 nm gaps, which required expensive tools and highly specialized technicians. However, this filtration technique is attractive as it has a relatively simple set-up and packing into a separation channel can occur in a bonded chip. However, the complexity of making the filter as well as the time required fabricating micrometers thick crystals may be limiting.

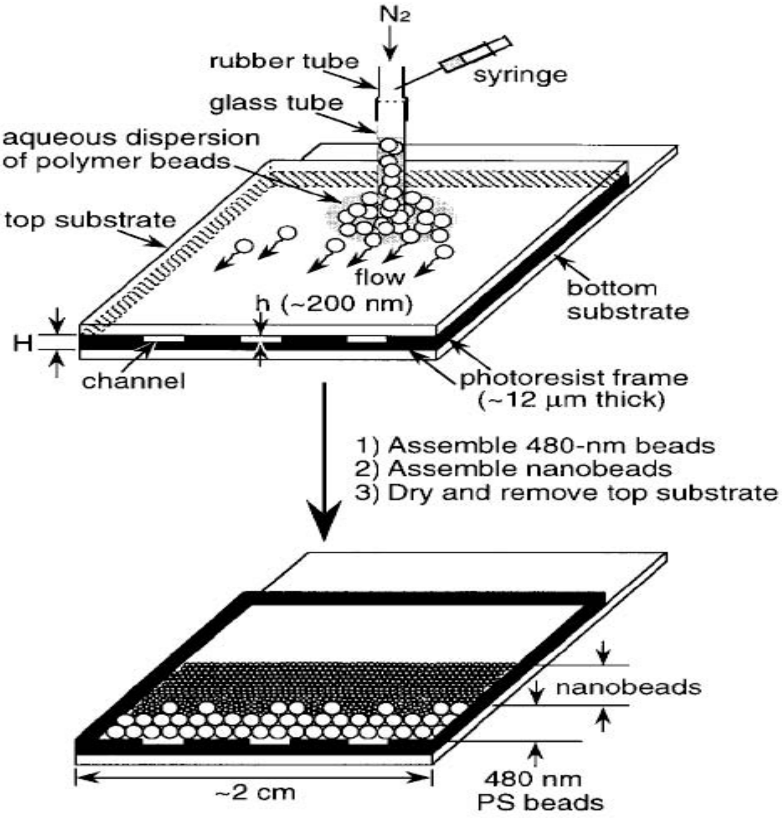

Figure 5.2: Apparatus design used by Gates *et al.*[49] 200 nm gaps are etched into the photoresist frame. Once the chip is sealed, 480 nm PS beads are injected into the chip and the solvent is pushed through the 200 nm gap using N_2. Smaller beads are then packed using the same technique where the 480 nm beads act as a filter. From Gates *et al.*[49]

Centrifugation was used by Lee *et al.*[50] to form silica colloidal crystals in a microfluidic channel. Six chips were fabricated on a single glass wafer with PDMS bonded on top (Figure 5.3). The wafer was spun at 40-1600 rpm for 15-60 min in order to get colloidal crystals into the channels from the reservoirs. The reservoirs were required to stock the silica suspension and spontaneous colloidal crystallization had to be initiated prior to spinning the chip. The colloidal suspension then filled the channels by capillary force. Crystallization began at the back end of the channel, i.e. where the suspension came into contact with the atmosphere. Centrifugation as a technique is appealing as it is rapid and crystallization occurs inside a bonded chip. However, a reservoir of several ml dimensions would need to be integrated into the chip, which would result in added complexity in the chip design and fabrication.

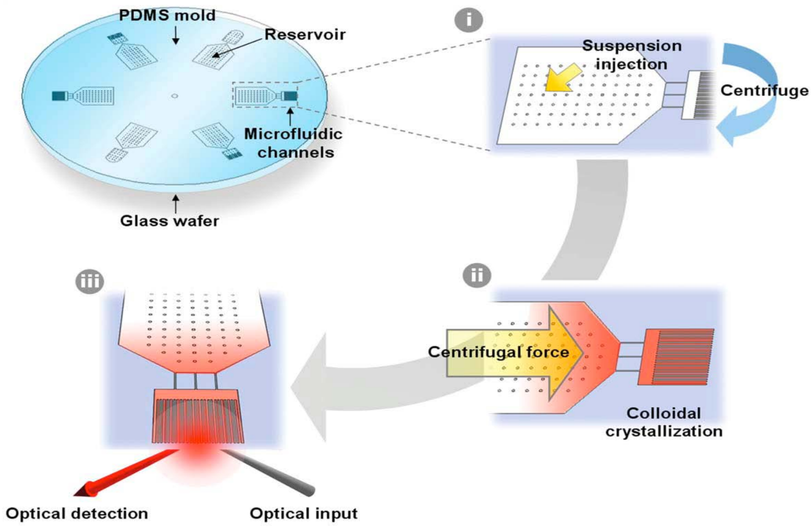

Figure 5.3: Design used by Lee *et al.*[50] (i) Injection of colloidal suspension into the reservoir and application of centrifugal force. (ii) Colloidal crystallization driven by centrifugal force applied to the microfluidic unit. (iii) Detection of the optical reflectance spectra.

Evaporation-driven convective self-assembly is one of the most versatile techniques used and produces highly ordered structures[31,33]. Evaporation-driven convective self-assembly encompasses different techniques such as vertical lifting and capillary forces to induce crystallization. The general mechanism is described in Figure 5.4.

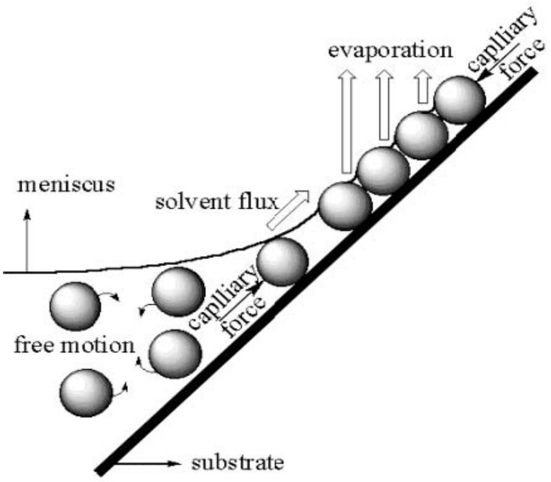

Figure 5.4: General mechanism of evaporation-driven convective self-assembly. From Cong *et al.*[30]

Vertical lifting or dip drawing is a technique where the substrate (on which the colloidal crystal is grown) is pulled out of the colloidal suspension at a slow, constant rate[31]. The pulling of the substrate from the colloidal suspension creates a meniscus at the substrate outer solution interface. It is at the meniscus that crystallization occurs. The main advantage of this technique is that controlling the speed of the substrate controls the thickness of the formed crystal[32]. However, many defects, especially cracks, are formed because of the stress created at the final drying stage[39]. At the end of the drying stage, interparticulate forces induced by the drying of the meniscus of water between the particles, force the beads to come into contact. These forces create a stress onto the crystal, eventually creating cracks. This technique was improved upon by adding a silica precursor to the suspension[40]. The silica precursors undergo a sol-gel polymerization process. The colloidal crystal is, therefore, in a silica matrix, which remains intact under the stress engendered during the drying process. Although this technique was simple to set-up, expensive servomotors are required in order to keep the lifting speed slow and constant. Zhou *et al.*[38] proposed a derivative technique, which consisted of pumping the solution instead of lifting the substrate. The substrate in this technique was put inside a container containing the colloidal suspension. The colloidal suspension was then pumped out of the container. The thickness of the resulting crystals was a function of the flow rate; the slower the flow rate, the thicker the crystal. This technique resulted in a high quality crystal and was simpler than vertical lifting as a regular peristaltic pump was used. However, using these techniques the substrate is completely covered by the colloidal crystal and so is not suitable for fluidic channels.

Capillary force induced crystallization[30, 51] is a technique often used to deposit colloidal crystals into fluidic channels. Capillary forces draw the colloidal particles suspension into the channel. The main prerequisite for this technique is that the channel must be of a small enough depth and width so that this spontaneous action can occur (*e.g.*, water will rise 14 cm in a 200 μm in diameter glass tube). Crystallization occurs at the meniscus as it is also an evaporation-driven self-assembly technique. This technique does not offer direct control of the crystal thickness, as the depth of the channel will dictate the thickness of the crystal. In addition, crystal defects such as cracks can be formed using this technique. However, by controlling the evaporation rate of the solvent, *e.g.*, using humidity chambers, a significant reduction of the cracks can be observed. This technique can be carried out for both closed and open chips. When the chip is closed, the evaporation rate of the solvent decreases at the crystallization point, thus increasing packing time. This technique would allow specifically for a fluidic channel to be packed with an ordered crystal (under controlled conditions) making this technique a good candidate for on-chip templated monolith formation.

5.2 TEMPLATE FORMATION

As discussed in the previous section, the separation channel on the base piece of CD1 was gold sputtered so that it could be used as the working electrode of a three-electrode electrochemical cell. The validity of the electrochemical cell was demonstrated by ferricyanide electrochemistry. The second step of the structured monolith fabrication was the formation of a PS colloidal crystal inside the separation channel. This colloidal crystal was required as a template to induce a PANI inverse opal-type structure. The template was required to be ordered as it would result, as explained in Section 1.5, in a decrease of the A-term of the Van Deemter equation, thus decreasing the theoretical plate height, i.e., increasing the column efficiency.

A range of different approaches was investigated in order to assemble closed packed structures of PS beads in the separation channel. Different approaches to make colloidal crystals demonstrated that the most convenient technique was to use capillary forces to pack the channel. In this instance, this technique was unsuitable as the channel was too wide and capillary action could not take place. As alternatives, filtration, ink-jet printing, and evaporation driven convective self-assembly, were used. The quality of the formed crystal was assessed by SEM imaging the crystal. Of these techniques, filtration and ink-jet printing were found not to be suitable as no ordered (closed packed) structures were obtained. Using evaporation-driven convective self-assembly, ordered structures resulted albeit with many defects. However, defects could be reduced using controlled condition making evaporation-driven convective self-assembly the most effective technique used. The results obtained are discussed herein.

5.2.1 FILTRATION

As discussed in Section 5.1.2.3, filtration has been used as a technique by Velev[48] and Gates *et. al*[35,49] to form highly organized and large colloidal crystals. In CD1, attaching a filter membrane over the outlet hole was not practical as when pressure was exerted on it, membrane breakdown was observed.

Despite this drawbacks, filtration was first investigated as a technique to closely pack PS beads into the separation channel with the advantage being that packing could occur when the chip was closed, *i.e.* when the upper and base pieces of the chip were sealed. However, due to the large volume of the channel, the high pressure required to filter the PS beads and leaking problems, a pre-crystallization step was required and was performed as reported by Sawada *et al.*[52].

As seen in Figure 5.5, the individual flakes formed during pre-crystallization packed together but did not merge to form the desired single crystal. Therefore this technique was not suitable for creating the required colloidal crystal template needed to microstructure the monolith.

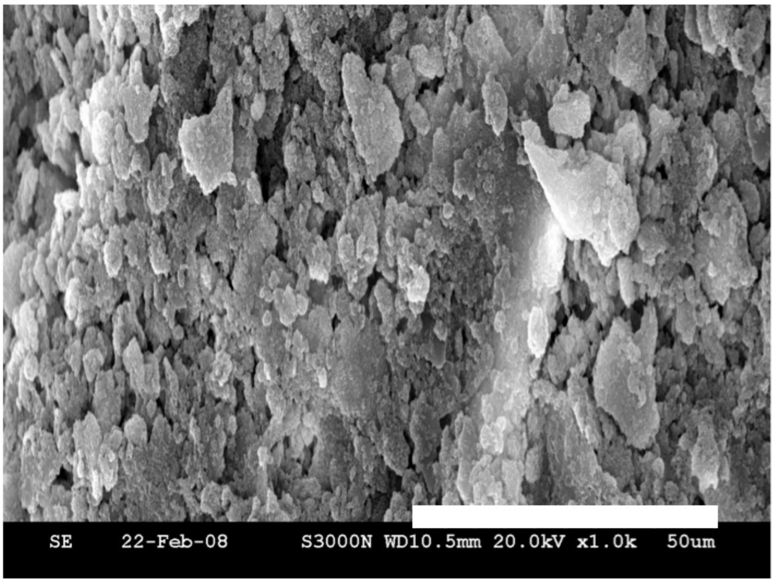

Figure 5.5: SEM image of the packing resulting from filtration (scale bar: 50 μm, magnification: 1,000). The pre-crystallized flakes are still clearly visible and no ordered structure is observed.

5.2.2 INK-JET PRINTING

Ink-jet printing of PS beads was examined as a possibility for depositing the PS beads into the separation channel. Ink-jet printing is used routinely to deposit material according to a 2-dimensional specification. It can be easily automated and thus it could be used to build up 3-dimensional structures of materials by repeatedly printing material over a defined 2-dimensional area. Indeed, it could be envisaged that an array of chips could be fabricated and packed using ink-jet printing before the chips were cut from the wafer. However, there was a drawback of this technique as in order to prevent blocking of the printhead nozzles only small, diluted PS bead suspensions could be used.

Figure 5.6 shows an image of a typical template fabricated by ink-jet printing. A non-ordered structure was easily seen after 100 prints of the PS beads suspension. This could be the result of high velocities used in piezoelectric printing to eject material from the printhead onto the substrate. The clogging of the printhead was also an issue. The nozzles of the printheads for this ink-jet printer were only 20 µm in diameter and so, in order to prevent clogging, diluted particle suspensions with particle mean diameter significantly smaller than 20 µm had to be used to prevent clogging of the printhead nozzles. As a consequence, only PS beads suspension of 1% (w/v) with particle diameters not exceeding 200 nm could be used.

This technique only permitted PS beads of small mean diameter to be printed. However, 1 µm PS beads were required to form the template in order to achieve a pore size in the monolith large enough to avoid electrical double layer superposition (as discussed in Chapter 3, Section 3.2.3.2). In addition, no ordering in the template was obtained. As such, this non-versatile technique resulting in poor templating was abandoned.

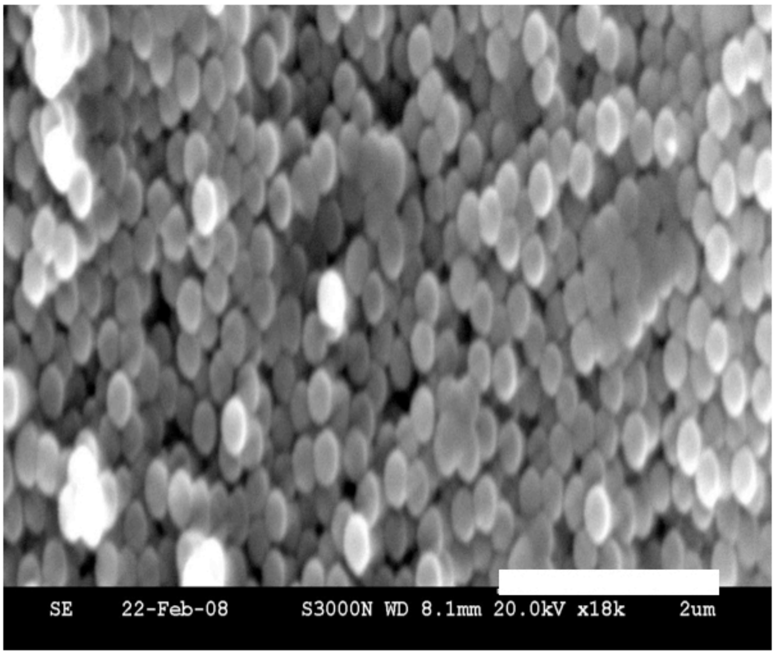

Figure 5.6: SEM micrograph of ink-jet printing of 100 prints of 200 nm PS beads suspension (1% (w/v)) on PET. (Scale bar 2μm, magnification 18,000).

5.2.3 EVAPORATION-DRIVEN CONVECTIVE SELF-ASSEMBLY TECHNIQUES

Evaporation-driven convective self-assembly was also investigated and was performed according to Chapter 2, Section 2.4.5.1.1. It was initially carried out at room temperature, where volumes of the suspension were dropped (20 μl) into the channel by pipette. However, at room temperature, the drying of the suspension was prohibitively long for this technique to be rendered useful. In order to promote a faster rate of evaporation, and hence a more rapid packing of the channel, the base piece of CD1 was placed in an oven at 75ºC for 15-20 min subsequent to dropping suspension volumes. 75ºC was chosen as it is below the PS glass transition temperature (~100ºC) and it allows rapid water evaporation. Figure 5.7 shows a template fabricated using this technique. It is clear that the vast majority of the template is well ordered. However, evaporation driven convective self-assembly is time consuming, taking several days even at elevated temperatures to build a template of the required thickness.

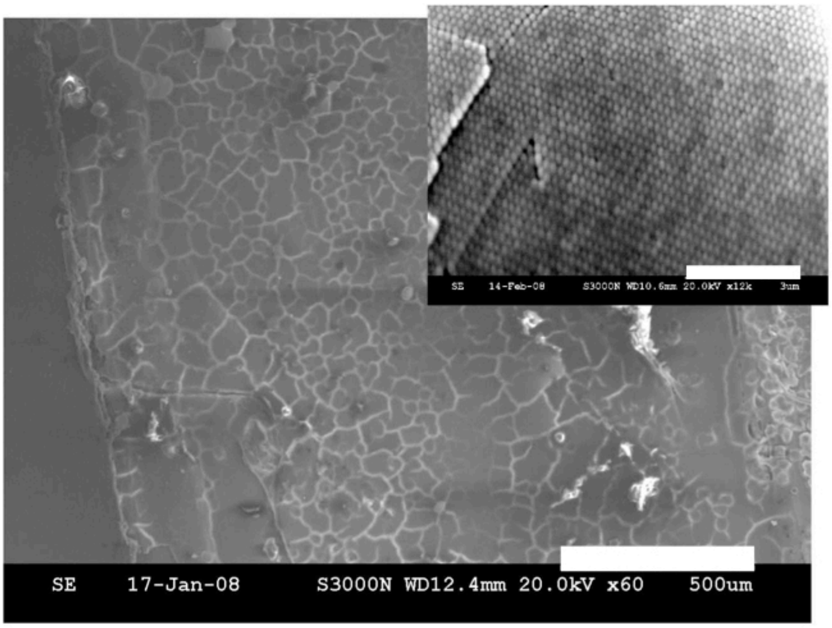

Figure 5.7: SEM of PS beads packed using evaporation-driven convective self-assembly from a PS beads suspension (200 nm, 1% (w/v)). (Scale bar: 500 μm, magnification: 60). Insert close up (scale bar 3 μm, magnification 12k)

Evaporation-driven convective self-assembly was enhanced by adhering a material around the separation channel that was substantially more hydrophobic than the PMMA chip surface. The material chosen was the PSA with the release liner intact, which was found to be hydrophobic. Thus the PMMA channel walls were more hydrophilic than the surface area outside the channel on the base piece of the chip. Thus, in surface energy directed evaporation-driven convective self-assembly, the volume of PS beads suspension deposited was confined to the channel, resulting in quicker packing with less cracks (Figures 5.8 and 5.9). In order to achieve rapid crystallization of the PS beads, the chip was placed in an oven at 75ºC after dropping a volume of suspension. Figure 5.9 shows the effects of charging that resulted from defects in the crystal. During gold sputtering step necessary to prepare non-conductive sample for SEM analysis, the gold layer deposited in the cracks may have been thinner than on the crystal structures. Therefore charging could be observed in these areas. In addition, mirrored electrons could also induce charging like images. As demonstrated by Shaffner *et al.*[53], the sample could reflect electrons directly to the detector when of tubular shape or at edges of the sample, thus creating charging effect on the sample.

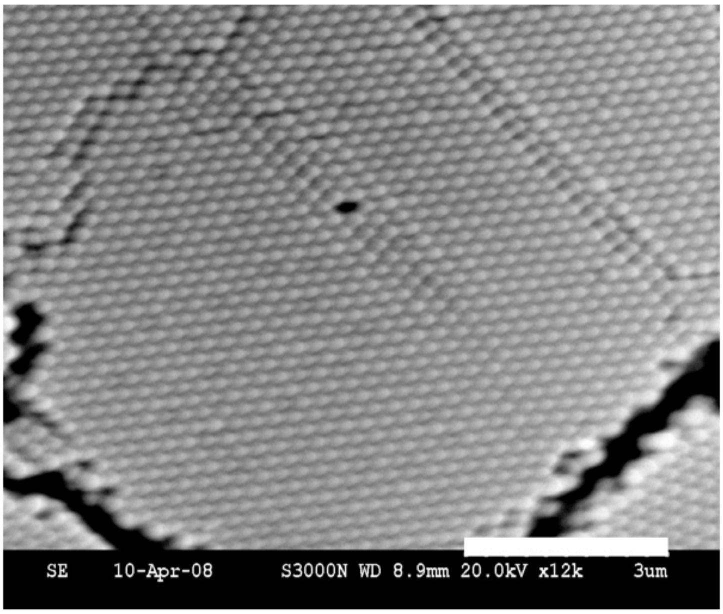

Figure 5.8: SEM of 200 nm PS beads packed into the separation channel using surface energy directed evaporation-driven convective self-assembly (scale bar 3 µm, magnification 12k).

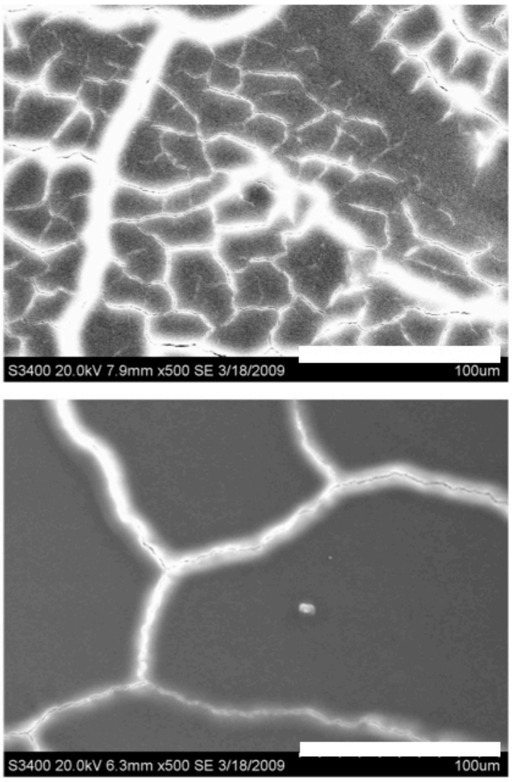

Figure 5.9: SEM of template made with evaporation-driven convective self-assembly (top) and surface energy directed evaporation-driven convective self-assembly (bottom) (magnification: 500, scale bar: 100 µm).

To understand why the surface energy directed evaporation-driven convective self-assembly produced more ordered crystals with fewer defects, an understanding of the crystallization mechanism is required. In both the evaporation-driven convective self-assembly packing techniques described above, the resulting crystals were faced centered cubic (FCC). Figures 5.7 and 5.8 show the (1,1,1) plan of the FCC structure. The (1,1,1) plan is parallel to the channel surface. This FCC structure is the most stable as the Gibbs free-energy is lower than in the hexagonal close packed structure by about 0.05R[54] (R: perfect gas constant). Evaporation-driven convective self-assembly is not yet fully understood but it has been proven that capillary force and convective particle flow during solvent evaporation are the governing factors for ordering (Figures 5.10 and 5.11). It was also shown that the particle substrate electrostatic interactions are of primary importance. Indeed, if the substrate is positively charged and the particles carry a negative surface charge, then the particle would be immobilized without order on the substrate surface thus limiting the convective flux of particle and disordering the formed structures[55].

When the PS bead suspension was deposited for evaporation-driven convective self-assembly, crystallization commenced outside the channel at the base of the droplet as illustrated in Figure 5.10. This was observed as a colloidal crystal ring was formed around the separation channel on the base piece of the chip surface. For the surface energy directed assembly, the mechanism of crystallization is different and described in Figure 5.11. In this case, crystallization occurred both on the sides of the channel and in the centre of the channel. In the first approach, the majority of the PS beads are deposited outside of the separation channel whereas in the surface energy directed packing, the constraining of the PS beads suspension inside the channel induced a much greater number of layers of PS beads to be deposited in the channel at a time (as the number of particles in the channel was greater than in the evaporation-driven convective self assembly), resulting in a more efficient packing. The convective flux of particles during the evaporation process dragged the particles toward the edge of the drop. Thus fewer particles remained in the suspension when the edge of the drop reached the channel borders. Moreover, the larger number of PS beads constrained in the channel by surface energy directed packing, resulted in larger crystals forming at the liquid surface[56]. Thus when completely dried, fewer cracks, which are the joints between several single crystals formed at the liquid surface, are created. Removal or, at least, further reduction of cracks could be achieved by reducing the evaporation rate of the solvent, *i.e.* by reducing the temperature and/or controlling the humidity of the atmosphere during the drying process.

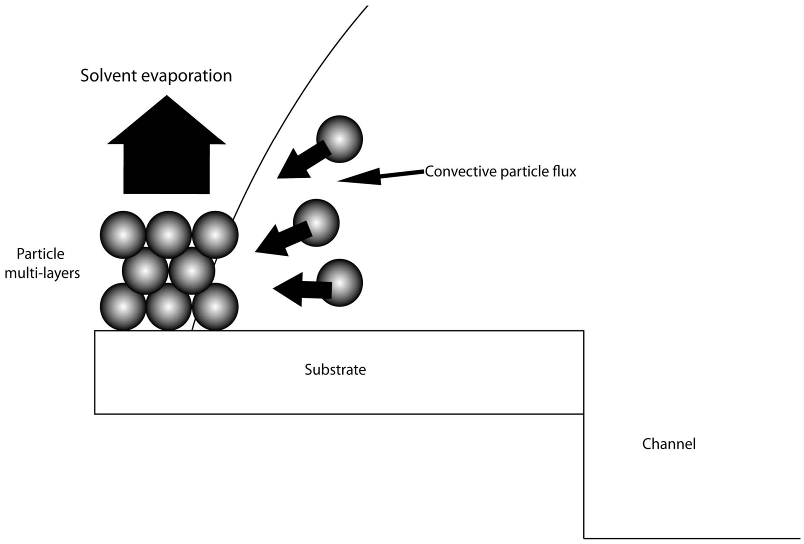

Figure 5.10: Scheme of the evaporation-driven convective self-assembly at the edge of a drop.

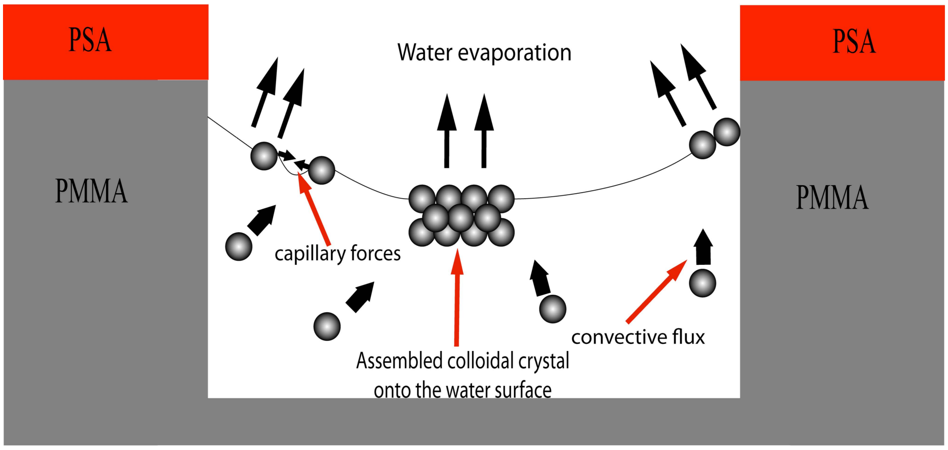

Figure 5.11: Scheme of the evaporation-driven convective self-assembly inside a channel. Adapted from Im *et al.*[56]

Although large colloidal crystal domains were created, neither of the techniques described above were close to ideal. The evaporation driven convective self-assembly techniques provided good ordered templates in an open channel, *i.e.* the chip was not bonded leading to a template whose depth was not necessarily consistent with the depth of the channel. This technique cannot be applied in closed channels as evaporation of solvent could not occur. Moreover, the template created by evaporation driven convective self-assembly was wider than the channel dimension making bonding impossible, as removal of the template is very fragile. Thus removal of the PS colloidal crystal from the outer surface of the chip resulted on the destruction of the template within the channel. However, these templates were good enough to investigate the growth of PANI through it for monolith fabrication. It was decided that the structure of the templated PANI would be investigated by electropolymerizing the monomer in open channel, *i.e.* when the channel was not sealed. The evaporation-driven convective packing technique was chosen as the method to fabricate the template for aniline polymerization, as it was found a convenient method that resulted in mostly ordered structures. Surface energy directed evaporation driven convective self-assembly was not used as the PSA needed to be precisely machined to the dimensions of the channel, which was not immediately feasible.

5.3 POLYANILINE TEMPLATING

The final step of the PANI monolith fabrication was fabrication of the PANI polymer itself. This Section discusses the electropolymerization of aniline within the channel from the gold electrode, through the template. The quality of the monolith was assessed by its physical structure (formation of inverse opal (ordered) or hollow spheres (disordered)). The separation properties will be assessed at a later stage, when structural reproducibility is achieved.

5.3.1 TEMPLATE

Capillary or chip electrochromatography (CEC) comprises the use of electroosmotic flow (EOF) through a chromatographic stationary phase, thus combining the benefits of a plug like flow with the chromatographic properties of a stationary phase resulting in a very effective separation method. Moreover, the flat profile of the EOF is used to obtain sharp peaks. In CEC, the Van Deemter equation applies. The use of a micro-structured monolith (of any material) on-chip should therefore improve reproducibility as well as efficiency and hence the resolution of separations. However, the EOF used in CEC induces some structural restrictions when designing a monolith. EOF is induced by the polarization of the electrical double layer situated at the monolith surface[57]. The electrical double layer thickness is commonly between 10 and 100 nm[57]. It has been demonstrated that in order to retain the flat profile of the EOF, the ratio between pore diameter and the electrical double layer thickness should be kept greater than 50 to 100[58]. By maintaining the electrical double layer thickness as low as possible, *i.e.* around 10 nm, a pore size of over 500 nm would be required for a flat EOF. As a consequence of the potential loss of the EOF flat profile when the pore size is too small, the pore interconnections must also be greater than 500 nm. Therefore, 1 μm PS beads were chosen as the template material.

In order to investigate the influence of bead concentration over template formation, 10% (w/v), 1% (w/v) and 0.1% (w/v) 1μm PS beads suspensions were used to form the template. Deionized water was used to dilute the 10% (w/v) stock solutions for the lower concentrations. As seen in Figure 5.12, no structural differences between the templates made from different PS suspensions could be observed. The particle-to-particle distance (centre of a particle to centre of the nearest particle) is approximately 1.05 μm in all cases. However, the time to completely pack the channel with the beads varied from 30 min for the 10% (w/v) PS beads to several days for the most diluted suspensions. Thus, the 10% (w/v) PS beads resulted in optimum templating as the packing time was quickest without compromising on quality.

Figure 5.12 also revealed the (1,1,1) plan of the face centered cubic (FCC) arrangement of the beads. FCC structures are compact structures which means that the beads occupy maximum space (74% of the volume is occupied by the beads). The FCC structure is the optimal structure for this research as this will provide a small skeleton size with large flow through pores, which have been demonstrated (see discussion in Section 1.5) to be of primary importance for chromatographic separations.

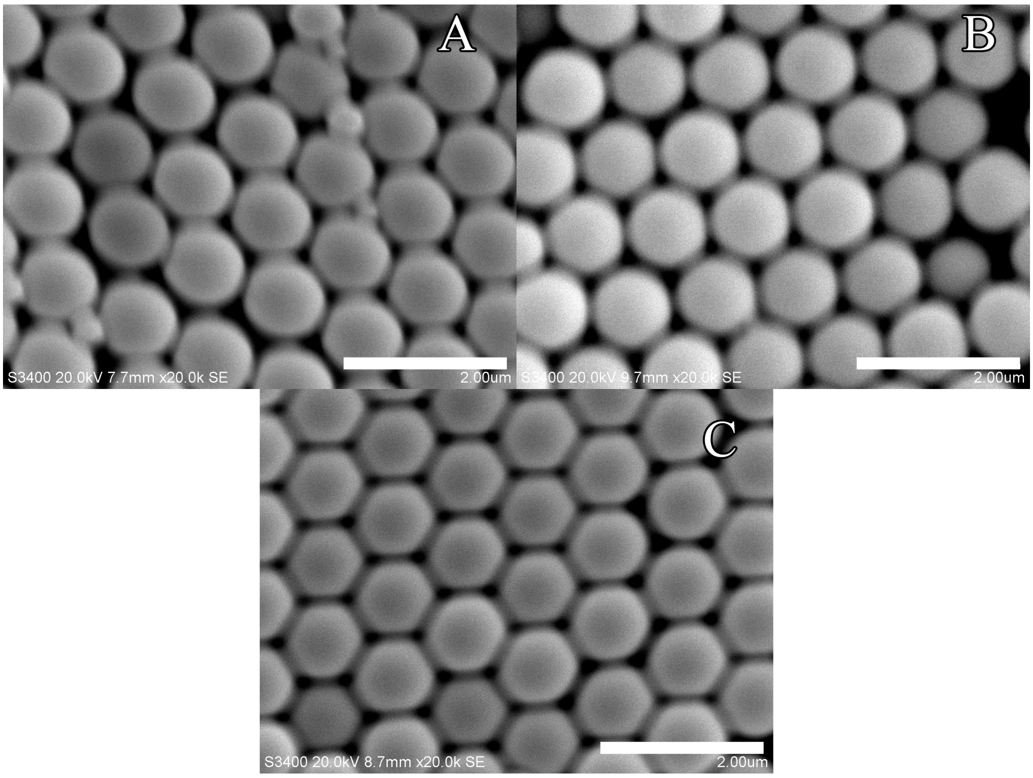

Figure 5.12: Templates fabricated in CD1 separation channel from 10% (w/v) (A), 1% (w/v) (B) and 0.1% (w/v) (C) PS beads suspensions. (Magnification: 20,000, scale bar 2 μm).

5.3.2 POLYANILINE MONOLITH FORMATION

Electropolymerization of aniline monomer was carried out in HCl (1 M) electrolyte onto the gold sputtered separation channel through the template. No additional polymer dopant such as PVS or PSS[41, 45, 47] was used. These high molecular weight polyelectrolyte dopants are often used to dope PANI as it is claimed that it helps maintain conductivity of the polymer as well as maintaining structural strength within the polymer[59]. When electropolymerization was first investigated, PVS and PSS were used as dopants. However, after 1 hour of polymerization, the polymer was not fully grown through the template. By removing the dopant from the monomer solution, the polymer grew more rapidly suggesting that the diffusion of the large dopant molecules through the template to the polymerization sites was limiting the kinetics of the polymerization. The diffusion of such large species through a close packed structure was limited and thus had to be omitted. In the absence of dopant, the PANI grew through the template in less than 20 min (thickness: 20 μm approx.) as confirmed by SEM. Bulk, non-templated PANI was observed showing that it had grown from the working electrode through the template and continued to grow as non-templated bulk polymer above the template (Data not shown).

Figure 5.13 shows the voltammograms generated for a scan rate study of the PANI/PS bead composite on-chip. These voltammograms were performed in an open chip format with the reference and auxiliary wire electrodes in the upper piece being used as the electrodes to complete the electrochemical circuit. The voltammograms confirmed the presence of PANI: the redox peaks of PANI are clearly seen at approximately -100 mV, +300 V, +400 V and +900 mV *vs.* Ag/AgCl. A slow electron transfer rate within the polymer can be deduced by observing the shift in potential when increasing the scan rate. The peak for the oxidation from leucoemeraldine to emeraldine shifted from +200 mV at 20 mV/s to +400 mV at 200 mV/s. The slow electron transfer was also seen at higher scan rates, as the redox peaks were broad and undefined. When the scan rate was faster than the rate of electron transfer, there was not sufficient time for the electrons to arrive at the electrode surface before the oxidation state of PANI changed.

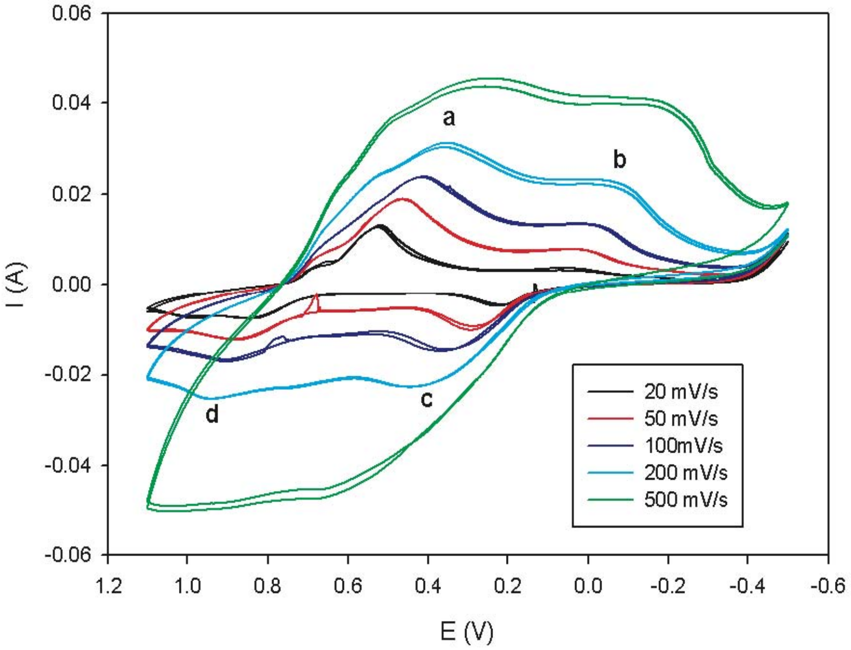

Figure 5.13: Scan rate study of PANI grown potentiostatically (7 min in HCl (1M) at a potential of +900 mV *vs.* Ag/AgCl) through the PS template to form a PANI/PS composite on chip.

The high current magnitudes observed (10^{-2} A) are due to the quantity of polymer (0.2 mm^3 calculated as 25% of the channel volume (20 μm deep) as the template is a compact structure) that was deposited within the channel.

PANI was successfully electropolymerized through the template. The PANI film exhibited slow electron transfer as the film thickness and volume of PANI present was large. However, the presence of PS bead template could have also contributed to the slow electron transfer rate because no electrolyte was in contact with the polymer where the PS beads were, resulting in a slow doping/dedoping of the polymer during redox processes. Unfortunately, this hypothesis could not be confirmed, as the template could not be removed whilst the polymer remained on-chip.

Typical SEM micrographs of the templated polymer after template removal are displayed in Figure 5.14, where it can be seen that a mixture of two structures, disordered hollow spheres and ordered inverse opal were obtained on the same chip using 1% (w/v) PS beads. These images were obtained according to Chapter 2, Section 2.4.9.1 by removing PANI/PS beads composite from chip and subsequently dissolving the PS beads. The observation of both types of structure was unexpected - both were present in approximately equivalent quantities. Although defects were observed in the PS templates, the vast majority of the crystal was ordered. Thus it would have been expected that the vast majority of the PANI monolith would be inverse opal-like in structure.

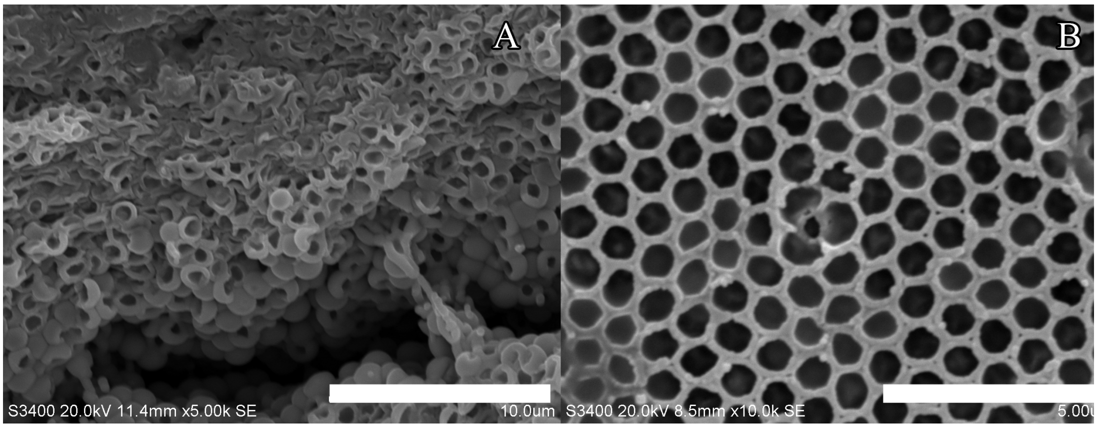

Figure 5.14: Disordered hollow spheres structure (A) and ordered inverse opal structure (B) of the PANI monolith grown through a template of PS beads (1% (w/v), 1 μm) packed by evaporation driven self-assembly in the separation channel. (Magnification: 10,000 (A), 5,000 (B), scale bar: 10 μm (A), 5 μm (B)). Potensiostatic polymerization of aniline performed at +900 mV *vs.* Ag/AgCl for 20 min.

The dependence on the choice of electropolymerization technique was investigated to see if this could affect the resulting PANI structure. Two techniques, potentiodynamic and potentiostatic polymerization were investigated. No structural differences were observed between the potentiodynamically and potentiostatically polymerized PANI monoliths (data not shown) as both hollow spheres and inverse opal-like structures were observed within the monoliths when the template was fabricated from 1% (w/v) PS beads. As the FCC structure of the template is compact in nature, the volume of PANI required to fill the PS beads-packed channel is just 26% of the channel volume. Thus the physical confinement of PANI within the voids between the PS beads dictates the structure of the polymer rather than the polymerization technique.

One important observation was that the pore diameter was approx. 750 nm in the resulting inverse opal structures whereas the PS beads used as template were 1 µm (Figure 5.15). This is due to an expansion or swelling of the PANI after template removal.

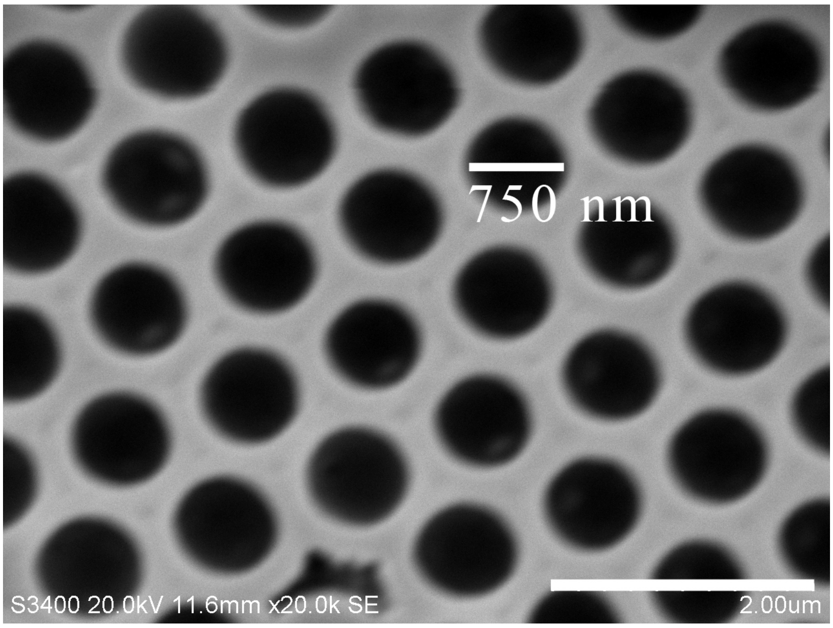

Figure 5.15: PANI inverse opal obtained upon potentiostatic polymerization (+ 900 mV *vs.* Ag/AgCl, 20 min) of aniline through ordered PS beads (1% (w/v), 1 µm). PS beads were removed by immersing monolith in toluene for 24 h. (magnification: 20,000; scale bar: 2 µm).

5.3.3 EFFECT OF INITIAL PS SUSPENSION SURFACTANT CONCENTRATION ON THE PANI MONOLITH STRUCTURE

It was observed previously that PS beads used at a range of concentrations resulted in equivalent ordered template formation (Figure 5.12). However, Figure 5.13 demonstrated that both ordered and non-ordered PANI structures could result from this ordered template. Further investigation showed that by using a 10% (w/v) PS bead concentration, hollow spheres, i.e. a disordered structure, of PANI resulted while with a template fabricated from 1% (w/v) PS beads, both hollow sphere and inverse opal structures were obtained (Figure 5.16). Using even lower concentrations, a template fabricated from 0.1% (w/v) PS beads, inverse opal structures, *i.e.* ordered structures only were observed. Therefore, despite having an identical ordered PS template both ordered and non-ordered PANI structures resulted from these templates, where the amount of disorder appeared to be dependant on concentration of PS beads used (Figure 5.16). This result was unexpected given that the structure of the bare template was observed to be equivalent for all concentrations. Therefore, the differences in polymer structure observed may be attributed to changes in the colloidal crystal template upon exposure to the aniline monomer solution. When the template was re-wetted with the aqueous monomer mixture, the inter-particle interactions appeared to become weaker with increasing the PS bead concentration, and as such an ordered PS template could become disordered at high PS bead concentrations.

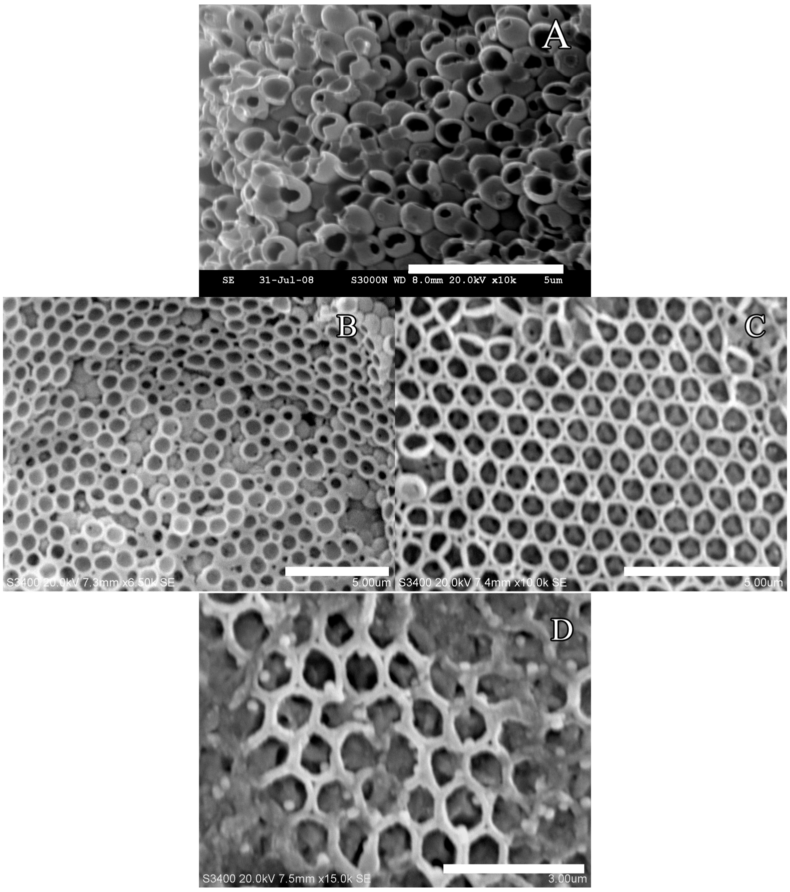

Figure 5.16: PANI monolith structures grown through close packed PS templates: (A) hollow spheres resulting from 10% (w/v) PS beads (magnification: 10,000; scale bar 5 μm), (B) hollow spheres resulting from 1% (w/v) PS latex (magnification: 6,500; scale bar 5 μm), (C) inverse opal resulting from 1% (w/v) PS latex (magnification: 10,000; scale bar 5 μm), (D) inverse opal resulting from 0.1% (w/v) PS latex (magnification: 15,000; scale bar 3 μm). Potensiostatic polymerization of aniline was carried out in all instances at +900 mV *vs.* Ag/AgCl for 20 min.

Given that the stock 10% (w/v) suspensions were diluted with deionized water to obtain lower concentrations, all species contained in the suspensions were also diluted. These were commercial suspensions purchased from Duke Scientific Ltd. who provided that a stabilizing surfactant was present and was anionic at a concentration of between 0.2 -0.5% (w/v). In order to investigate if the change in rewetted template structure was due to changes in surfactant concentration, the suspensions were centrifuged three times and re-dispersed in deionized water in order to remove surfactant. After the final centrifugation, the PS beads were redispersed in different concentrations of the anionic surfactant sodium dodecyl sulfate (SDS) (0.01% (w/v), 0.1% (w/v) and 1% (w/v)). Figure 5.17 shows that by varying the concentration of surfactant in the suspensions while maintaining the PS beads at a constant concentration (10 ± 1% (w/v)) the resulting PANI structure could be controlled. Figure 5.17A and B show the inverse opal ordered structure with pore interconnections when 0 and 0.01% (w/v) surfactant were present, respectively. Figure 5.17C shows that by increasing surfactant concentration to 0.1% (w/v), the resulting structure of the PANI monolith was bimodal in nature as a mixture of inverse opal and hollow spheres were observed. When utilizing SDS at a high concentration of 1% (w/v), the PANI structure obtained was predominantly hollow sphere (or disordered) in structure (Figure 5.17D). This result indicates that it was the surfactant concentration that had a direct effect on the resulting polymer structures. Using a high SDS concentration for template formation disordered hollow sphere PANI monolith structures resulted while low concentrations of surfactant present permitted the desired ordered inverse opal PANI monolith structures.

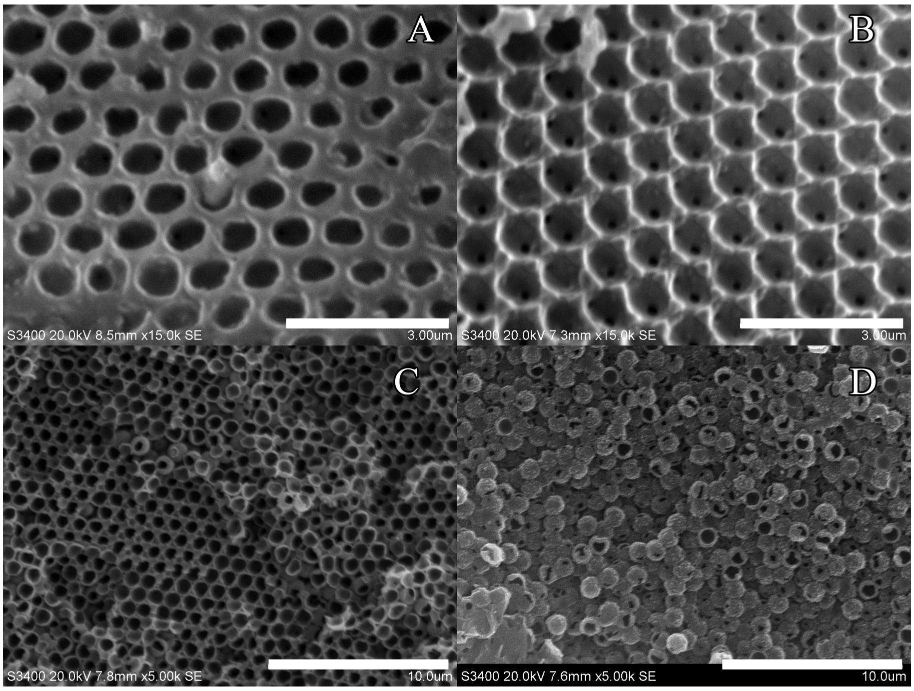

Figure 5.17: PANI structures resulting from 10% (w/v) PS beads dispersed in: (A) deionized water, (B) 0.01% SDS, (c) 0.1% SDS, (d) 1% SDS. Potentiostatic polymerization performed in all instances at +900 mV *vs.* Ag/AgCl for 20 min. magnification: 15,000 (A) and (B); 5,000 (C) and (D). Scale bar: 3 µm (A) and (B); 10 µm (C) and (D).

Zhou *et al.*[60] showed previously that an increase in SDS concentration in colloidal suspensions lowered inter-particle interactions during a colloidal crystal drying process. When the concentration of SDS approached the CMC, this lead to a mixture of hexagonal and cubic crystals as the rearrangement of the beads from their initial rectangular structure to low Gibbs energy crystals (face centered cubic (FCC), hexagonal compact (HC)) became more difficult. During the crystallization process a phase of rearrangement is necessary to obtain a crystal as stable as possible, i.e. with the lowest Gibbs energy. The rearrangement of the beads to a low Gibbs energy crystal such as FCC or HC was prohibited when large amounts of surfactants were used because the inter-particle forces were too weak as the surface tension was too low. In other words there was not enough force between particles for them to move and rearrange. In our case, at high surfactant concentrations, these initial observations were not made as an ordered low Gibbs energy crystal was observed for all SDS concentrations upon template formation. It was only when the colloidal crystals were rewetted by the monomer solution that the crystals became disordered. However, the template inter-particle forces still contributed to the final PANI structure. At high SDS concentrations (1% (w/v)) (significantly above the CMC) the template disintegrated when immersed in the aqueous monomer solution confirming low inter-particle and low substrate to particle forces induced by the surfactant.

In addition, it is well known that surfactant adsorbs on the PS beads surface, when surfactant is present in a PS bead suspension. On increasing the surfactant concentration, the number of surfactant molecules adsorbed to each particle increased, thus increasing the charge density on the particle surfaces. When rewetting the template, the coulombic forces created by the charge repulsion on the particle surfaces may compete with the attractive long-range forces (Van Der Waals forces) (Figure 5.18). When coulombic repulsive forces were greater than attractive forces, the colloidal crystal could be destabilized as the particles repulsed each other when rewetted. Zeta potential measurements of the PS beads suspension at different SDS concentration showed an increase of the zeta potential, therefore of the charged carried at the beads surface from -60 mV to -120 mV upon increase of SDS concentration.

In summary, it is believed that when the surfactant concentration was sufficiently high, the charge on the beads surface increased with increasing surfactant concentration and the monomer mixture may have destabilized the template because of the electrostatic particles repulsion. The charge opposition between the PS beads surface and the monomer probably lead to disorganized hollow spheres as the PANI growth occurred from the beads surface (Figure 5.18A). However, when the surfactant concentration was low, the template may not have been destabilized, *i.e.* the electrostatic repulsion between particles was not greater than the long-range attractive forces. Thus, when rewetted, the colloidal crystal structure integrity was preserved. During the polymer growth from the beads surface, the ordered inverse opal structure was achieved due to geometrical confinement of the polymer induced by the template (Figure 5.18B).

In order to achieve the hollow sphere disordered structure (as opposed to a porous bulk polymer) the PANI had to grow from the beads surface. The negative surface of the PS beads induced hollow spheres, as the positively charged monomer interacted electrostaticaly with the PS beads surface. Thus the electrostatic interactions between the PS beads surface and the monomer orientated the PANI growth from the beads surface.

In Figure 5.16C, it can be seen that the growth of the PANI occurred from the beads surface as a “hole” remained in the middle of the template cavities where PANI can grow. Indeed, the electrostatic interactions between the PS beads and the monomer and/or oligomers formed guided the polymerization from the surface of the latex beads. However, due to strong inter-particle interactions, an ordered inverse opal structure with pore interconnections was obtained.

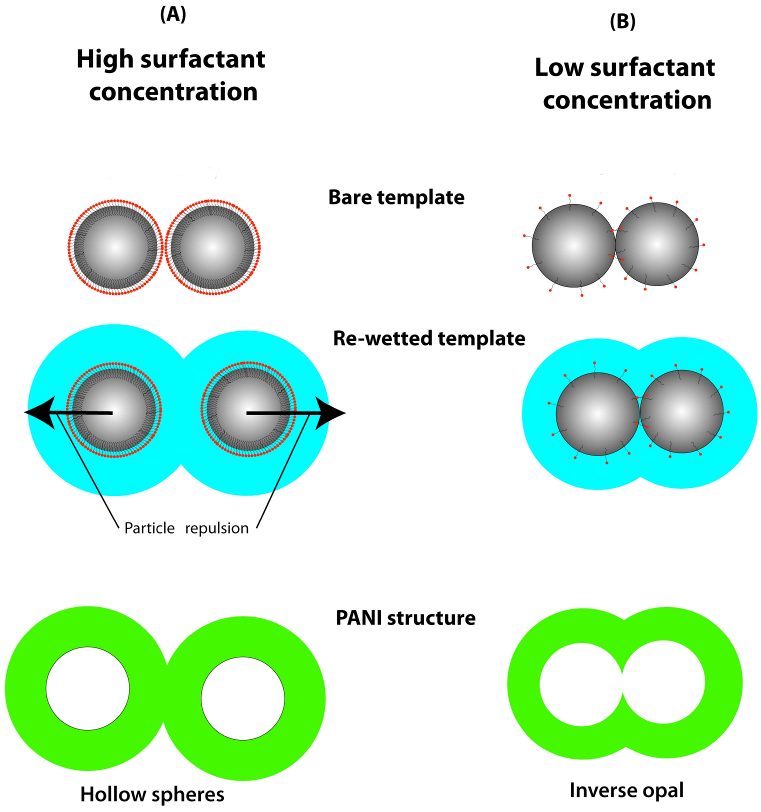

Figure 5.18: Schematic of the rewetting mechanism leading to (A) disordered hollow sphere structure in the presence of high concentration of surfactant and (B) ordered inverse opal structure without or with trace amount of surfactant.

From a separation point of view, inverse opal PANI structures have been shown to be macroporous in nature, which would imply that these materials would be suitable for large molecule separations, *i.e.* proteins and DNA. There is no evidence of a mesoporous structure and thus, these structures would not be suited to separate small molecules. However, it should be noted that all SEM images displayed were taken after the PANI was dried. Lizarraga *et al.*[61] showed that the PANI volume and morphology could be controlled by application of a potential. This publication showed that the volume occupied by PANI varied with applied potential. This phenomenon could be investigated at a later stage for EMμ, potentially permitting EMμ to separate small molecules.

5.4 CONCLUSION

Different techniques were used in order to obtain the colloidal crystal template in the main channel of CD1. The filtration and ink-jet printing methods were not suitable as they lead to disordered templates. Evaporation driven self-assembly techniques provided efficient packings with highly ordered templates but defects were observed. Moreover, these packings were only achieved in open channels and it was not possible to subsequently seal the channel. However, by tuning the evaporation conditions (*i.e.* temperature and humidity) it may be possible to remove these defects. Successful PS bead template formation, appropriate for EMμ, was not achieved for CD1.

In the second part of this chapter, a micro-structured PANI monolith was successfully fabricated in the microfluidic channel by templating PANI with colloidal crystals (1 μm PS beads). It was found that the concentration of surfactant contained in the PS bead templating suspensions was responsible for the particle-to-particle interactions in the crystal, *i.e.* the template stability. Although at all concentrations of surfactant, a close packed crystal structure was obtained, the higher the surfactant concentration the poorer the template stability. As PANI grew from the PS beads surface, a non-ordered (destabilized) template in the presence of high surfactant concentration lead to a hollow spheres structures whereas strong particle-to-particle interactions (stable crystal) in low surfactant concentration lead to the desired inverse opal structure.

In conclusion, a microstructured PANI monolith, formed by electropolymerization through an ordered PS bead scaffold, which was subsequently removed, was successfully achieved. The parameter controlling the final monolithic structure (*i.e.* hollow sphere or inverse opal), namely control of surfactant concentration, was elucidated. While it was demonstrated that CD1 was not suitable for PS template formation, the knowledge gained about PANI formation can be applied to CD2.

5.5 REFERENCES

1. Cheng, F.; Tao, Z.; Liang, J.; Chen, J., *Chemistry of Materials* **2007,** *20* (3), 667-681.
2. Lai, M.; Riley, D. J., *Journal of Colloid and Interface Science* **2008,** *323* (2), 203-212.
3. Thomas, A.; Goettmann, F.; Antonietti, M., *Chemistry of Materials* **2008,** *20* (3), 738-755.
4. Velev, O. D.; Kaler, E. W., *Advanced Materials* **2000,** *12* (7), 531-534.
5. Holmberg, K.; Jönsson, B.; Kronberg, B.; Lindman, B., *Phase Behaviour of Concentrated Surfactant Systems*. John Wiley & Sons, Ltd: 2003; p 67-96.
6. Attard, G. S.; Bartlett, P. N.; Coleman, N. R. B.; Elliott, J. M.; Owen, J. R.; Wang, J. H., *Science* **1997,** *278* (5339), 838-840.
7. Bartlett, P. N.; Marwan, J., *Microporous and Mesoporous Materials* **2003,** *62* (1-2), 73-79.
8. Braun, P. V.; Osenar, P.; Twardowski, M.; Tew, G. N.; Stupp, S. I., *Advanced Functional Materials* **2005,** *15* (11), 1745-1750.
9. Crossland, E. J. W.; Ludwigs, S.; Hillmyer, M. A.; Steiner, U., *Soft Matter* **2007,** *3* (1), 94-98.
10. Khatri, M. S.; Schlorb, H.; Fahler, S.; Schultz, L.; Nandan, B.; Bohme, M.; Krenek, R.; Stamm, M., *Electrochimica Acta* **2009,** *54* (9), 2536-2539.
11. Lee, J. I.; Cho, S. H.; Park, S.-M.; Kim, J. K.; Kim, J. K.; Yu, J.-W.; Kim, Y. C.; Russell, T. P., *Nano Letters* **2008,** *8* (8), 2315-2320.
12. Richman, E. K.; Kang, C. B.; Brezesinski, T.; Tolbert, S. H., *Nano Letters* **2008,** *8* (9), 3075-3079.
13. Deng, Y.; Yu, T.; Wan, Y.; Shi, Y.; Meng, Y.; Gu, D.; Zhang, L.; Huang, Y.; Liu, C.; Wu, X.; Zhao, D., *Journal of the American Chemical Society* **2007,** *129* (6), 1690-1697.
14. Maeda, Y.; Shimoi, Y.; Ogino, K., *Polymer Bulletin* **2005,** *53* (5), 315-321.
15. Cameron, N. R., *Polymer* **2005,** *46* (5), 1439-1449.
16. Menner, A.; Ikem, V.; Salgueiro, M.; Shaffer, M. S. P.; Bismarck, A., *Chemical Communications* **2007,** (41), 4274-4276.

17. Brown, I. J.; Sotiropoulos, S., *Electrochimica Acta* **2001,** *46* (17), 2711-2720.

18. Menner, A.; Salgueiro, M.; Shaffer, M. S. P.; Bismarck, A., *Journal of Polymer Science Part A: Polymer Chemistry* **2008,** *46* (16), 5708-5714.

19. Xin, L.-Y.; Zhang, X.-G.; Zhang, G.-Q.; Shen, C.-M., *Journal of Applied Polymer Science* **2005,** *96* (5), 1539-1543.

20. Chen, F.; Kitai, A. H., *Thin Solid Films* **2008,** *517* (2), 622-625.

21. Wang, Z.; Liu, S.; Wu, P.; Cai, C., *Analytical Chemistry* **2009,** *81* (4), 1638-1645.

22. Dauginet-De Pra, L.; Demoustier-Champagne, S., *Thin Solid Films* **2005,** *479* (1-2), 321-328.

23. Menon, V. P.; Lei, J.; Martin, C. R., *Chemistry of Materials* **1996,** *8* (9), 2382-2390.

24. Parthasarathy, R. V.; Martin, C. R., *Chemistry of Materials* **1994,** *6* (10), 1627-1632.

25. Warren, S.; Doaga, R.; McCormac, T.; Dempsey, E., *Electrochimica Acta* **2008,** *53* (13), 4550-4556.

26. Prakash, A.; Majumdar, S.; Devi, P. S.; Sen, A., *Journal of Membrane Science* **2009,** *326* (2), 388-391.

27. Mukai, S. R.; Nishihara, H.; Tamon, H., *Chemical Communications* **2004,** (7), 874-875.

28. Nishihara, H.; Mukai, S. R.; Yamashita, D.; Tamon, H., *Chemistry of Materials* **2005,** *17* (3), 683-689.

29. Nishihara, H.; Iwamura, S.; Kyotani, T., *Journal of Materials Chemistry* **2008,** *18* (31), 3662-3670.

30. Cong, H.; Cao, W., *Langmuir* **2003,** *19* (20), 8177-8181.

31. Fu, Y.; Jin, Z.; Liu, Z.; Liu, Y.; Li, W., *Materials Letters* **2008,** *62* (27), 4286-4289.

32. Jiang, P.; Bertone, J. F.; Hwang, K. S.; Colvin, V. L., *Chemistry of Materials* **1999,** *11* (8), 2132-2140.

33. Velev, O. D.; Lenhoff, A. M., *Current Opinion in Colloid & Interface Science* **2000,** *5* (1-2), 56-63.

34. Yang, X.; Jin, Y.; Zhu, Y.; Tang, L.; Li, C., *Journal of The Electrochemical Society* **2008,** *155* (1), J23-J25.
35. Gates, B.; Xia, Y., *Advanced Materials* **2000,** *12* (18), 1329-1332.
36. Stein, A.; Schroden, R. C., *Current Opinion in Solid State and Materials Science* **2001,** *5* (6), 553-564.
37. Waterhouse, G. I. N.; Metson, J. B.; Idriss, H.; Sun-Waterhouse, D., *Chemistry of Materials* **2008,** *20* (3), 1183-1190.
38. Zhou, Z.; Zhao, X. S., *Langmuir* **2003,** *20* (4), 1524-1526.
39. Teh, L. K.; Tan, N. K.; Wong, C. C.; Li, S., *Applied Physics A: Materials Science & Processing* **2005,** *81* (7), 1399-1404.
40. Wang, L.; Zhao, X. S., *The Journal of Physical Chemistry C* **2007,** *111* (24), 8538-8542.
41. Luo, X.; Killard, A. J.; Morrin, A.; Smyth, M. R., *Chemical Communications* **2007,** (30), 3207-3209.
42. Luo, X.; Killard, A. J.; Smyth, M. R., *Chemistry – A European Journal* **2007,** *13* (7), 2138-2143.
43. Luo, X.; Vidal, G. D.; Killard, A. J.; Morrin, A.; Smyth, M. R., *Electroanalysis* **2007,** *19* (7-8), 876-883.
44. Wang, D.; Caruso, F., *Advanced Materials* **2001,** *13* (5), 350-354.
45. Tian, S.; Wang, J.; Jonas, U.; Knoll, W., *Chemistry of Materials* **2005,** *17* (23), 5726-5730.
46. Han, S.; Briseno, A. L.; Shi, X.; Mah, D. A.; Zhou, F., *The Journal of Physical Chemistry B* **2002,** *106* (25), 6465-6472.
47. Bartlett, P. N.; Birkin, P. R.; Ghanem, M. A.; Toh, C.-S., *Journal of Materials Chemistry* **2001,** *11* (3), 849-853.
48. Velev, O. D.; Tessier, P. M.; Lenhoff, A. M.; Kaler, E. W., *Nature* **1999,** *401* (6753), 548-548.
49. Park, S. H.; Gates, B.; Xia, Y., *Advanced Materials* **1999,** *11* (6), 462-466.
50. Lee, S.-K.; Yi, G.-R.; Yang, S.-M., *Lab on a Chip* **2006,** *6* (9), 1171-1177.
51. Park, J.; Lee, D.; Kim, W.; Horiike, S.; Nishimoto, T.; Lee, S. H.; Ahn, C. H., *Analytical Chemistry* **2007,** *79* (8), 3214-3219.

52. Sawada, T.; Suzuki, Y.; Toyotama, A.; Iyi, N., *Japanese Journal of Applied Physics\ 40* (Part 2, No. 11B\), L1226\.

53. Shaffner, T. J.; Veld, R. D. V., *Journal of Physics E: Scientific Instruments* **1971,** *4* (9), 633.

54. Woodcock, L. V., *Nature* **1997,** *385* (6612), 141-143.

55. Yan, Q.; Gao, L.; Sharma, V.; Chiang, Y.-M.; Wong, C. C., *Langmuir* **2008,** *24* (20), 11518-11522.

56. Im, S. H.; Park, O. O.; Kwon, M. H., *Macromolecular research* **2004,** *12* (2), 189-194.

57. Liapis, A. I.; Grimes, B. A., *Journal of Chromatography A* **2000,** *877* (1-2), 181-215.

58. Hlushkou, D.; Kandhai, D.; Tallarek, U., *International Journal for Numerical Methods in Fluids* **2004,** *46* (5), 507-532.

59. Gaikwad, P.; Shirale, D.; Gade, V.; Savale, P.; Kakde, K.; Kharat, H.; Shirsat, M., *Bulletin of Materials Science* **2006,** *29* (4), 417-420.

60. Zhou, Z.; Li, Q.; Zhao, X. S., *Langmuir* **2006,** *22* (8), 3692-3697.

61. Lizarraga, L.; Andrade, E. M.; Molina, F. V., *Electrochimica Acta* **2007,** *53* (2), 538-548.

CHAPTER 6 FURTHER STUDIES ON CONDUCTING POLYMER MICROSTRUCTURES ON-CHIP INCLUDING AN AFM-BASED ACTUATION STUDY

6.1 INTRODUCTION TO ATOMIC FORCE MICROSCOPY (AFM)

Atomic force microscopy (AFM) is part of scanning probe microscopy (SPM). In 1982, Binnig and Rohrer[1] developed the first Scanning Tunneling Microscope (STM) and reached a resolution of 0.1 nm for the first time. The STM was built on the principle that when a metallic probe approaches the surface of an electrically conductive material, a tunneling current results due to changes in the local density of electronic states at the sample. The spatial resolution is then directly related to the size of the probe used. This method is only applicable for conductive samples; however, the probing technique has been applied to other probe/sample interactions, resulting in techniques such as AFM.

AFM is based on the interatomic forces between the scanning probe and the sample's surface. AFM is used for topographic studies of samples as well as mapping chemical identities at a surface or to study the mechanical properties of the near surface region.

In simple terms, a tip is microfabricated on a flexible cantilever. The tip is then brought close to the sample and the cantilever is deflected from its original position by the interaction forces between the tip and the sample. The cantilever deflection is measured using a laser reflected from the cantilever surface into a position sensitive photodiode detector (Figure 6.1) and the piezo-electric device adjusts the height of the cantilever for the deflection to remain constant.

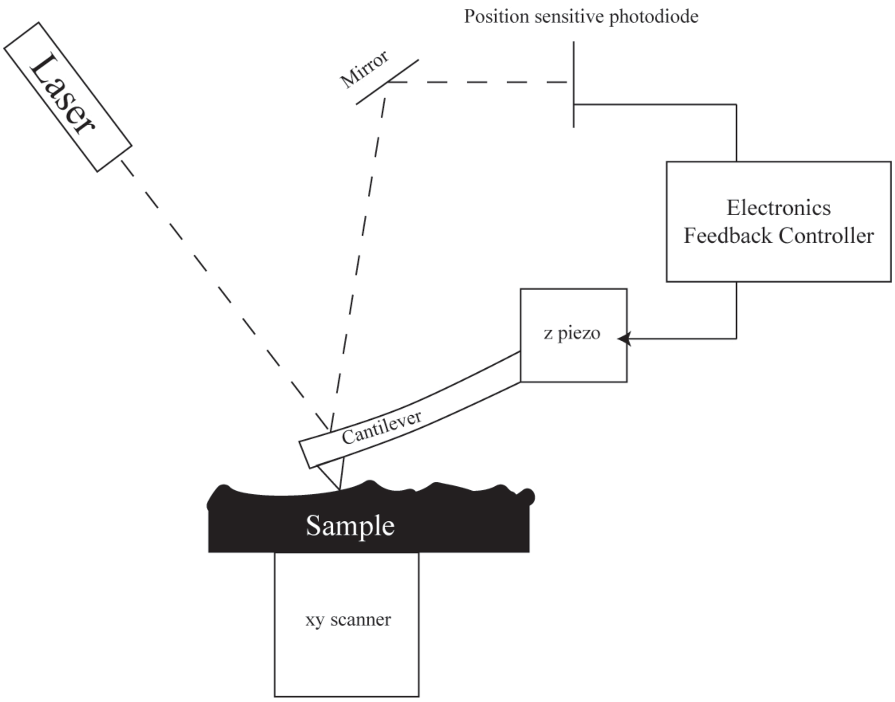

Figure 6.1: Schematic of AFM instrumentation. Adapted from Braga and Ricci[2]

A feedback system is usually present in AFM instrumentation to avoid collisions between the sample and tip. The AFM used in this study is a hybrid between a probe scanned and a sample-scanned AFM. The piezo-electric device is used to maintain interaction forces between the tip and sample constant by moving the sample in the z-direction while the sample is scanned in the x and y directions from the stage (Figure 6.1). The voltage applied on the piezo-electric device to maintain constant force is recorded and is proportional to the movement of the tip, thus to the sample topography. As a consequence, for each x,y coordinate the topography is known and thus, the 3-dimensional topography of the full sample can be established.

AFM imaging can be performed in several modes. In contact mode, also called static mode, the tip is moved on the sample surface and the cantilever deflection is used as the feedback to measure the topography of the sample, as described above. However, this technique is highly affected by noise and drift. When close to the surface, attractive forces between the tip and the sample can be high and result in the tip physically contacting the sample. As a consequence, this technique is usually used by making contact between the tip and the sample when the interaction forces are repulsive and/or when the physical nature of the sample is hard so that the tip cannot penetrate the sample.

In contrast to static mode, several dynamic AFM modes exist: non-contact mode with amplitude or frequency modulation and tapping mode being the most popular. However, only tapping mode will be discussed here as it is the mode which will be used in PPy actuation study. In tapping mode the cantilever is oscillated slightly under its resonance frequency. When the tip is near the sample surface, the interaction forces decrease the amplitude of the cantilever oscillations. The amplitude of the oscillation is measured with the laser and photodiode detector and used as feedback for the piezo-electric. The piezo-electric adjusts the distance between the tip and the sample so that the oscillation amplitudes are constant. This mode was developed to overcome the problem of the tip “sticking” to the sample in dynamic modes. Tapping mode is the most used mode nowadays as it is the mode with least noise and drift problems.

AFM can also be used for samples immersed in liquid. It is regularly used to probe biological samples (*e.g.* cell membranes). In liquid, tapping mode is usually used. However, the thermal resonance frequency of the cantilever as opposed to its own resonance frequency is used for acquiring topographical information due to the resistance of the liquid on the cantilever.

6.1.1 CONDUCTIVE POLYMER ACTUATION MONITORED BY AFM

AFM has been widely used to study the morphology and electrochemical properties of PPy[3-8] and PANI[9-14]. In addition, PPy and PANI have the property of undergoing volume changes when changing oxidation state[15, 16]. As a consequence, they can act as actuators. Electrochemical-AFM (EC-AFM) can be used to monitor this actuation. EC-AFM of electroactive polymer involves performing AFM in electrolyte while electrochemical switching of the polymer is taking place, using a three-electrode electrochemical cell.

Singh *et al.*[12] studied the volume changes of PANI with porous, micro-tubular and microwired structures electropolymerized on highly oriented pyrolytic graphite in Cl^- and SO_4^{2-} media. An increase of volume was observed in the oxidized state because of the intake of solvated anions. However, on PANI/PS sulfonate (PSS) the increase in volume was observed in the reduced state due to the intake of solvated cations to preserve electro-neutrality of the polymer (see Chapter 4 section 4.1.3.1.2). Figure 6.2 shows the change in volume in a porous PANI film electrochemically grown on highly oriented pyrolytic graphite. It can be seen that the pore size of the PANI depends on the applied potential. They found changes in volume of more than 33% in microwired structured PANI. They also studied PANI nanoparticles and observed a volume variation from 15% to approximately 90% when +200 mV oxidation potential was applied.

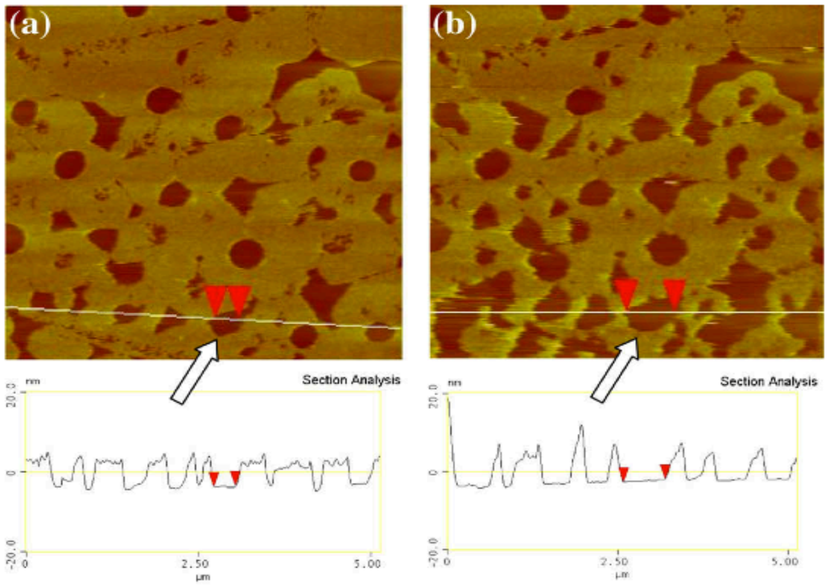

Figure 6.2: AFM images of PANI polymerized on highly oriented pyrolytic graphite with height plots in 0.1 M HCl at (A) +200 mV and (B) -200 mV, both *vs.* Ag/AgCl. From Singh *et al.*[12]

Suárez *et al.*[17] studied the initial stages of PPy electropolymerization by EC-AFM. Preliminary measurements were also performed on the actuation of the PPy films. A volume change from 25 to 50% was reported on freshly prepared PPy/ClO_4^- films upon first reduction of the film after its preparation (PPy film are prepared in oxidized form of the polymer) (Figure 6.3).

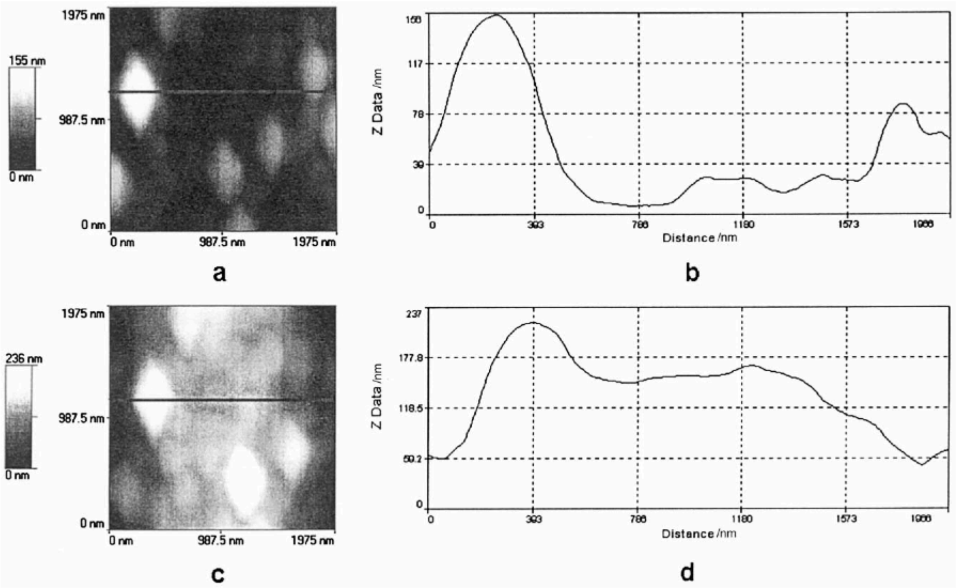

Figure 6.3: *In-situ* AFM images (left) and cross sections (right) of the topographic changes induced by the expansion during the first step of reduction of fresh PPy film, when the potential was switched from (a, b) 200 to -800 mV and from (c, d) -800 mV to 200 mV. Potentials are given vs. SCE. From Suárez *et al.*[17]

Smela *et al.*[18] presented an EC-AFM study on PPy/dodecylbezene sulfonate (DBS) film actuation. PPy/DBS films with a thickness of about 1.5 µm were prepared on gold electrodes. The electrodes were patterned so that rectangular shaped films were obtained with widths ranging from 10 to 30 µm. A line across the width of a rectangle was selected and AFM images were taken along this line while cycling the potential applied to the polymer in 0.1 M NaDBS. Figure 6.4 summarizes the results obtained. It was observed that a 60-100% volume change occurs during the first reduction/oxidation process but only a 30-40% volume change was observed thereafter. The change in volume is due to the exchange of solvated cations between the polymer and the electrolyte during the redox process. The first redox process stabilizes the polymer and the amplitude of actuation remains constant after this initial change in volume.

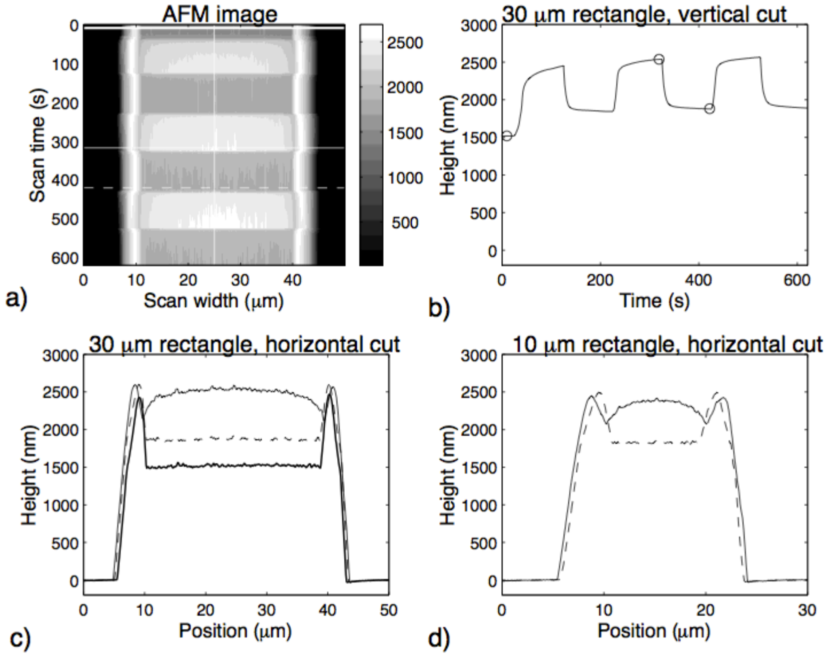

Figure 6.4: a) AFM image obtained from a patterned PPy rectangle nominally 30 μm wide at 0.825 Hz from voltage steps: 0V, 20s ; ±1V, 100s; 0V, 100s; ±1 V, 100 s; 0 V, 100 s; etc, b) Vertical cut at the position of the vertical white line in a) showing the change in height of the PPy over time, c) Horizontal cuts at 0 V before cycling (heavy line) and for applied potentials of ±1 V (solid line) and 0 V (dashed line) corresponding to the white lines in a) and circles in b), d) Horizontal cuts as for c) but for a narrower, 10 μm wide rectangle. From Smela *et al.*[18]

Higgins *et al.*[5, 19] studied PPy films actuation using EC-AFM. They electropolymerized PPy/PSS onto gold electrodes which were placed under the AFM for actuation monitoring[19]. It was found that actuation amplitude was dependant on film thickness and cycling speed. In order to assess reproducibility of actuation of several cycles, cyclic voltammetry was used. Figure 6.5 presents typical AFM images observed for a 3 μm film at different scan rates and corresponding height profiles. The strain and strain rate are used here as a way to compare films more efficiently than just regarding the actuation amplitude. The strain is the ratio between the actuation amplitude and the film thickness. It was found here that the thinner the films, the higher the strain was. Values of 350% have been reported for film thicknesses below 100 nm. Finally, it was concluded that the strain limitation in thick films was probably due to the film structures and properties, such as porosity and ionic conductivity.

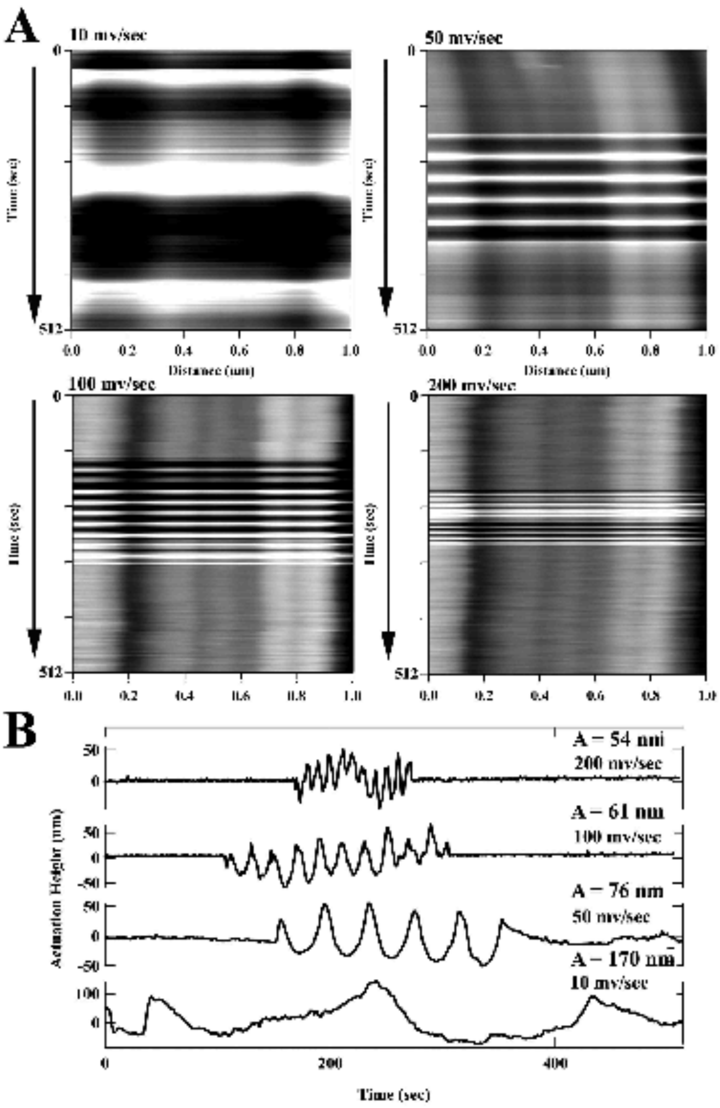

Figure 6.5: (A) ECAFM height images of the PPy/PSS film in 0.05 M NaPSS during CV (CV) measurements performed with an applied potential ramping from -500 to +500 mV at 10 mV/s (2 cycles), 50 mV/s (5 cycles), 100 mV/s (10 cycles), and 200 mV/s (10 cycles). The frequency and time over which the cyclic height changes occurred in each image correspond to the CV cycle number and scan rate. (B) Cross sectional height profiles taken vertically through each image showing the actuation height changes. The mean peak-to-peak actuation height, A, is given above each corresponding height profile. From Higgins *et al.*[19]

In a more recent paper, Higgins *et al.*[5] reported AFM studies on PPy thin films with different dopants. The roughness of the films, Young's moduli and actuation properties are presented. It was found that the films with the smallest

Young's modulus (doped using chondroitin sulfate A and poly(2-methoxyaniline-5-sulfonic acid)) had the highest strain of all studied films (Figure 6.6).

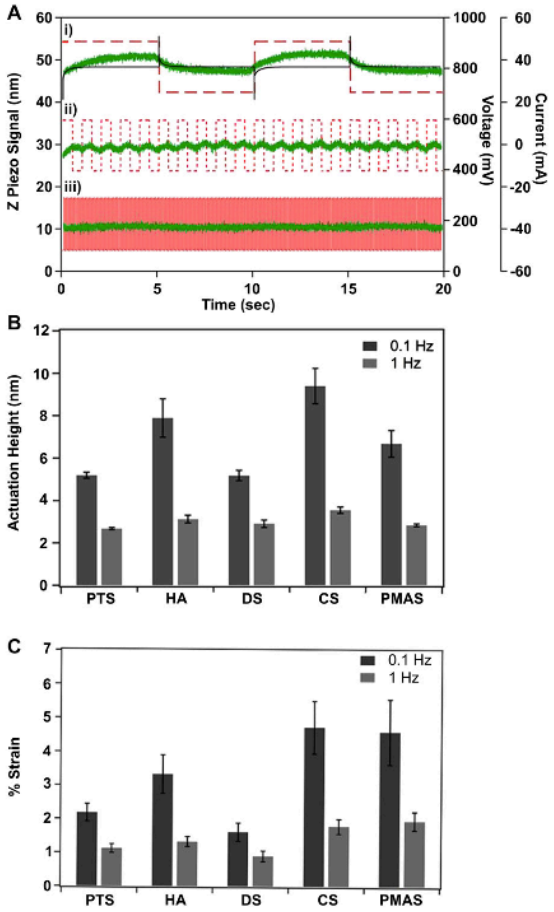

Figure 6.6: A. Example of PPy/CS data for biphasic waveform stimulation and actuation with different frequencies. Red dashed line represents the voltage signal, green thick line represents the Z-piezo signal and black thin line represents the current signal; i) 0.01 Hz; ii) 0.1 Hz; iii) 1 Hz. B. Histogram of mean actuation height for 0.1 and 1 Hz stimulation. C. Histogram of mean% strain for 0.1 and 1 Hz stimulation. All error bars are standard error. From Higgins *et al.*[5]

6.1.2 SUMMARY

EC-AFM is therefore the technique of choice to investigate actuation of electroactive polymer due to its high resolution and 3D-topography capabilities. PPy was shown to actuate with large amplitude for the first actuation and that actuation amplitude remained constant thereafter.

In addition, it was shown that dopant and film thickness influenced greatly the actuation mechanism of electroactive polymer.

In this chapter, growth of a microstructured PANI monolith in CD2 microchannels is demonstrated. The interaction monomer/template is shown to govern the final PANI structure. A PPy inverse opal within this microfluidic channel is also demonstrated and structural optimization is performed to investigate actuation of PPy inverse opals in microchannels by AFM.

Finally, an AFM study reveals that potentially unidirectional deformation of the PPy inverse opal structure occurs when applying a reduction potential to a PPy/DBS inverse opal films due to geometric restriction.

6.2 POLYANILINE MICROSTRUCTURES IN MICROCHANNELS

6.2.1 COLLOIDAL CRYSTALLIZATION IN MICROFLUIDIC CHANNELS

As discussed in chapter 5, the first step towards a microstructured monolithic microchip is the fabrication of a colloidal crystal within a microfluidic channel to use as a template for electroactive polymer growth. Colloidal crystallization in microfluidic channels is well documented[20-23] and the most common technique for this involves the use of capillary action that can be induced in microchannels (<200 μm). Typically one opening of a microchannel is immersed in the colloidal suspension. The opening at the other end of the microchannel must remain in open above the level of the suspension. The channel fills due to capillary action induced by the channel dimensions and channel walls' hydrophilicity. Evaporation induced self-assembly, as described in Figure 6.7, was used to pack the microfluidic channel in CD2. However, the gold-sputtered channel created an energy barrier that the capillary action could not overcome initially. Only the bare cleaned glass channel was successfully packed with a colloidal crystal. Cleaning the gold with UV-ozone plasma did not overcome the energy barrier issue. A prewetting step was introduced before crystallization in order to improve wettability of the gold-modified channel, thus the channel was first completely dipped in deionized water. The prewetting of the channel before immersing in colloidal suspension enabled capillary action to be induced over the whole length of the channel.

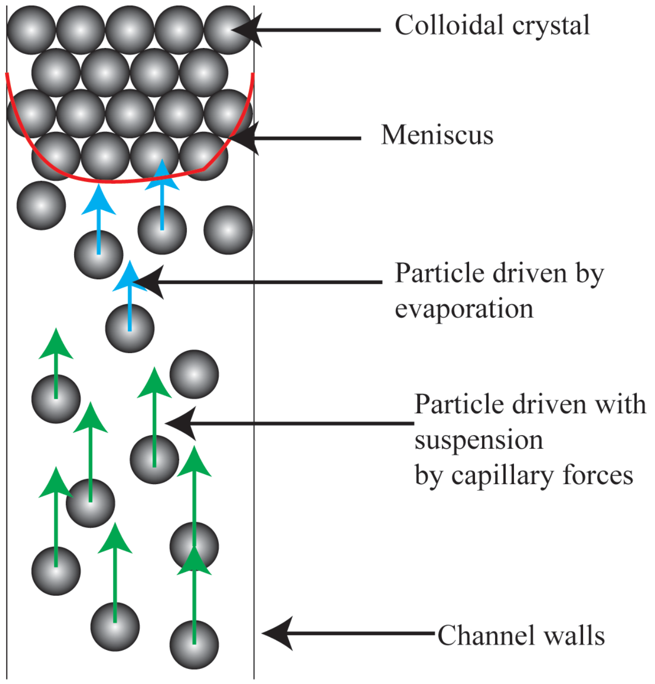

Figure 6.7: Schematic of colloidal crystallization mechanism in microfluidic channels.

Figure 6.8 shows a photograph of a typical microfluidic channel containing a colloidal crystal grown using this technique. The red/pink tint on the colloidal crystal is due to the diffraction of the light. This diffractive property indicates formation of a high quality crystal. The quality of the crystal was confirmed by SEM imaging. Typical SEM images of the PS colloidal crystals formed are shown in Figure 6.9. It can be seen that the crystal formed was polycrystalline (Figure 6.9-A and B) and FCC with the (1,1,1) plan parallel to the bottom of the channel. This result matches the structure that was observed for the colloidal crystallization in CD1. However, this method was more facile and rapid and resulted in more reproducible thicknesses of crystals than those observed previously in CD1 (Chapter 5, Section 5.2.3). In the larger channels (CD1), colloidal crystal thicknesses could not be controlled and therefore, crystal reproducibility was not possible. In CD2 microchannels, however, the crystal thickness was equal to the channel depth (Figure 10-A) and could be easily reproduced.

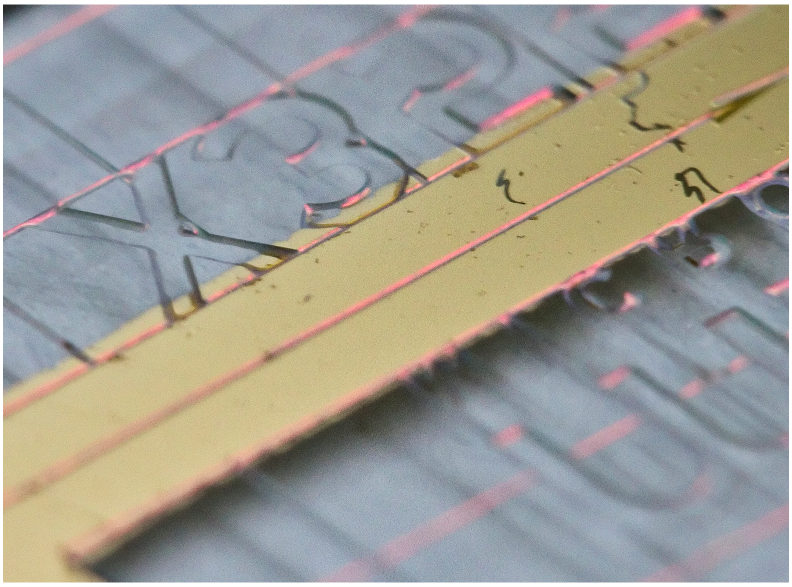

Figure 6.8: Photograph of the PS colloidal crystal grown in microfluidic channel using capillary action to drive the crystallization from a 1% (w/v), 1 μm PS beads suspension.

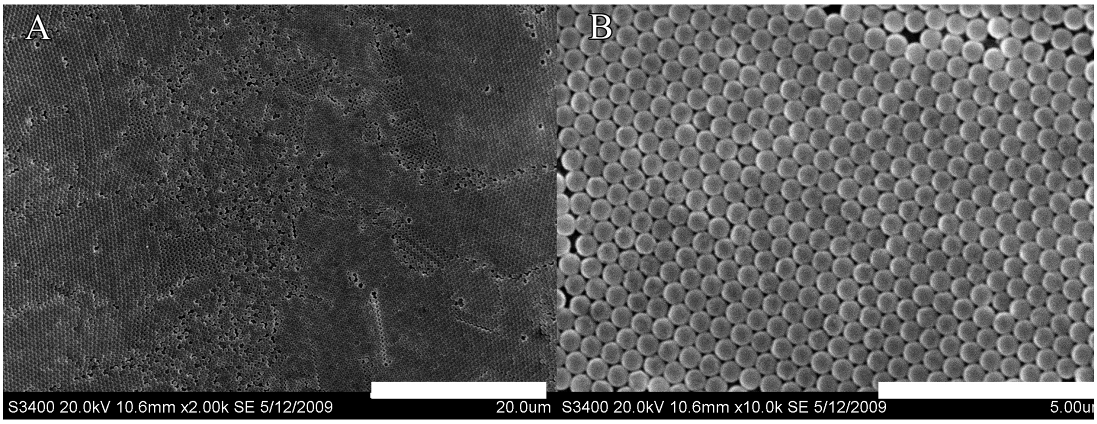

Figure 6.9: SEM images of colloidal template formed in CD2 using capillary action directed self-assembly of 1 μm, 1% (w/v) PB bead suspension. (A) Magnification, 2,000; scale bar: 20 μm and (B) magnification: 10,000; scale bar: 5 μm.

From Figure 6.10-A, it was observed that the base of the colloidal crystal was not in contact with the substrate and so a void existed between the part of channel walls and the crystal. This was attributed to a shrinkage of the crystal during the last stage of its drying process. The interparticle attraction increased when drying the last meniscus remaining between particles, thus leading to a shrinkage. These voids were due to shrinkage forces with a direction perpendicular to the channel wall. Because of the narrow width of the channel, these forces were small and, as a consequence, did not lead to cracking of the colloidal crystal. Maximum shrinkage was observed at the bottom of channel, possibly due to the heat conductivity of glass during the drying process. In Chapter 5, it was shown that cracks appeared in the crystals fabricated in CD1 (*i.e.* large channel) due to shrinkage in the final stage of colloidal crystal drying process. In the microchannel of CD2, cracks also appeared (albeit to a lesser extent) for the same reason. The cracks were in the confined space of the channel and perpendicular to the channel walls, which indicates that the shrinkage forces parallel to the channel walls were important and were responsible for the cracking of the colloidal crystal (Figure 6.10-B).

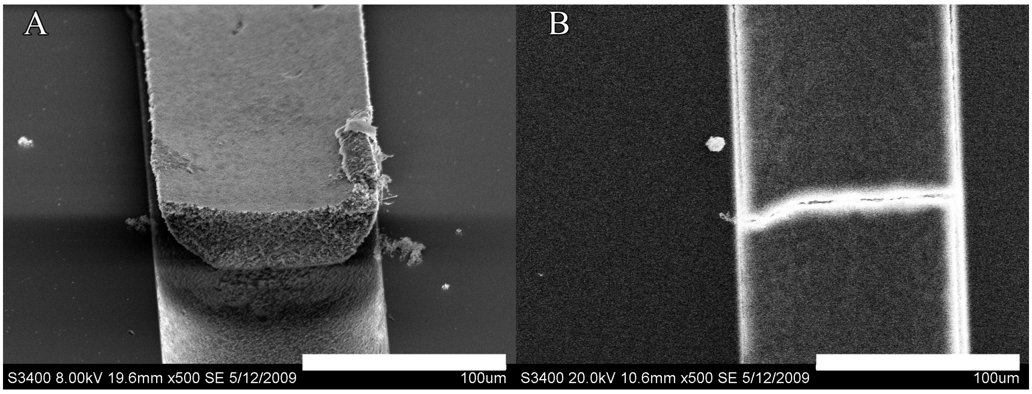

Figure 6.10: Typical SEM images of colloidal crystals grown in CD2 using capillary action directed self-assembly of 1 μm, 1% (w/v) PS bead suspension. Magnification: 500; scale bar: 100 μm.

When the colloidal crystal was immersed in aqueous solution, *i.e.* in the aniline monomer solution, it was observed that the colloidal crystal detached from the channel walls indicating a low adhesion force between the substrate (glass, gold) and the crystal. To stabilize the crystal, colloidal crystal-modified chips were heated to 100ºC and 110ºC, respectively for 30 min. By heating the crystal to just above the glass transition temperature (Tg), a sintering of the crystal occured[24, 25], bonding the beads together as well as on the surface. After heat treatment, the colloidal crystal remained in the channel when immersed in the monomer mixture. SEM imaging was used to ensure voids remained between the colloidal beads so that PANI and PPy could be polymerized through the template (Figure 6.11). At 100ºC (Figure 6.11A), voids between the beads were observed and a material could be grown within the space of these voids. However, at 110ºC (Figure 6.11B), complete sintering of PS beads occurred and no voids remained, indicating that PS existed as bulk, non-porous material and therefore no material could be microstructured using 110ºC as sintering temperature.

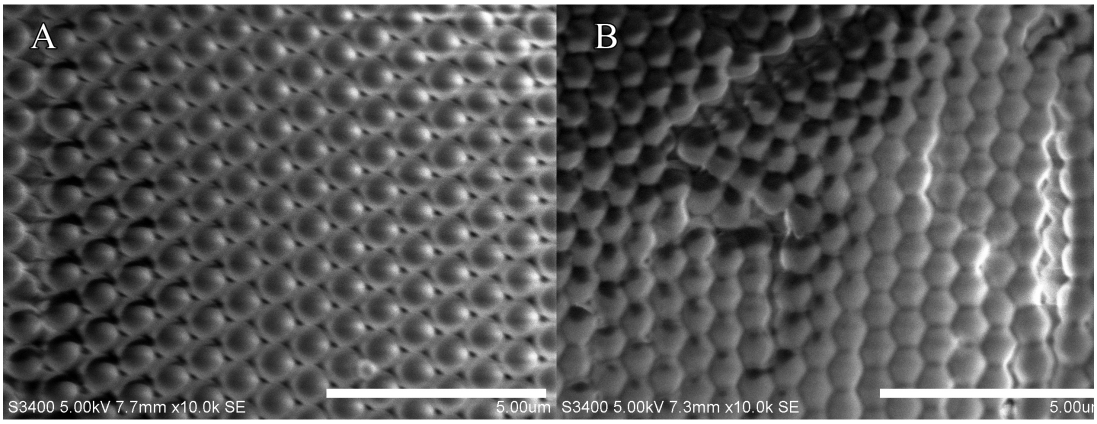

Figure 6.11: Colloidal crystal sintered at (A) 100ºC for 30 min and (B) 110ºC for 30 min. (Magnification 10,000; scale bar: 5 μm)

6.2.2 POLYANILINE MICROSTRUCTURES IN CLOSED MICROCHANNELS

After sintering of the colloidal crystal template, the upper and base pieces of CD2 were bonded. The aniline monomer solution was pumped through the colloidal crystal which was modified to prepare for polymerization. However, due to the small size of the PS beads used (1 μm) for the colloidal crystal formation and hence the high flow resistance of the colloidal crystal (Darcy's law, see Chapter 3, Section 3.2.2.2), a very high backpressure was needed. The microfluidic chip could not withstand such a pressure and leakage points appeared at the channel inlet despite the use of the chip holder. The growth of PANI within a closed channel was compromised. Larger beads (3-5 μm) would be needed to be able to achieve a flow of monomer solution through the colloidal crystal-modified microchannel. However, commercially available beads with diameters > 1 μm are poly(styrene-co-divinyl benzene) where divinyl benzene acts as a cross-linker. These highly cross-linked polymer beads cannot be dissolve in toluene, chloroform or acetone and therefore this approach could not be utilized for this project.

As an alternative it was decided to grow the PANI in an open channel configuration, *i.e.* prior to chip bonding. The base piece was immersed in monomer mixture (0.2 M aniline in 1 M HCl) and polymerized for 5, 15, 30 and 60 min at +900 mV *vs.* Ag/AgCl. The beads were then dissolved from the monolith in toluene overnight. Typical SEM images of the inverse opal structures observed for each of the polymerization times are shown in Figure 6.12.

From Figure 6.12, four observations can be made. First, the thickness of the PANI film increased with increasing polymerization time. 30 min polymerization time was needed to complete the polymerization of inverse opals within the channel. However, as seen in Figure 6.12C the PANI inverse opal structure was not bonded to the channel walls, which could create channeling when performing separation using this monolith. However, when a thin film of PANI was grown, *i.e.* polymerization time < 5 min, the PANI inverse opal film seemed to be bonded to the channel walls (Figure 6.13) as no voids were observed between the channel walls and the PANI film. SEM imaging requires samples to be dry. However, during the drying process, the polymer can shrink[26]. When the thickness of the polymer is increased, the shrinkage forces became more pronounced and so for polymer thicker than 10 μm, a delamination of the polymer from the channel walls was observed. However, when wet, it is expected that the polymer expands and so no voids between the channel walls and the monolith should exist. However, this has not been investigated for this project.

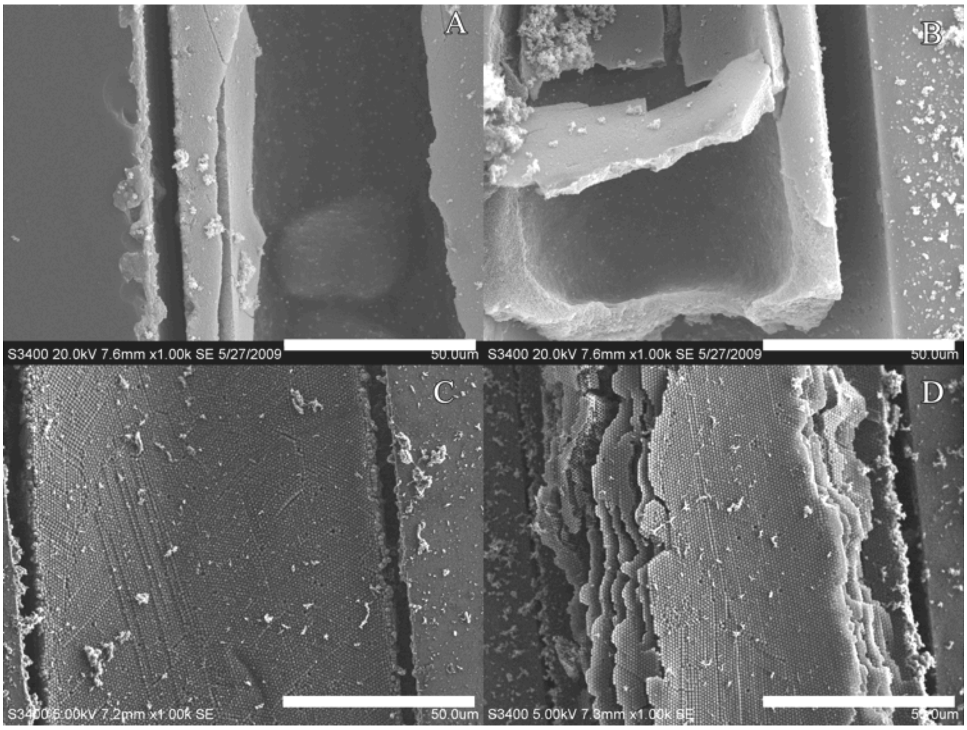

Figure 6.12: PANI inverse opals prepared from 0.2 M aniline solution in 1 M HCl potentiostatically at +900 mV vs. Ag/AgCl for (A) 10 min, (B) 15 min, (C) 30 min, (D) 60 min. (n=10) (Magnification: 1,000; Scale bar: 50 µm).

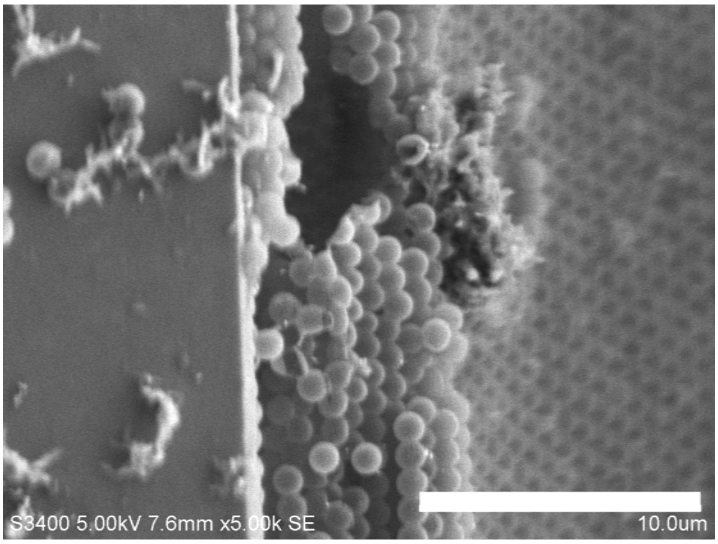

Figure 6.13: Channel wall/PANI inverse opal monolith interface. Polymerization: 5 min at +900 mV *vs.* Ag/AgCl. (Magnification 5,000; scale bar: 10 µm)

Secondly, no thick film was observed outside of the channel. As the full base of the chip was sputtered with gold, a uniform growth of the polymer in and out of the channel was expected. However, the PANI seemed to grow preferentially inside the channel. In Figure 6.12, little or no PANI growth was observed outside the channel. After polymerization, when rinsing the microchips with deionized water, any PANI formed outside the channel was removed. This showed the lack of adhesion of the film in this area. In the channel however, the colloidal crystal template provided a scaffold for the growth of PANI. The template acted as a supporting material, thus enabling the growth of 3-dimensional PANI monoliths.

Thirdly, it was evident the PANI did not grow uniformly from the channel walls into the centre. Instead, it grew from the channel walls as expected, but also “capped” the channel (Figure 6.12B and 6.14) by growing across the channel at the highest point in the channel. Figure 6.14 shows a cross section of an inverse opal PANI monolith grown for 10 min at +900 mV *vs.* Ag/AgCl where the PS template was removed. Fom Figure 6.14 it is clear that a PANI film grew across the channel, “capping” it. The growth of this “cap” was maybe due to higher current densities at the sharp channel edges. In addition to the higher current densities, the template provided the physical support needed for the growth of PANI from these edges. Moreover, monomers diffusing from the bulk solution to the electrode surface encountered polymerization sites at these edges and likely reacted there, as the diffusion through the template could prove difficult.

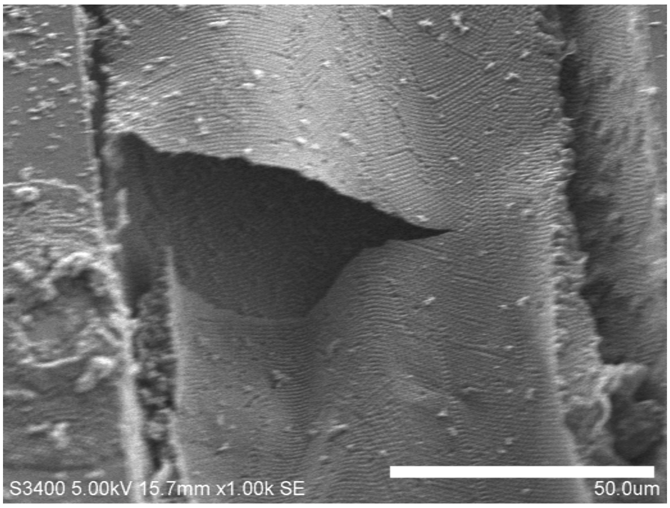

Figure 6.14: Cross section of the microfluidic channel “cap” made after 10 min polymerization of aniline at +900 mV *vs*. Ag/AgCl.

The last two observations, preferential growth in the channel and “capping” of the channel were observed by polymerizing aniline in the channels without the template. As shown in Figure 6.15, the polymerization of aniline for 30 minutes resulted in polymer growth over the complete base of the chip. There was no preferential growth in the channel as the surface in the channel and on the remaining chip are equivalent. Thus it can be concluded that the reason for preferential polymerization in the channel was the PS template. Without the template, the thickness of the PANI film was 5 ± 2 µm (average over 10 measurements in one channel) whereas when template was present, the channel was full so a thickness of 55 µm was achieved (Figure 6.12C). The thickness of the film grown without template was estimated by SEM measurements (Data not shown). The width of the remaining empty channel was measured by focusing on the PANI grown outside the template. The width of the remaining empty channel was therefore out of focus and was measured. Bare channel width being 110 µm, the thickness of the PANI film was then calculated.

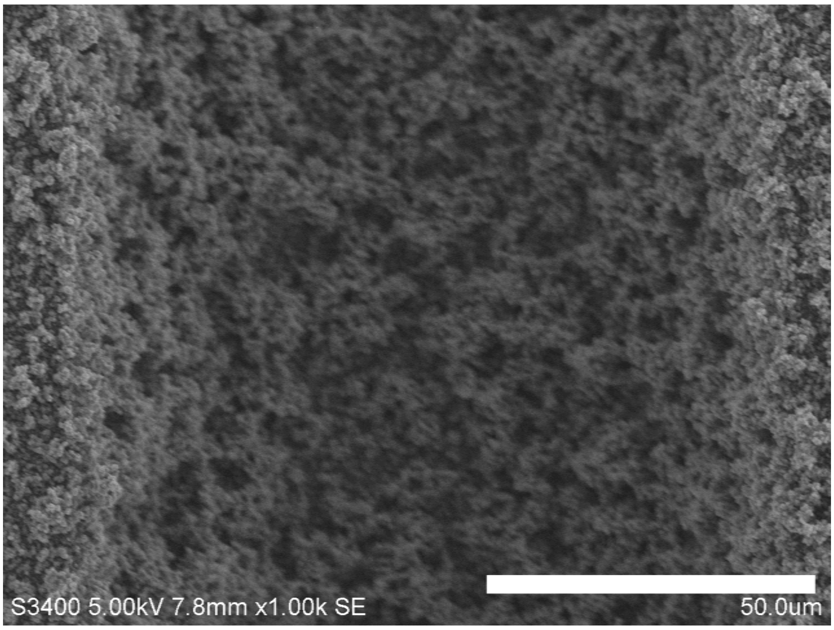

Figure 6.15: PANI polymerized 30 min at +900 mV *vs.* Ag/AgCl in the channel without template.

Finally, it was observed from Figure 6.12D that when aniline was polymerized for excessive periods of time, the inverse opal structure detached from the channel to allow for continued growth of bulk polymer to the channel walls. One may have expected the newly formed polymer to grow on top of the inverse opal structure. Polymer grown on top of the inverse opal structure may have been washed when rinsing the chip with deionized water or polymerization of aniline may not have been possible due to reasons of prohibitive resistivity or energetics. Thus, polymerization of polymer continued at the channel walls and not on top of the structured polymer. Figure 6.16 confirmed that the polymer growth at the channel walls after 60 min of polymerization had a bulk morphology and was is not micro-structured.

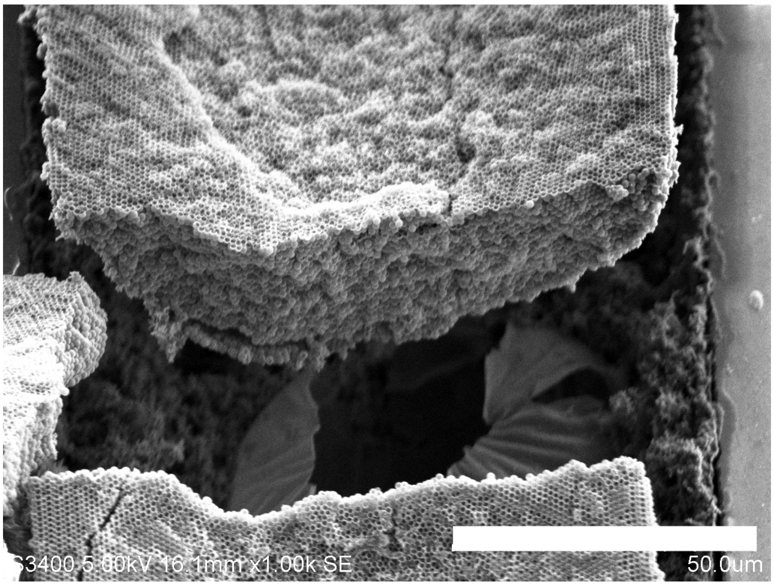

Figure 6.16: Inverse opal PANI monolith polymerized for 60 min at +900 mV *vs.* Ag/AgCl with PS template removed. (n=10) (Magnification: 1,000; scale bar 50 µm)

It is possible that polymer did grow directly on top of the templated polymer but this was removed when the chip was rinsed with deionized water. However, the polymer that grew at the gold modified channel walls was more stable and remained adhered to the walls after washing. The bulk polymer chains may have interpenetrated the polymeric chains of the microstructure polymer as microstructured polymer remained in the channel after washing.

The electrochemical behavior of the microstructured polymer was the same as demonstrated in Chapter 4 (data not shown). Indeed, it was only a PANI/PS composite on a gold electrode as it was polymerized prior to chip bonding and its electrochemical behavior could only be assessed before dissolving the PS template as silver-loaded epoxy glue dissolved in toluene, thus dissolving the silver loaded epoxy glue making the electrical connection.

PANI was grown as a microstructured monolith in the channel using a 30 min polymerization time as optimum. When the base and upper pieces of the chip were bonded and deionized water pumped through using a syringe pump, no flow could be achieved through the monolith. When looking at an SEM image of an area of the monolith where a crack perpendicular to the sidewalls of the microchannel was in the template (Figure 6.17), no flow-through pores existed; hence no flow could be achieved. The PS beads used for fabricating the template are negatively charged and, as shown in the previous chapter and demonstrated by Luo *et al.*[27], the electrostatic interactions between the monomers, oligomers and polymer drive the polymerization around the beads. Hence, at both ends of the inverse opal PANI monolith as well as throughout the bulk structure in the template cracks, the polymer grew according to electrostatic interaction around the beads so that no flow-through pores could exist, thus completely impeding flow.

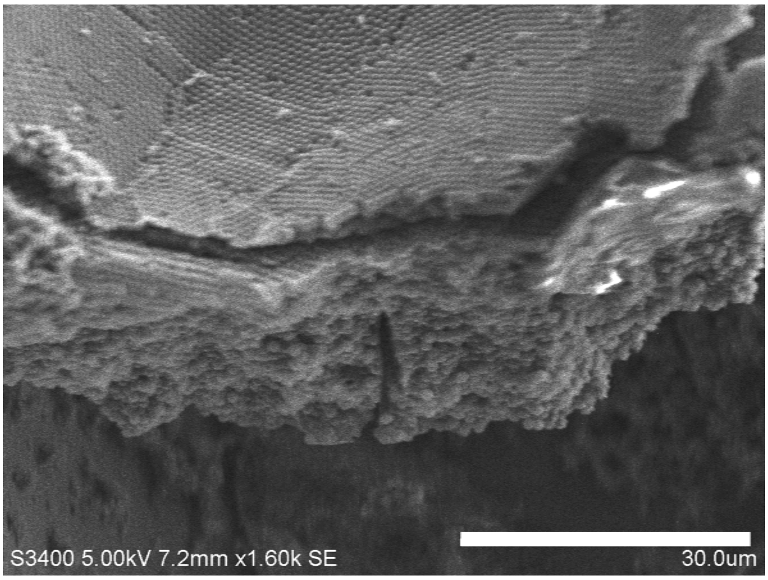

Figure 6.17: SEM image of an area of PANI inverse opal monolith grown for 30 min at +900 mV vs. Ag/AgCl. Area shown is where polymer was grown at a crack in the template. (n=10) (Magnification: 1600; scale bar 30 µm).

6.3 POLYPYRROLE MICROSTRUCTURES IN MICROCHANNELS FOR EC-AFM ANALYSIS

In order to monitor the actuation of conducting polymers by AFM in microchannels, PPy was used instead of PANI for two reasons. First, PPy is electroactive at neutral pH and does not need acidic media for switching. Thus EC-AFM can be used without any risk of damaging the AFM head due to acidic vapors, which could corrode electronic components. Secondly, its actuation/volume changes in response to applied potential are greater than with PANI so any changes in structures, heights, *etc* should be easier to detect.

For the AFM study, the sample was required to be as smooth as possible in the macro-scale as AFM (± 2 µm) cannot record large variations in height. In addition, the polymer thickness needed to be small (< 5 µm) in order to be able to lower the AFM cantilever into the channel without interference from polymer grown from the channel sidewalls.

Pyrrole was polymerized through a PS bead colloidal crystal template fabricated as discussed in Section 6.2.1 by electropolymerizing pyrrole (0.2 M in 5.7 mM NaDBS) at +850 mV *vs.* Ag/AgCl. In this section, the dopant and time effect on the growth and resulting morphology of the templated polymer were assessed.

Firstly, the effect of polymerization time was studied for PPy/DBS. PPy/DBS was polymerized in the channel, through the PS template for 5, 10 and 15 min. The PS template was subsequently removed. Figure 6.18 shows typical SEM images for the PPy monolith grown for the three different polymerization times. After 5 min, large PPy/DBS islands were visible (Figure 6.18A) but the monolith was not homogeneous as bare gold was still observed. After 10 min polymerization, the sample thickness became more homogeneous in some places (Figure 6.18B) and the inverse opal structure was shown to possess interconnecting pores (visual assessment of images). However, reproducibility was an issue, film thicknesses were not reproducible and homogeneous when PPy/DBS was polymerized for 10 min. Triplicates of the 10 min polymerization displayed structures, similar to the one showed here for 15 min polymerization (Figure 6.18C). However, image quality was poor and was not shown here. The globular structure of PPy/DBS, as shown in Figure 6.18-C was similar to that reported elsewhere[5]. This was the typical structure, which could not be imaged by AFM because the film was too thick and large variations in the surface topology existed.

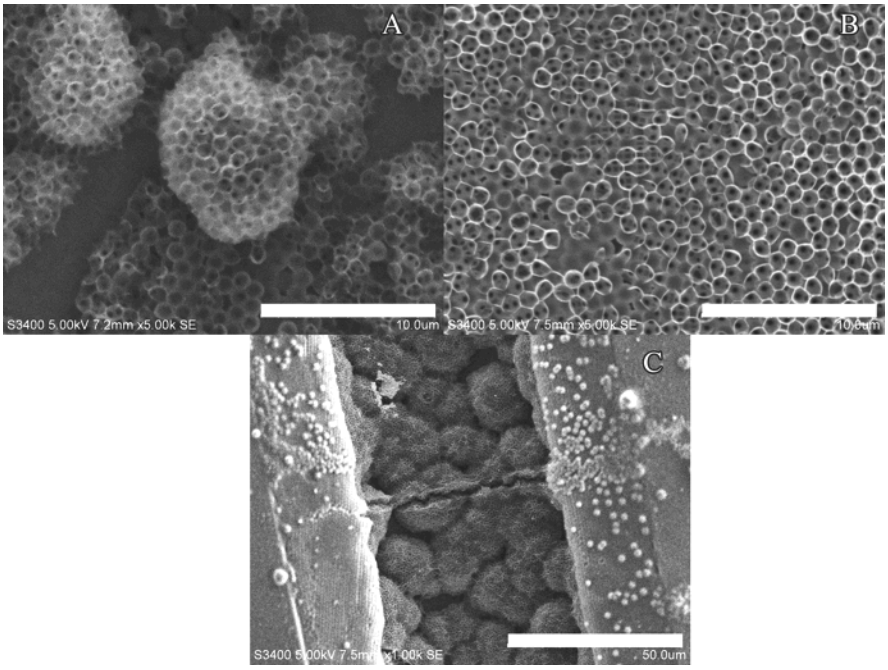

Figure 6.18: SEM images of PPy/DBS grown potentiostatically at +850 mV *vs.* Ag/AgCl for (A) 5min, (B) 10 min and (C) 15 min. Magnifications: (A) and (B) 5,000; (C) 1,000. Scale bars: (A) and (B) 10 µm, (C) 50 µm.

None of the above structures met all requirements for AFM imaging. To polymerize more homogeneous polymers, the rate of polymerization was decreased by using a two-fold decrease in the monomer concentration so that a 0.1 M pyrrole solution was employed. However, with DBS as dopant, the globular structure remained (Data not shown). The dopant used was changed from DBS to *para*-toluene sulfate (PTS). As demonstrated by Higgins *et al.*[5] a similar structure to DBS was obtained, *i.e.*, a globular structure at long polymerization times, or islands of PPy when short polymerization times were used (Data not shown).

PSS was also investigated as a dopant. It was shown in Chapter 5 with PANI that the diffusion of this dopant through the PS beads template prohibited fast polymerization. However in an effort to obtain even polymer thickness, PSS was explored in this instance. Figure 6.19 shows typical SEM images of PPy/PSS grown for 5 and 10 min. After 5 min, a sub-monolayer of PPy was grown due to the slow rate of polymerization that resulted from the slow diffusion of large polyelectrolyte molecules through the template and this sub-monolayer was homogeneous. After 10 min, a PPy film with a homogeneous thickness was polymerized to the channel surface. This PPy coating met all the requirements for the AFM study, namely low film thickness, homogeneous, inverse opal structure and good structural reproducibility. PPy/PSS grown for 10 min at +850 mV *vs.* Ag/AgCl, was, therefore, suitable for the AFM study of conducting polymer actuation in microchannels.

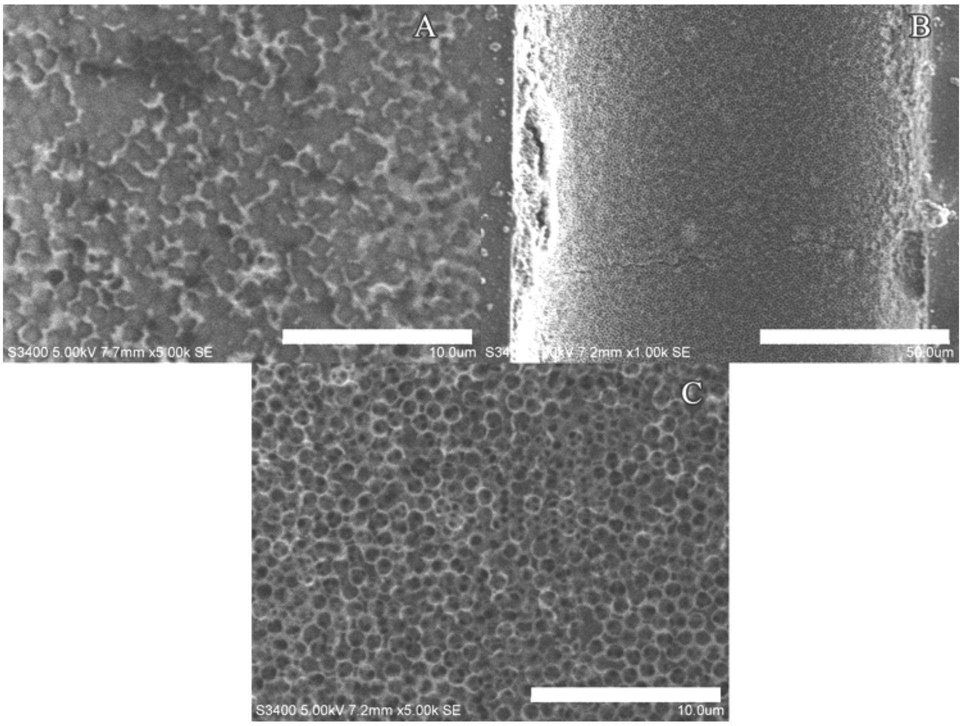

Figure 6.19: SEM images of PPy/PSS polymerized at +850 mV *vs.* Ag/AgCl for (A) 5 min and (B) and (C) 10 min. Magnifications: (A) and (C) 5,000; (B) 1,000. Scale bars: (A) and (C) 10 µm; (B) 50 µm.

6.4 AFM STUDY OF POLYPYRROLE ACTUATION

6.4.1 FEASIBILITY OF AFM STUDY IN MICROCHANNELS

A preliminary study of imaging of PPy in a microchannel using AFM was performed in air. All images presented in this section were taken in AFM tapping mode. Firstly, the tip and cantilever were carefully inserted into the microchannel with the cantilever being parallel to the channel wall. The cantilever and holder were lowered slowly to make contact with the polymer deposited on the channel surface taking care to ensure the AFM head, holding the tip and cantilever, was not in contact with the microchip. A 20 x 20 μm scan was then recorded (Figure 6.20). It can be seen that the scan was stopped after ~12 μm was imaged. The scan was stopped as the cantilever came into contact with the sidewall of the channels. It was subsequently found that a 10-15 μm zone in the centre of the channel could be imaged. To prevent excessive cantilever damage, the scanning zone was restricted to 7 x 7 μm to avoid issues caused by misaligning the tip with the channel centre.

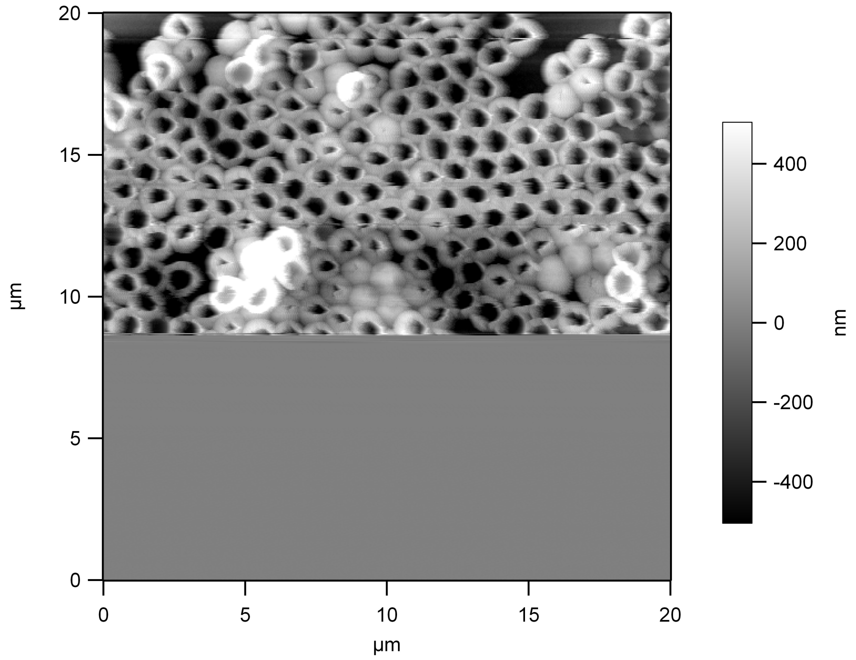

Figure 6.20: Partial AFM image of PPy/DBS inverse opals in the microchannel of CD2. Image taken in air in spot A (Figure 6.21).

Images could also be taken close to the sidewall where the polymer had grown. Using a 10 min electropolymerization time, 7 x 7 μm scans could be recorded close to the sidewalls without the tip "falling" into the channel. Figure 6.21 summarizes where images were taken in the microchannel using AFM.

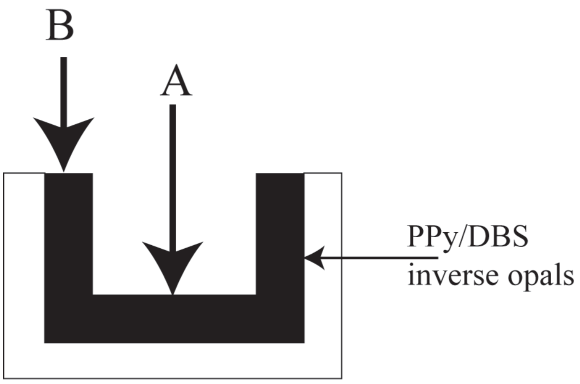

Figure 6.21: Schematic of AFM imaging spots: (A) center of the channel, (B) near the sidewall of the channel. Cross sectional view of the channel.

Imaging conditions were optimized to obtain the best tracking of the surface. It was found that a medium stiffness cantilever was optimum for PPy surface tracking.

When an area of the PPy film with ordered inverse opals was identified (fraction of PPy inverse opal <10% over the length of the channel (30 mm)), scans were recorded (Figure 6.22 A). The height profile (Figure 6.22 B) was obtained following a line drawn using the software (Figure 6.22 A, red line). The pores were found to be 1 µm wide and 500 nm deep, corresponding to the expected inverse opal structure after replication of the PS colloidal crystal template (1 µm beads used). As opposed to what was found for PANI (Chapter 5, Section 5.3.3), no shrinking of the polymer was observed upon dissolution of PS beads in toluene. Figure 6.22 B also demonstrated the consistency of the pores and PPy skeleton sizes.

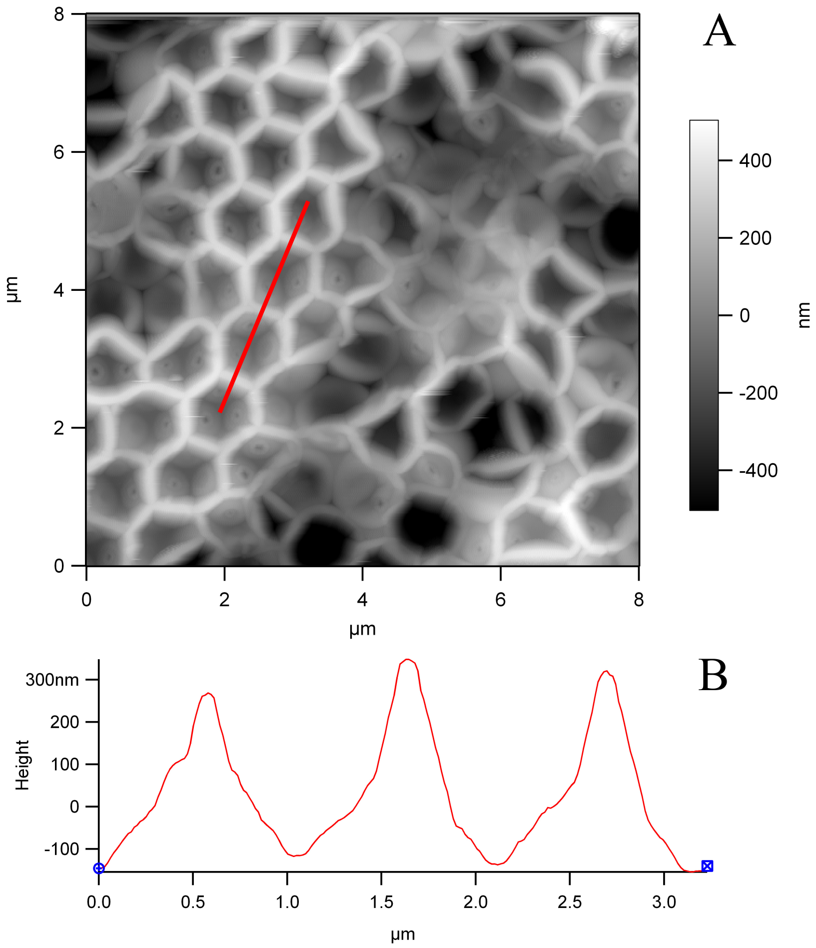

Figure 6.22: (A) AFM image of PPy/DBS in air and (B) height profile taken along the red line in (A). Image taken in air in spot A (Figure 6.21).

An electrochemical cell needed to be integrated on the base piece of the microfluidic chip in order to allow imaging in liquid while performing electrochemical switching of the polymer. The electrochemical cell was required to be leak free and could not be more than ~1.5 mm deep in order for the AFM tip holder not to contact the electrochemical cell. Two different designs have been used.

Firstly, a PDMS gasket (1 mm thick) 30 mm long and 15 mm wide, with a 2 cm long and 13 mm wide cut was fabricated and applied to the base piece surface to define the electrochemical cell. A leak test was performed using deionized water and no leaks were observed. However, on introduction of the AFM tip holder, the cell started leaking at the chip/gasket interface. When producing the base piece for CD2, Micronit etched a grid and their logo onto the chip. By capillary action, the electrolyte filled the etched grid underneath the PDMS gasket. On introduction of the AFM tip holder, the pressure exerted on the electrolyte forced liquid to flow from the etched grid, leading to leakage of the electrochemical cell.

Secondly, Blu-Tack was used to define the electrochemical cell. The Blu-Tack was capable of successfully sealing off the etched grid channel and could be shaped to any desirable shape. In addition, Blu-Tack helped to physically retain the auxiliary and reference electrodes in the cell.

The auxiliary electrode comprised of platinum mesh and the reference used was an Ag wire coated with AgCl from a commercial reference electrode (Figure 6.24). The tip of each electrode was slightly bent to contact the electrolyte while being maintained horizontally on the AFM stage.

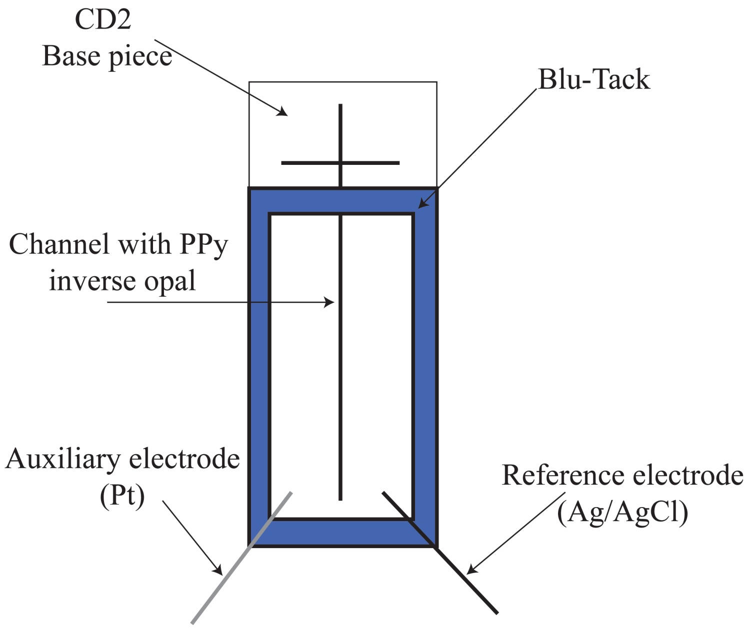

Figure 6.24: Schematic of electrochemical cell used for EC-AFM studies of PPy actuation.

6.4.2 POLYPYRROLE ACTUATION IN MICROCHANNELS

Once the imaging parameters and the electrochemical cell were optimized, a spot for imaging was identified. The imaging area was 7 x 7 µm and the length of the possible imaging area was about 1.5 cm. As the inverse opal quality along a single sample and among all samples was not uniform (as samples were prepared before optimization for AFM studies), identifying a suitable area for imaging was time consuming. In addition AFM imaging time was not insignificant – a scan took approximately 17 min. SEM was also used to map the high quality areas as it allowed rapid scanning of the whole sample and was therefore a more suitable technique to determine where AFM images should be taken.

Once a suitable imaging spot was found it was imaged using AFM in air, then immersed in electrolyte (NaDBS, 0.1 M). Figure 6.25 shows two images of the same area in air and in electrolyte. When moving from imaging in air to imaging in liquid the AFM tip holder was lifted up, the electrochemical cell was filled with electrolyte and the AFM head was lowered onto the surface again as close to the same spot as was possible.

From Figure 6.25, a swelling of the polymer upon addition of electrolyte was observed. During swelling, a rearrangement of the structure was observed. When the sample was dry, the structures collapsed and were revealed by the swelling occurring upon addition of electrolyte. The interconnecting pore diameter was calculated to be 150 ± 10 nm. The pore size observe in liquid remained the same as observed on Figure 6.22. However, the interconnecting pores in Figure 6.25 B were more clearly defined than in Figure 6.22 and the PPy walls observed around each pore decrease from approximately 200 nm in air to 100 nm in liquid, possibly due to the 3-dimensional PPy swelling.

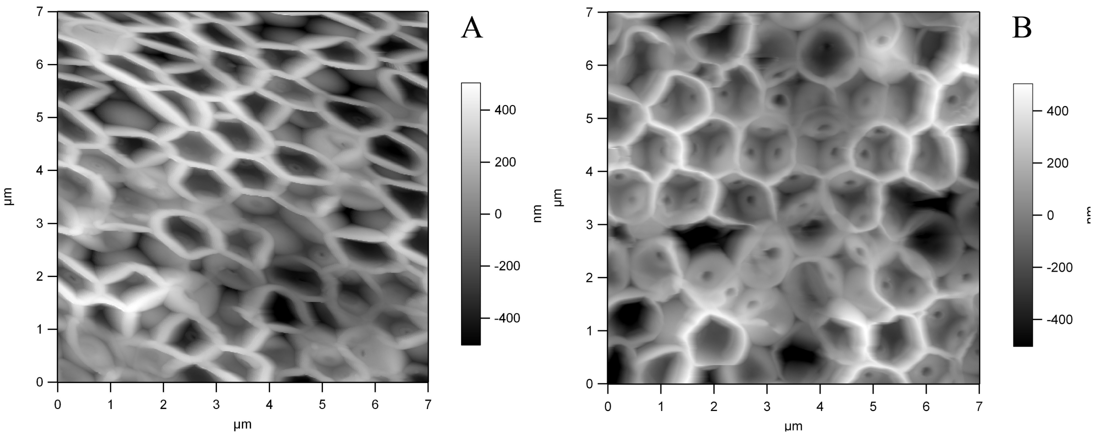

Figure 6.25: AFM images of PPy/DBS inverse opals taken in air (A) and in electrolyte (B). Image taken in spot A (Figure 6.21).

It was hoped that when employing the EC-AFM, the primary and interconnecting pores could be imaged during an actuation process. This would prove the potential for microstructured conducting polymers for dynamic, electrochemically controllable stationary phases.

A line was chosen on Figure 6.25 B, and the area under the line was imaged while applying a triangular potential ramp to actuate the PPy samples. 10 cycles from 0 mV to -1200 mV at 20 mV/s were performed prior to imaging in order to stabilize the polymer actuation and to confirm redox peaks at -200 mV and -1000 mV (Data not shown). Figure 6.26 A shows the area (under the line) selected for the actuation imaging, and Figure 6.26 B shows the actuation of this line area over time. During the 17 min of image capture, 22 potential cycles were carried out. For each cycle, the topographic profile of the selected area was recorded in order to detect any changes in pore and interconnecting pore size. It could be interpreted that the interconnecting pores were opening and closing when the polymer was oxidized and reduced, respectively (Figure 6.26 B). However, by recording the height of the piezo-electric crystal over time, a correlation was found between the height and the potential sweep wave (data not shown). As the polymer actuated, the thickness of the polymer was varied (change in polymer volume), which could also explain the change in piezo-electric crystal height. However, as discussed by Higgins *et al.*[19] the influence of the electrical field from the electrochemical cell on the piezo-electric crystal cannot be neglected. In order to evaluate this influence, a scan was performed onto the flat non-polymer coated glass surface outside the channel. Changes in height were observed and were of the same order of magnitude as those observed on Figure 6.26 B (data not shown). The change in height observed in Figure 6.26 B was probably due to both PPy volume change and to the electrical field but it was not possible to isolate one phenomenon from the other.

In addition, an image was taken of the area of the PPy scanned during cyclic voltammetry study, while maintaining a constant potential at -1200 mV. This was carried out to confirm the loss of interconnecting pores when the polymer was in its reduced state. However, interconnecting pores were visible (data not shown) but this could have been caused by a loss in the redox properties of the polymer, and hence actuation properties of PPy, due to an over-reduction of the polymer at this potential. Redox transitions could not be visually observed by a color change in the polymer. No change in color was observed when applying the -1200 mV, which would signify the polymer was no longer redox active. This experiment would need to be carried out on a freshly grown polymer. This has not yet been carried out.

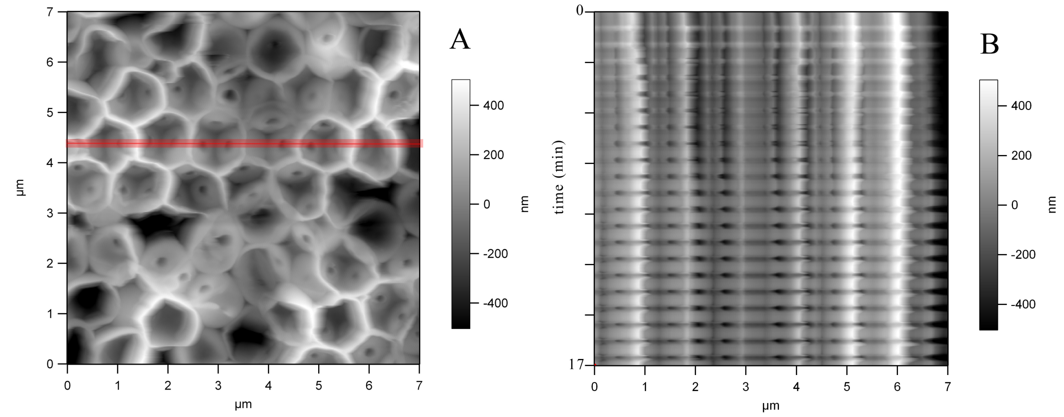

Figure 6.26: AFM images of (A) PPy/DBS inverse opals in electrolyte and (B) scan of the red line (A) during cyclic voltammetry.

To attempt to overcome the influence of the electrical field on the piezo-electric AFM crystal, images of the PPy in electrolyte were taken while maintaining constant potentials of 0 mV and -1200 mV. For each potential, the AFM tip was brought in “contact” with the PPy surface to ensure imaging of the surface without disturbing the piezo-electric crystal.

Figure 6.27 shows the same area imaged at (A) 0 mV and (B) -1200 mV taken in imaging spot A (Figure 6.21). When in its reduced state (- 1200 mV), it can be seen that the pores were anistropically deformed (Figure 6.27 B). The pore diameter in imaging spot A (Figure 6.21) remained 1 µm parallel to the channel wall but was reduced to about 200 nm in the direction perpendicular to the channel walls. Only a partial image could be observed because of the globular macrostructure of the PPy/DBS polymer. In a 1 µm wide area (perpendicular to the channel walls), 7 rows of pores can be seen whereas in its oxidized state (Figure 6.27 A), 7 rows of pores were seen in a 6 µm wide area. Therefore a 600% contraction in the direction perpendicular to the walls was observed.

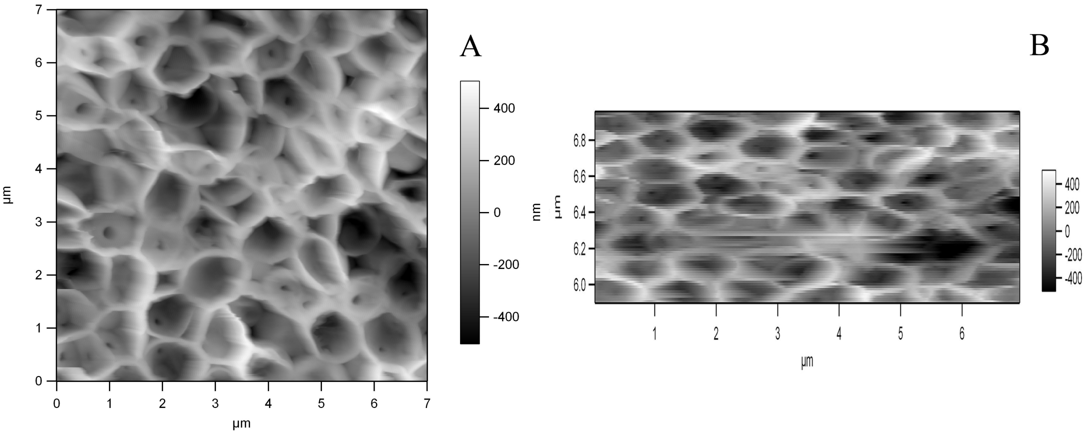

Figure 6.27: AFM images of the same spot of PPy/DBs inverse opals at 0 mV (A) and -1200 mV (B) *vs.* Ag/AgCl. Different scales on A and B.

In addition Figure 6.28 shows PPy/DBS “closed” inverse opals at the wall of the channel (Imaging spot B, Figure 6.21) at 0 mV (Figure 6.28 A) and -1200 mV (Figure 6.28-B), along with their height profile (Figure 6.28 C). The height profile in red and blue correspond to the red and blue line drawn on Figure 6.28 A and 6.28 B, respectively. In this instance, the height decreased when applying a reduction potential. This height decrease was attributed to an elongation of approximately 10% of the inverse opals perpendicular to the channel walls, observed when the polymer became reduced at -1200 mV (Figure 6.28 C). This provided more evidence that the polymer may be actuating primarily in a single direction, perpendicular to the walls of the channel.

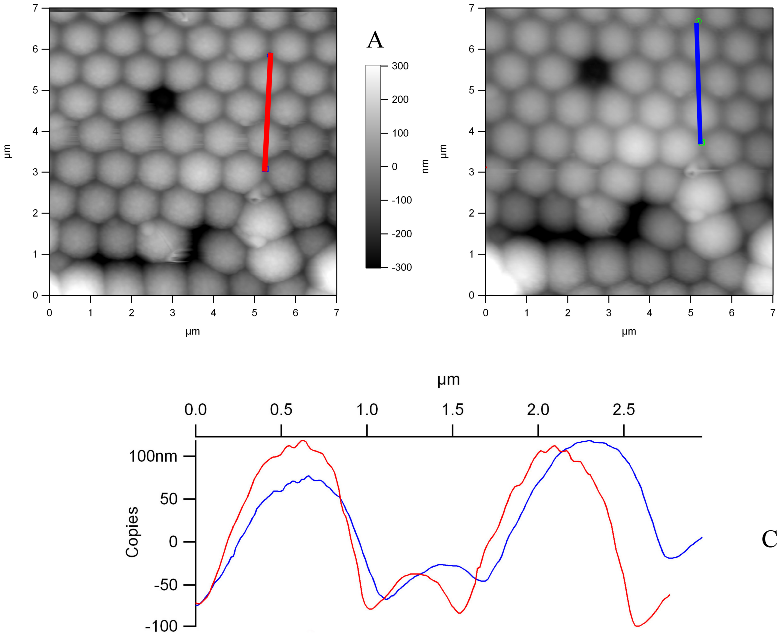

Figure 6.28: AFM images of the same spot of inverse opals situated at the channel walls at 0 mV (A) and -1200 mV (B) vs. Ag/AgCl. (C): height profile along the red line in (A) (red graph) and the blue line in (B) (blue graph).

It is believed that when a reducing potential was applied to the polymer, the volume increase that was observed was due to the intake of solvated cations. As the fluidic channel was not full, the void space available for expansion was the centre of the channel. The PPy deposited on the channel sidewalls (imaging spot B, Figure 6.21) may have pushed the polymer in the center of the channel from each side, thus, “squashing” the pores, leading to a anisotropic but maybe not uniform deformation of the pores situated in the centre of the channel (imaging spot A, Figure 6.21, Figure 6.27). A schematic of the proposed mechanism of PPy actuation in microfluidic channel is given Figure 6.29. Observed film delamination would tend to confirm this conclusion. After maintaining the potential at -1200 mV for a long time (> 30 min) the gold sputtered electrode and polymer film delaminated from the glass surface (observed with AFM microscope used to align laser on cantilever, Data not shown) on the channel walls and “rolled” towards the channel center as if the forces perpendicular to the channel walls created by the volume change during reduction were large enough to delaminate the gold electrode.

If this actuation mechanism is confirmed, this could have dramatic effects on separation when performed with stationary phase in its expanded form. This anisotropic pore deformation would create radial heterogeneities in the monolithic stationary phase and therefore, band broadening would be increased due to different flow velocities in the flow-through pores. The chip efficiency would, therefore, be decreased. However, change in pore size for the PANI monolith would probably not be to this degree as PPy actuation magnitude is greater than for PANI[15, 16].

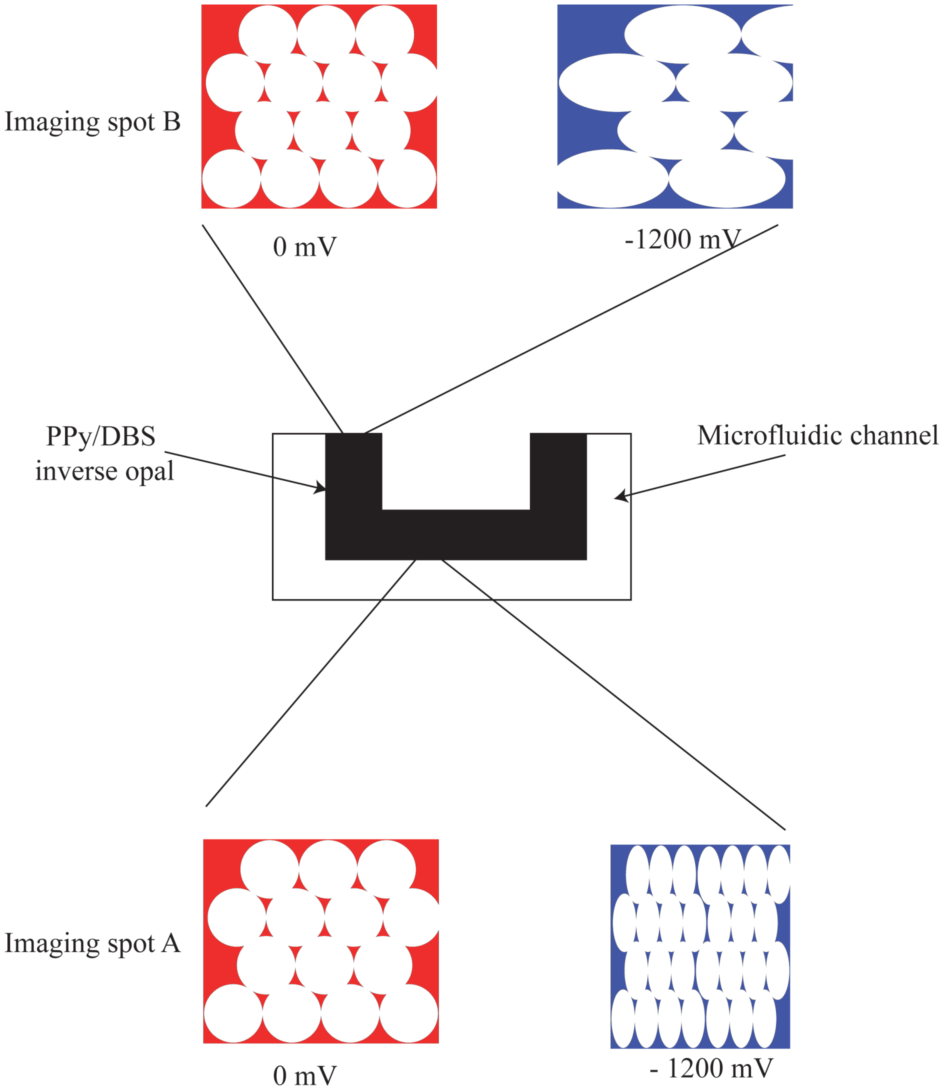

Figure 6.29: Schematic of proposed PPy/DBS actuation: (A) direction of volume changes (cross sectional view), (B) top view when the polymer is oxidized, (C) top view when polymer is reduced.

6.5 CONCLUSION

Colloidal crystals for microstructuring conductive polymers have been successfully grown in microfluidic channels in CD2 using capillary action as the driving force. Evaporation induced self-assembly was used to grow the colloidal crystals and capillary action supplied the crystallization site with PS beads. Crystals were of high quality and the thickness of the crystals was equivalent to the depth of the channel, so that no non-structured bulk polymer material should form during monolith fabrication.

However, very high backpressures were generated for the sintered crystals and thus no flow could be generated through the crystals. Therefore, electropolymerization of PANI in a closed channel configuration was not possible. When polymerizing the PANI inverse opal monolith in open channel configuration, no flow was achieved after chip bonding because of the template-monomer and oligomer electrostatic interactions. The polymer grew fully around the beads; therefore, no flow through pores existed at the entrance and exit of the channel where the monolith was present. Defects or cracks formed during colloidal crystallization drying stage also contributed to high backpressures as PANI fully coated the beads at the crack interfaces perpendicular to the sidewalls.

The effects of polymerization time, pyrrole concentration and dopant nature on its morphology were investigated in order to grow a thin film of an inverse opal PPy structure in the microfluidic channel for AFM study. However, the AFM study presented here was carried out before PPy structure optimization.

AFM was used to investigate the effect of PPy volume changes (actuation) on the pores sizes and shape during electrochemical switching. This was carried out to demonstrate the feasibility of an electrochemically switchable stationary phase for dynamic on-chip separations. It is possible that when electrochemically reduced PPy/DBS volume increased at the sidewalls of the channel, this caused the pores to anisotropically deform towards the centre of the channel, thus deforming pores present in the center in the opposite direction. The mechanism of actuation in the microchannels is still under investigation.

6.6 REFERENCES

1. Binnig, G.; Rohrer, H., *Reviews of Modern Physics* **1987,** *59* (3), 615.
2. *Atomic Force Microscopy - Biomedical methods and applications*. Humana Press: 2004.
3. Dong, H.; Cao, X.; Li, C. M., *ACS Applied Materials & Interfaces* **2009,** *1* (7), 1599-1606.
4. El, K. M.; Naggar, A. H.; Naranjo-Rodriguez, I.; Dominguez, M.; Hidalgo-Hidalgo, d. C. J. L., *Synthetic Metals* **2009,** *159* (5-6), 541-545.
5. Gelmi, A.; Higgins, M. J.; Wallace, G. G., *Biomaterials* **2010,** *31* (8), 1974-1983.
6. Hui, F.; Li, B.; He, P.; Hu, J.; Fang, Y., *ElectroChemical Communications* **2009,** *11* (3), 639-642.
7. Marandi, M.; Kallip, S.; Sammelselg, V.; Tamm, J., *ElectroChemical Communications* **2010,** *12* (6), 854-858.
8. Pelto, J.; Haimi, S.; Puukilainen, E.; Whitten, P. G.; Spinks, G. M.; Bahrami-Samani, M.; Ritala, M.; Vuorinen, T., *Journal of Biomedical Materials Research Part A* **2010,** *93A* (3), 1056-1067.
9. Gueizado-Rodriguez, M.; Lopez-Tejeda, M.; Escalante, J.; Guerrero-Alvarez, J. A.; Nicho, M. E., *Materials Chemistry and Physics* **2010,** *124* (1), 389-394.
10. Kuila, B. K.; Stamm, M., *Journal of Materials Chemistry* **2010,** *20* (29), 6086-6094.
11. Prakash, S.; Rao, C. R. K.; Vijayan, M., *Electrochimica Acta* **2008,** *53* (18), 5704-5710.
12. Singh, P. R.; Mahajan, S.; Rajwade, S.; Contractor, A. Q., *Journal of ElectroAnalytical Chemistry* **2009,** *625* (1), 16-26.
13. Sutar, D. S.; Tewari, R.; Dey, G. K.; Gupta, S. K.; Yakhmi, J. V., *Synthetic Metals* **2009,** *159* (11), 1067-1071.
14. Zhou, J.-z.; Weng, S.-h.; Lin, Z.-h., *Dianhuaxue* **2009,** *15* (3), 241-244.
15. Wallace, G.; Spinks, G. M.; Kane-Maguire, L. A. P.; Teasdale, P. R., Properties of Polypyrroles. In *Conductive Electroactive Polymers*, CRC Press: 2008, pp 103-136.

16. Wallace, G.; Spinks, G. M.; Kane-Maguire, L. A. P.; Teasdale, P. R., Properties of Polyanilines. In *Conductive Electroactive Polymers*, CRC Press: 2008, pp 179-196.
17. Suarez, M. F.; Compton, R. G., *Journal of Electroanalytical Chemistry* **1999,** *462* (2), 211-221.
18. Smela, E.; Gadegaard, N., *Advanced Materials* **1999,** *11* (11), 953-957.
19. Higgins, M. J.; McGovern, S. T.; Wallace, G. G., *Langmuir* **2009,** *25* (6), 3627-3633.
20. Kuo, C.-W.; Shiu, J.-Y.; Wei, K. H.; Chen, P., *Journal of Chromatography A* **2007,** *1162* (2), 175-179.
21. Lin, Y.; Herman, P. R.; Xu, W., *Journal of Applied Physics* **2007,** *102* (7), 073106/1-073106/4.
22. Miguez, H.; Yang, S. M.; Ozin, G. A., *Langmuir* **2003,** *19* (8), 3479-3485.
23. Miguez, H.; Yang, S. M.; Ozin, G. A., *Appied Physics Letters* **2002,** *81* (14), 2493-2495.
24. Qu, X.; Shi, Y.; Tang, Y.; Chen, L.; Jin, X., *Journal of Colloid and Interface Science* **2002,** *250* (2), 484-491.
25. Yang, L.; Ge, X.; Wang, M.; Song, L.; He, X., *Materials Letters* **2008,** *62* (3), 429-431.
26. Bartlett, P. N.; Birkin, P. R.; Ghanem, M. A.; Toh, C.-S., *Journal of Materials Chemistry* **2001,** *11* (3), 849-853.
27. Luo, X.; Killard, A. J.; Morrin, A.; Smyth, M. R., *Chemical Communications* **2007,** (30), 3207-3209.

CHAPTER 7 CONCLUSIONS

The aim of this project was to obtain the electrochemical growth of an electroactive microstructured PANI monolith in microfluidic channels. To achieve electropolymerization of PANI within microfluidic channels, an electrochemical cell with a valid electrochemical behavior was embedded within the channel. A fundamental study of fast PS colloidal crystal template fabrication (required to microstructure the PANI monolith) was undertaken and the parameters influencing the PANI growth through the template were investigated. Finally, actuation of electroactive polymers in microchannels was investigated in order to understand the influence that actuation could have on chromatographic separation (the long term goal of EMµ project).

Two different microfluidic Chip Designs were investigated for the production of such a monolith.

CD1 was designed in our laboratory for flow through biosensing. An electrochemical cell was built in a fluidic channel in order to grow PANI as sensing material as well as to monitor targeted analytes. The electrochemical cell was close to ideal as proven by ferricyanide electrochemistry. However, for separations and EMµ project, this CD1 microfluidic chip had several drawbacks. First, it was fabricated from polymethylmethacrylate (PMMA). PMMA dissolved when dissolving the PS colloidal crystal template. Secondly, due to the width of the separation channel (2 mm), evaporation-induced self-assembly had to be used to fabricate the colloidal crystal. The colloidal crystals formed in these channels had a high thickness dispersity within one crystal. Therefore, parts of the channel were overloaded with colloidal crystal and parts of the channel were not fully packed with template. As a consequence, the large fluidic channel was not suitable to fabricate colloidal crystal templates reproducibly. In addition, CFD proved this chip was far from ideal for chromatographic separation in LC mode. The sudden change in channel width and depth between the injection, detection and separation channels created six stagnant zones with a combined volume of 15% of the overall channel. These stagnant zones would produce large band broadening due to the diffusion of analyte from the moving mobile phase into them. It could then be concluded than CD1 microfluidic chip was not suitable for EMµ project.

A new chip design was needed to ensure flow velocity profiles issues were addressed. Base piece of CD2 were fabricated in glass by wet etching by Micronit® so that the use of solvent through the chip was allowed. The channels were all the same width and depth (110 μm x 50 μm respectively). CFD proved that flow velocities generated through the chip were uniform so that this chip could be used for chromatographic separations. In addition, colloidal crystallization in microfluidic channels of such sizes is a well-known process and is facile to set-up. A combination of capillary forces and evaporation induced self-assembly resulted in high quality colloidal crystals with reproducible thicknesses equal to the depth of the channel. Three-electrode set-ups were investigated to fabricate the electrochemical cell necessary for electropolymerization and its control. A three-electrochemical cell fabricated by screen-printing silver onto polyethylene terephtalate (PET) was investigated using ferricyanide electrochemistry. A difference of about 200 mV was found between a commercial reference Ag/AgCl electrode and the pseudo-reference. The electrochemistry of ferricyanide was not fully reversible but quasi-reversible and the flow rate was found to have no influence on the electrochemistry. Therefore it was suitable but not ideal for EMμ. PANI was electropolymerized within the microfluidic channel using this three-electrode electrochemical cell. However, primary current distribution was found to drive the polymerization close to the auxiliary electrode. The PANI polymerized using this set-up was electroactive and switchable as shown by cyclic voltammetry.

Parameters influencing polymer growth through the PS colloidal crystal template were investigated. It was found that the diffusion of large dopant molecules, usually used to increase polymer conductivity and structural stability, through the template proved difficult. Therefore, self-doped PANI monoliths were polymerized through the template. In addition, surfactant concentration in the original PS beads suspensions used to fabricate the template was found to have significant influence on the resulting PANI structures. When utilizing high surfactant concentration, hollow sphere structures were obtained, while low surfactant concentrations lead to inverse opal structures. This phenomenon is probably due to electrostatic repulsion of the beads when rewetting the template coupled with the electrostatic attraction between the aniline monomer and the PS beads.

Attempts to fabricate PANI inverse opals in bonded microfluidic chip were not successful due to the flow resistance created by the template. No flow could be achieved through the template, thus prohibiting polymerization. PANI inverse opals were, therefore, fabricated prior chip bonding. However, due to the beads monomer electrostatic attraction, PANI grew around the beads at the entrance and end of the polymerization area. As a consequence, no opening pores were formed, thus, no flow could be achieved through the monolith.

Finally, PPy inverse opals were electropolymerized prior to chip bonding to investigate redox induced actuation by AFM. PPy was used as an analogue to PANI to investigate its actuation as it did not required acidic media for switching and thus could be used under an AFM probe. AFM results need to be confirmed but it appears that because of the confinement of the polymer, the pore size increased perpendicularly to the channel walls for the polymer situated near the walls and the force created by the expansion of the polymer near the walls "squeezed" the pores situated in the "middle" of the chip perpendicular to the channel walls, the pore size being constant parallel to the channel walls.

Overall, a successful electrochemical cell was embedded within a microfluidic channel and PANI was electropolymerized using it. Colloidal PS crystals were also fabricated and inverse opals structures were obtained within the microfluidic channel.

CHAPTER 8 FURTHER DEVELOPMENTS

Chip Design 2 (base and upper pieces) was designed for the electropolymerization and control of a microstructured monolith for chromatographic separations. Electrochemical cell design to convert a microfluidic channel into a flow-through electrochemical reactor was successful. Chip Design 2 could therefore potentially be utilized for continuous electrochemical reactions. This would add a new tool to microfluidic platforms.

8.1 CHIP DESIGN 2 ASSESSMENT FOR CHROMATOGRAPHIC SEPARATION UNDER PRESSURE DRIVEN AND ELECTROOSMOTIC FLOW

Chip Design 2 (CD2), presented in Chapter 3 and 4, has shown potential for application in EMμ and thus performance for chromatographic separation needs to be assessed. As shown in Chapter 4, Figure 4.22, electrodes for a capacitively coupled contactless conductivity detector (C^4D) have been included on the screen-printed upper piece of the microfluidic chip. First, using a PDF and without stationary phase, the viability of the detector needs to be tested. A study is undergoing and preliminary results show a response of the detector to plugs of NaCl at different concentrations. However, the responses are not stable, probably due to electro-magnetic and vibration interferences. The chip has been placed in a Faradic cage, to help eliminate the electro-magnetic interferences. The design of the electrodes for the C^4D needs to be optimized in term of electrode size and gap width between the two electrodes. A Faradic shield between the two electrodes should not be necessary as they are in anti-parallel configuration.

Following optimization of the detector, the influence of PANI on electroosmotic flow should be addressed by using a coating of PANI electrochemically grown in the microfluidic channel. PANI emeraldine base carries a positive charge on its surface and glass carries a negative charge. Therefore an EOF of opposite direction could be generated on each material. However, by altering the surface property of the aniline by switching between its different oxidation states, the EOF generated on the PANI surface could be altered. Therefore, using a neutral analyte, such as caffeine, the velocity of the generated EOF could be assessed, thus ascertaining the influence of PANI on the overall EOF velocity. PANI could then serves as an EOF enhancer, modifier or suppressor for chip electrophoresis.

8.2 FUTHER DEVELOPMENTS IN ON-CHIP ELECTROCHEMICAL CELL DESIGN

Development of on-chip electrochemical cells have been driven in the last decade by the incorporation of three-electrode cells on-chip for electrochemical detection after separation or enzymatic reaction for biosensing (see Chapter 4 Section 4.1.2). To date few devices incorporate a fully functional on-chip electrochemical flow through cell capable of performing electrochemical reactions[1, 2]. In Chapters 3 and 4, CD2 was shown to be potentially suitable for both separations and for performing electrochemical reactions on-chip (*i.e.* electropolymerization of aniline). However, the electrochemistry of ferricyanide was only quasi-reversible and the electrode configuration lead to inhomogeneous growth of PANI along the length of the working electrode due to primary current densities. In order to remedy this issue, a new Chip Design is required.

From the two-electrode cell design presented by Simms *et al.*[1] and discussed in Chapter 4, a three-electrode electrochemical cell design could be derived. By modifying the existing two electrodes (steel and glassy carbon) to a working and a combination of reference and auxiliary electrodes, a three-electrode electrochemical cell could be formed (Figure 8.1). The reference and auxiliary electrodes could be fabricated by screen-printing or by using the lift-off method. The lift-off method would be preferential as a greater number of metals can be deposited. Ideally platinum would be deposited as the auxiliary electrode and silver (coated with AgCl) as a pseudo-reference electrode. The working electrode, on the other end, could be fabricated by lift-off from carbon, gold or platinum for optimal electrochemistry. Several designs would need to be investigated (*e.g.* serpentine, interdigit, *etc*) in order to determine which electrode configuration would be most suited for electropolymerization of conductive polymer and subsequent control of the polymer. The distance between the auxiliary and reference electrodes and the working electrode should be kept constant along the working electrode and the surface area of the auxiliary electrode should be maximized so that the electrochemical reactions are not limited by surface area. In addition, channel size should be kept to a minimum so that capillary action induced colloidal crystallization could be performed to fabricate the sacrificial template necessary to microstructure the electroactive polymer monoliths.

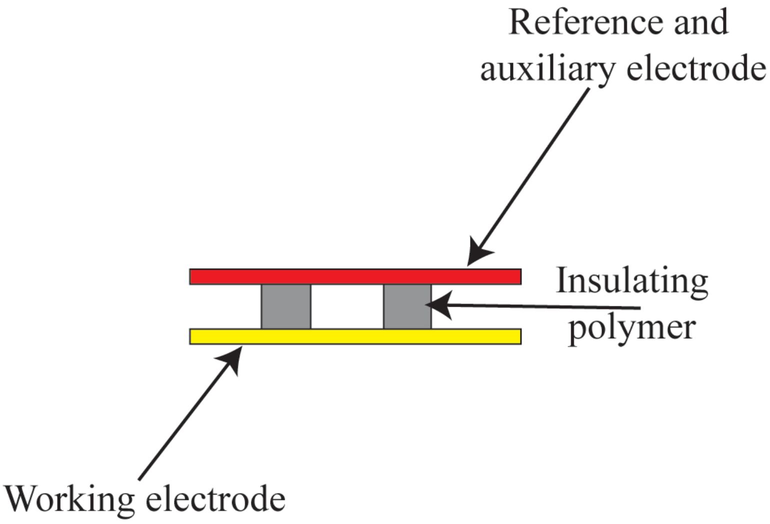

Figure 8.1: Scheme of cross section of proposed microfluidic chip suitable for EMμ.

The benefits of this design would be that the electrochemistry performed in such an electrochemical cell would be as close to ideal as possible. By having a constant auxiliary electrode to working electrode distance, primary current distribution should not influence polymer growth in specific areas of the working electrode and thus polymer growth should be homogeneous through the whole length of the channel. However, polymerization times could be increased to polymerize the desired thickness as the working electrode would not include the channel walls (as in CD2). Such a microfluidic device would also be extremely beneficial to the field of microfluidics and lab-on-chip technology in general by adding a novel tool to perform continuous flow-through electrochemical reactions in microfluidic platforms.

8.3 FURTHER DEVELOPMENTS OF TEMPLATES TO MICROSTRUCTURE ELECTROACTIVE POLYMER ON CHIP

In the microfluidic devices presented in this research, electropolyamerization of aniline occurred prior to chip bonding because no flow of monomer mixture was achieved through the template when the chip was bonded. To limit channeling (presence of a gap between the stationary phase and one or several channel walls) at its minimum electroactive polymers need to be polymerized directly in closed chip so that no gap is formed between stationary phase and channel walls upon chip bonding.

The use of PS beads of diameter greater than 1 µm needs to be employed in order to achieve significant flow rate through the colloidal crystal template. However, in commercially available PS bead suspensions with diameter superior to approximately 3 µm, PS is cross-linked with divinyl benzene. The cross linker makes these beads insoluble in common solvent. 3 µm particles should enable a sufficient monomer mixture flow for polymer electropolymerization. In addition, it was shown in chapter 6, that the use of PS beads with a negative surface charge would create monolith with no pores at the entrance and end of it because of monomers (oligomers)-template electrostatic attraction. The use of PS beads carrying a positively charged surface is therefore recommended. The electrostatic repulsion of the template and monomers (oligomers) would create open pores at the entrance and end of the monolith so that a flow can be applied through it. I could also increase the interconnecting pores in the monolith, as no polymer would be formed near the beads contact points.

However, the resistance to the flow would increase when growing the polymer through the template. If the resistance increases to a level where no flow can be achieved, a new templating method would be needed. As seen in Chapter 5, several templating methods have been discussed and colloidal crystal template seemed to be the best templating method available to microstructure the monolith for the EMµ project. However flow needed through the template is an issue.

Of the templating methods described in Chapter 5, only the use of membrane and possibly high internal phase emulsions (HIPE) could give structured electroactive polymer by electropolymerization. The use of a membrane, however, gives rods or tubules so they cannot be used. HIPE could be used by using the aqueous monomer mixture, as the continuous phase and organic solvent as the dispersed phase. After loading the emulsion through the channel, the aqueous monomer mixture could be electropolymerized. After polymerization, application of a flow should wash the dispersed phase leading the desired structured material. However, application of an electric field could disrupt the emulsion leading to a phase separation thus to loss of the microstructure of the monolith.

This approach would improve the permeability of the monolith and would suppress the issue of applying a flow through a hard template. However, the monolithic material formed using this technique would not show any ordered structures, therefore column efficiency would not be increased as much as if using a periodically ordered structure (see Chapter 1, Section 1.5).

Another alternative would be to use a crack-free colloidal crystal template and to replicate it with gold nanoparticles as done by Velev[3] before bonding the chip. After removal of the colloidal crystal, an inverse opal structure of gold is obtained. The chip can then be bonded. The gold inverse opal is then used as an electrode and a thin film of electroactive polymer could be deposited onto it by electropolymerization.

This approach would create robust monolith with controllable properties. The pore size could be controlled by the size of the colloidal particles used as sacrificial template, by the amount of polymer electropolymerized on the gold inverse opals and, probably, by actuating the polymer at the surface of the electrode[4]. In addition, when switching the electroactive polymer, no channeling would be created by the change of volume of the polymer. According to the AFM study performed in Chapter 6, the actuation of electroactive polymer inverse opal structures deform the pores due to changes in the polymer volume by the intake of solvated ions. The change in polymer volume could lead to channeling as the polymer is only in contact with three of the four faces of the channel. This would be prevented prevented by the incorporation of the gold inverse opal.

If these improvements were successfully incorporated into EMμ, this ambitious project could be realized. This could have a considerable impact on the LOC community, as it would be the first device to enable dynamic separations on microfluidic device. In addition, the growth of such structures in microfluidic devices could potentially be used for manipulating flows on microfluidic device as they could be used as electro-valves or filters with adjustable pores.

8.4 REFERENCES

1. Simms, R.; Dubinsky, S.; Yudin, A.; Kumacheva, E., *Lab on a Chip* **2009,** *9* (16), 2395-2397.

2. Illa, X.; Ordeig, O.; Snakenborg, D.; Romano-Rodriguez, A.; Compton, R. G.; Kutter, J. P., *Lab on a Chip* **2010,** *10* (10), 1254-1261.

3. Velev, O. D.; Tessier, P. M.; Lenhoff, A. M.; Kaler, E. W., *Nature* **1999,** *401* (6753), 548-548.

4. Wu, Y.; Nolan, L.; Coyle, S.; Lau, K. T.; Wallace, G. G.; Diamond, D. In *Polypyrrole based Switchable Filter System*, 29th Annual International Conference of the IEEE Engineering in Medicine and Biology Society, Lyon, France, Lyon, France, 2007; pp 4090-4091.

LIST OF PUBLICATIONS AND PRESENTATIONS

PAPERS

- Jeremy Galineau, Aoife Morrin, Malcolm R. Smyth, Blanaid White.
  Fast colloidal crystallization in fluidic channels
  Manuscript in preparation

- Jeremy Galineau, Blanaid White, Aoife Morrin, Malcolm R. Smyth
  Effect of surfactant on conducting polymer templated microstructures
  Manuscript in preparation

- Jeremy Galineau, Blanaid White, Aoife Morrin, Malcolm R. Smyth
  Electrochemical actuation of microstructured polypyrrole in microfluidic channels

  Manuscript in preparation

POSTER PRESENTATIONS

- **Analytical Research Forum**

University of Hull, United Kingdom, 21-23 July 2008

EMμ: the next generation of separation science

Jeremy Galineau, Blanaid White, Aoife Morrin, Malcolm R. Smyth

- **Pittcon**

Chicago, Il, USA

Colloidal crystallization in fluidic channels: towards optical chromatography

Jeremy Galineau, Blanaid White, Aoife Morrin, Malcolm R. Smyth

5th best poster award in its category

- **21st International Ion Chromatography Symposium (IICS 2009)**

Malahide, Co. Dublin, Ireland, 21-24 September 2009

EMμ: The next generation of separation science

Jeremy Galineau, Blanaid White, Aoife Morrin, Malcolm R. Smyth

- **Lab-on-a-Chip European Congress 2009**

Dublin, Ireland, 19-20 May 2009

Development of a Fully Integrated Microfluidic Device for Electromodulated Liquid Chromatography with C4D Detection

Jeremy Galineau, Blanaid White, Aoife Morrin, Malcolm R. Smyth

Best Poster award

ORAL PRESENTATIONS

- **HPLC 2009**

Dresden, Germany, 28th June - 2nd July 2009

EMμ: The next generation of separation science

- **National Center for Sensor Research 10th anniversary Symposium**

Dublin City University Ireland, 22nd October 2009

EMμ: The next generation of separation science

APPENDIX 1: CHIP DESIGN 1

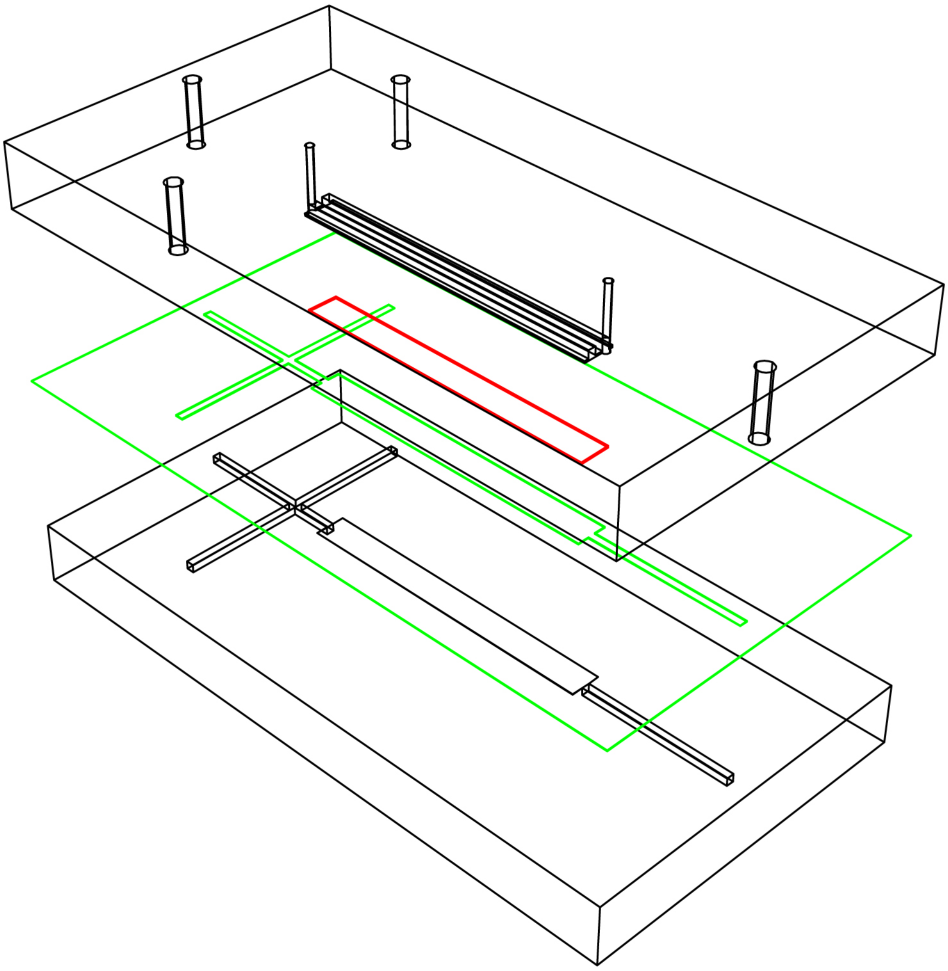

Appendix 1.1: 3-dimensional representation of CD1 with base and upper pieces (black), pressure sensitive adhesive (green) and PVDF membrane (red).

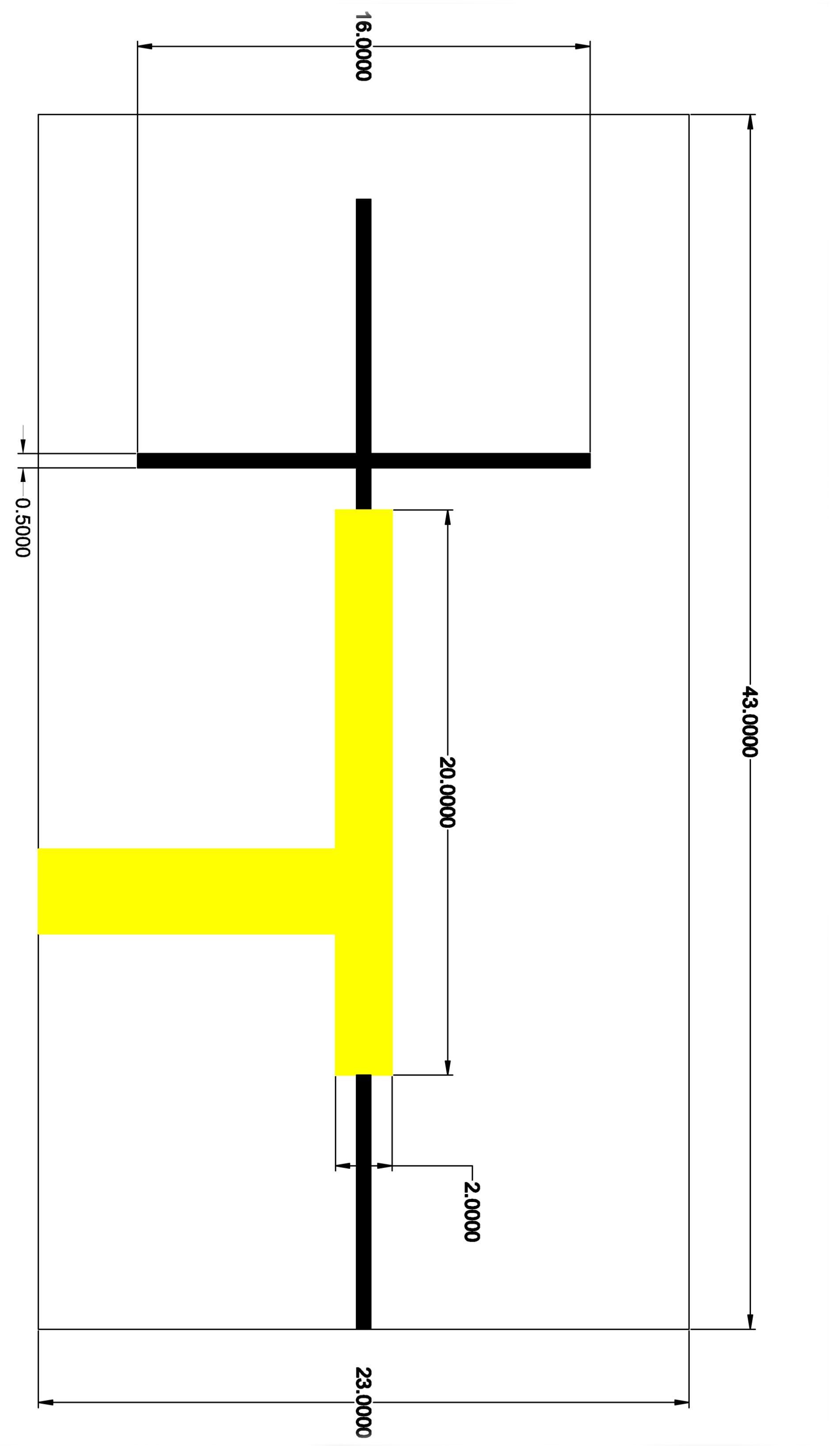

Appendix 1.2: Base piece of CD1 chip with a T-bare gold-sputtered (yellow) in the fluidic channel coating serving as the working electrode and the electrical connection from the working electrode to the edge of the chip.

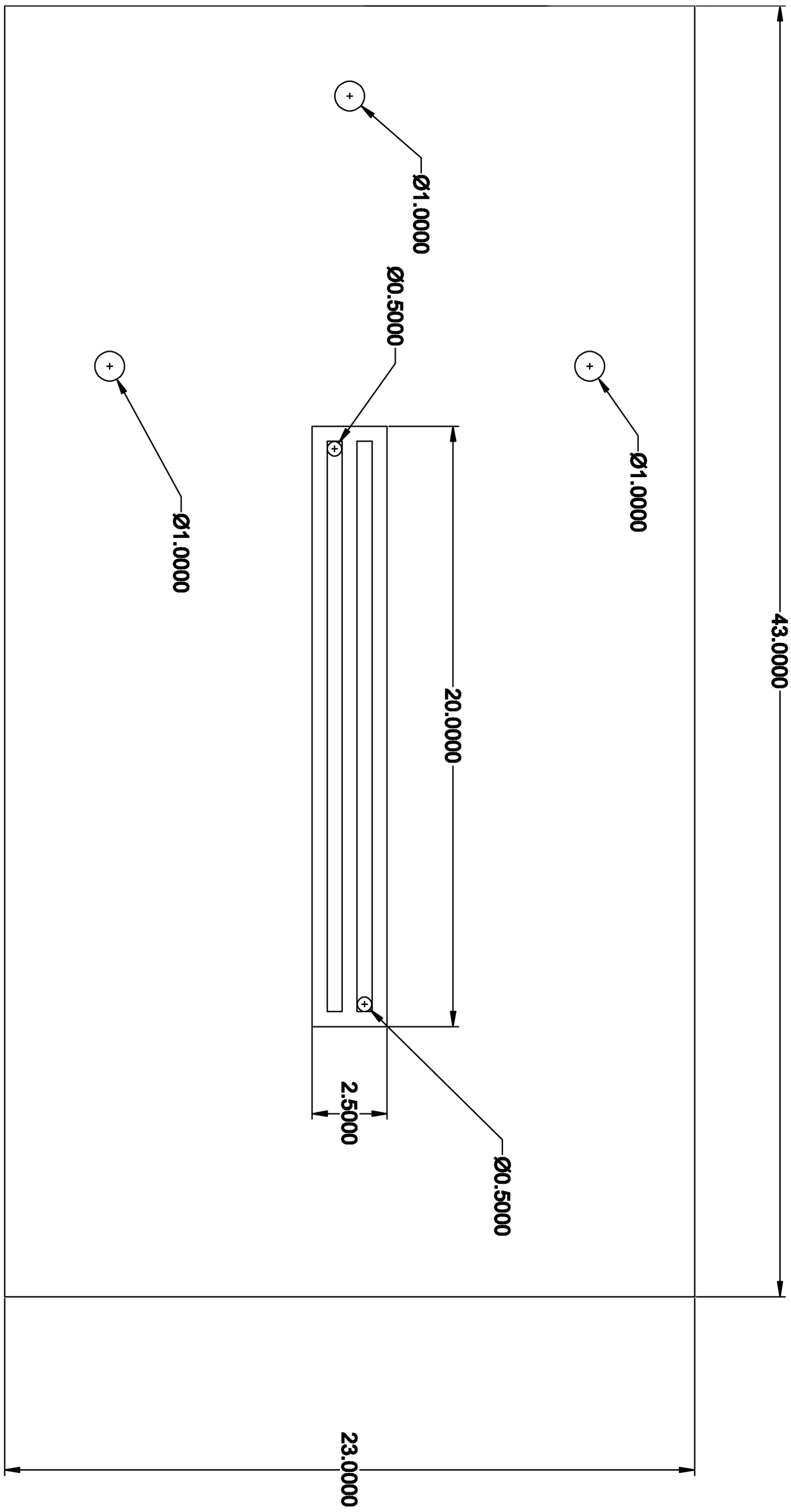

Appendix 1.3: Upper piece of CD1 chip showing the two channels for housing the reference and auxiliary electrodes and the pocket to house the PVDF membrane.

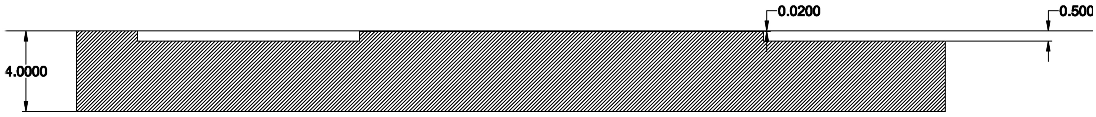

Appendix 1.4a: Longitudinal cross section of the base piece of CD1 chip. Injection and detection channels are 500 µm deep and the separation channel 20 µm deep.

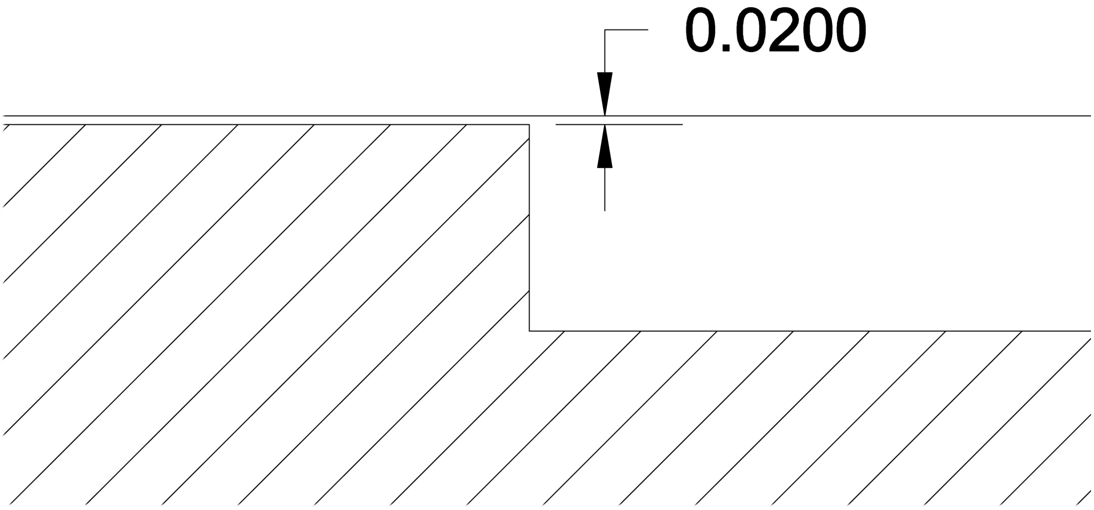

Appendix 1.4b: Close up of Appendix 1.4a at the junction between the separation and detection channels. The same junction exists between the injection and separation channels.

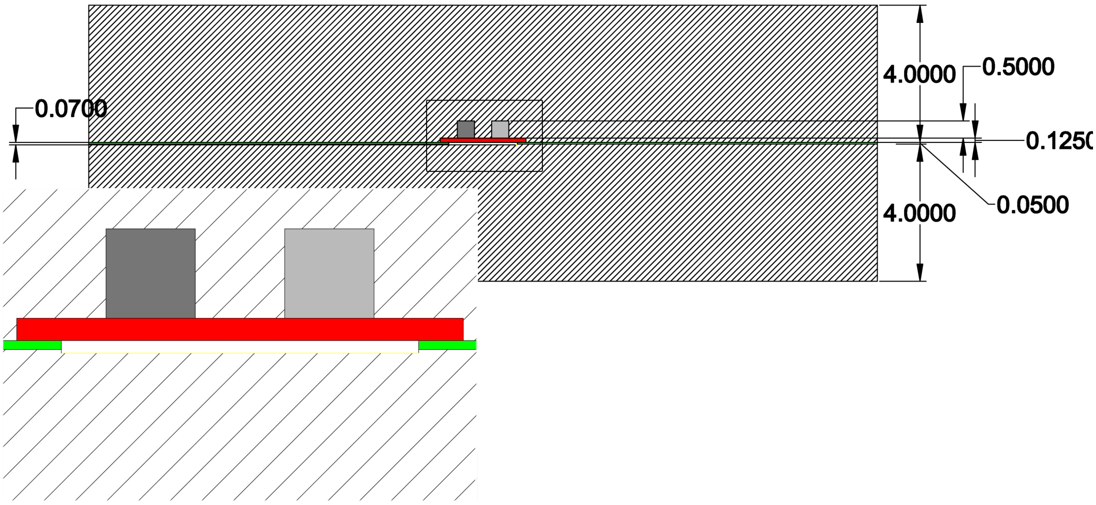

Appendix 1.5: Cross section of bonded CD1 chip showing PSA (green), PVDF membrane (red), reference electrode (dark grey) and auxiliary electrode (light grey).

APPENDIX 2: CHIP DESIGN 2

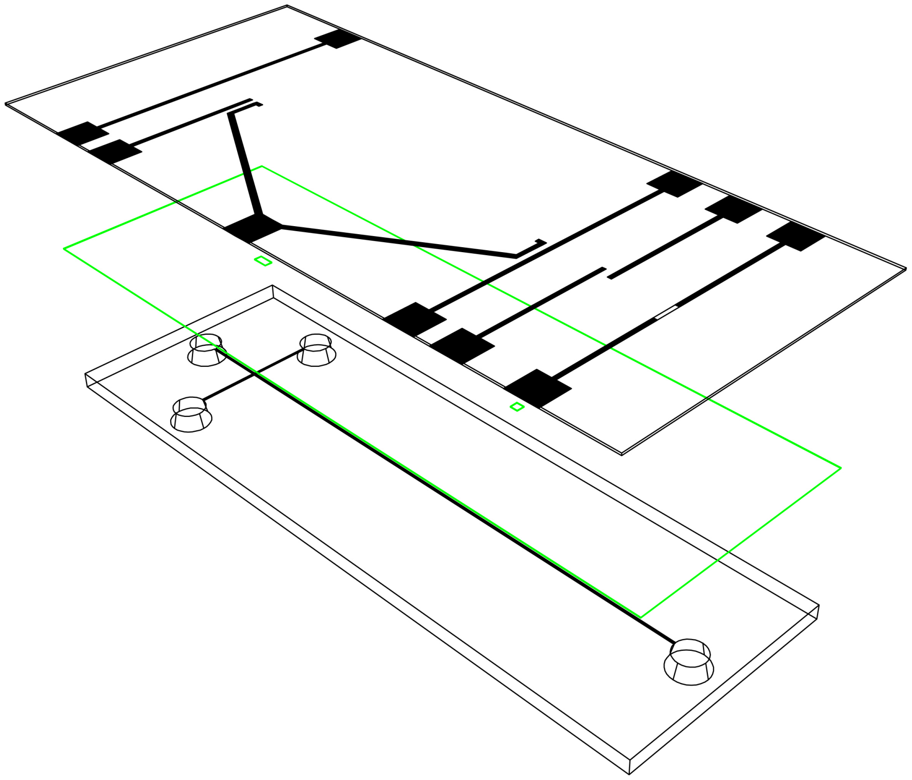

Appendix 2.1: 3-dimensional representation of CD2 chip showing base and upper pieces (black) and PSA (green).

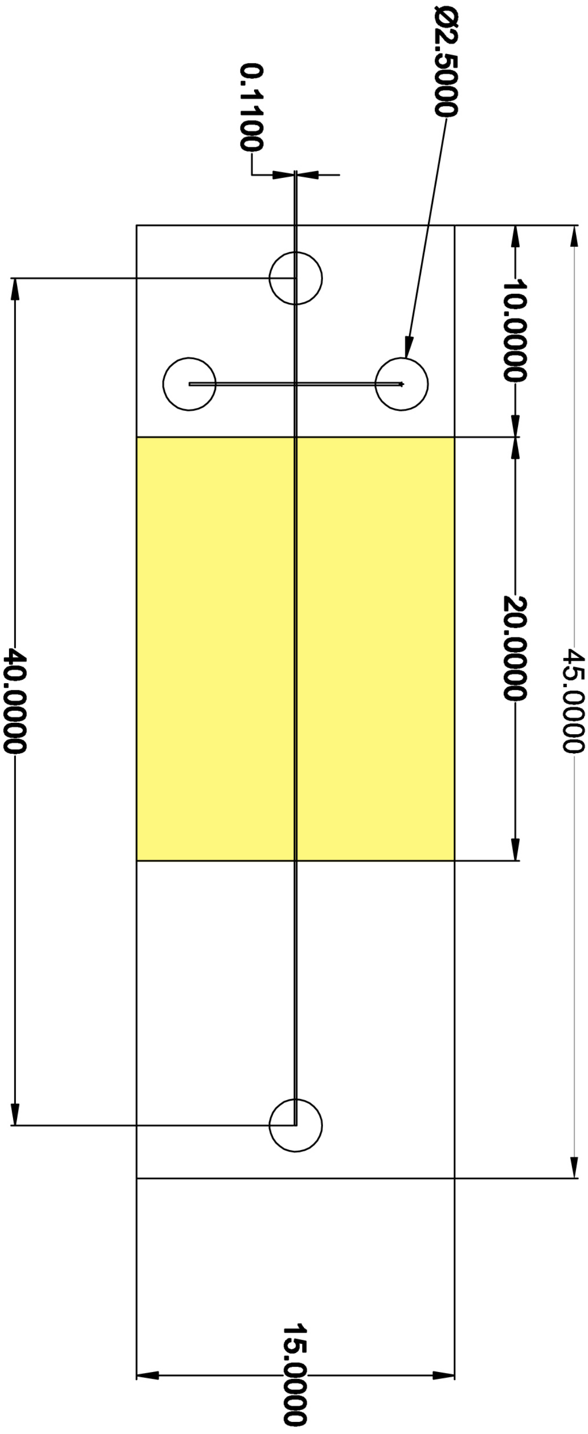

Appendix 2.2: Base piece of CD2 chip. Gold-sputtered electrode film serving as the working electrode is displayed in yellow.

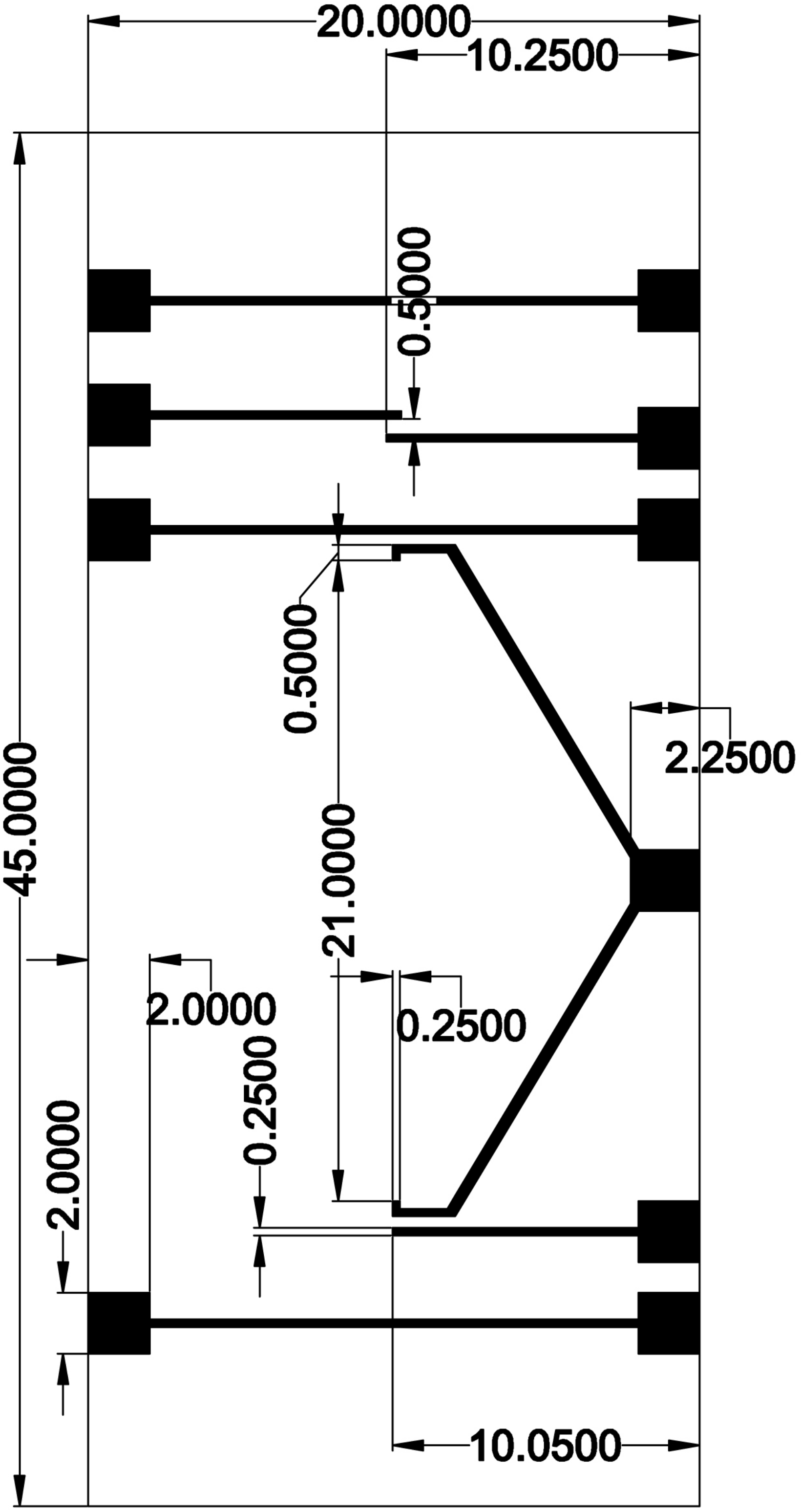

Appendix 2.3: Upper piece of CD2 chip. Electrodes (black) are screen-printed using a silver paste onto PET substrate.

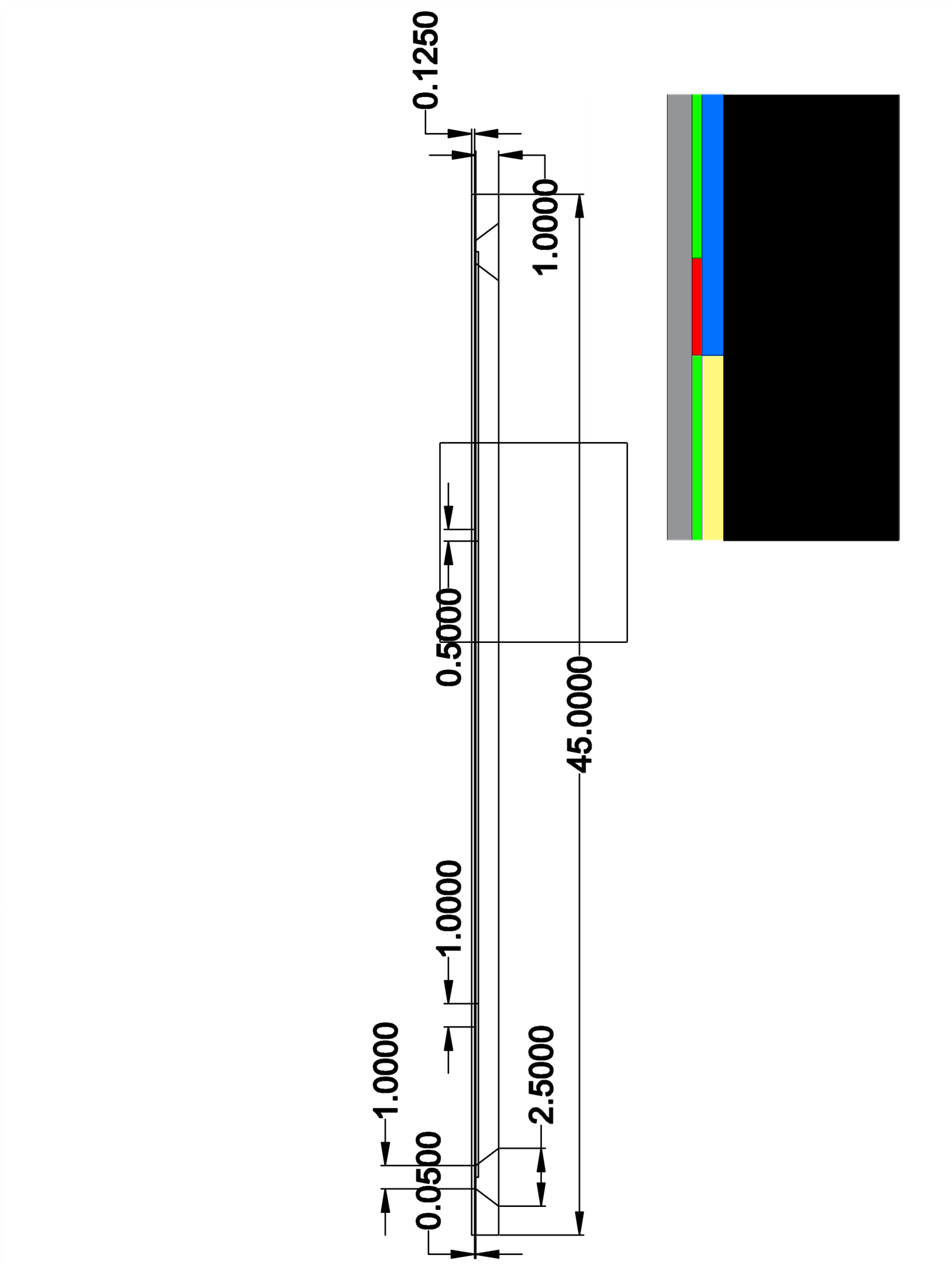

Appendix 2.4: Longitudinal cross section of closed CD2. Insert: close up on the region contained in the black square showing upper piece (grey), PSA (green), PSA cut (red), gold-sputtered channel (working electrode) (yellow), channel (not gold sputtered (blue), glass (black).

APPENDIX 3: CHIP HOLDER

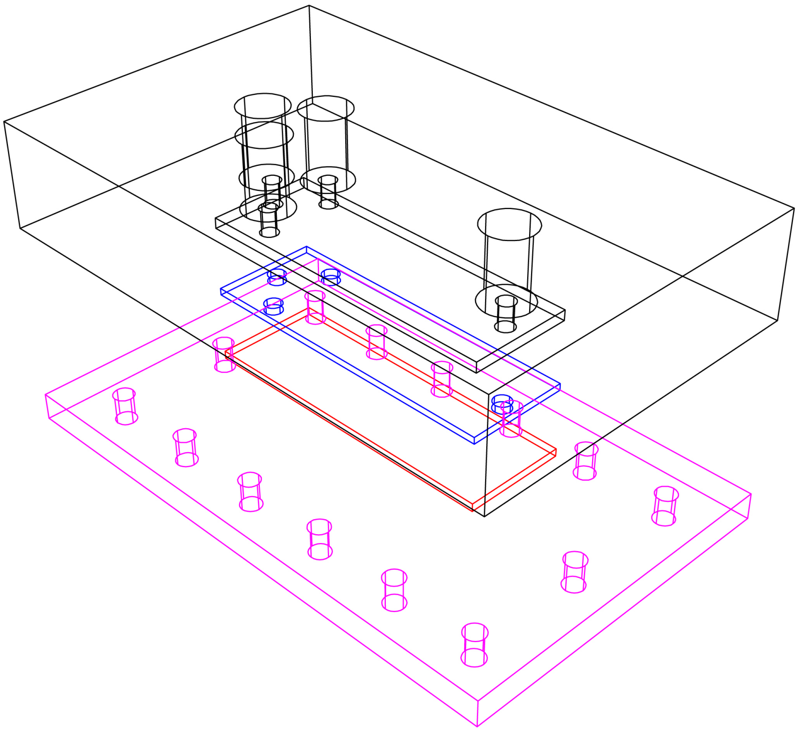

Appendix 3.1: 3D representation of the chip holder (base piece (magenta) and upper piece (black) with PDMS gasket (blue) and bonded CD2 (red). For visibility, holes for bolts in the upper piece are omitted.

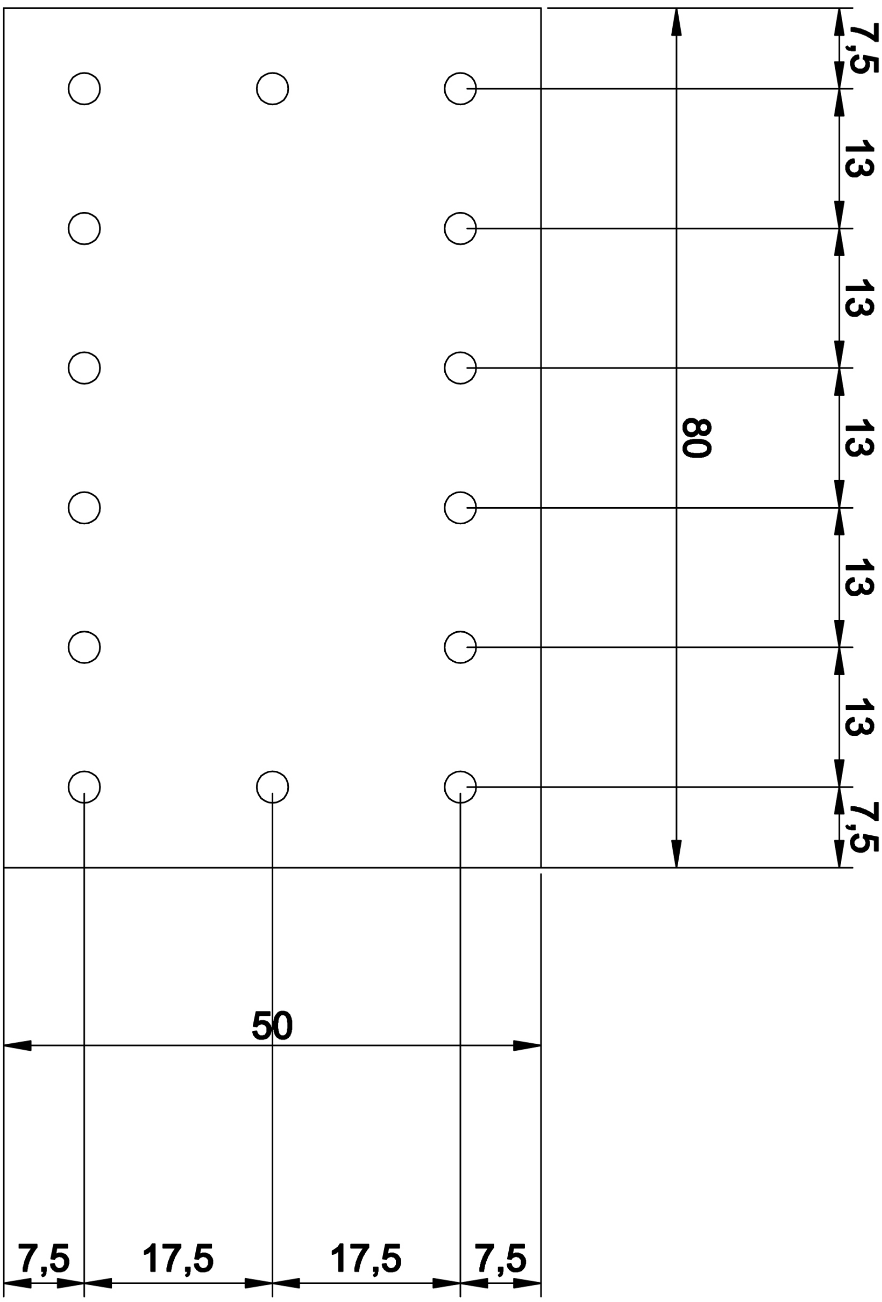

Appendix 3.2: Base piece of the chip holder

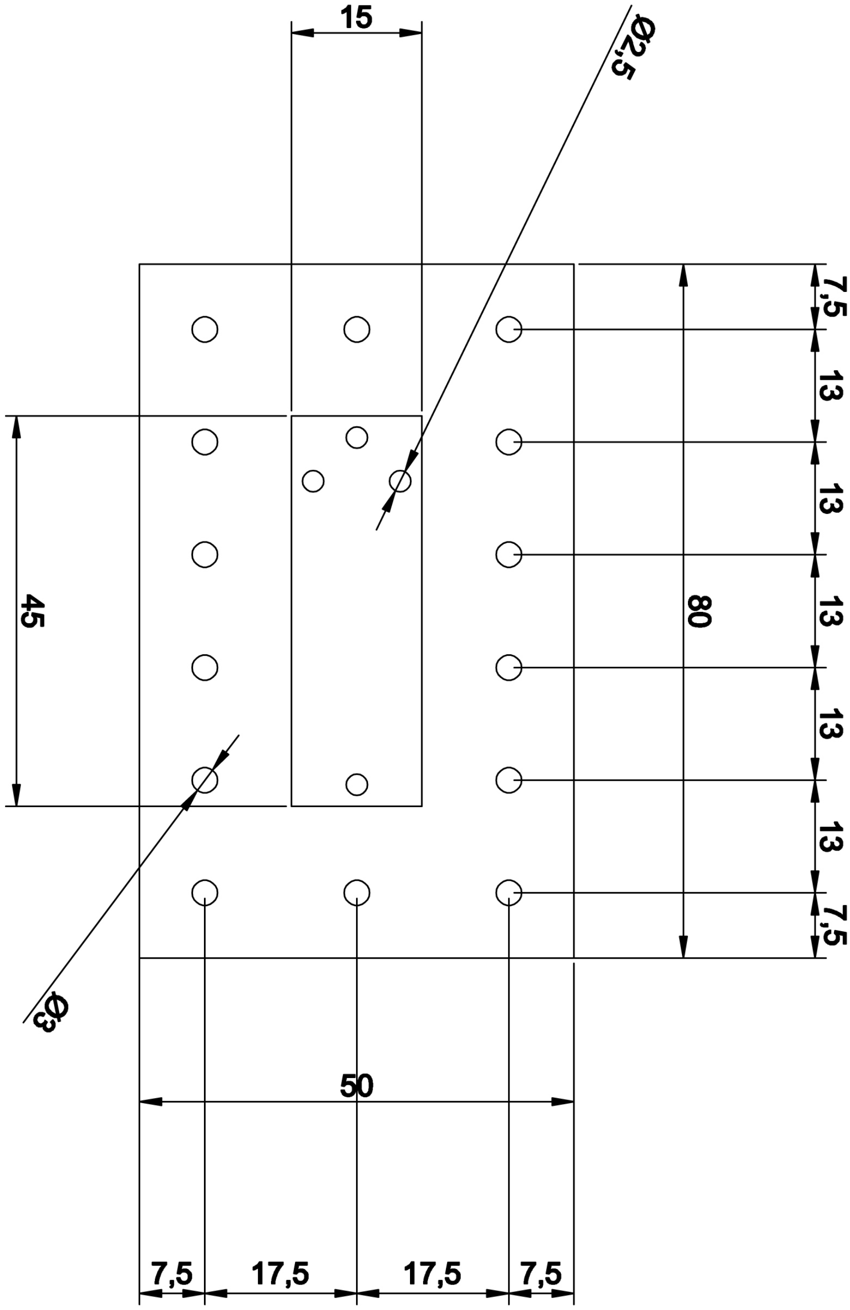

Appendix 3.3: Upper piece of the chip holder (side facing the chip)

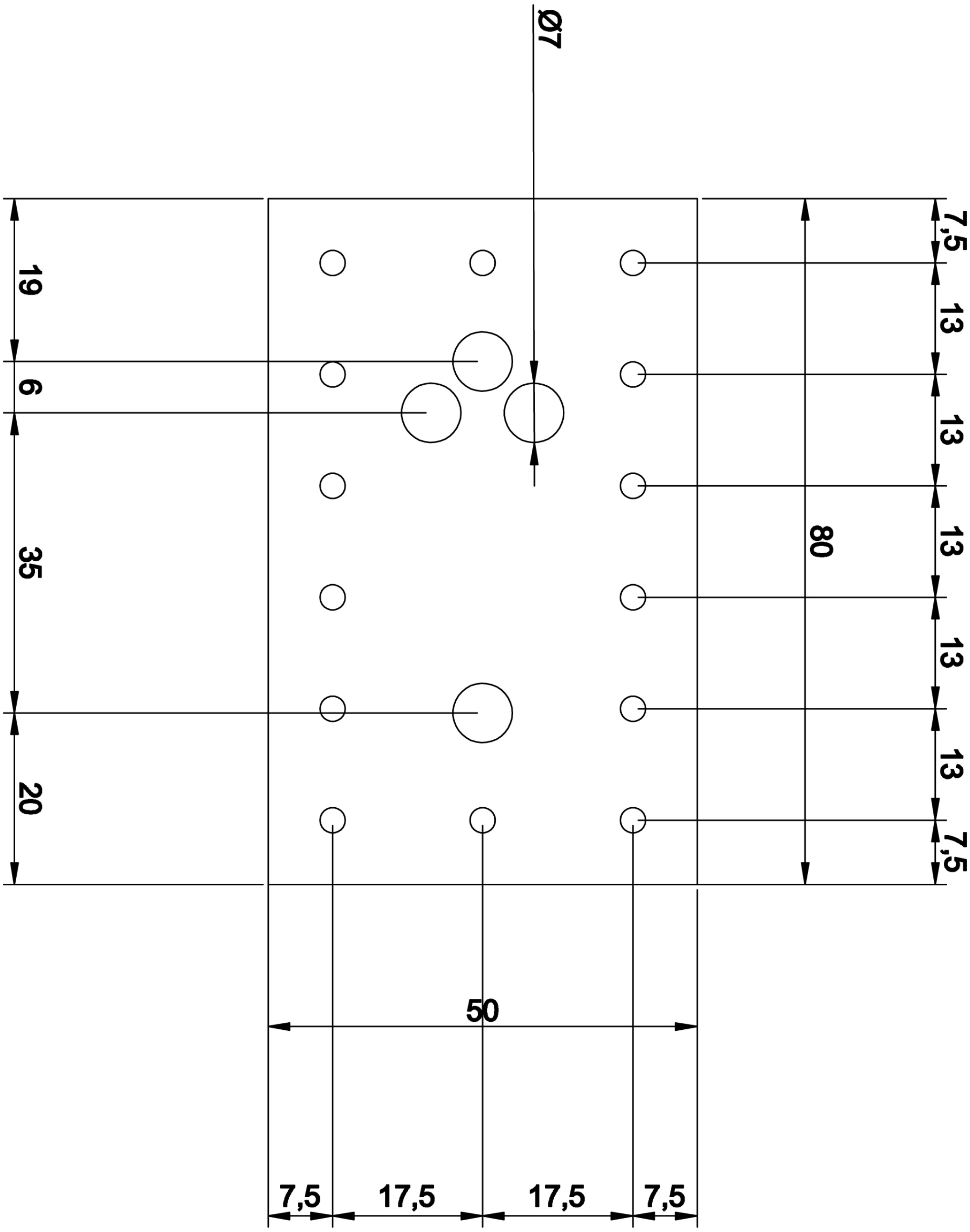

Appendix 3.4: Upper piece of the chip holder (external face). The 7 mm holes are threaded for fluidic connections.

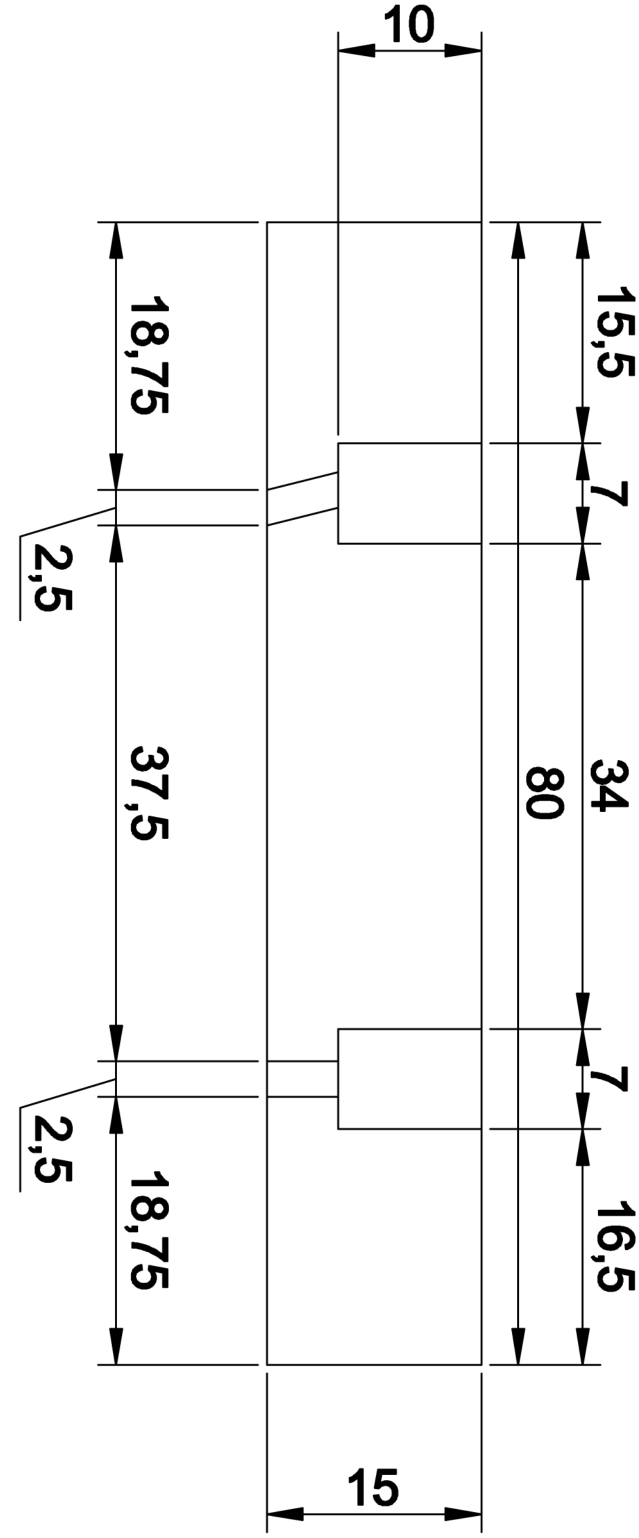

Appendix 3.5: Longitudinal cross section of the upper piece of the chip holder.